Synthesis and high-temperature oxidation of ternary carbide coatings on zirconium-based alloy cladding

Zur Erlangung des akademischen Grades

Doktor der Ingenieurwissenschaften

Von der KIT-Fakultät für Maschinenbau des

Karlsruher Instituts für Technologie (KIT)

genehmigte

Dissertation

von

Chongchong Tang

aus Henan, China

Tag der mündlichen Prüfung: 12.02.2019

Hauptreferent: Prof. Dr. Hans Jürgen Seifert

Korreferent: Prof. Dr. Jochen M. Schneider

Abstract

Zirconium-based alloy claddings used for current light water reactors (LWRs) possess a variety of desirable features in steady-state normal operation, however, constraints regarding fast degradation, rapid exothermic reaction with high-temperature steam associated with hydrogen generation in accident scenarios motivate the requisite to develop enhanced accident tolerant fuel (ATF) claddings. One reasonable solution to improve the accident tolerance of the zirconium alloy cladding in accidental conditions while preserving its excellent behavior under normal operating conditions is external surface modification via such as coatings deposition. In addition, protective coatings applied to the zirconium alloy claddings offer the potential benefits of drastically reduced corrosion and degradation during normal operation, which are expected for application within the design framework of both current and future generation LWRs. The $M_{n+1}AX_n$ (MAX) phase materials comprise an extended family of layered, hexagonal ternary carbides and nitrides. They combine many attractive properties of both ceramics and metals stemming from their unique layered crystal structures and bonding characteristics; certain Al-MAX phases also possess excellent high-temperature oxidation resistance and chemical compatibility with select coolants such as hot water and molten lead. The objectives of this work are to synthesize and to evaluate three Al-containing MAX phase carbides (Ti_2AlC, Zr_2AlC and Cr_2AlC) as potential protective coatings on Zircaloy-4 substrates with an emphasis on their high-temperature oxidation performance in steam.

Oxidation of one commercial bulk Al-MAX phase Ti_2AlC (Maxthal 211®), as reference/benchmark material, in steam in the temperature range of 1400°C - 1600°C was investigated to validate its high-temperature oxidation resistance and ascertain its potential as protective coatings. Oxidation of bulk Ti_2AlC MAX phase ceramic at 1400°C and 1500°C formed a continuous coarse α-Al_2O_3 scale with randomly distributed Al_2TiO_5 isolated areas on the surface. The oxide scale thickening rate of Ti_2AlC is more than three orders of magnitude lower than that of Zircaloy-4 at 1400°C and the maximum tolerance temperature of Ti_2AlC in steam is approximately 1555°C. Therefore, these findings hold great promise of Al-containing MAX phase carbides, especially Ti_2AlC, as oxidation resistant coating on zirconium-based alloy claddings.

An innovative two-step approach has been established, i.e. first magnetron sputtering of nanoscale elemental multilayer stacks and subsequently thermal annealing in argon, for potential growth of phase-pure MAX phase coatings. The crystallization behavior and phase evolution of the as-deposited multilayers during annealing were systematically investigated using a diverse range of characterization and analytical techniques. The mechanical properties of designated coatings were evaluated by means of scratch tests and nanoindentation. Thermal annealing of the nanoscale elemental multilayer stacks (transition metal layer/carbon layer/aluminum layer) in argon revealed that onset crystallization temperatures of the Ti_2AlC and Cr_2AlC MAX phase from competing binary carbides and intermetallic phases locate at around 660°C and 480°C, respectively. Phase-pure Ti_2AlC and Cr_2AlC coatings were successfully fabricated, but the formation of a mixed ternary Zr(Al)C carbide rather than the Zr_2AlC MAX phase was confirmed. Both MAX phase coatings have a basal-plane preferred orientation with the *c*-axis

perpendicular to the sample surface and the multilayer stacks. The Zr/C/Al coatings crystallized to a cubic, solid solution Zr(Al)C phase with a B1 NaCl crystal structure. The phase evolution during annealing appears associated with the thermodynamic stability of corresponding MAX phases and their counterpart binary carbides.

Coatings of altered designs with respect to introducing diffusion barrier or overlayer were deposited on Zircaloy-4 substrates. The coating thicknesses are 5~6 μm. Oxidation performance and degradation of these coatings during exposure in steam at elevated temperatures were investigated by thermogravimetric analysis and examining the microstructural evolution of the coating-substrate system. Steam oxidation tests found no protective effect of the Ti_2AlC and Zr(Al)C based coatings with significant spallation and cracking from around 1000°C. Growth of an Al_2O_3-rich layer with TiO_2 or ZrO_2 layer beneath for the Ti_2AlC and Zr(Al)C based coatings, respectively, was observed rather than a dense alumina layer. The failure of the Ti_2AlC and Zr(Al)C based coatings from 1000°C can be attributed to the low thickness of the coatings, high interdiffusion rate between coating and substrate and potential phase transformation of the oxide products. The Cr_2AlC-based coatings possess superior oxidation resistance up to at least 1200°C and autonomous self-healing capability with a thin and dense α-Al_2O_3 layer growth. Another design with a thin Cr overlayer above the Cr_2AlC coating was further developed to eliminate potential fast hydrothermal dissolution of Al during normal operation.

Moreover, first neutron radiography investigations of hydrogen permeability through the Ti_2AlC and Cr_2AlC MAX phase coatings on Zircaloy-4 substrates were reported. Hydrogen permeation experiments through non-oxidized and pre-oxidized Ti_2AlC and Cr_2AlC MAX phase coatings on Zircaloy-4 evidenced that both coatings are robust hydrogen diffusion barriers and impede hydrogen permeation into the matrix efficiently. The unique microstructural features of the coatings, namely free of columnar growth and highly basal-plane textured grains owing to the two-step approach, improve their efficiency in limiting hydrogen permeation as a barrier.

Zusammenfassung

Zirkoniumlegierungen finden aufgrund ihrer guten Eigenschaften bei Betriebsbedingungen in Leichtwasserreaktoren (LWR) weltweit Einsatz als Hüllrohre für den nuklearen Brennstoff. Bei Störfallbedingungen mit den damit verbundenen hohen Temperaturen führt die exotherme Oxidation von Zirkonium in Wasserdampf allerdings zur Freisetzung von Wasserstoff und Wärme sowie zur Verschlechterung der mechanischen Eigenschaften der Hüllrohre. Insbesondere nach den Fukushima Reaktorunfällen wird deshalb weltweit nach Reaktormaterialien (Brennstoff, Hüllrohre) mit erhöhter Unfalltoleranz (ATF – accident tolerant fuels) gesucht. Eine naheliegende Lösung dafür ist die Beschichtung von Zirkonium-Hüllrohren mit oxidationsresistenten Materialien, die die Eigenschaften von Hüllrohren sowohl während des Betriebes als auch bei Störfallbedingungen verbessern. $M_{n+1}AX_n$ (MAX) Phasen sind dafür eine erfolgversprechende Materialfamilie. Diese ternären Karbide oder Nitride kombinieren aufgrund ihrer speziellen Schichtstruktur Eigenschaften von Metallen und Keramiken. Al-MAX-Phasen sind für ihre sehr guten Korrosions- und Oxidationseigenschaften bekannt. Im Rahmen dieser Arbeit wurden drei Al-haltige MAX Phasen-Karbide (Ti_2AlC, Zr_2AlC und Cr_2AlC) als potentielle Schutzschichten für Zirkoniumlegierungen synthetisiert und charakterisiert.

In einem ersten Schritt wurde die Oxidation der kommerziellem Al-MAX Phase Ti_2AlC (Maxthal 211®) im Temperaturbereich 1400°C - 1600°C in Wasserdampf untersucht. Bei Temperaturen von 1400°C und 1500°C bildeten sich auf der Oberfläche der Bulkproben durchgängige und schützende α-Al_2O_3 Schichten mit zufällig verteilten Al_2TiO_5 Bereichen. Die Oxidschichtdicken auf diesen Proben waren bei 1400°C um drei Größenordnungen geringer als bei Zirkoniumlegierungen. Die maximale Temperatur für die Bildung einer schützenden Oxidschicht in Dampf lag bei ca. 1555°C. Basierend auf diesen erfolgversprechenden Ergebnissen mit Bulkmaterial wurden die drei oben genannten aluminiumhaltige MAX Phasen für die Herstellung von Schutzschichten ausgewählt.

Für die Synthese dieser Beschichtungen wurden mittels Magnetronsputtern nanometerdicke Schichtfolgen der entsprechenden Elemente auf dem Substrat abgeschieden und diese zur Bildung von phasenreinen Schichten thermisch geglüht. Das Kristallisationsverhalten der Beschichtungen wurde mittels verschiedener Methoden in Abhängigkeit von der Temperatur untersucht. Die mechanischen Eigenschaften der Schichten wurden mittels Ritzversuchen und Nanoindentierung analysiert. Die Glühversuche resultierten in phasenreinen Ti_2AlC und Cr_2AlC MAX Phasen bei 660°C bzw. 480°C. Im System Al-Zr-C konnten keine einphasigen MAX Beschichtungen synthetisiert werden; stattdessen wurde ternäres Zr(Al)C Karbides erhalten. Die beiden erfolgreich synthetisierten MAX Phase weisen eine kristallographische Orientierung der c-Achse senkrecht zur Oberfläche des Substrats und der Multilagen auf. Die Zr/C/Al Beschichtungen kristallisierten in einer kubischen Mischkristallphase mit B1 NaCl Struktur. Die unterschiedlichen Phasenbildungen in den drei Systemen konnten mit den relativen thermodynamischen Stabilitäten der MAX Phasen sowie der entsprechenden binären Karbide erklärt werden.

Optimierte Beschichtungen mit Diffusionsbarrieren und Oberflächenschutzschichten wurden auf Zircaloy-4 Substraten mit einem Dicken von 5-6 µm aufgebracht. Das Oxidations- und Degradationsverhalten dieser Schichtsysteme bei hohen Temperaturen wurde mittels Thermogravimetrie und metallographischen Untersuchungen charakterisiert. Ti_2AlC und Zr(Al)C basierte Beschichtungen bildeten bei 1000°C keine schützende Oxidschichten aufgrund von Abplatzungen und signifikanter Rissbildung. Das Versagen der Ti_2AlC und Zr(Al)C Schichten wurde mit hohen Diffusionsraten zwischen Beschichtung und Substrat sowie Phasenübergängen der gebildeten Oxide erklärt. Dagegen weisen die Cr_2AlC Beschichtungen ein ausgezeichnetes Oxidationsschutzverhalten bis zumindest 1200°C durch die Bildung einer schützenden α-Al_2O_3 Schicht mit ausgeprägten Selbstheilungseigenschaften auf. Zur Unterdrückung der hydrothermalen Korrosion von Aluminiumoxid bei Betriebsbedingungen wurde ein Schichtsystem mit zusätzlicher Cr Schutzschicht entwickelt.

Die Wasserstoffpermeabilität von Ti_2AlC und Cr_2AlC MAX Schichten wurde mittels Neutronenradiographieuntersuchungen bestimmt. Beide Beschichtungssysteme erwiesen sich als robuste Barrieren für die Wasserstoffdiffusion in das Zircaloy Substrat.

Insbesondere die in dieser Arbeit mit innovativen Verfahren entwickelten Cr_2AlC basierten Schichtsysteme haben ein großes Potential für die Anwendung als Oxidationsschutz für unfalltolerante Zircaloy-Hüllrohre in Kernreaktoren.

Table of Contents

List of Figures

List of Tables

List of Symbols

a	Thermodynamic activity
A	Pre-exponential factor
A_c	Projected contact area (cm^2)
B	Magnetic flux density (T)
C	Concentration (mol/m^3)
D	Diffusion coefficient (m^2/s)
d	Distance (nm)
E	Electric field (V/m)
E_a	Activation energy (J/mol)
E_B	Binding energy (eV)
E_K	Kinetic energy (eV)
E_r	Reduced Young's modulus (GPa)
E_Y	Young's modulus (GPa)
G	Gibbs free energy (J/mol)
ΔG	Gibbs free energy change (J/mol)
h	Planck constant (J·s)
h_i	Indentation displacement (m)
H	Enthalpy (J/mol)
H_i	Indentation hardness (GPa)
I	Neutron intensity ($neutrons \cdot cm^{-2} \cdot s^{-1}$)
J	Diffusion flux ($mol \cdot m^{-2} \cdot s^{-1}$)
k'	Parabolic constant
L_c	Critical load of failure in scratch tests (N)
Δm	Mass change (g)
n	Integer

N	Atomic number
N_i	Number density (m^{-3})
p	Gas pressure (Pa)
p_i	Partial pressure (Pa)
P	Applied load in nanoindentation (N)
R	Gas constant ($J \cdot mol^{-1} \cdot K^{-1}$)
R_a	Arithmetic average surface roughness (nm)
S	Entropy (J/mol)
ξ	Area (cm^2 or m^2)
t	Time (s)
T	Temperature (K or °C)
T_m	Melting temperature (K or °C)
V	Molar volume (m^3)
υ	Poisson's ratio
ν	Frequency (Hz)
Δw	Raman shift (cm^{-1})
x	Thickness (μm)
θ	Incident angle (°)
λ	Wavelength (nm)
λ_0	Excitation wavelength (nm)
σ_i	Microscopic neutron cross section (barns)
Φ_s	Work function (eV)
Σ_{total}	Total macroscopic neutron cross section (barns)

List of Abbreviations

2D	Two-dimensional
3D	Three-dimensional
AC	Alternating current
AES	Auger electron spectroscopy
ATF	Accident tolerant fuels
BDB	Beyond-design-basis
BWR	Boiling water reactor
CEM	Controlled evaporator mixer unit
CVD	Chemical vapor deposition
CTE	Coefficients of thermal expansion
DB	Design-basis
DC	Direct current
ECCS	Emergency core cooling systems
ECR	Equivalent cladding reacted
EDS	Energy dispersive X-ray spectroscopy
EPMA	Electron probe micro-analyzer
FFT	Fast Fourier transform
FIB	Focused ion beam
Gadox	Gadolinium oxysulphide
GIXRD	Grazing incidence X-ray diffraction
HAADF	High-angle annular dark-field imaging
HIP	Hot isostatic pressing
HIPIMS	High power impulse magnetron sputtering
HRTEM	High resolution transmission electron microscopy
HVOF	High velocity oxygen fuel
ICON	Imaging with cold neutrons
LOCA	Loss of coolant accident

LWR	Light water reactor
OTS®	Oxygen trap system
PSI	Paul Scherrer Institute
PVD	Physical vapor deposition
PWR	Pressurized water reactor
RF	Radio frequency
SAED	Selected area electron diffraction
SEM	Scanning electron microscope
SHE	Standard hydrogen electrode
SINQ	The Swiss Spallation Neutron Source
SPS	Spark plasma sintering
SZM	Structure zone model
TBC	Thermal barrier coating
TEM	Transmission electron microscope
TM	Transition metal
TMN	Transition metal nitride
TOF	Time-of-flight
UO_2	Uranium oxide
WDS	Wavelength dispersive X-ray spectroscopy
XPS	X-ray photoelectron spectroscopy
XRD	X-ray diffraction
YSZ	Yttria-stabilized-zirconia
Zircaloy	Zirconium-tin-based alloy
Zr	Zirconium
α-Zr	Hexagonal close-packed Zirconium
β-Zr	Body-centered cubic Zirconium

1 Introduction

Worldwide economic prosperity and stability deeply depend on energy security and stability [1]. Access to sustainable, reliable and affordable sources of energy as well as enhancing efficiency in energy conversion and/or storage drives the strong need for innovative advanced materials that can withstand extremely harsh environment for many years. Nuclear power plants represent one of reliable and clean ways of producing electricity. However, high energy density combined with high temperature and pressure, as well as the highly corrosive and radioactive environment in the nuclear core challenge the performances of in-core structural components, especially of zirconium (Zr)-based alloy fuel claddings, in both normal and off-normal operating conditions [2]. In order to improve the safety, reliability and economics of water-cooled nuclear power reactors, development and deployment of advanced accident tolerant fuels (ATF) became of worldwide interest in the nuclear community at least since the 2011 Fukushima accident [3–6].

In this chapter, the first section explains the background of development of ATF claddings for light water reactors (LWRs). The performance of state-of-the-art Zr-based alloy fuel claddings in LWRs will be briefly summarized. Then, the status of materials development of ATF claddings and the concept of MAX phase materials will be given. Finally, the research motivation and thesis organization will be described.

1.1 Background

Nuclear power generates approximately 14% of the electricity consumed with more than 400 reactors in operation worldwide, reaching 391 GW(e) at the end of 2016 [7]. The vast majority of these reactors are LWRs with predominantly pressurized water reactors (PWRs) and boiling water reactors (BWRs). These two types of reactors account for majority of electricity generated by nuclear power [7]. In terms of nuclear fuel, uranium dioxide (UO_2) or other fissile actinide oxide powders are pressed and sintered into fuel pellets. These ceramic fuel pellets are enclosed in long alloy tubes termed fuel cladding [2]. The fuel claddings are made of zirconium-based alloys. Their typical dimensions are ~1 cm outer diameter, ~4 m long and 0.6 mm wall thickness [6]. The single fuel rods are packed together into fuel assemblies to construct the nuclear reactor core [2].

Figure 1.1 displays the schematic view of a PWR fuel assembly. A typical nuclear reactor core is usually composed of hundreds of fuel assemblies. During operation, fuel assemblies are immersed in the primary water circuit, in which the water circulates through the core to pick up and transport the heat released by the uranium fission reaction to produce nuclear electricity. The Zr-based alloys are utilized for some additional structural components of fuel assembly, such as grid spacers in PWRs and channel boxes in BWRs [2].

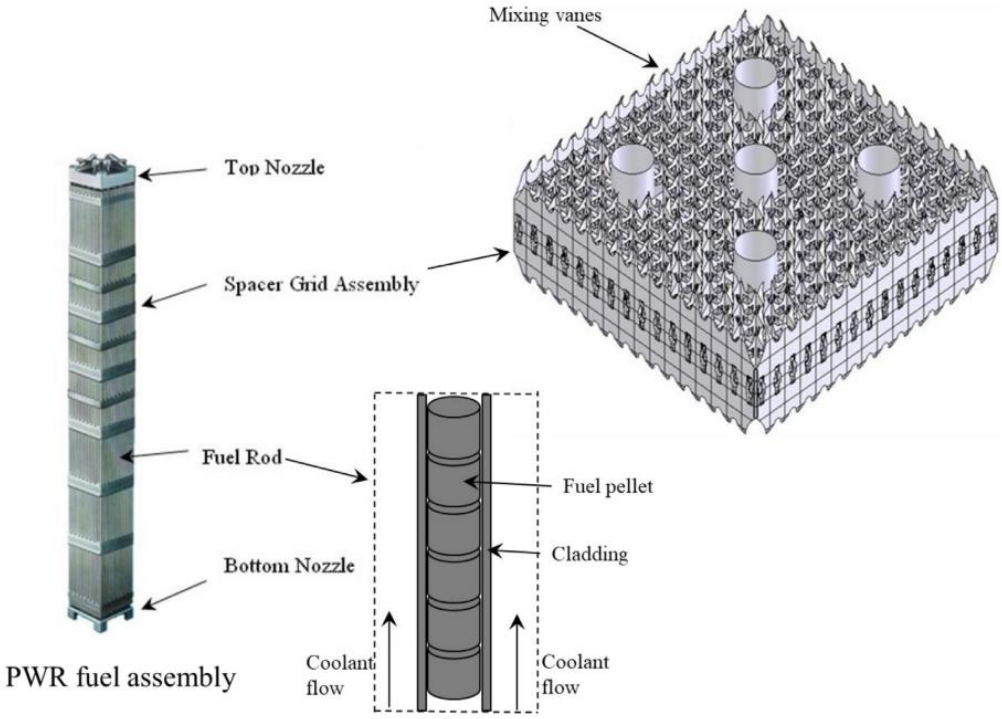

Figure 1.1 Schematic view of a PWR fuel assembly [8].

The selection and development of zirconium-based alloys as fuel claddings occurred in the 1950s as replacement for components made of stainless steel [9]. With Zr as the dominating constituent, this family of alloys feature multiple desirable properties, e.g. low thermal neutron absorption cross section, excellent corrosion performance under normal operation, and good mechanical properties under neutron irradiation [10,11]. The Zr-based alloy cladding constitutes one important barrier against the release of radioactive materials into the primary circuit [11]. The cladding integrity during service is crucial to maintain nuclear safety. Advanced nuclear grade zirconium-based alloys exhibiting optimized performances under normal conditions have been deployed via decades of intensive investigation and development [4]. However, one inherent limitation of Zr-based alloys during accidental scenarios, namely the extremely fast oxidation kinetics with high-temperature steam, cannot be improved by optimizing their chemical compositions and/or manufacturing processes [4,12]. The main category of accident scenarios involves loss of cooling capability inside the core, which leads to depressurization in the core and eventually drives up the fuel temperature due to insufficient heat removal [3]. Thus, the structural components in the core are exposed to a high-temperature steam atmosphere. Once the temperature of Zr-based alloy cladding exceeds around 1000°C, significant degradation and self-catalyzed oxidation of the claddings initiate, resulting in rapid heat release and hydrogen generation from the exothermic oxidation reaction between zirconium and steam [3]. Consequently, the fuel, cladding and core structures are at risk of failure and melting. In worse cases, hydrogen explosion and release of highly-radioactive fission products into the environments can happen, which was profoundly realized after the severe accident at the Fukushima Daiichi plants in 2011 [13].

Development and deployment of accident tolerant fuel (ATF) aiming to improve fuel/cladding reliability and safety of water-cooled nuclear reactors during both normal conditions as well as accident scenarios became a worldwide interest in the nuclear materials field after the Fukushima accident [4,6]. By definition, ATF materials should tolerate the loss of active cooling capability in the reactor core for a considerably longer period of time and up to higher temperatures that offer improved coping time under accident scenarios [6,14]. At the same time, they should provide equivalent or superior performance compared to current UO_2/Zr-based alloy cladding fuel systems during normal operational conditions [14]. The crucial performances with respect to fuel cladding are improved oxidation kinetics and reduced oxidation rate in high-temperature steam, and substantial reduction of heat and hydrogen production [3,14,15]. Thus, the advanced ATF claddings should tolerate much higher temperature, for instance temperature exceeding 1200°C, for a considerably longer period during accident scenarios. Two principal strategies are being investigated and evaluated worldwide. One solution is to develop innovative cladding materials with significantly reduced oxidation kinetics, such as FeCrAl-based alloys [9] and SiC-based composites [16], aiming to replace conventional zirconium alloys. These new cladding concepts feature advantages on some characteristic but drawbacks on others, which involves long-term input and trivial engineering redesign of the nuclear reactor cores [4,6]. Another more near-term strategy could be surface modification of currently accessible zirconium-based alloy fuel claddings, via deposition of inherent oxidation resistant coatings, to improve their oxidation resistance, since this solution does not considerably modify the existing well-developed UO_2/Zr-based alloy cladding fuel design [6].

1.2 Zr-based alloy cladding for LWR

Zirconium (Zr) is a transition metal, and it has an atomic number of 40 and an atomic mass of 91.22. Its melting point is 1855°C and the density at standard temperature and pressure (0°C, 100 kPa) is 6.5 g/cm^3. Zirconium exhibits a hexagonally close-packed crystal structure (α-Zr) at room temperature. It undergoes phase transformation at around 865°C, and becomes to a body-centered cubic crystal structure (β-Zr). The high chemical reactivity makes zirconium not exist as a native metal in nature. Commercial zirconium metal typically contains a small amount of hafnium (1–3%). For nuclear applications, hafnium must be removed because hafnium has around 600 times higher neutron absorption cross-section than zirconium.

First zirconium-based alloys used for nuclear fuel claddings were developed in the 1950s by US Nuclear Navy programs. High-temperature and high-pressure water is used as the coolant in LWRs. It was found that the corrosion performance of zirconium alloys by coolant water worsened as the alloy became purer and almost any modification by alloying addition initially increased its corrosion resistance [11]. A systematic alloy development program aimed to improve both corrosion resistance and mechanical properties and led ultimately to the family of classical zirconium-tin-based alloys (named Zircaloy) used as claddings. Most common claddings initially used in commercial nuclear reactors are Zircaloy-4 in PWRs and Zircaloy-2 in BWRs. New generation of advanced fuel claddings, such as M5®, ZIRLO™, and E365, have been developed mainly by slightly optimizing the chemical composition [4]. These alloys show improved corrosion resistance during normal operations compared to the classical Zircaloy-2 and

Zircaloy-4 alloys [7,9,15]. Table 1-1 gives the chemical composition of representative commercial Zr-based alloys used as fuel claddings. The improved performance of modern claddings under normal conditions allow increased power density and operating temperature for power upgrades, burnup extension for waste minimization, and reduced refueling downtime for economic competitiveness of nuclear reactors [6,14,18].

Table 1-1 Typical commercial zirconium-based alloys used as claddings in water-cooled reactors.

Alloy	Nominal alloy composition (wt.%)						
	Sn	Nb	Fe	Cr	Ni	O	Zr
Zircaloy-2	1.5	-	0.15	0.1	0.05	0.1	Bal.
Zircaloy-4	1.5	-	0.2	0.1	-	-	Bal.
ZIRLO™	1.0	1.0	0.1	-	-	0.1	Bal.
M5®	-	1.0	-	-	-	0.14	Bal.
E365	1.2	1.0	0.35	-	-	-	Bal.

The temperature and pressure during normal operational conditions inside the core are around 330°C and 15.5 MPa for PWR, 285°C and 7.5 MPa for BWR. Owing to the combination of high-temperature and high-pressure, the coolant water is in sub-critical state and acts as a highly corrosive medium [6]. The corrosion of zirconium by hot water can be simply written as follows:

$$Zr + 2H_2O \rightarrow ZrO_2 + 2H_2 \quad (1\text{-}1)$$

During normal operation, a thin oxide film grows on the surface of zirconium alloys because of waterside corrosion. The corrosion kinetics is usually divided into two stages, termed pre- and post-transition [19]. The initial pre-transition regime follows an approximate cubic or sub-parabolic oxidation rate characterized by growth of a thin, black, tightly adherent oxide scale. Once the thickness of this oxide film exceeds a critical value (generally 2-3 μm), cracking of the oxide film appears because of accumulation of compressive stresses due to volume expansion upon oxide formation (the Pilling-Bedworth ratio of ZrO_2:Zr is 1.56) and oxide phase transformation [19]. Correspondingly, the growth kinetics increases to a post-transition linear rate. Recent observations also show that a series of successive cubic curves lies between the pre- and post-transition stages due to re-growth of a protective zirconia layer beneath the previously non-protective porous layer [19]. As mentioned above, small concentrations of additional alloying elements can significantly alter the corrosion kinetics of zirconium alloys. Figure 1.2 displays the oxide thickness evolution of Zircaloy-4 and of M5® alloys, respectively, during autoclave corrosion testing under simulated PWR normal conditions. The curves indicate the cyclic behavior of the corrosion kinetics (separated by vertical dotted lines) and the reduced corrosion rate of the advanced alloy M5®.

An important constraint associated with the use of zirconium alloys as fuel claddings in reactor normal operation is hydrogen absorption. Hydrogen is generated predominantly by the water corrosion reaction

(Equation 1-1) along with by radiolysis of water. A small amount of the hydrogen ions (protons) diffuses through the ZrO_2 oxide layer into the zirconium metallic matrix. Once the solubility limit of hydrogen in the Zr metal is exceeded, it can precipitate as brittle hydrides (ZrH_x, x=1, 1.6 or 2), leading to a remarkable reduction of ductility and fracture toughness of the cladding tube [6]. Hydrogen embrittlement degrades the mechanical performance of the Zr-based alloy claddings, challenging the physical integrity of the cladding tube especially during off-normal conditions [20].

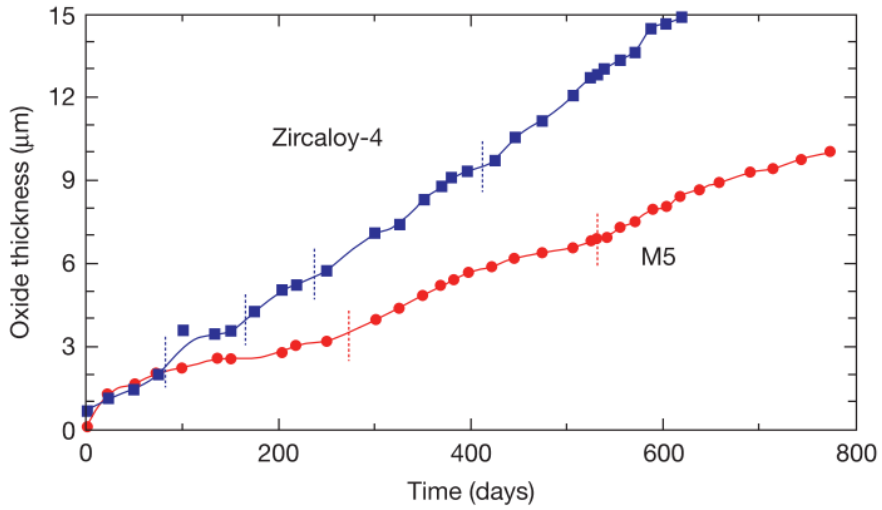

Figure 1.2 Oxide thickness evolution of Zircaloy-4 and of M5 alloys during autoclave corrosion testing under simulated PWR normal conditions showing the cyclic nature of the corrosion kinetics and reduced corrosion rate of M5® [19].

The degradation mechanisms of Zr-based alloy fuel claddings under design-basis (DB) and beyond-design-basis (BDB) accident scenarios of LWRs have been widely analyzed and investigated [3,21–23]. Figure 1.3 summarizes the evolution of a fuel rod under a typical loss of coolant accident (LOCA) condition extending into the beyond design basis scenario together with four key performance features of ATF concepts for improved safety margins [3].

In such typical accident scenarios, the decay heat in the core and the stored energy in the fuel boil off the remaining coolant water to steam [3]. The claddings undergo ballooning and burst at temperatures in the range of 700–1200°C, and are oxidized by the high-temperature steam. The high-temperature oxidation in steam leads to the formation of an external ZrO_2 layer accompanied by an internal oxygen-stabilized α-Zr(O) layer beneath before the cladding is completely consumed, as shown in Figure 1.4 [24]. The oxidation kinetics is generally described by a parabolic law for this entire category of alloys except in case of breakaway oxidation (linear kinetics) for long-term scenarios at intermediate temperatures [24]. With respect to the design-basis LOCA, the Emergency Core Cooling System (ECCS) activates and quenches the core by injecting coolant water [6]. Due to the brittle character of both the oxide and the oxygen-stabilized α-phase, oxidation progressively weakens the mechanical properties of the cladding. In order to maintain the mechanical stability of the cladding during reflooding and quenching, the peak-clad

temperature should be limited to 1204°C and the equivalent cladding reacted (ECR) to 17% of the initial cladding thickness (US regulatory LOCA criteria) [6,9]. In case of severe accident scenarios without reflooding, accelerated oxidation of the fuel cladding and detrimental interactions (e.g., low melting temperature eutectic phase formation) are initiated as shown in Figure 1.3 with the progression of the accidents. The exothermic oxidation reaction can release comparable or even more heat than the decay heat, which dramatically accelerates the rise of the core temperature and the meltdown of the core [3]. The destruction of the containment buildings and release of highly radioactive fission products into the atmosphere may occur due to detonation by-product hydrogen [6]. Rapid self-catalytic exothermic oxidation reactions along with physical degradation of the Zr alloy claddings can significantly exacerbate the course of accident progression, which highlights the importance of adopting robust cladding material with improved accident tolerance.

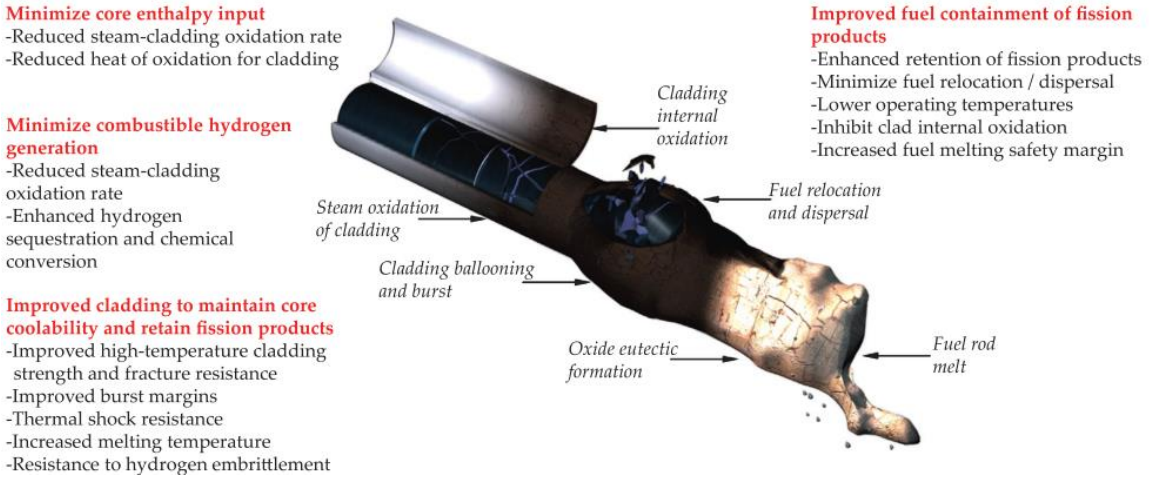

Figure 1.3 Evolution of a fuel rod under LOCA condition extending into the beyond design basis scenario along with four key performance features of ATF concepts for improved safety margins [3].

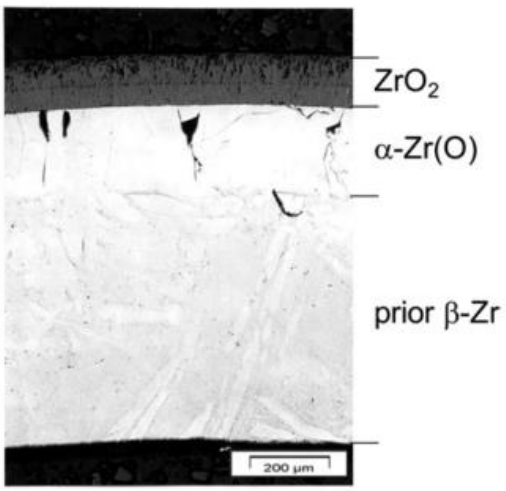

Figure 1.4 Micrographs of oxide layer on Zircaloy-4 claddings oxidized in steam and quenched in water [24].

1.3 Accident tolerant fuel (ATF) cladding concepts

The key performance features of ATF cladding materials for improved safety margins are reduced steam oxidation kinetics with simultaneously minimized hydrogen generation and enthalpy input, as well as improved strength to maintain core coolability and retain fission products as summarized in Figure 1.3. Two pathways are currently under consideration.

1.3.1 Alternative cladding materials

As aforementioned, one approach to achieve larger safety margins in the event of severe accident scenarios is to replace the current Zr-based alloy cladding with new materials exhibiting much lower oxidation rates and/or less heat and hydrogen production [4]. This approach comprises mainly three types of materials, namely FeCrAl-based alloys [9], SiC composites [16] and Mo-based alloys [25]. Each class of materials features some desirable performance, but also a variety of critical challenges needs to be solved. FeCrAl-based alloys (typically with ~20 wt.% Cr and 5 wt.% Al) exhibit an excellent corrosion/oxidation resistance under both normal conditions and accident scenarios originating from the growth of protective Cr_2O_3 and Al_2O_3 scales, respectively [26]. They also provide the potential for improved strength compared to current Zr alloys. The main issues related to FeCrAl-based alloys include relatively low melting temperature, high neutron capture cross section, and high tritium permeation rate [4,27]. SiC-based composites are considered as a novel cladding material due to their low thermal neutron absorption cross section, excellent high-temperature oxidation resistance exceeding 1600°C, as well as their good radiation resistance and retention of strength [28]. The SiC-based composites have few drawbacks, for example weak mechanical properties with high brittleness, a high weight loss rate due to dissolution of the silica scale under normal conditions, a low thermal conductivity after irradiation, and their handling in hermetic sealing is difficult [29,30]. Refractory Mo-based alloys offer the advantages of outstanding strength and creep behavior at high temperatures and a high melting temperature (2623°C). However, they exhibit poor oxidation performance due to the formation of volatile products under high-temperature oxidizing environments. Thus, they would need an adherent oxidation-resistant surface coating [25]. In addition, Mo-based alloys also come at the expense of neutronic absorption penalty like FeCrAl-based alloys that will increase the cost of fuel enrichment [31]. These potential accident-tolerant cladding alternatives of novel materials remain a long-term solution and are still in the early stages of development.

1.3.2 Coated Zr-based alloy claddings

Another more mid-term solution to improve the performance of the cladding in accidental conditions while preserving its excellent behavior under normal operating conditions is via surface engineering to modify the external surface of current zirconium alloys with oxidation resistant coatings. High-temperature oxidation resistant coatings have seen numerous applications to protect structural materials, like carbon composites, refractory metals and superalloys, from fast degradation and oxidation to improve the reliability and life of components at elevated temperatures [32,33]. Additionally, coated Zr-based alloys may offer the benefits of negligible impact on neutron economics and fuel cycle cost in case of thin coatings and of reduced hydrogen absorption during normal operation allowing for high burnup of the

fuel. One critical concern associated with coatings is that the enhanced accident tolerance entirely relies on the physical integrity of the coating, which may partially or completely get lost due to coating defects or damages [4].

Various materials have been proposed and examined as protective coatings on Zr alloys. The coatings studied can be broadly divided into three categories: metallic coatings, ceramic coatings and multilayer coatings. The relevant coating studies based on the three categories are summarized below [6]:

-metallic coatings: Al, Cr, Ni, Cr-Al, FeCrAl, Zr-Si

-ceramic coatings: SiC, Ti_2AlC, TiN, TiAlN, CrN, CrAlN

-multilayer coatings: Mo/FeCrAl, Al/Al_2O_3, Cr/CrAl, Cr/CrN, TiN/Ti, TiAlN/TiN

Metallic coating materials generally offer the benefits of excellent adherence, high toughness and ductility, high thermal conductivity and easy fabrication [6]. However, some undesirable features could occur during fabrication and application. Carr et al. have investigated the Al/Zr diffusion couples and deposited aluminum layers on Zr alloy substrates by magnetron sputtering with subsequently controlled heat-treatment [34]. Both treated specimens revealed the formation of a thick, brittle Al-Zr intermetallic layer at the interface. The Al coatings showed low protection during steam oxidation at 1000°C, which was attributed to formation of surface defects such as cracks. Cr coatings have been synthesized on Zr-based alloys by a variety of deposition techniques. All results confirmed that a Cr coating was highly adherent to the substrate and offered good corrosion and oxidation resistance due to growth of a stable Cr_2O_3 scale [35,36]. Kim et al. expected to further increase the high-temperature oxidation resistance of a pure Cr coating by a CrAl layer via laser cladding process [37]. However, significant mixing of CrAl coating metal with the Zr substrate occurred during the laser surface treatment, which deteriorated the oxidation resistance of the coated compound [37]. Surface modification with Ni [38] coatings by electroplating on Zircaloy-4 substrates was achieved. The coatings were thermal treated at 760°C in order to realize better adherence. However, heat treatment led to formation of a series of brittle intermetallic compounds within surface cracks. Isothermal oxidation tests were performed merely up to 370°C, and the improvement of the oxidation resistance of the coated Zr alloys was foreseen to be limited to low temperatures.

FeCrAl-based alloys were also examined as potential coating materials considering their good performance under both normal and accidental conditions. However, several studies confirmed that the performance of such coatings was severely restricted once the oxidation temperature exceeded 1000°C due to high mutual diffusion rates and low temperature eutectic reaction (~18 wt.% Fe at 950°C) with the Zr alloy substrate [39–41]. Yeom et al. deposited Zr-Si coatings of three stoichiometries (Zr_2Si, ZrSi, and $ZrSi_2$) by magnetron sputtering and found that coatings with $ZrSi_2$ stoichiometry showed better oxidation resistance at 700°C in air due to the formation of a thin protective oxide layer consisting of nanocrystalline SiO_2 and $ZrSiO_4$ phases in an amorphous matrix [42]. Higher oxidation temperature around 1000°C led to cracking of the coatings with only weak improvement; pre-oxidation at lower temperature (700°C) was adopted to mitigate this issue.

Ceramic coatings studied previously mostly were carbides and nitrides. Ceramics generally exhibit high hardness and good wear resistance, thus the fretting-wear and fretting-corrosion resistance of the cladding against the coolant flow likelihood to be improved [6]. One of the crucial challenges to be evaluated for ceramic materials as protective coatings is their brittle characteristics and poor toughness, making them susceptible to cracking/spallation when suffering high stresses [43]. Olayyan et al. deposited l μm thick SiC coatings using chemical vapor deposition (CVD) on Zircaloy-4 substrate [44]. Their results showed that a moderate level of substrate roughness resulted in a higher adhesion strength of the coatings. However, the SiC coatings did not survive and vanished after autoclave corrosion at 350°C and 200 MPa for 24 h [44]. Ternary carbides belonging to a family of materials with a structure formula $M_{n+1}AX_n$ (where "M", "A", and "X" are an early transition metal, an A-group element, and C and/or N, n=1, 2, or 3), called MAX phases, have also been evaluated as oxidation resistant coatings. The structures and properties of MAX phases will be described in next section. Some Al-containing MAX phases, especially Ti_2AlC and Cr_2AlC, possess excellent high-temperature oxidation resistance both in dry and in humid atmospheres attributable to the growth of a dense and protective thermally grown alumina scale [45]. Thus, Al-containing MAX phases have been proposed as fuel cladding materials and protective coatings for both current light water reactors and broader applications in the future nuclear industry [46]. High-velocity oxygen fuel (HVOF) deposition [47], cold spraying [48] and magnetron sputtering with subsequent laser annealing [49] have been adopted to produce Ti_2AlC MAX phase coatings on Zr-based alloys. Generally, cold spray and HVOF processes can fabricate relatively thick coatings (at least with a thickness of dozens of microns). However, these coatings typical have a relatively loose structure and contain a substantial amount of impurity phases. Due to those high-density defects, a minimum coating thickness was necessary for providing protective effect at high temperatures (>1000°C) in steam [47]. Formation of micro-cracks was observed for the Ti_2AlC coatings deposited by magnetron sputtering with subsequent laser surface treatment [49]. Steam autoclave tests were performed at 400°C and 10.3 MPa for 72 h and confirmed the protective effect of the coatings, but internal oxidation of the zirconium alloy substrate was also observed beneath the cracks. No high-temperature oxidation tests were reported. Refractory metal nitrides are commercialized for cutting tools and drill bits due to their high hardness [50]. Two kinds of nitrides, TiN and CrN (sometimes with additional Al incorporation aiming to improve their oxidation resistance) have been studied as protective coatings for fuel cladding [51–53]. During autoclave tests, both binary nitride coatings exhibited excellent corrosion resistance due to the formation of stable and slow-growing oxide scales, TiO_2 and Cr_2O_3, respectively. However, the TiAlN and CrAlN coatings have shown poor corrosion behavior since Al_2O_3 is unstable and dissolves rapidly in normal operating conditions (sub-critical water), leading to fast recession of the coatings. Pourbaix diagrams prove the unstable feature of SiO_2 and Al_2O_3 under simulated normal conditions observed by autoclave tests. Pourbaix diagrams, also known as a E_H/pH diagrams, map out the possible stable (equilibrium) phases of an aqueous electrochemical system [54]. Figure 1.5 shows the Pourbaix diagrams of Si, Al, Ti and Cr at 350°C, 25 MPa and ion concentration of 10^{-6} mol/kg [6]. The pH and electrochemical potential of the aqueous solution in PWR core are approximately 7.0 and −500 mV_{SHE}, respectively. In this case, Si and Al

form soluble aqueous ions or hydroxides rather than solid SiO_2 and Al_2O_3 oxides, while stable TiO_2 and Cr_2O_3 oxides exist for Ti and Cr as seen in Figure 1.5. Obviously, ZrO_2 also remains stable in sub-critical water since the state-of-art fuel claddings are made of Zr-based alloys.

Multilayer coatings are often featured by enhanced mechanical properties and corrosion performance compared to single layer coatings [55]. Several multilayer coating models have been proposed as oxidation and corrosion protective coatings on zirconium alloys. For instance, Al/Al_2O_3 [56] and Cr/CrN [57] multilayer coatings aimed to improve the adherence strength of the coatings with a thin metallic layer as bonding interlayer. Mo/FeCrAl coatings (Mo interlayer as diffusion barrier) were designed to alleviate the reaction/interdiffusion between the FeCrAl coating and the Zr substrate during high-temperature oxidation [41]. Cr/CrAl [58] and TiN/Ti [59] multilayer coatings targeted to improve the damage resistance of coatings. Due to repetitive renucleation mechanisms of defects at each interface, the multilayer structures were supposed to restrain the expansion and propagation of undesirable defects, such as microcracks and pores, within the coatings [6]. Another approach was to synthesize functional layered coatings by utilization of corrosion-resistant coatings and oxidation-resistant coatings simultaneously in a multilayer sequence, like in a TiAlN/TiN multilayer coating [60], that could permit the coatings protective via formation of correspondingly desirable oxide scale under dissimilar conditions. However, up to now validation of such multilayer coatings mainly focused on one specific scenario, their performance under both normal and accident conditions lacks adequate assessment.

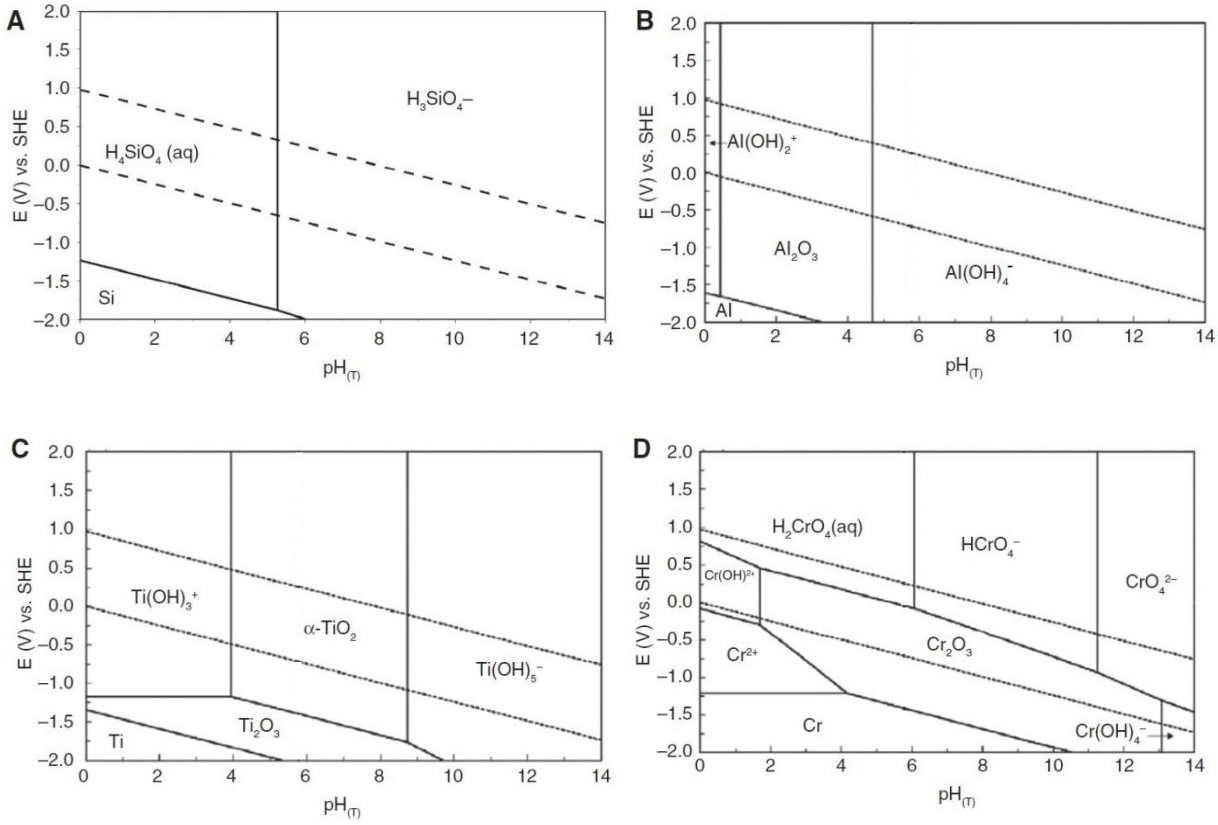

Figure 1.5 Pourbaix diagrams for (A) Si, (B) Al, (C) Ti and (D) Cr at 350°C, 25 MPa and 10^{-6} mol/kg. SHE means standard hydrogen electrode [6].

1.4 MAX phase materials

Layered ternary compounds denominated by the general formula $M_{n+1}AX_n$ (known as MAX phases) comprise a large class of nanolaminated carbides and nitrides [61–63]. These compounds crystallize in the hexagonal crystal structures (space group $P6_3/mmc$, 194) with two formula units per unit cell [63]. Their unique layered structure can be viewed as the near-close-packed M layers interleaved with pure A-group element layer, accompanied by the X atoms filling the M_6X octahedral cages between the M atoms [61]. Here M is primarily an early transition metal, A is mostly elements from groups 13 and 14, and X represents C or N [61]. Figure 1.6 shows the crystal structure of various MAX phases. The different n (typical 1-3) values indicate the numbers of transition metal carbide and/or nitride layers separated by the A elemental layer [61], as presented in Figure 1.6. The different MAX phase stoichiometries are often referred to as 211 for n=1, 312 for n=2, and 413 for n=3. The size of the unit cell increases along the *c*-axis with progressively increasing n values.

Discovered by Nowotny and coworkers in the 1960s these phases remained largely unexplored until the 1990s [64,65]. In 1996, Barsoum and El-Raghy reported on the synthesis of fully dense, predominantly single-phase samples of Ti_3SiC_2 and revealed it to possess an extraordinary combination of attributes of both metals and ceramics [66]. The unusual, often unique, properties renewed growing interest on the fabrication, characterization and implementation of MAX phase materials [61–63,67–71]. Later on, it was found that this extended family of materials share many common attributes and properties. This unusual combination of properties is traceable to their unique atomic chemistries and layered crystal structures. The covalent-ionic M-X bonds in the MAX phases are exceptionally strong and are comparable to those in the MX binaries, and the metallic M–A bonds are relatively weak [71,72]. Therefore, similar to counterpart MX phases, MAX phase compounds own low density, high melting points, high stiffness values, excellent high-temperature mechanical properties and thermal stability, and low thermal expansion coefficients [69]. Additionally, like metals, they are relatively soft and readily machinable, exhibit high thermal and electrical conductivities, thermal shock and damage tolerance, and sometimes oxidation and fatigue resistance [69]. In addition, they often exhibit highly anisotropic behavior of the hexagonal crystal [73].

Due to many combinations of M, A, X, and n, more than 70 MAX phases have been experimentally reported so far. The vast majority of MAX phases discovered up to now are 211s (Ti_2AlC, Cr_2AlC, Ti_2AlN, V_2AlC, Nb_2GaC etc.) with smaller number of 312s (Ti_3SiC_2, Ti_3AlC_2, Ta_3AlC_2 etc.) and 413s (Ti_4AlN_3, Nb_4AlC_3, Ti_4GaC_3 etc.) [70,73]. In addition, MAX phases can form solid solutions on the M, A and/or X sites. Various solid solution structured MAX phase materials have been processed and characterized [74,75], for instance $(TiNb)_2AlC$ and $(VCr)_3AlC_2$ on the M sites, $Ti_3(SiGe)C_2$ on the A sites and $Ti_3Al(CN)_2$ on the X sites. Some of the solid solutions exist even when one of the end members does not, which allows further tailoring the physical, chemical and mechanical properties of the MAX phases. The number of MAX phases and their solid solutions continues to expand [76,77].

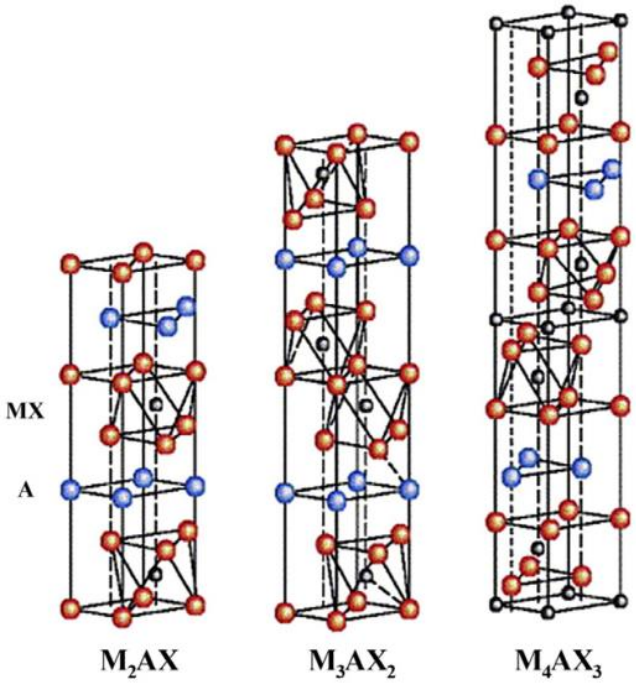

Figure 1.6 Crystal structures of the 211, 312, and 413 MAX phases [63].

A ubiquitous problem in the synthesis of higher order ternary or quaternary compounds from two or more reactants is the retention of stable intermediate phases. This problem is also the major issue confronting the synthesis of MAX phase compounds. When minor impurity phases are present, the strength, oxidation resistance and ductility of MAX phase are generally reduced [78]. Original efforts on the production of MAX phase bulk products are with a particular emphasis on reducing residual impurity phases. Hot isostatic pressing (HIP) and spark plasma sintering (SPS) represent the most common and important methods to produce bulk MAX phase materials [67,68]. The raw materials are typical corresponding stoichiometric or slightly off-stoichiometric elemental and/or binary ceramic powders [62]. To ensure these original materials completely react and form the corresponding MAX phase structure, a reasonably high pressure and temperature together with long dwell time is required. Normally, a minor amount of impurity phases, usually original counterpart binary carbides or nitrides, retain in the final products [66,67]. Afterwards, it was found that the majority MAX phases can be synthesized as thin films or coatings at relatively low temperature, several hundred degrees lower compared to the synthesis of bulk MAX phase materials [63]. This provides an opportunity to utilize the desirable properties of both MAX phases and substrate materials within convenient technological processes and at reduced costs [63]. A variety of processes has been established for the synthesis of MAX phase thin films. A large part of pioneering work on synthesis of MAX phase thin films was achieved using magnetron sputtering technology, either using elemental targets or compound targets [79–88]. The MAX phase coatings can be synthesized *in-situ* during sputtering with a high deposition (substrate) temperature or *ex-situ* by deposition of nanoscale multilayers or amorphous films that are subject to subsequent annealing [63,88]. In addition to magnetron sputtering, other physical vapor deposition (PVD) processes such as pulsed laser

deposition [89], cathodic arc evaporation [90], high power impulse magnetron sputtering (HIPIMS) [87], as well as chemical vapor deposition (CVD) [91], and spray techniques [92,93] have been adopted to synthesize MAX phase thin films or coatings.

Due to their exceptional chemical and physical properties, MAX phases attract growing interest for structural and non-structural applications in harsh environments in the form of both bulk materials and thin films. Their high temperature oxidation resistance, largely, determines their capabilities in oxidizing conditions. Some Al-containing MAX phases have proved to be alumina forming with self-healing capabilities during high-temperature oxidation [94]. The most oxidation-resistant MAX phase is Ti_2AlC, followed by Ti_3AlC_2, which form an adherent and protective Al_2O_3 scale that can withstand thermal cycling beyond 1300°C [95–97]. Cr_2AlC also forms a protective Al_2O_3 layer and has superb oxidation resistance. However, the oxide scale shows relatively low adherence and spalls off during thermal cycling [98,99]. Recently, MAX phases also have attracted increasing interest in examining their radiation response mechanisms as potential candidates for application in nuclear reactors [100–102]. Findings suggest that the MAX phases can maintain phase stability and crystallinity (at high temperatures), and are generally resistant to amorphization when subjected to neutron irradiation and/or heavy ion irradiation even at high dose conditions. Therefore, several Al-containing MAX phases will be evaluated as protective coatings on Zr-based alloys for potential application as ATF claddings in this study.

1.5 Research motivation and thesis organization

Generally, materials enabling high-temperature oxidation resistance rely on establishment of an external, slow-growing, thermally grown oxide scale. The most common and effective oxide scales in humid atmospheres are Cr_2O_3, Al_2O_3, and SiO_2. As reviewed in Section 1.3, chromium coatings on Zr-based alloys offer improved performances during both normal and accident conditions owing to growth of Cr_2O_3 scales. However, a Cr_2O_3 scale grows very fast, and chromia also forms various volatile hydroxides in steam at temperatures above around 900°C generally restricting its application to somewhat lower temperatures [103]. Materials within service temperatures higher than 1100°C in oxidizing (steam) atmosphere typically rely on growth of Al_2O_3 and SiO_2 scales. However, SiO_2 and Al_2O_3 are unstable in subcritical aqueous solutions under normal operational conditions in nuclear reactors. The motivation of this study is to search for aluminum-containing MAX phase compounds as coatings on Zr-based alloys that may offer the capability to form a stable oxide scale (like ZrO_2, TiO_2, and Cr_2O_3) during normal operations while growth of Al_2O_3 scale during accident scenarios. The coatings target to provide protection of Zr-based alloy substrates from fast oxidation beyond 1200°C in steam. Up to now, only rare studies have been dedicated to exploring MAX phases as innovative coating materials on Zr alloys and examining oxidation behavior of MAX phase coatings in steam. The knowledge gained from this thesis work will contribute to evaluate if MAX phase coatings can be an alternative solution for ATF claddings.

The techniques previously utilized to fabricate coatings on Zr-based alloys can be categorized into three main categories: physical vapor deposition (PVD), chemical vapor deposition (CVD), and spraying. The coating thicknesses change significantly from a few to hundreds of microns depending on the deposition

techniques. In case of coatings on Zr-based alloys for nuclear applications, thin, dense, and adherent coatings are favorable in order to negligibly affect the design of the core. The temperatures needed for CVD processes are usually very high (up to 1000°C and above), and thus not directly applicable to many alloys. In case of spraying method, it is typically difficult to obtain dense coatings with a thickness smaller than 30 μm. Most groups working on coatings finally retained PVD, especially magnetron sputtering, as fabrication method since it can coat the substrates at low temperatures (from room temperature up to around 500°C) with high quality coatings. In addition, magnetron-sputtering process can be operated at thermodynamic non-equilibrium conditions, which allows for many complex thin film designs. In case of synthesizing MAX phase thin films, magnetron sputtering also offers the advantage of flexible controlling of the three elemental fluxes via, for instance, co-deposition from elemental targets to yield high-quality films. Therefore, magnetron sputtering, one established PVD technique, was selected as coating method in this study.

As a family of high-ordered ternary compounds, synthesis of high purity, particularly phase-pure polycrystalline MAX phase coatings on technically relevant substrates often remains a challenge. However, the presence of impurities, regardless of in bulk or in coating, degrades their oxidation performance. To overcome this issue, an innovative two-step approach, i.e. magnetron-sputtering of nanoscale elemental multilayer stacks with subsequent ex-situ heat treatment in argon, is elaborated for potential synthesizing phase-pure MAX phase carbide coatings. The unique multilayer architecture within the as-deposited coatings has a nano-layered structure similar to the layered structure of MAX phase and guarantees a short diffusion length during subsequent annealing (to initiate the growth of MAX phase via elemental multilayer interdiffusion and reaction). This approach may also reduce the crystallization temperature of the MAX phase due to chemical energy stored in such reactive multilayers. Ternary carbide coatings in three systems (Ti- , Zr- , Cr- C-Al) are fabricated on both researching substrates (alumina, SiO_2/Si) as well as on the functional Zircaloy-4 substrates, and their high-temperature oxidation mechanisms will be examined. The phase evolution and crystal growth during film deposition and heat treatment are explored, which likely offers some guidance for tailor-made synthesis of phase-pure MAX phase materials. Oxidation performances of the coatings presented herein can give some insights into utilization of these MAX phases as potential oxidation-resistant and protective coatings in a wide range of applications.

This thesis consists of eight parts. Chapter 1 gives an introduction and motivation for launching this study.

Chapter 2 describes the fundamental concepts concerning thin film synthesis and high-temperature oxidation. Intensive analysis and characterization techniques adopted and materials used in this study are briefly reviewed.

Chapter 3 presents the oxidation behavior of bulk Ti_2AlC MAX phase in high-temperature steam up to 1600°C. The experimental work performed here in steam atmosphere is more prototypic for nuclear accidental conditions since the majority previous oxidation studies were carried out in air. The findings will show the remarkable oxidation resistance of bulk Ti_2AlC in high-temperature steam and reveal the

potential of aluminum-containing MAX phases, especially Ti_2AlC, for the application as oxidation resistant coatings.

The following three chapters, Chapter 4, 5 and 6, present the results of the experiments that attempt to deposit Ti_2AlC, Zr_2AlC and Cr_2AlC MAX phase coatings by annealing the as-deposited elemental nanoscale multilayer stacks and examine the high-temperature oxidation behavior of coated Zircaloy-4 in steam. Phase-pure Ti_2AlC and Cr_2AlC MAX phase coatings are successfully fabricated, but the formation of a mixed ternary Zr(Al)C carbide rather than the Zr_2AlC MAX phase is confirmed in case of the Zr-C-Al coatings. The microstructural and phase evolutions of the coatings during annealing will be systematically investigated; the oxidation kinetics, oxidation mechanisms and protective effect of the three types of coatings will be addressed and discussed.

Chapter 7 reports the hydrogen permeation behavior of Cr_2AlC and Ti_2AlC MAX phase coated Zircaloy-4 by neutron radiography because hydrogen absorption dramatically degrades the mechanical properties of zirconium alloys. In addition, there are no reports on the hydrogen permeation behavior through MAX phase coatings before.

The final Chapter 8 summarizes the findings of previous chapters, and offers conclusions and outlook for future work.

2 Fundamentals, methods and materials

The fundamental concepts concerning thin film synthesis and high-temperature oxidation involved in this thesis are presented in this chapter. In particular, the basic principles and microstructure evolution during film growth of one popular deposition technique utilized herein, namely magnetron sputtering, are addressed in section 2.1. Section 2.2 briefly describes the theory of high-temperature oxidation of bulk materials and protective coatings with respect to thermodynamic backgrounds and oxidation kinetics. Additionally, various analysis and characterization techniques adopted are described in section 2.3. Materials used in this study are given in the final section 2.4.

2.1 Thin film synthesis

One of the most straightforward approaches to enhance or modify the surface properties of a material while preserving its preferable bulk features is to deposit a thin film or coating on it. A thin film or coating is a layer of material with thickness in the range of few atomic layers up to hundreds of micrometers, depending on the scope of application, at the surface of another underlying material [104,105]. Thin films or coatings have seen numerous applications in a wide variety of engineering systems. For example, decorative coatings possess a wide range of colors and shades. Coatings for electronic and optical applications offer for example specific photoelectric performance for semiconductor devices and electronic displays [106]. Hard nitride coatings with high hardness and wear resistance aiming to prolong the life of manufacturing tools [107]. In gas-turbine engines, thermal barrier coatings (TBCs) protect structural components from the high-speed hot gas stream for the purpose of improved durability and energy efficiency [32].

Thin films can be produced via various deposition technologies. The most common and important technologies for thin film synthesis and deposition can be categorized as follows: evaporation methods, glow-discharge processes, gas-phase chemical processes and liquid-phase chemical techniques depending on the forms of the source materials that are coated on the substrates [105]. Thin film technologies can also be categorized based on, for instance vacuum or non-vacuum, plasma or non-plasma processes [104]. Criteria for selecting a suitable thin-film deposition process is highly depending on performance requirements of the final product, and advantages, limitations as well as economy of each process technology.

2.1.1 Magnetron sputtering

Sputtering represents one of the most widely utilized thin film fabrication techniques using glow-discharge processes. Historically, sputter deposition has been broadly categorized under the term "physical vapor deposition" (PVD). In PVD processes, materials are vaporized from a solid or liquid source by heat or by bombardment with energetic particles, then the vapor is delivered to the substrate surface via passing through a vacuum or low pressure gaseous (or plasma) environment and finally condensates onto the

substrate to generate thin films [105]. Apart from sputtering, other major categories of PVD techniques include thermal evaporation, cathodic arc evaporation, and ion plating. Another type of vapor deposition technique that bases on chemical reaction is "chemical vapor deposition" (CVD). In CVD, volatile precursors decompose and/or react on the surface of substrates to yield the desired films [105]. Plasmas may possibly be used to "activate" and partially decompose the precursor species in CVD reactors [108]. The process is called plasma-enhanced CVD (PECVD) or plasma-assisted CVD (PACVD) [108].

Figure 2.1 shows a schematic illustration of typical sputtering phenomena. A bombarding energetic particle, particularly a gas ion, is accelerated through an accelerating potential to approach the target surface. The incident ions used for bombardment are typically Ar ions, due to their chemical inertness and low cost. Once the impinging ion collides with the target surface, it triggers a collision cascade in the near-surface zone of the solid body; partial momentum of the impinging ion is transferred to the surface atoms, which may be ejected (sputtered) [104]. In addition, some of the bombarding particles are reflected and some are implanted into the surface. The lowest energy of the impinging particle that can result sputtering, i.e. sputtering threshold energy, is considered at around 25 eV, which is about the energy needed for atomic displacement in solids [108]. In general, distribution of sputtered atoms' kinetic energy ranges from a few eV to 30 eV, which is much higher than that of thermally evaporated atoms or clusters. Thus, the sputtered atoms have high surface mobility on the substrate surface and can condense into continuous, smooth, and dense films. On the other hand, sputtering is not only used as thin film deposition process. It can be also used as an etching process, and it is commonly used for surface cleaning and as a means in chemical surface analysis methods.

The glow discharge or plasma in sputtering process is a partially ionized gas, consisting of positive ions and electrons to be a good electrical conductor [104]. A simple method of generating a glow discharge is by applying an electrical potential between two electrodes in a vacuum vessel containing a low-pressure gas. Thus, a typical, simple sputtering apparatus (diode sputtering) usually consist of two plates acting as electrodes, a vacuum chamber, and a power supply. After being evacuated the chamber is usually filled with low-pressure argon. The sputtering target is employed as the cathode and generally the substrate is positioned on the anode, which is regularly at the ground potential. The strong electric field between the electrodes will accelerate the natural existence of electrons (e.g. cosmic radiation) headed for the anode, and the gas atoms are ionized once the electrons gain sufficient energy [104]. Positive ions are produced via atoms or molecules undergoing an inelastic collision with an energetic electron. The gas ions are accelerated towards the cathode and leads to electrons emission and sputtering upon bombardment at the cathode [108]. The electrons can again produce new electron–ion pairs. In order to initiate and sustain plasmas, a threshold breakdown voltage is required. The threshold breakdown voltage of a particular gas and electrode material is dependent on the distance between the electrodes (pd) and the product of the pressure as expressed by Paschen's law [108]. The threshold breakdown voltage first decreases to reach a minimum, and then rises steeply again with increasing pressure at a constant distance. Typical plasma in a PVD process is often weakly ionized plasma, i.e. the degree of ionization is low with the rest being neutrals.

In the diode sputtering, the applied voltage can be direct current voltage (DC Sputtering) or alternating current voltage (Radio-Frequency (RF) Sputtering). DC Sputtering is commonly used for electrically conductive targets. For sputtering of insulating materials, high frequency RF power supplies can be used. However, in diode sputtering the electrons follow a short, direct route to the anode (the substrate) so the ionization efficiencies are relatively low. A fairly high process pressure is required to increase the probability of ionization collisions and thus the sputtered atoms have a short mean-free path (the mean distance traveled by particles between successive collisions) and go through many collisions with gas atoms, greatly reducing the amount actually reaching the substrate, i.e. the deposition rates are low. In addition, sputtered particles undergo an energy loss in collisions that degrades the film properties, and overheating effects of the substrates can occur due to intensive electron bombardment [107].

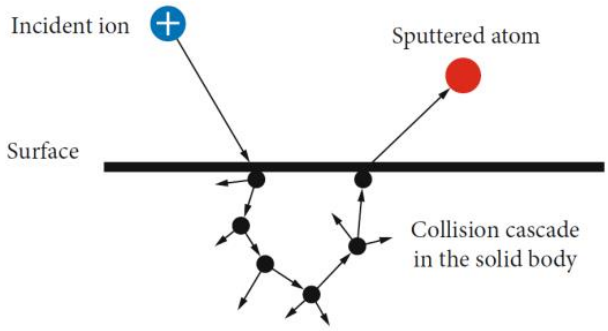

Figure 2.1 Schematic illustration of typical sputtering phenomena [104].

The limitations of basic sputtering process have been overcome by the development and implementation of magnetron sputtering. Magnetron sputtering employs a magnetic field, by an appropriate arrangement of permanent magnets or electromagnetics, to constrain the electrons which can be deflected to stay near the target surface [108]. Figure 2.2 shows a schematic illustration of a simple planar magnetron sputtering system. In a crossed E and B field, electrons follow helical paths around magnetic field lines, known as the $E \times B$ drift [108]. The applied magnetic field traps electrons to increase their number density, which substantially increases the probability of an ionizing electron-atom collision [109]. A dense plasma can be obtained near the target region thanks to the increased ionization efficiency. This, in turn, results in higher ion bombardment effect of the cathode target and higher deposition rates of the coatings. Moreover, the increased ionization efficiency achieved allows the sputtering system to be maintained at lower operating pressures [109], which minimizes impurities incorporated into the growing film. The typical operating pressure range for magnetron sputtering is 0.1~1 Pa.

Magnetron sputtering sources with various geometrical configurations are commercially available now, including planar, cylindrical, and tubular magnetrons. The sputtering targets can vary from a single element to alloys and compounds, or a multiple-piece construction. Generally, sputtering can preserve good maintenance of target stoichiometry, but some dissociation of compounds [105]. By adjusting the deposition chamber configurations, multiple targets can be co-sputtered at the same time to produce

complex compositional, metastable and multilayer coatings. By intentionally mixing the inert sputter gas with other reactive gases like for examples O_2, N_2, or CH_4, thin films of various composition and microstructure can be fabricated by simply sputtering a pure metallic target, known as reactive sputtering. In addition, a negative (bias) potential may be deliberately applied to the substrate during deposition in order to have concurrent energetic particle bombardment (known as bias sputtering), which can reduce the contamination and densify the depositing film [108]. Now many efforts have been devoted to developing hybrid magnetron sputtering systems that combine magnetron sputtering with other thin film technologies, for instance high-power impulse magnetron sputtering (HIPIMS), in order to better manipulate the growth process and film properties [110,111].

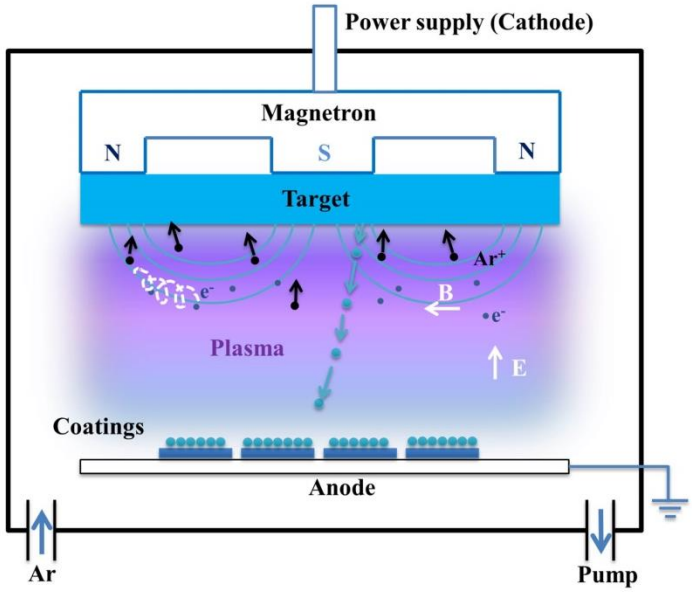

Figure 2.2 Schematic illustration of a magnetron sputtering system.

2.1.2 Microstructure evolution during film growth

Diverse properties of materials are dictated fundamentally by the nature of chemical bonding among their constituent atoms and their microstructures on a variety of length scales [107]. Thin films or coatings can exhibit a wide variety of distinguishable microstructures with respect to, for instance, phase composition, crystallographic orientation, grain size and defect density [107,112]. The microstructure of thin films can be designed and manipulated by choice of the deposition configurations, such as substrate temperature, residual gas pressure and substrate bias during deposition. Extensive studies aiming to understand the correlation between film micro- and macro-structure and growth parameters have been carried out during the past decades [50,113].

Figure 2.3 illustrates individual atomic-level processes responsible for adsorption and crystal growth on substrate surfaces during film growth [114]. The incoming atoms can be reflected, absorbed onto the substrate surface or re-evaporated, depending on the incoming flux, the sticking coefficient and the

trapping probability [114]. The adatoms diffuse and nucleate forming clusters to minimize the overall surface energy. Surface and bulk diffusion, i.e. the migration energy of adatoms, represent the determining atomic processes which control the microstructure evolution during film deposition. Three typical growth mechanisms involved in the initial stage formation of thin film are as follows [114,115]:

1. Island growth (Volmer Weber)
2. Layer-by-layer growth (Frank–van der Merwe)
3. Mixed growth (Stranski–Krastanov)

Figure 2.4 is a schematic representation of the three main growth modes under various surface coverages. Island growth mode occurs when the incoming atoms (adatoms) preserve stronger bonding with themselves than those of the adatom with the surface. They are featured by a sluggish surface diffusion, leading to the formation of localized three-dimensional (3D) clusters. These nucleated clusters eventually combine with each other through coalescence to form a continuous thin film in order to minimize the surface energy [114]. In contrast, when the vaporized atoms show stronger bonding with the substrate surface, layer-by-layer growth mode may occur. Hence, adatoms bond preferentially to surface sites resulting in atomically smooth and fully formed two-dimensional (2D) layers [114]. Stranski–Krastanov growth mode represents a combination of both layer-by-layer growth and island growth mechanism during development of thin films. In the initial stage, the adsorbed atoms are nucleated to form the thin film by a two-dimensional layer-by-layer growth mode, and then the thin film is transformed into a three-dimensional island growth mode [114]. Transition from the layer-by-layer to island-based growth occurs at a critical layer thickness, which highly depends on the physical and chemical properties, such as surface energies and lattice parameters, of the film and substrate [114,115].

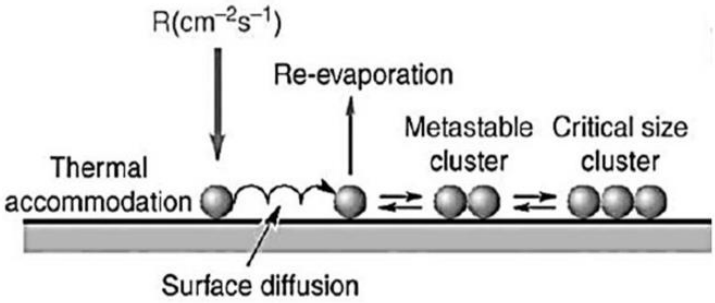

Figure 2.3 Schematic diagram of processes of nucleation and early stage of film growth [114].

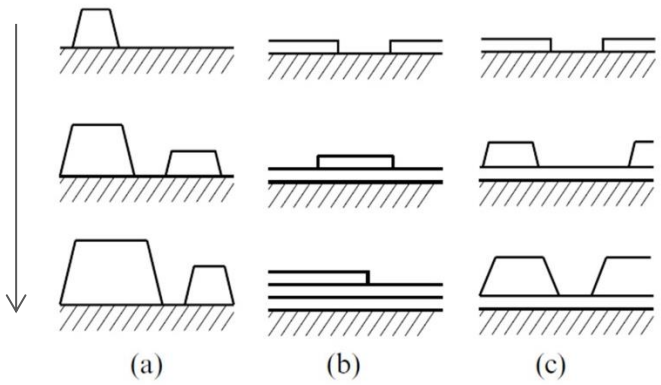

Figure 2.4 Schematic representation of the three growth modes: (a) island, or Volmer–Weber growth; (b) layer-by-layer, or Frank–van der Merwe growth; (c) layer-plus-island, or Stranski–Krastanov growth [115].

Structural investigations of thick polycrystalline films and coatings led to the establishment and refinement of structure zone models (SZMs), which systematically classify structural evolution of the films as a function of growth parameters during physical vapor deposition [115]. Obviously, the mobility of the condensing atoms or particles essentially relies on the energy of the arriving particles and the substrate temperature. Increasing the substrate temperature will naturally raise the diffusion capability of the adatoms. The working gas pressure is also important to modify the film structure by alternating the average kinetic energy of incoming atoms. The atoms emerging from the cathode lose energy when the atoms impact with the gas particles by crossing the discharge area. The higher the working gas pressure, the smaller the average kinetic energy and thus atoms with reduced mobility condense on the substrate surface.

Figure 2.5 shows the schematics of typical structures of thin film deposited by PVD and the structure zone model of Thornton, which is characteristic especially for magnetron sputtered thin films. Zone 1 corresponds to a low-temperature deposition at which adatom diffusion is negligible. The thin film is characterized by a porous structure consisting of tapered crystallites or it is even a completely amorphous network, separated by voids. The film surface is rough and develops in a fractal geometry. A transition zone appears at higher growth temperatures as Zone T. Now the surface diffusion becomes significant, thus a pronounced columnar structure formed in this Zone T, which is composed of a series of dense fibrous grains with no void boundaries. The adatom diffusion largely overcomes the roughness of the substrate and the initial nucleation, leading to a smooth surface [112]. The transition between Zones T and 1 shifts to lower temperatures with decreasing gas pressure as shown in the schematic representation due to the increasing energy of incoming atoms. Zone 2 represents a region of growth temperatures typically with $0.4 < T/T_m < 0.8$, where both surface and bulk diffusion occur. A wide columnar, dense structure with a rather smooth surface characterizes these films. The columnar grains tend to have a strong texture and increase in width with increasing T/T_m. At the highest substrate temperatures volume diffusion dominates, yielding equiaxed recrystallized grains of Zone 3 [116]. The working gas pressure has proved to

be of only little influence on the structure at high deposition temperatures. The main features of different zone structures for sputtered film are summarized in Table 2-1.

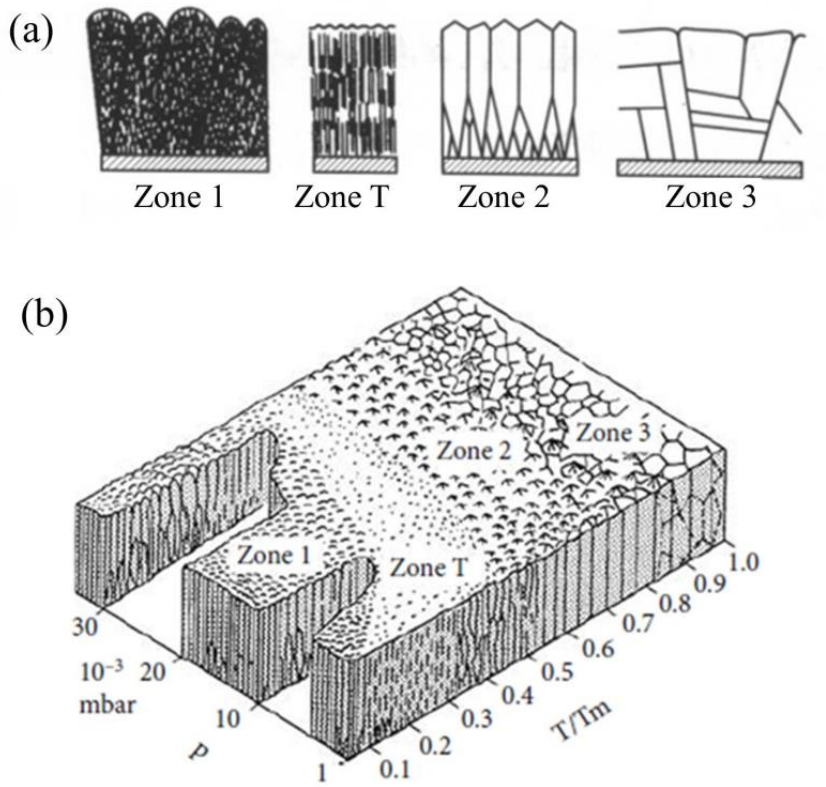

Figure 2.5 Microstructural evolution of film deposited by PVD as a function of deposition temperature and gas pressure, (a) Four typical structures, and (b) structure zone model (SZM) of Thornton. T is the deposition temperature, T_m is the coating-material melting temperature (both expressed in degrees K) and p is gas pressure [116].

Table 2-1 Structural characteristics and film properties of structure zone models for sputtered film [117].

Zone	T/T_m	Structural Characteristics	Film Properties
1	<0.1 at 0.15 Pa to <0.5 at 4 Pa	Tapered crystals, dome tops and voided boundaries.	High dislocation density, hard.
T	0.1 to 0.4 at 0.15 Pa, ~0.4 to 0.5 at 4 Pa	Fibrous grains, dense grain boundary arrays.	High dislocation density, hard, high strength, low ductility.
2	0.4 ~0.8	Columnar grains, dense grain boundaries.	Hard, low ductility.
3	0.4 ~1.0	Large equiaxed grains, bright surface.	Low dislocation density, soft recrystallized grains.

2.2 Fundamental aspects of high-temperature oxidation

Numerous materials, particularly those in common technical applications, are non-stable when exposed to an oxidizing environment and will react to form oxides [118]. High-temperature oxidation and corrosion

of materials is an important issue in a wide range of applications. Oxidation and degradation of components at elevated temperatures, for example in power plants, gas turbines and fuel cells are some specific examples. The prediction of material lifetimes and improvement of oxidation protection methods require the knowledge of which reaction products form and in what sequence and the rate of reaction [118]. The thermodynamic driving forces of specific chemical reactions determine which oxidation products can form during oxidation of a particular material [119]. The oxidation rate or oxidation kinetics depends on the physical state of the oxide products, the chemical nature of the transport processes within the oxide scale and the ability of the scale to maintain a physical barrier between the reactant phases [119].

2.2.1 Thermodynamic fundamentals

To predict which reaction products expected form, e.g., in selective oxidation of alloys/materials, during high-temperature oxidation requires the determination of whether or not a particular element/component in a material can react with the gas phase. The second law of thermodynamics describes the possibility of whether or not a reaction can occur. Since most high-temperature service conditions are constant temperature and pressure, the stability of a system can be expressed in terms of the total Gibbs free energy (G) [120],

$$G = H - TS \tag{2-1}$$

where H is the enthalpy and S is the entropy of the system. Under these conditions, the second law states that the free-energy change (ΔG) of a process will reveal the spontaneity of the reaction [118]:

$\Delta G < 0$, spontaneous reaction expected;

$\Delta G = 0$, equilibrium;

$\Delta G > 0$, thermodynamically impossible process.

In terms of high-temperature oxidation, the typical reaction of a metal with gaseous oxygen or steam can be written as:

$$2M + O_2 = MO \quad \text{(in oxygen-containing atmosphere)} \tag{2-2}$$

$$M + H_2O = MO + H_2 \text{ (in steam-containing atmosphere)} \tag{2-3}$$

where M is the reacting metal, MO is its oxide (the oxide can have variable stoichiometry, for example MO_2 or M_2O_3, for simplicity here use MO). The ΔG is expressed as:

$$\Delta G' = \Delta G^{\circ} + RTln\left(\frac{a_{MO}}{a_M^2 a_{O_2}}\right) \tag{2-4}$$

or in steam:

$$\Delta G' = \Delta G^{\circ} + RTln\left(\frac{a_{MO}a_{H_2}}{a_M a_{H_2O}}\right) \tag{2-5}$$

where $\Delta G°$ is the Gibbs free-energy change when all species are in their standard states, R is the gas constant, T is the temperature and a is the thermodynamic activity which describes a given species deviating from the standard state. The activity for a given species can be expressed as:

$$a_i = \frac{p_i}{p_i^0} \tag{2-6}$$

where p_i is either the partial pressure of a gaseous species or the vapor pressure over a condensed species and p_i^0 is the partial pressure corresponding to the standard state of species i.

The standard Gibbs free energy of formation versus temperature for metal oxidation reactions and the corresponding dissociation pressures of the oxides are conveniently summarized as Ellingham diagrams such as shown exemplarily in Figure 2.6 [118]. In the Ellingham diagram, the M and MO are considered as pure component, and their activities are assumed as unity. In addition, all reactions are normalized to same quantity of oxygen, i.e. 1 mol of O_2. At equilibrium conditions, the equation (2-4) can be re-written as

$$\Delta G^0 = RTln p_{O2} \tag{2-7}$$

The p_{O2} expresses the equilibrium oxygen partial pressure at which the metal and the oxide coexist, i.e. the dissociation pressure of the oxide. Values of p_{O2} can be obtained directly from the oxygen nomograph by drawing a straight line from the origin marked O through the Gibbs free energy line at the temperature of interest and reading the oxygen partial pressure from its intersection with the scale at the right side labelled p_{O2} [118]. Values for the equilibrium H_2/H_2O or CO/CO_2 ratio can be obtained in a similar way from the point marked H or C, respectively. The stabilities of various oxides then can be compared directly on the diagram, i.e., the lower the position of Gibbs free energy line, the more stable is the oxide [118]. Therefore, Ellingham diagrams are helpful in understanding oxidation tendencies. In principle, when considering the oxidation of materials consisting of multiple elements, the activity of each element must be taken into account. Selective oxidation of less noble elements which form higher thermodynamically stable oxide (like Al_2O_3 and Cr_2O_3) commonly occurs, depending on the chemical composition and the oxidation conditions [118,121]. For instance, selective oxidation of aluminum leading to the growth of alumina during high-temperature oxidation of commercial FrCrAl alloys has been commonly observed [119].

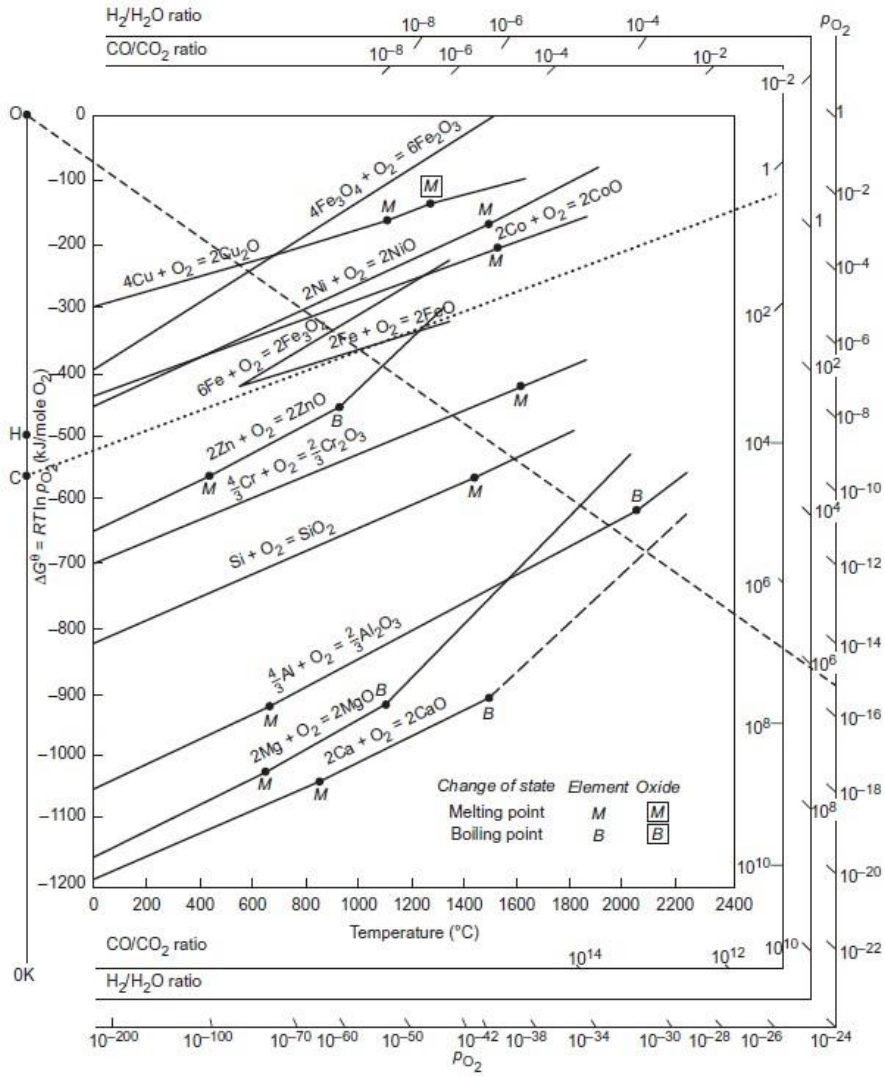

Figure 2.6 Ellingham diagram showing the Gibbs free energy of formation for selected oxides as a function of temperature, together with corresponding equilibrium p_{O2} and H_2/H_2O and CO/CO_2 ratios [118].

2.2.2 Oxidation rate and kinetics

The oxidation reaction of a component with the gaseous atmosphere in most application situations is undesirable and one attempt to reduce the oxidation rate upon such reaction occurs. A profound understanding of high-temperature oxidation reaction mechanisms requires not only knowledge of the thermodynamic fundamentals to predict the oxide formation but also knowledge on the transport process to evaluate the reaction rates and kinetics.

In most cases (except internal oxidation), high-temperature oxidation results in the growth of a solid oxidation product (an external oxide scale) that separates the two reactants. The oxide scale can consist of a single phase or multiphase, and sometimes it is amorphous. To further proceed the oxidation reaction, one or both reactants must penetrate the oxide scale, i.e. the oxidizing gas must be transported to the oxide/metal interface and/or the metal atoms must be transported through the oxide layer to the oxide/gas interface [118]. The oxidation kinetics varies widely depending on the penetration rate.

Oxidation processes are complex and oxide growth can be typically subdivided into five main steps. These steps are: (1) delivery of the oxidant to the scale/gas interface via gas mass transfer, (2) incorporation of the oxidant into the oxide scale, (3) delivery of reacting metal from the alloy to the alloy/scale interface, (4) incorporation of metal into the oxide scale, (5) transport of metal and/or oxidant through the scale [118]. Figure 2.7 depicts a schematic cross-sectional view of reactions and transport processes involved in the growth of an oxide scale during oxidation in oxygen [118]. During steady-state oxidation stage at which a dense oxide scale forms, the reaction can proceed only through solid-state diffusion. It is well-known that oxides are ionic in nature and there are either highly stoichiometric or non-stoichiometric ionic compounds. Non-stoichiometric ionic compounds are known as semiconductors including two types, i.e. Negative (n-type) semiconductors and Positive (p-type) semiconductors. Negative carriers transfer the electrical charge in n-type semiconductors, which are provided with an excess of metal ions or a deficit of non-metal ions. While p-type semiconductors with positive carriers originate from either an excess of non-metal ions or a deficit of metal ions. Various kinds of defects exist in crystal structures, for example vacancies or interstitials [120]. Thus, it is reasonable to postulate that electronic and ionic transport processes through the oxide scale are accompanied by ionizing phase-boundary reactions, and that the growth of new oxides at which position is dependent upon whether cations or anions are transported through the oxide layer [118].

Assuming that the cationic transport across the oxide layer controls the growth rate of oxide scale and that thermodynamic equilibrium is established at each interface, the classical Wagner's parabolic oxidation kinetics can be deduced [118]. As shown in Figure 2.7, the outward cation flux ($j_{M^{2+}}$) is equal and opposite to the inward flux of cation defects (here assuming to be vacancies, j_{V_M}). According to Fick's first law of diffusion, $j_{M^{2+}}$ can be expressed by the following equation:

$$j_{M^{2+}} = -j_{V_M} = D_{V_M} \frac{C''_{V_M} - C'_{V_M}}{x} \tag{2-8}$$

Here D_{V_M} is the diffusion coefficient for cation vacancies, C''_{V_M} and C'_{V_M} are the vacancy concentrations at the scale/metal and scale/gas interfaces, respectively, and x is the oxide scale thickness. In thermodynamic equilibrium conditions, the value of C''_{V_M}-C'_{V_M} is constant and the equation reduces to

$$j_{M^{2+}} = \frac{1}{V_{ox}} \frac{dx}{dt} = D_{V_M} \frac{C''_{V_M} - C'_{V_M}}{x} \tag{2-9}$$

where V_{ox} is the molar volume of the oxide and t is the oxidation time. Thus, the growth rate of the oxide scale is given by:

$$\frac{dx}{dt} = \frac{k'}{x} \tag{2-10}$$

where $k' = D_{V_M} V_{ox} (C''_{V_M} - C'_{V_M})$. Integrating and noting that $x = 0$ at $t = 0$, one obtains the following equation

$$x^2 = 2k't \tag{2-11}$$

which is the classic parabolic rate law and k' is the parabolic rate constant. The rate constant will vary with oxidation temperature according to the Arrhenius equation, which indicates the dependence of the reaction rate constant on the absolute temperature:

$$k' = -Ae^{-E_a/RT} \quad \text{or} \quad lnk' = -\frac{E_a}{RT} + lnA \tag{2-12}$$

where A is the pre-exponential factor and E_a is the activation energy of the oxidation reaction. Another common and straightforward expression of the parabolic rate law is the measurement of the mass increase per unit surface area of the specimen since the mass gain can be easily recorded *in-situ* by a thermal balance during oxidation. Thus, equation (2-11) can be re-written as:

$$\left(\frac{\Delta m}{\xi}\right)^2 = 2k't \tag{2-13}$$

where Δm is the mass gain and ξ is the area over which the reaction occurs.

In most cases, oxidation of metals and alloys at elevated temperatures follow parabolic oxidation kinetics. According to this law, oxidation and consumption of the material will be gradually slowed down with the thickening of the oxide scale. The defects in the oxide and their mobility largely determine the oxidation rate. Figure 2.8 compares the parabolic oxidation rate constants of various common oxide scale forming materials in steam fitted to an Arrhenius relationship [15]. It can be seen that the most effective oxides for protecting the subjacent matrix from fast consumption are scales made of chromia, alumina and silica. A thin, adherent and slow-growing oxide layer develops on the surface during high-temperature oxidation of those scale-forming materials. It is necessary to point out that chromia can form volatile suboxides (in oxygen) or hydroxides (in steam) at temperatures above around 900°C which generally restrict its application to somewhat lower temperatures, particularly in high-speed flow environments [103]. The basis for developing of oxidation resistant engineering alloys is to add suitable amounts of specific alloying elements, typically Al, Cr, or Si, into the matrix, which may form corresponding highly protective scales during application.

Due to the simplified treatment of diffusion-controlled oxidation and more complex oxidation reaction processes occurring in real situations, other oxidation kinetics are often observed. For instance, in the early stages of high temperature oxidation of thin oxide scale growth, logarithmic kinetics is commonly observed [118]. Under certain conditions the oxidation can proceed at a constant rate obeying a linear rate law, like breakaway oxidation of Zr-based alloys [12] and FeCrAl-based alloys [119]. Oxidation induced stresses, including growth or thermal stress, develop as the reaction progresses, which may result in void formation, crack or spallation of the oxide scale, thus increasing the degradation rate and oxidation rate [118]. Oxides may be in the form of liquids or volatiles at high temperatures, alternating the oxidation kinetics to more complex situations [16].

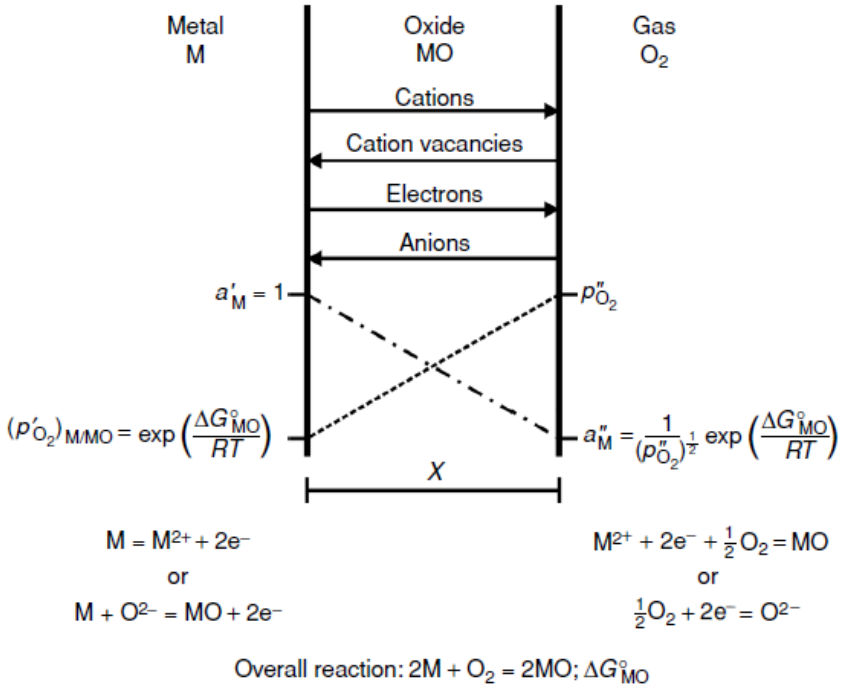

Figure 2.7 Typical reactions and transport processes involved in the growth of an oxide scale during oxidation in oxygen [118].

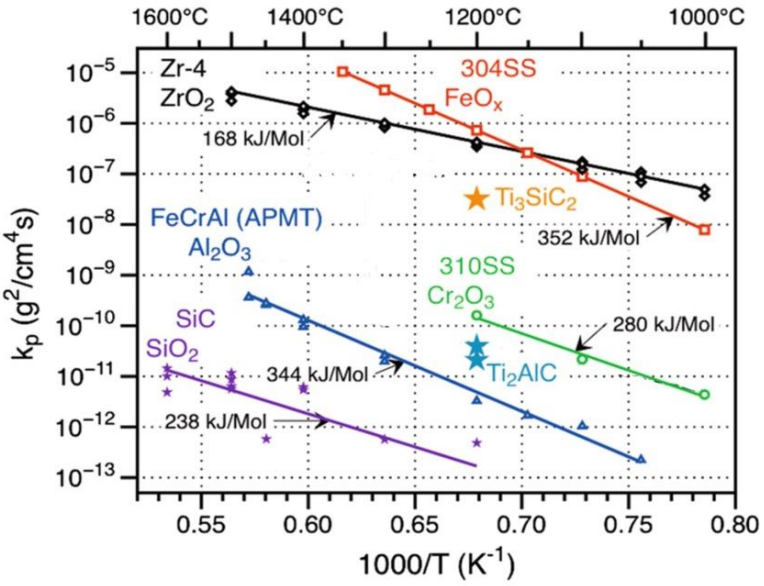

Figure 2.8 Arrhenius plot of parabolic oxidation rate constants for various oxide scale forming materials in steam with the resulting oxidation activation energies noted [15].

2.2.3 Degradation of oxidation-resistant coatings

The oxidation mechanisms and degradation phenomena of oxidation-resistant coatings are essentially similar as those described above for bulk materials. However, additional constraints arise with coatings,

mainly chemical and mechanical compatibility with the substrate, which may remarkably restrict their service life [122].

Because coatings are normally thin, they hold a limited reservoir of the scale-forming elements (typical Cr, Al or Si). Thus, interdiffusion/reaction between the coatings and the substrates can deplete the scale-forming elements and introduce undesirable elements into both the coating and the substrate [118,122]. Therefore, interdiffusion may further degrade the performance of the coatings and alter or modify the mechanical properties of the underlying substrate. Mechanical constraints, largely arising from thermal expansion mismatch, can also lead to degradation of the coating, for instance by cracking, delamination and spallation.

2.3 Analysis and characterization techniques

Extensive analysis and characterization techniques are implemented in this study to determine the chemical and phase composition, microstructure and mechanical properties of materials, which helps to unravel why different materials show diverse properties and behaviors and to further manipulate the specific performance requirements.

2.3.1 X-ray diffraction (XRD)

X-ray diffraction (XRD) is a rapid, non-destructive analytical technique to identify the crystalline phases present in materials and to characterize the structural properties (for example strain state, crystallographic texture, grain size) of these phases [123]. It can also be used to determine lattice parameters of a crystalline material and serve for quantitative phase analyses.

XRD methods rely on the diffraction of X-rays by periodic atomic planes of crystals in a characteristic manner. X-rays are high-energy electromagnetic waves with a wavelength ranging from 10^{-3} to 10^{1} nm. When an incident beam of monochromatic X-rays interacts with a target, it is scattered by the electrons of the lattice atoms [123]. The scattered X-rays undergo constructive and destructive interference, known as diffraction process. The constructive interference from X-rays scattered by the atomic planes in a crystal can be observed and the prerequisite for constructive interference from diffracting planes can be described by Bragg's Law:

$$2d\sin\theta = n\lambda \tag{2-14}$$

where d is the spacing between diffracting lattice planes, θ is the incident angle in degree, n is any integer, and λ is the wavelength of the beam. The shape and intensities of the diffracted signals is dependent on the type and arrangement of atoms in the lattice structure of materials [124].

Lab X-ray diffractometers are generally composed of an X-ray tube, a sample holder, primary and secondary optics, a goniometer, and an X-ray detector. In the vacuum X-ray tube, electrons are emitted by heating a tungsten filament. Then the electrons are accelerated using a high potential electric field. The accelerated electrons are directed to impinge an anode target material, which then emits X-rays. Figure 2.9 provides a schematic presentation showing some of important interactions between a solid specimen and

an incident beam of electrons [116]. The interactions of electrons with matter generate a range of signals as shown in Figure 2.9, which are collected and used for material characterizations. The mechanism of generating X-ray is described herein and others will be explained later in corresponding sections. Two effects can generate the X-ray photons. The first is electrons deceleration contributing to the emission of X-ray photons with a broad continuous distribution of wavelength [123]. The second is electrons from outer shells jumping into a vacancy of inner shells where the original electrons are ejected, with a characteristic X-ray radiation depending on the primary and final shell position of the electrons, as shown in Figure 2.9 [123]. Thus, a superimposition of a continuous X-ray spectrum and of characteristic X-ray radiations can be obtained. Figure 2.10 is a schematic presentation of intensity over wavelength distribution of the X-ray radiation produced by an X-ray tube. In general, only the characteristic radiation with the highest intensity is used in XRD measurements, and most of the remaining radiation is removed. Thus, the X-ray spectrum is filtered to produce monochromatic radiation, which is then collimated and directed onto the sample surface. One of the most popular anode materials for monochromatic radiation is copper and the radiation used is Cu $K_{\alpha 1}$ (λ=0.154049 nm).

The Bragg-Brentano geometry, also known as $\theta/2\theta$ arrangement, is the most common configuration in laboratory diffraction instruments. In this geometry, the specimen is rotated at a speed which is one half the angular velocity of the detector, i.e. varying the incidence angle of the incoming X-ray beam by θ and the scattering angle (detector) by 2θ. The diffracted intensity is measured as a function of 2θ and the orientation of the specimen, which yields the diffraction pattern [123]. In this geometry only the specific orientated lattice planes (parallel to the sample surface) will diffract the X-rays, thus this setup is common used for polycrystalline materials having many crystallites in random orientations, known as powder diffraction.

In terms of characterization of thin films (that often show a particular, preferred crystallographic orientation), advanced X-ray diffractometers with additional rotation axes are available. For example, two common setups are used in form of grazing incidence X-ray Diffraction (GIXRD) and XRD pole figure measurements. In GIXRD, the incoming X-ray beam is fixed at small incident angles that slightly above the critical angle for total reflection of the film material [125]. So, the often intense signal arising from the substrate can be avoided, and the collected information stems mostly from the thin film itself [125]. GIXRD can therefore greatly improve the surface sensitivity and allow a depth-profiling mode by varying the incidence angle. A XRD pole figure is a method of displaying crystallographic texture in a stereographic projection, with a specified orientation relative to the specimen. Such a figure shows the variation of pole density with pole orientation for a selected set of crystal plane [126]. Pole figure measurements collect the diffracted intensity at a fixed 2θ angle via tilting and rotating the sample from sample surface normal direction [125]. In addition, in situ XRD methods are also developed for the investigation of processes under temporally changing conditions, such as high pressures, mechanical loading, and temperature variations in high temperature ranges (known as high-temperature XRD) [123].

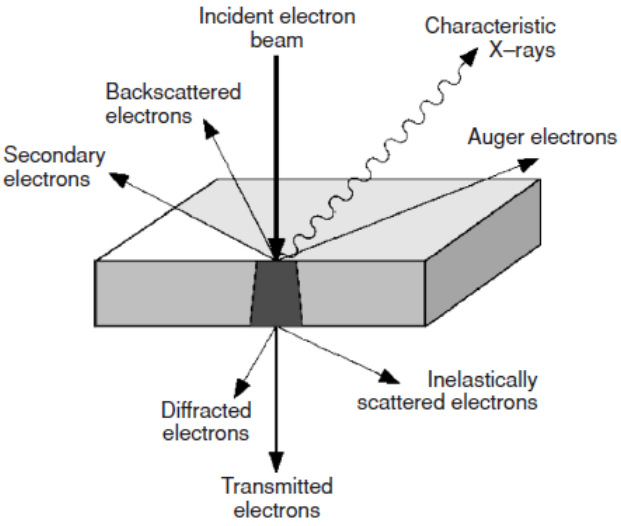

Figure 2.9 Schematic presentation of the interactions of an incident electron beam with a solid specimen [118].

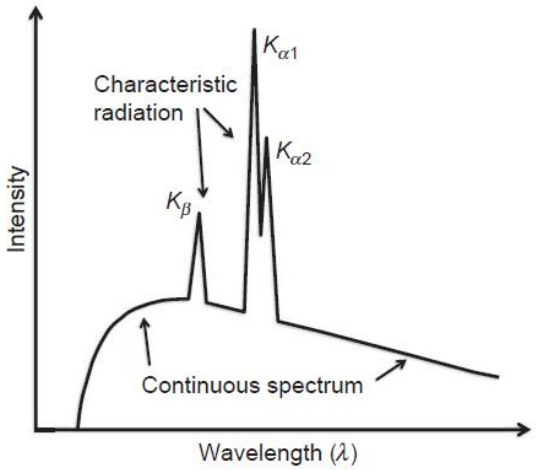

Figure 2.10 Schematic presentation of intensity over wavelength distribution of the X-ray radiation produced by an X-ray tube showing the continuous and the characteristic spectrum [123].

2.3.2 Raman spectroscopy

Raman spectroscopy is one of the vibrational spectroscopic techniques which is frequently used to collect information on molecular vibrations and crystal structures [127]. Light interacts with matter in several ways. The photons in a light may be scattered when it interacts with matter. In most cases, an elastic scattering process occurs and there is no energy conversion. However, a tiny proportion of the scattering exist via an inelastic process. The inelastic scattering of the incident light from a sample and shifted in frequency by the energy of its characteristic molecular vibrations is known as Raman scattering [127].

Figure 2.11 is a schematic representation of energy-level diagram involved in Raman spectroscopy. When an intense monochromatic light beam (laser) impinges on the sample, the light photons interact with the molecule within the sample and distorts (polarizes) the electron cloud around the nuclei to create a

transient state referred as a virtual state [127]. This state is a short-lived, non-stable state; thus, the photon will be rapidly re-radiated as scattered light. The vast majority of the stored energy is re-radiated at the identical frequency as that of the incident exciting light photons. This process is called elastic scattering and known as Rayleigh scattering. However, during the scattering process if nuclear motion is induced, energy will be transferred either from the incident photons to the molecules or from the molecules to the scattered photons [127]. The scattering now is an inelastic process and the energy of the scattered photons is different from that of the incident photon, i.e. frequency change of the scattered light, which is known as Raman scattering [127]. Raman scattering occurs in two situations, Stokes Raman scattering and anti-Stokes Raman scattering. Stokes Raman scattering represents the absorption of energy from the incident photon by the original ground vibrational state of the molecule and it transitions to a higher energy excited vibrational state (Figure 2.11). However, few molecules may exist in an excited state, and scattering from these states to the ground state involves transferring energy to the scattered photons, called anti-Stokes scattering [127]. Normally, the probability of molecules in an excited vibrational state is considerably lower than that of molecules in the ground state [127]. Consequently, the intensity of Stokes Raman scattering is substantially higher than that of anti-Stokes Raman scattering. In a classic Raman measurement, the signals of Stokes Raman scattering are collected and the Rayleigh scattered light is blocked using a filter for simplicity.

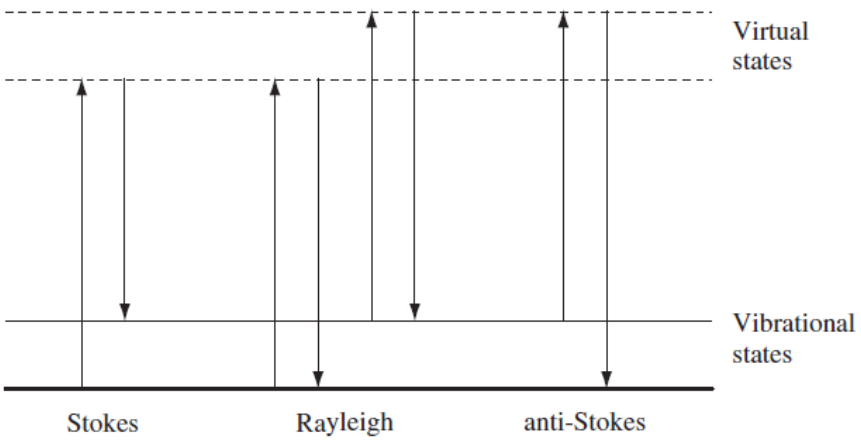

Figure 2.11 Schematic representation of the Rayleigh and Raman scattering processes [127].

Raman spectra are usually reported as the intensity of scattered light against wavenumber (the reciprocal of wavelength, called Raman shift). In order to transform between the spectral wavelength and the wavenumbers, the following formula can be used [127]:

$$\Delta w = \frac{1}{\lambda_0} - \frac{1}{\lambda_1} \tag{2-15}$$

where Δw is the Raman shift expressed in wavenumbers, λ_0 is the excitation wavelength, and λ_1 is the scattered light wavelength. The unit of inverse centimeters (cm^{-1}) is commonly used for expressing wavenumbers in Raman spectroscopy. The characteristic Raman spectral patterns are used to identify

substances and to quantitatively or semi-quantitatively evaluate the proportion of a specific substance in a sample.

2.3.3 X-ray photoelectron spectroscopy (XPS) and Auger electron spectroscopy (AES)

X-ray Photoelectron Spectroscopy (XPS) and Auger electron spectroscopy (AES) are two widely used techniques for probing chemical and compositional surface environment. XPS and AES measure the energy of electrons emitted from the top 0 to 10 nm of a material [128].

XPS process involves ionization of an atom by a photon of sufficiently short wavelength (i.e., high energy), ejecting photoelectrons from the sample. When a sample is irradiated with monoenergetic X-rays of photon energy $h\nu$ (h is the Planck constant and ν is the frequency), an electron can be ejected from a core level of an atom based on the photoelectric effect. The process of photoemission is shown schematically in Figure 2.12(a). The kinetic energy (E_K) of the ejected electron is then experimentally quantitatively analyzed by an electron spectrometer, which depends on the energy of the photon. The parameter that identifies the electron specifically is the binding energy of the electron (E_B), stemming from both its original element and occupied atomic energy level. In the XPS process, the relationship among the parameters involved can be expressed as:

$$E_B = h\nu - E_K - \Phi_s \tag{2-16}$$

Where Φ_s is the spectrometer work function, which is the minimum energy needed to remove an electron from the Fermi level of a solid to the vacuum [128]. The binding energy of the electron can be calculated via measuring the three quantities on the right-hand side of the equation. In consequence, a typical XPS spectrum is presented as a plot of intensity of the photoelectrons identified versus their binding energy in a specific range. The photoelectrons which are excited and escape without energy loss constitute the characteristic peaks in the spectrum; those which undergo inelastic scattering and suffer energy loss result in the background of the spectrum [128]. The position of the peaks directly measures the binding energy of the electrons in the orbitals and identifies the element concerned; the intensities of the peaks give information to determine the ratios of the elements in the outermost layer. The small chemical shifts (difference from elemental state) in the binding energy of an element, arising from differences in the chemical potential and polarizability, are utilized for identification of its chemical bonding state in the specimen.

Another possibility during the ionization of an atom by a photon is the ejection of an Auger electron as shown in Figure 2.12(b). Photoelectron emitted from a core level will leave a shell vacancy. An electron in an outer shell with higher energy can fill this shell vacancy. In order to comply with the principle of the conservation of energy, two processes are possible. The emission of an X-ray photon may occur or another electron may be ejected from the atom. This electron is termed as Auger electron (Figure 2.12(b)). Their energies are element specific, which is irrespective of the primary beam composition or its energy and represents the characteristic material quantity [128]. Thus, in XPS process Auger electrons are produced as a consequence of the transitions between electron levels. In addition, Auger electrons can be

generated by many other excitations, such as bombardment by electrons or protons. One most common method is irradiation of samples with a finely focused electron beam, as illustrated in Figure 2.9. The fine focus of an X-ray beam is challenging, thus, the use of a finely focused electron beam for AES measurement enables a higher spatial resolution to achieve during surface analysis than that achievable in XPS [128]. A concentration-depth profile can be obtained by combining XPS/AES measurements with ion milling (sputtering) the surface of specimen with an ion beam.

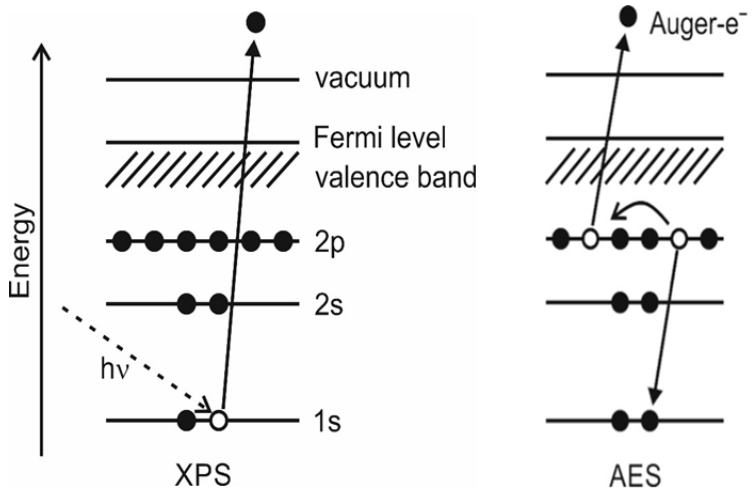

Figure 2.12 Schematic representation of the (a) XPS process showing photoionization of an atom by the ejection of a 1s electron and (b) AES process [128].

2.3.4 Scanning electron microscopy (SEM)

A scanning electron microscope (SEM) is one kind of electron microscope to scan and image the surface of a sample using a focused electron beam. The important interactions between a solid specimen and an incident beam of electrons have been schematically presented in Figure 2.9 [118].

Secondary electrons are electrons that emit from the superficial layer of a sample material via inelastic interactions between the primary electron beam and the specimen atoms, in case they have sufficient energy to escape the sample surface. The electrons in the primary electron beam can undergo elastic scattering and are reflected or back-scattered known as backscattered electrons. Since larger atoms are much stronger scatters of electrons than light atoms, and therefore the number of the backscattered electrons is proportional to atomic number of an element. If energy of the incident electron beam is sufficient, it will knock electrons from inner shells of an atom [118]. Characteristic X-rays and Auger electrons also can be emitted from the solid as described before. Some of the electrons can penetrate the specimen if the specimen is sufficiently thin. These electrons will comprise a transmitted beam and a diffracted beam of electrons. The various signals are collected and examined, corresponding, to acquire information about the surface topography, microstructure and chemical composition of the samples.

Secondary electrons and backscattered electrons are commonly used for imaging samples in SEM. Owing to the low energy of secondary electrons, these electrons originate from the top surface of the specimen.

The number density of secondary electrons that escape is also dependent on the local tilt of the specimen surface [123]. Thus, secondary electrons are most valuable for screening the morphology and topography of samples and images with a well-defined, three-dimensional appearance can be produced. Using the signal of secondary electrons, the image resolution can be up to 10 nanometers or better. With respect to backscattered electrons, their number density increases accompanied by the increasing average atomic mass of specimen atoms. During BSE imaging, the heavy element rich areas appear brighter. Therefore, backscattered electrons are most valuable for illustrating contrasts of regions having different chemical compositions.

In addition, X-rays emitted from the specimen are usually counted and used for quantifying the chemical composition and for mapping the elemental distribution. Specific X-ray energies or wavelengths are selected and counted via detectors, using energy dispersive X-ray spectroscopy (EDS) or wavelength dispersive X-ray spectroscopy (WDS) [123]. In EDS, the number of X-rays of all wavelengths emitted from a sample is accumulated. In contrast, WDS utilizes the diffraction of X-rays from crystals to select X-ray wavelengths of interest. Compared with EDS, WDS is generally more precise with lower detection limits due to its superior X-ray peak resolution and a lower background noise. However, EDS yields a broad spectrum of wavelengths or energies simultaneously and is typically more efficient requiring a much shorter counting time. Another similar technique is electron probe micro-analyzer (EPMA) which utilizes an electron microprobe. The primary importance of an EPMA is the capability to acquire precise, quantitative elemental analyses on the micron scale or nanometer scale [129].

2.3.5 Transmission electron microscopy (TEM)

Transmission electron microscopy (TEM) is another major type of electron microscopy in which an electron beam is transmitted through a thin specimen and then collected to create images (Figure 2.9). It can provide significantly high spatial resolution examination of specimens to the atomic level due to the smaller de Broglie wavelength of electrons. This technology allows scientists to investigate the atomic structure, defects, crystallinity and morphology at specified positions of a substance.

Electrons are generated from an electron gun either by a field emitter or by thermal emission using a cathode in TEM. The electrons are accelerated in an electric field using electromagnetic coils operated with voltages of typically ~100−300 kV. Then the electron beam is focused by a system of electromagnetic lenses and apertures onto a specimen. Here, it is required that the specimen is thin enough to transmit the electron beam, known as electron transparency. TEM specimens should be less than 100 nanometers thick, and therefore the sample preparation for TEM analyses is a complex procedure. The common methods to thin the specimen include mechanical milling, chemical etching, ion etching and milling. Finally, the objective lens gathers the electrons after interacting with the sample to create images [124].

A modern TEM imaging system can be operated at different modes and the two basic operation modes are imaging and diffraction modes. The most common imaging ones are bright-field (BF) imaging, dark-field (DF) imaging and high angle annular dark field (HAADF) imaging [124]. The contrast formation of

acquired images depends upon the mode of operation. Two types of electrons, unscattered and scattered, exist after the primary electron beam interaction with the sample. Electrons which are scattered, either elastically or inelastically, as they pass through the sample move at an angle to the axis of the electron beam [124]. In the BF mode, the scattered electrons are blocked and the transmitted electrons (i.e. unscattered electons) are focused to form an image. The contrast formation in this mode mainly comes from the sample having variable thickness or density. In DF imaging, the direct transmitted beam is blocked while one or more diffracted beams (scattered electrons) are permitted to go through the objective aperture [123]. DF mode is a powerful role in the study of crystals and crystal defects, for instance grain size and orientation, planar defects, stacking faults and dislocations, due to the strong interactions of diffracted beams with the specimen [124]. In addition, a high angle annular dark field (HAADF) detector can collect the electrons which are inelastically scattered through very high angles, as shown in Figure 2.9. HAADF images are powerful in analyzing materials chemistry at the atomic scale since they contain high contrast discrepancies assuming local variation in atomic number (Z-contrast) of the specimen [124]. Advanced TEM instruments are usually equipped with scan coils, which allow scanning a focused beam of electrons across the specimen, known as scanning-TEM (STEM) [124].

Electron diffraction is another basic operation mode of TEM and one common method is called selected area electron diffraction (SAED). The electrons are elastically scattered by the lattice planes obeying the Bragg's law and diffraction patterns can be obtained by adjusting the magnetic lenses [124]. The interested areas can be selected using an aperture. The SAED patterns can provide information on phase identification, determination of lattice parameter and space group, analysis of grain texture and structural defects [123].

2.3.6 Mass spectrometry

Mass spectrometry is a powerful analytical technique with both qualitative and quantitative applications. The overall process in a typical mass spectrometry procedure comprises first conversion of sample molecules into gaseous ions, with or without fragmentation, then characterization of the ions by means of their mass-to-charge ratios (m/z) and relative abundances [130].

A mass spectrometry instrument generally is made up of three major components: an ion source, an analyzer and a detector system. The gaseous ions from the substance of interest are produced from, for instance an electron ionization source or a chemical ionization source. In the analyzer, an electric or magnetic field is applied to accelerate and deflect the ions; ions are separated and counted based on their mass-to-charge ratio [130]. Two main types of analyzer are available, namely the time-of-flight (TOF) analyzer and the quadrupole mass analyzer [130]. The TOF analyzer distinguishes the different ions by the time it takes for one ion to reach the detector since the lighter ions of the same charge will travel faster than the heavier ions. In a quadrupole analyzer, an oscillating electrical field is exerted to the rods and ions are separated based on the steadiness of their trajectories [130]. A wide range of m/z-values can be scanned by continuously varying the applied voltage. The relative abundance of the distinguished ionic species is recorded by the detector system. In a mass spectrum, the ion current is plotted as a function of

the mass-to-charge ratio. The resolved ions offer relevant information concerning the chemical nature and assembly of their precursor molecules. The ion abundance quantifies the amount of a known species.

2.3.7 Nanoindentation

Nanoindentation is a recognized method for characterizing the mechanical properties of materials at the micro/nanoscale. Nanoindentation are routinely adopted to measure the hardness and elastic modulus of materials, now considerable progresses have been achieved in the evaluation of additional mechanical parameters, for instance creep behavior, fracture toughness and residual stress [131].

A nanoindentation experiment are performed within the material to be tested, an indenter tip and sensors and actuators executing and measuring the mechanical load and indenter displacement [131]. Nanoindenter tips are conventionally made of diamond, and come in various shapes, like spherical, cube corner or pyramidal (Berkovich) indenters. Most nanoindentation measurements use a simple load–unload cycle. For a typical nanoindentation test, the hard indenter is pressed into a tested material's surface where the applied force and the corresponded indenter displacement are continuously recorded [132].

A typical load-displacement (P–h_i) curve is depicted in Figure 2.13. One can extract the hardness and modulus of elasticity of the specimen material from the load-displacement curves. The hardness can be calculated as:

$$H_i = \frac{P}{A_c} \tag{2-17}$$

where H_i is the indentation hardness, P is the applied load and A_c is the projected contact area. Generally, both elastic and plastic deformations contribute to the maximum displacements; some degree of recovery occur due to relaxation of elastic strains during unloading. The plastic depth and the geometrical sizes and shape of the indenter are used to calculate the projected area in contact with the indenter [132]. Extrapolation of slope of the initial unloading curve to zero loads offers the plastic depth of indentation, as shown in Figure 2.13. The slope of unloading in the load-depth response is adopted to acquire the elastic properties of the sample as follows:

$$\frac{dh_i}{dP} = \frac{1}{2h_c}\left[\frac{\pi}{24.5}\right]^{1/2}\frac{1}{E_r} \tag{2-18}$$

where dh_i/dP is the change in depth with load during the initial linear region of the unloading curve, h_c is the plastic depth for an ideal Berkovich pyramidal indenter and E_r is the reduced Young's modulus [132]. The reduced Young's modulus comprises the elastic deformation that takes place in the tested specimen and in the indenter. The reduced Young's modulus connects to the Young's modulus through the following relationship obtained from contact mechanics:

$$\frac{1}{E_r} = \frac{(1-\upsilon^2)}{E_Y} + \frac{(1-\upsilon_o^2)}{E_o} \tag{2-19}$$

where E_Y and υ are Young's modulus and Poisson's ratio of the sample and E_o and υ_o are the same quantities of the indenter.

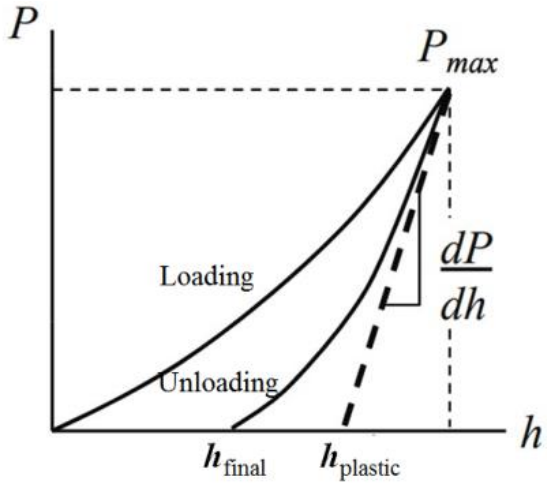

Figure 2.13 A typical load-displacement curve from a nanoindentation experiment using a depth-sensing indentation tester [132].

2.3.8 Scratch test

Scratch testing is an important method to evaluate the practical adhesion strength and mechanical failure modes of thin films or coatings on diverse substrates. During the test, a diamond stylus of defined geometry is drawn across the flat surface of a coated specimen at a constant speed and a defined normal force (constant or progressively increasing) for a defined distance [133].

Generally, appearance of micro-cracks for hard coatings within the scratch track occurs before failure of the coatings. The minimum load at which the first crack arises is defined as the "lower critical load" L_{c1}, and the load corresponding to complete delamination or peeling off the coating is the "higher critical load" L_{c2} [133,134]. An optical or electron microscope can be used to measure the distance along the scratch track from its starting point to the selected damage feature. It is necessary to point out that this technique does not quantify the fundamental adhesion bond strength of a coating-substrate system [133]. It presents an engineering evaluation of the practical (extrinsic) adhesion strength between the coating and the substrate, which relies on the complex interaction of the applied parameters and the coating/substrate properties [133].

2.4 Materials

Two MAX phase products, registered as Maxthal 312® (Ti_3SiC_2) and Maxthal 211® (Ti_2AlC), are commercially available. In case of high-temperature oxidation of bulk Ti_2AlC, a dense Maxthal 211® plate is supplied by Kanthal/Sandvik, Sweden. The measured density is around 3.99 g/cm^3 (99% of the theoretical value). Rectangular specimens for oxidation experiments with a dimension of approximately 3 × 6 × 10 mm^3 are sliced by using a conventional band saw.

Five high-purity cylindrical elemental plates of titanium (Ti: 99.95%, FHR Anlagenbau GmbH), zirconium (Zr: 99.5%, FHR Anlagenbau GmbH), chromium (Cr: 99.95%, FHR Anlagenbau GmbH), graphite (C: 99.95%, Schunk Kohlenstofftechnik GmbH) and aluminum (Al: 99.95%, FHR Anlagenbau GmbH) are

used as materials sources for magnetron sputtering. For this purpose, these plates are bonded onto a water-cooled copper backplate and then are used as targets for magnetron sputtering in this study. The plates are ~6 mm thick and 75 mm in diameter.

A variety of substrates will be used in this study for various purpose, including Si(100) wafer and Si(100) wafer with an amorphous 1 μm thermally grown SiO_2 layer on the surface (SiO_2/Si), polycrystalline Al_2O_3 substrates (MTI Corporation, USA) and Zircaloy-4 substrate (ANF GmbH, Germany). The Si, SiO_2/Si and Al_2O_3 substrates are in a rectangular shape and the geometry of the substrates is 0.375 – 0.5 × 10 × 10 mm^3. The Si wafers and SiO_2/Si substrates are used for specific chemical composition analyses to identify the coating elements. The SiO_2/Si and Al_2O_3 substrates are selected for heat treatment of the as-deposited coatings aiming to prevent significant reaction or interdiffusion between coatings and substrates. The suitable annealing temperatures for the formation of crystalline MAX phase structures identified from the SiO_2/Si and Al_2O_3 substrates will be chosen as processing temperature of coatings on Zircaloy-4 substrates.

The chemical composition (wt.%) of the Zircaloy-4 substrates is as follows: Sn ~1.4, Cr ~0.10, Fe ~0.22, O ~1000 ppm, Zr balance. Two shapes of samples are used. In case of oxidation test of coated Zircaloy-4, the samples are thin slices with size of 0.575 × 10 × 10 mm^3. The two main sides of Zircaloy-4 specimens are firstly ground with SiC paper, followed by polishing using active oxide polishing suspensions, and finally rinsed with distilled water. The finished average surface roughness (Ra) is around 50 nm. Only the two polished sides will be coated and four edges of the substrate are not able to cover. With respect to the hydrogen permeation experiments, solid cylinder specimens with one side polished are used as substrates. A brief overview of the materials used as well as their geometry can be found in Table 2-2.

Table 2-2 Overview of the materials used as well as their geometry.

Type	Name	Size (mm)	Remarks
Bulk Materials	Ti_2AlC (Maxthal 211®)	~3 × 6 × 10	-
Targets	Ti, Zr, Cr, C, Al	6 ×Φ75	-
Substrates	Si(100) wafer SiO_2/Si Alumina	0.375 – 0.5 × 10 × 10	One side polished and coated
	Zircaloy-4 (Plate)	0.575 × 10 × 10	Two main sides polished and coated
	Zircaloy-4 (Solid cylinder)	~14 × Φ12	One base side polished and coated

3 High-temperature oxidation of bulk Ti_2AlC MAX phase in steam

With respect to nuclear applications, Ti_2AlC has been considered as structural material and protective coating due to combining attractive properties of both ceramics and metals, altogether with an excellent oxidation resistance. The majority of previous investigations on its oxidation behavior were performed in air, and only few studies were found on oxidation in steam, but these studies were carried out at low temperatures. However, the typical scenarios in case of nuclear accidents are related with high-temperature steam atmospheres. Therefore, high-temperature oxidation behavior of bulk Ti_2AlC, as reference/benchmark material to validate its potential application as oxidation-resistant coatings, in steam up to 1600°C was initially investigated. The oxidation mechanisms and failure behaviors of bulk Ti_2AlC samples were elucidated on the basis of its oxidation kinetics and the microstructural evolution of thermally grown oxide scales on the surface. The maximum tolerant temperature of bulk Ti_2AlC ceramic in steam has been determined by a transient test. The results revealed its superb oxidation resistance up to 1400°C and its ability to withstand temperatures up to around 1550°C in steam, thus showing promising application prospects as oxidation-resistant protective coatings in humid atmospheres.

3.1 Introduction

In the Ti-C-Al system, two MAX phases, namely Ti_2AlC and Ti_3AlC_2, have been successfully synthesized, and both have been intensively studied [67]. They are the most lightweight and oxidation resistant among the MAX phases reported so far [67]. There have been many studies exploring their oxidation behavior. Ti_2AlC and Ti_3AlC_2 exhibit a similar oxidation mechanism, but the Ti_2AlC MAX phase provides slightly better high-temperature oxidation resistance due to its higher Al content [45,67]. Isothermal oxidation of Ti_2AlC at low temperatures (500–900°C) in air showed an anomalous oxidation behavior, where the oxidation rates at 500–600°C is higher than that above 700°C. Morphological observation revealed that the poor protective ability of the oxide scale at low temperatures is due to the growth of metastable transition aluminum oxides and titania, and oxidation-induced cracks within the oxide scale as a result of volume change correlated with anatase to rutile phase transformation [135]. At higher temperatures, Ti_2AlC displays selective oxidation mechanisms (Al) and possesses excellent isothermal as well as cyclic oxidation resistance either in dry or in humid atmosphere [95–97,136–141]. The high diffusivity of Al element generally leads to the formation of a dense and protective α-Al_2O_3 layer on the surface. The discrepancy in coefficients of thermal expansion (CTE) between Al_2O_3 (8.5×10^{-6} K^{-1}) scale and Ti_2AlC ($8.2–9.6\times10^{-6}$ K^{-1}) substrate are trivial, making the α-Al_2O_3 scale adherent [67]. The oxidation rate of Ti_2AlC ceramic at temperatures above 1000°C in air has been defined by two different oxidation kinetics, i.e. parabolic or cubic, previously. The grain boundary diffusion mechanism together with grain coarsening effect for growth of alumina scales explained that the cubic rate low provides a better description for the oxidation kinetics in air, as reported in a critical review by Tallman et al. [45]. However, initial transient

oxidation associated with the rapid growth of a non-protective discontinuous TiO_2 layer scale has been seen before the steady-state oxidation period when alumina scale establishes [140,142]. At elevated temperatures, water vapor slightly accelerated the oxidation rate of Ti_2AlC, which was largely due to formation and fast diffusion of hydroxyl ions and increased oxygen vacancy concentration in the oxide scale [136,138]. In addition, a relatively high volume expansion arising from the formation of TiO_2 and Al_2O_3 oxides enables the Ti_2AlC an autonomous crack-healing capability during high-temperature oxidation [94].

Most previous investigations on the oxidation behavior of Ti_2AlC were performed in air, and only few studies are found on oxidation in steam. However, these studies were carried out only at temperatures below 1300°C, and the oxidation behavior of Ti_2AlC up to 1400°C in steam has never been reported. Under severe accident scenarios in nuclear reactors, the temperature in a nuclear core can achieve extremely high values, such as above 1500°C. Before considering potential application of the Ti_2AlC MAX phase for current LWRs and as high-temperature structural material, e.g. for energy-related system in moist atmosphere, it is of practical significance as well as scientific value to figure out its oxidation mechanisms in extreme high-temperature steam atmosphere. The purpose of this chapter is to explore the oxidation behavior of Ti_2AlC ceramic in the 1400°C – 1600°C range and its maximum temperature compatibility with steam [143].

3.2 Experimental arrangement

3.2.1 Sample preparation and analysis

The Ti_2AlC (Maxthal 211®) specimens were mechanically polished using 2400 grit SiC paper, then washed in ultrasonic solution with the sequence of 10 min deionized water, 10 min acetone, 10 min isopropanol, and finally dried in hot air before oxidation exposure [143]. In addition, the phase composition of the specimens was characterized by X-ray diffraction (XRD, Seifert PAD II) with Cu $K\alpha_1$ radiation (λ=0.15406 nm, 40 kV and 30 mA) in Bragg–Brentano geometry (θ-2θ) with a step size of 0.002 ° and a scan speed at 1 °/min. The surface was examined using a field-emission scanning electron microscope (SEM, Philips XL30S), equipped with an energy dispersive X-Ray spectrometer (EDS) for element analysis. Figure 3.1 shows the XRD pattern and Figure 3.2 is a SEM micrograph of a specimen before oxidation. The specimens are not pure Ti_2AlC MAX phase. They are composed of predominant Ti_2AlC MAX phase (~63 wt.%) with a certain quantity of Ti_3AlC_2 MAX phase (~29 wt.%) and other phases (~7 wt.% Ti-Al intermetallics and minor TiC) as identified by XRD. The specimens are fully dense with elongated MAX phase grains (Figure 3.2).

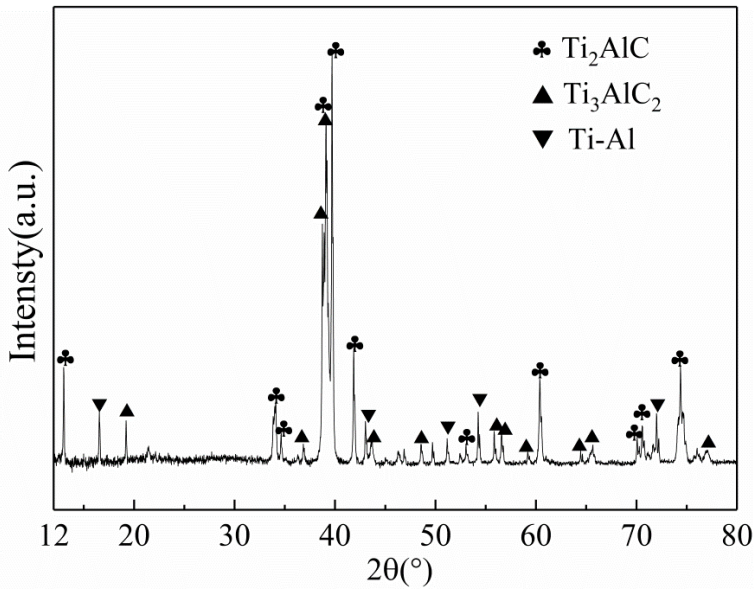

Figure 3.1 XRD pattern of a Ti_2AlC specimen (Maxthal 211®) in as-delivered state.

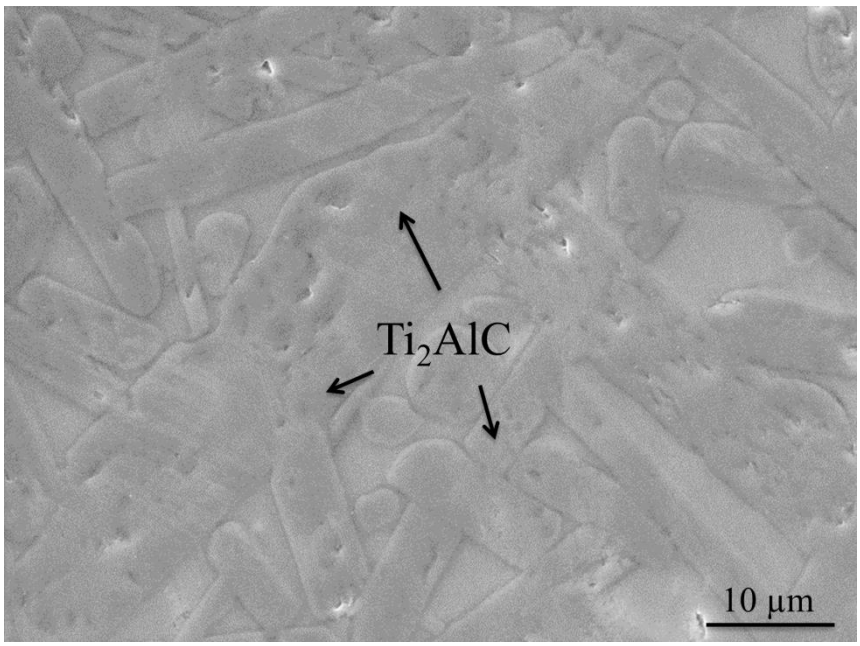

Figure 3.2 Surface SEM micrograph of a Ti_2AlC specimen (Maxthal 211®) in as-delivered state after polishing.

3.2.2 Oxidation and post-test examinations

All the oxidation experiments in this chapter were conducted using a alumina horizontal tube furnace, the so-called BOX rig, under atmospheric pressure. Figure 3.3 shows the schematic view of the BOX Rig. This equipment consists of a gas/steam supply system, a tube furnace, a quadrupole mass spectrometer (Balzers GAM 300) and a control system. The gas supply system includes two gas flow controllers (for carrier gas and other needed gas), one liquid flow controller (for liquid water) and a controlled evaporator mixer unit (CEM). In CEM, the liquid distilled water is evaporated and mixed with the non-condensable gases. The whole system was delivered by Bronkhorst High-Tech B.V. The tube furnace is made up of an

alumina reaction tube (inner diameter: 32 mm, length: 600 mm) and molybdenum heaters allowing for a maximum temperature of 1700°C (HTM Reetz GmbH, Berlin). For oxidation tests, the specimens were placed on a corundum sample holder with narrow face down and were positioned at the center of the furnace. The furnace temperature was controlled by a mantled thermocouple located in the upper part of the furnace tube near the sample. The specimens were isothermally oxidized in a flowing argon + steam atmosphere. Argon was used as the carrier gas and the reference gas for mass spectrometer analysis. All the specimens, except during one ramp test, were heated in high purity Ar (6N) atmosphere to the desired temperature with a gas flow rate of 40 l/h Ar, then the atmosphere was changed to 20 l/h Ar and 20 g/h H_2O (resulting in ~55 vol.% H_2O) for steam oxidation with different dwell times. The steam flow rate was selected at this level based on the instrument capability as well as to ensure no steam starvation during the oxidation process. Finally, after the isothermal exposure, the specimens were cooled down to room temperature by simultaneously changing the atmosphere back to high purity Ar with 40 l/h Ar flow rate. The flow rates of each gas are given in standard conditions herein. The heating and cooling rates were kept at 10 K/min. The off-gas was *in-situ* analyzed by the mass spectrometer. Eight different gaseous species, including H_2, CH_4, H_2O, N_2, CO, CO_2, O_2 and Ar, were determined. Figure 3.4 illustrates the typical temperature profile and concentration of Ar and steam in the flowing gas during an isothermal oxidation test. The off-gas tube from the furnace to the mass spectrometer was heated to about 150°C to prevent steam condensation. The mass spectrometer was calibrated for H_2 with certificated Ar-gas mixtures. The hydrogen release rate was treated as a continuous measure for the reaction kinetics.

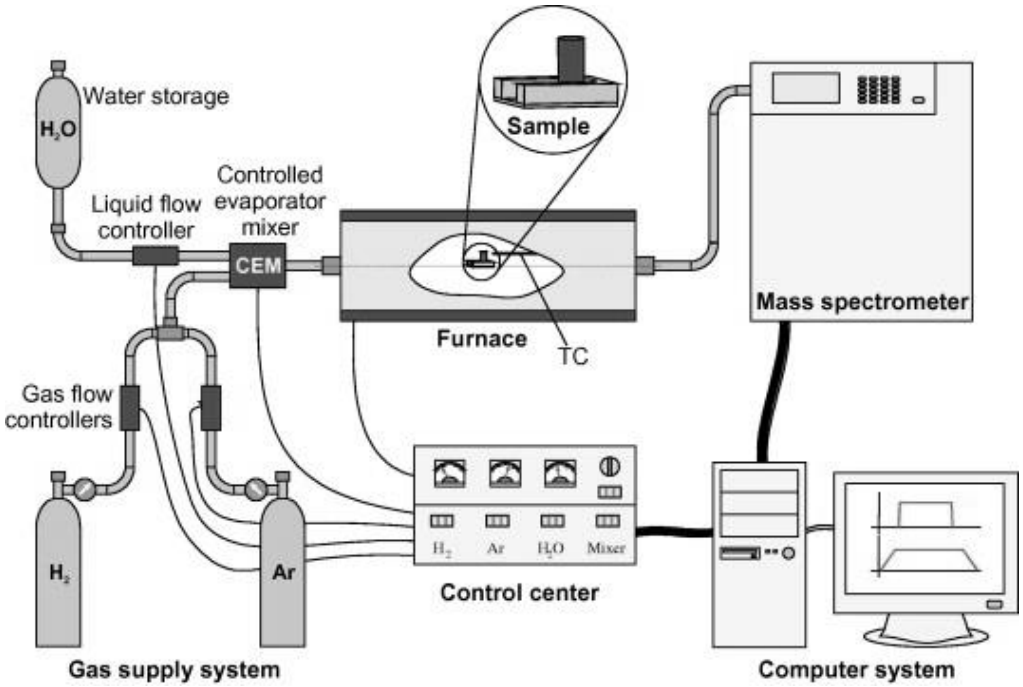

Figure 3.3 Schematic view of the BOX Rig for the high-temperature oxidation testing of bulk Ti_2AlC in steam containing atmosphere.

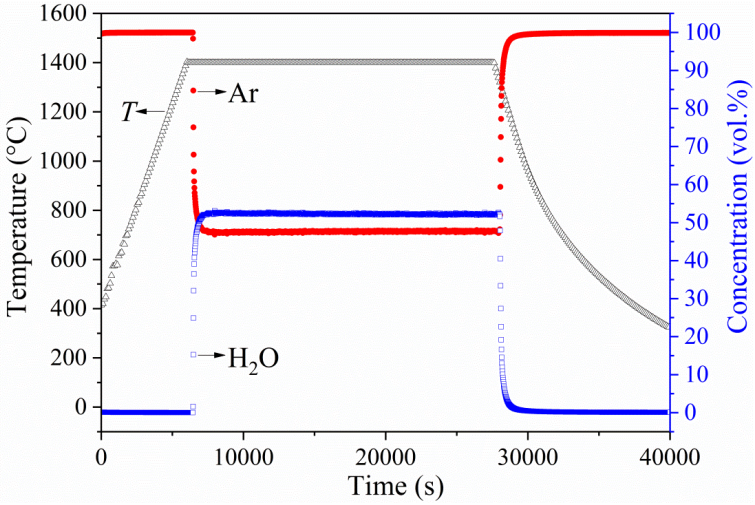

Figure 3.4 Typical temperature profile (grey) and concentration of Ar (red) and steam (blue) in the flowing gas during the isothermal oxidation test.

Isothermal oxidation at two temperatures, i.e. 1400°C and 1500°C, from 1 to 24 hours with 6 different periods and at 1600°C with one period (6 hours) were carried out. The ramp oxidation test was performed from 500°C to 1600°C in order to determine the maximum tolerant temperature of Ti_2AlC via the oxidation kinetics reflected by the hydrogen release rate. Before and after oxidation, the mass of the specimens was measured using an analytical balance (Ohaus Explorer, Switzerland) with a resolution of 0.0001 g. The phase compositions of the oxide scale on the oxidized samples were characterized using XRD similar as before oxidation. The surface and cross-sectional microstructure of the oxidized samples were observed and analyzed using SEM. For cross-sectional metallographic examination, the oxidized samples were mounted with epoxy resin. After sufficient hardening of the epoxy, the samples were first ground using resin bonded diamond grinding discs (Rubin 520/Saphir 350, Germany) starting from 220 down to 1200 grits, then polished with a sequence of 15, 6 and 3 μm diamond paste and finally rinsed with active oxide polishing suspensions and water. The polished samples were then cleaned using an ultrasonic bath in deionized water, followed by acetone. A thin layer of gold was deposited on the surfaces and cross sections of the oxidized samples before SEM observation (Rmitech K575, USA).

3.3 Results

3.3.1 Isothermal oxidation at 1400°C and 1500°C

The oxidation kinetics, i.e. mass change per unit area as a function of time, of the Ti_2AlC samples oxidized at 1400°C and 1500°C up to 24 hours in steam are shown in Figure 3.5. The mass gain increased slowly with prolonged exposure time up to 12 hours at 1400°C in steam. A faster oxidation rate was observed when the exposure time exceeded 18 hours. At 1500°C, the mass gains were significantly higher than that at 1400°C. Weight loss emerged due to significant spallation of the oxide scale when the exposure time reached 18 hours (shown later). The oxidation kinetics deviated from common parabolic kinetics at both temperatures; sub-parabolic and linear rate laws were adopted to better describe the oxidation kinetics at

1400°C and 1500°C, respectively. The solid curves in Figure 3.5 show the fitting results ignoring the last two points in each series. At 1400°C up to 12 hours, the time exponent of the sub-parabolic law was calculated as 0.399, suggesting a nearly cubic (1/3) oxidation kinetics. The oxidation kinetics changed from a sub-parabolic law to a linear law, i.e. breakaway oxidation, after prolonged exposure at 1400°C. This transition is supported by analyses of the surface morphology of the samples and by in-situ measurements of the hydrogen release rate, which will be shown later in this section. At 1500°C, the oxidation kinetics maintained a linear rate law from the initial stage of oxidation. The different growth kinetics combined with high values of correlation coefficients reflected different growth rate-limiting steps at 1400°C and 1500°C. The mass gain was only 3.24 mg/cm² after exposure in steam for 24 hours at 1400°C, revealing extraordinary oxidation resistance of Ti_2AlC MAX phase in steam.

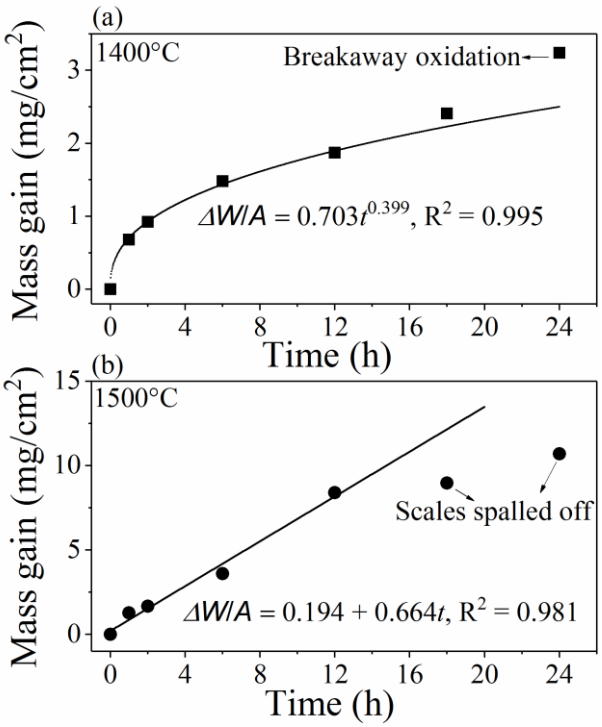

Figure 3.5 Oxidation kinetics of Ti_2AlC at (a) 1400°C and (b) 1500°C in steam. The solid curves indicate a well-fitting relationship between the mass gain and oxidation time up to 12 hours. In the fitting equations, ΔW/A is mass gain per unit area, t is oxidation time in hour, and R is coefficient of determination.

Figure 3.6 shows the post-test appearances of the samples after three different periods of oxidation testing: 1, 12 and 24 hours, respectively. In case of the Ti_2AlC samples oxidized at 1400°C, the oxide scales formed on the surface remained adherent, showing a compact structure after 12 hours oxidation. Partial delamination of the scale was observed, especially along the edges of the sample, after oxidation for 24 hours. However, the scale did not spall off. Apparently, a change of the appearances in color after oxidation at two different temperatures was observed, from black at 1400°C to gray at 1500°C. At 1500°C, the scale structure was relatively loose even after short time oxidation (1 hour) and large areas of the scale spalled off after oxidation for 24 hours.

It is suggested that the oxide scale formed on the surface of Ti_2AlC substrate lost protective effect at 1400°C after prolonged exposure and at 1500°C directly from the beginning of oxidation. The mechanical deformation (for instance delamination and formation of porous structure) and spallation of the oxide scales provide short-circuit diffusion paths for the oxidizing gas, correlating with the linear oxidation kinetics. The evolution of the appearances is in accordance with the change of mass gains versus oxidation time in Figure 3.5.

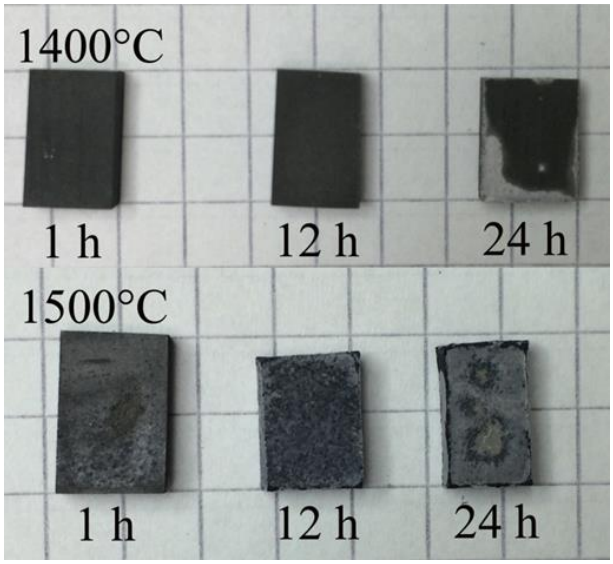

Figure 3.6 Post-test appearances of Ti_2AlC after oxidation at three different annealing times: 1, 12 and 24 hours. The grid in the picture is 5 mm.

Figure 3.7 shows the flow rates of three concerning gases (H_2, CO, CO_2) as a function of time for the Ti_2AlC samples oxidized at both temperatures for 18 hours in steam (similar flow rate behavior was observed for other tests). At the very early stage of oxidation, a similar tendency was observed for H_2 release rates at both temperatures 1400°C and 1500°C, i.e. the flow rates increased slowly to reach a peak or a plateau. This rising period of the hydrogen flow rates was around 1 hour at 1400°C and increased to 1.5 hours at higher temperature, i.e. 1500°C. After this first period of increasing H_2 release rate, the hydrogen flow decreased significantly at 1400°C, but slightly and slowly increased at 1500°C. The increasing hydrogen release rate during the initial period of oxidation at 1400°C demonstrated a faster oxidation rate at the early stage of oxidation compared to that at the steady-state stage, which can be attributed to the transient oxidation with rapid growth of titanium dioxide (this will be discussed later in more detail in section 3.4). The H_2 release rates then can be roughly described by an initial negative exponent law followed by a linear law at 1400°C, and by a constant linear law at 1500°C as shown by the fitting lines. Consistent with the mass gain data shown in the previous part, these observations indicate that the oxidation kinetics first followed a sub-parabolic law, then changed to a linear law at 1400°C and maintained a linear law at 1500°C. The flow rate of hydrogen during the steady-state oxidation at 1500°C (around 0.04 $l \cdot cm^{-3} \cdot h^{-1}$) is one magnitude higher than that at 1400°C (around 0.005 $l \cdot cm^{-3} \cdot h^{-1}$), demonstrating much faster oxidation rate at 1500°C than at 1400°C, in accordance with the mass gain

tendency presented in Figure 3.5. As shown in Figure 3.7, both CO and CO_2 gas flows were detected once Ti_2AlC samples were exposed to steam after eliminating the impact of atmosphere change. The flow rate of CO_2 is higher than that of CO. Hence, a small quantity of carbon element in the Ti_2AlC specimens was oxidized to form gaseous CO_2 and/or CO, mainly CO_2, during the oxidation process. A slight increase of the CO_2 flow rates was observed with prolonged exposure at both temperatures as shown with the dashed lines.

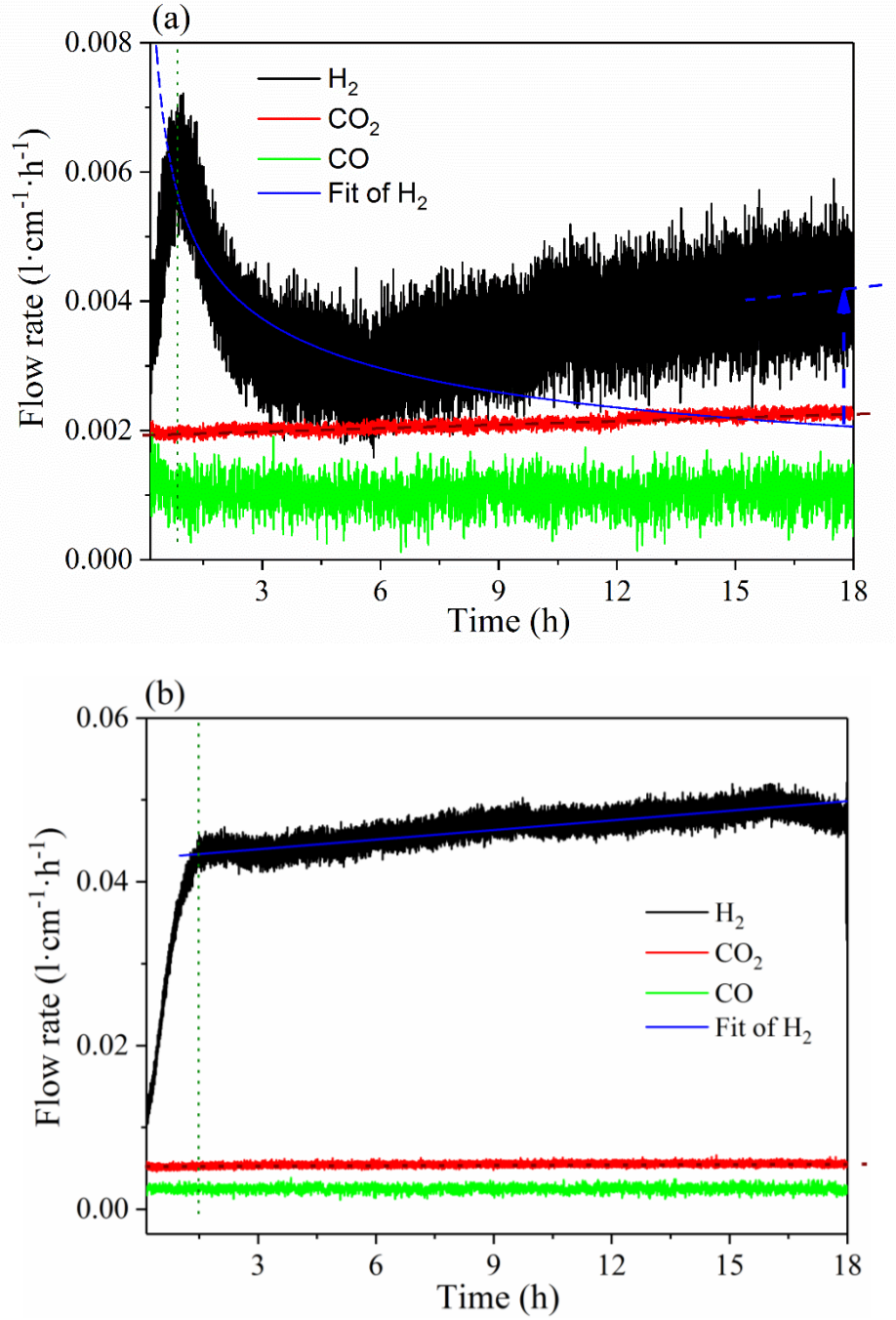

Figure 3.7 Flow rate per surface area of H_2, CO, CO_2 as a function of time for the Ti_2AlC samples oxidized in steam at (a) 1400°C and (b) 1500°C for 18 hours.

Figure 3.8 shows the XRD diffraction patterns of the Ti_2AlC surface after oxidation at 1400°C and 1500°C for six different periods in steam. Only three evident phases were detected, i.e. Ti_2AlC (JCPDS #29-0095), α-Al_2O_3 (JCPDS #43-1484) and Al_2TiO_5 (JCPDS #41-0285), for all the samples after oxidation. These findings revealed that oxidation of Ti_2AlC resulted in formation of α-Al_2O_3 and Al_2TiO_5. The relatively high intensity of diffraction signals from the Ti_2AlC substrate even after oxidation at 1400°C for 24 hours revealed that a thin layer of oxide scale formed on the surface of the Ti_2AlC substrate. The intensity of the diffraction signals associated with α-Al_2O_3 increased significantly at 1400°C and fluctuated at 1500°C (due to the partial spallation of the scale) with increasing oxidation time. The absence of a TiO_2 phase and the appearance of the Al_2TiO_5 phase indicate a reaction between TiO_2 and Al_2O_3 to form Al_2TiO_5. The phase diagram of the TiO_2 - Al_2O_3 system confirms that this reaction occurs at around 1200°C [144] and the Al_2TiO_5 phase was also observed in previous studies on Ti_2AlC oxidation above 1200°C [95,138]. It is necessary to notice that the signal intensity of the Al_2TiO_5 phase was significantly lower compared to those of Ti_2AlC and α-Al_2O_3 at both temperatures, suggesting that the content of Al_2TiO_5 was low and the predominant phase in the oxide scale was α-Al_2O_3.

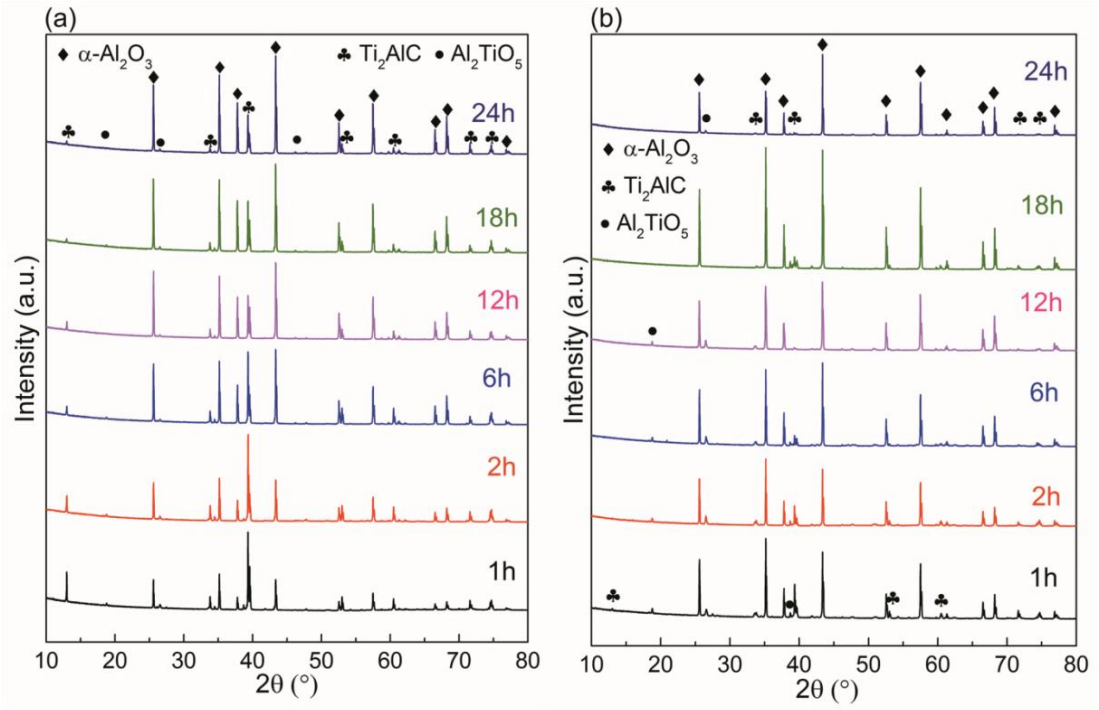

Figure 3.8 XRD patterns of oxide scales formed on the surface of Ti_2AlC after oxidation at (a) 1400°C and (b) 1500°C in steam for six different annealing times.

Figure 3.9 presents SEM micrographs of typical surface morphologies of Ti_2AlC after oxidation at 1400°C and 1500°C in steam after three different times with corresponding EDS measurements. After exposure at 1400°C for 1 hour, as shown in Figure 3.9(a), the surface of Ti_2AlC was rough, and it consisted of randomly isolated islands with large elongated grains embedded in a coarse surface layer with small irregular grains. EDS elemental analysis (Figure 3.9(g)) proved that the isolated islands were Ti-enriched, and the stoichiometry was close to Al_2TiO_5 as identified by EDS (point 1). The remaining surface was

covered by a dense alumina scale (point 2), showing a columnar grain structure. The density and size of the isolated islands decreased with prolonged exposure time at 1400°C. When the oxidation time reached 12 hours at 1400°C, as shown in Figure 3.9(b) with EDS line-scanning profiles (Figure 3.9(h)), these Ti-enriched islands were not observed anymore and the surface became coarser and consisted of a discontinuous Ti-enriched outer layer. Similar Ti-enriched isolated islands were also observed after oxidation at 1500°C for 1 hour, as shown in Figure 3.9(d) of a high-resolution image in right side (point 3, Al_2TiO_5), however their dimension was much smaller, i.e. by one order of magnitude. The other areas were covered by an alumina scale (point 4). The scale remained adherent and crack-free at 1400°C for 1 and 12 hours. However, partial detachment of the scale, especially along the edges, was observed on the sample oxidized at 1400°C for 24 hours as shown in Figure 3.9(c). The detached scale became considerably loose and porous compared to the undetached areas. Oxidation at 1500°C for 1 hour already triggered micro-cracks on the surface as shown in Figure 3.9(d). A loose structure of the oxide scale throughout the surface was obtained after oxidation for 12 hours, see Figure 3.9(e). These observations explain the different oxidation kinetics obtained at 1400°C and 1500°C. After oxidation at 1500°C for 24 hours, the scale showed significant spallation and cracking (Figure 3.9(f)).

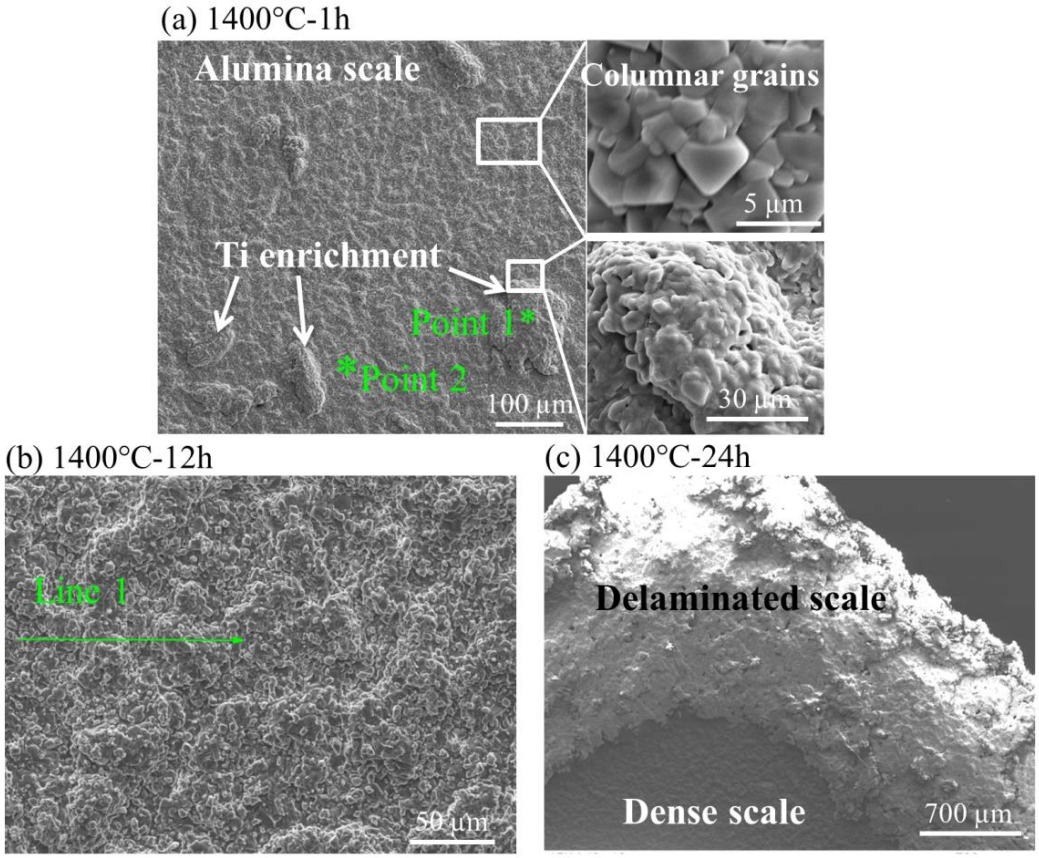

(Continued)

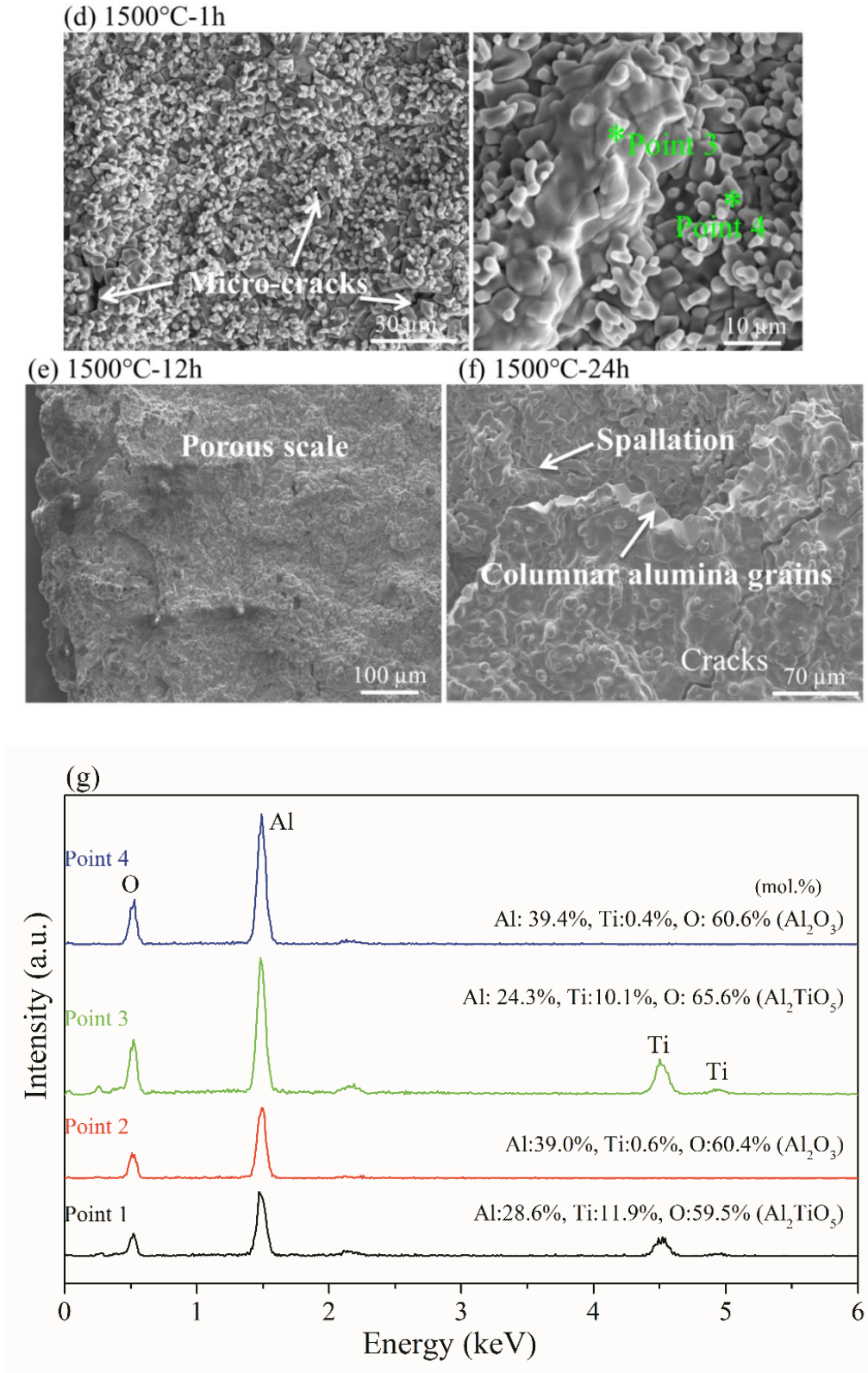
(d) 1500°C-1h
Micro-cracks
30 μm
*Point 3
*Point 4
10 μm
(e) 1500°C-12h
Porous scale
100 μm
(f) 1500°C-24h
Spallation
Columnar alumina grains
Cracks
70 μm
(g)
Point 4
O
Al
(mol.%)
Al: 39.4%, Ti:0.4%, O: 60.6% (Al2O3)
Point 3
Al: 24.3%, Ti:10.1%, O: 65.6% (Al2TiO5)
Ti
Ti
Point 2
Al:39.0%, Ti:0.6%, O:60.4% (Al2O3)
Point 1
Al:28.6%, Ti:11.9%, O:59.5% (Al2TiO5)
Intensity (a.u.)
0
1
2
3
4
5
6
Energy (keV)

(Continued)

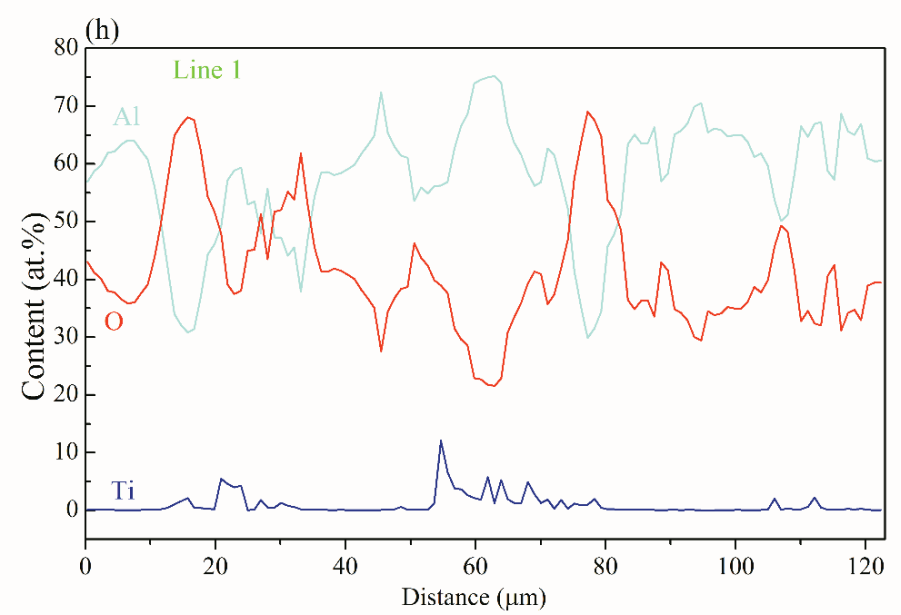

Figure 3.9 SEM micrographs of typical surface morphologies of Ti_2AlC after oxidation at 1400°C (a) 1 h, (b) 12 h (c) 24 h and 1500°C (d) 1 h, (e) 12 h (f) 24 h in steam with different periods, and corresponding (g) point and (h) line-scanning EDS measurements. (If not specifically stated, the image was taken in SE mode, similarly hereinafter).

The cross-sectional morphologies after three different oxidation times were also examined by SEM. Figure 3.10 shows SEM micrographs of a sample after oxidation at 1400°C in steam for 1 hour. Clearly, the alumina oxide scale maintained adherent and dense with a thickness of around 4 μm. The BSE image in Figure 3.10(b) identified the external large Al_2TiO_5 isolated islands above the α-Al_2O_3 scale. Micro-cracks were observed within the islands, but the scale was crack-free beneath these islands. As the exposure time increased to 12 hours (see SEM micrographs in Figure 3.11), the alumina oxide scale remained intact, and grew slowly to nearly 10 μm, indicating a reduced oxidation rate due to thickening of the alumina scale. However, the large Al_2TiO_5 isolated islands were not observed anymore. In turn, a thin, discontinuous Ti-enriched surface layer appeared on top of the alumina scale as shown by corresponding EDS mapping. No apparent binary carbide layer or Al-depleted and Ti-rich layer was observed beneath the Al_2O_3 scale by mapping. Alumina inclusions exist in the Ti_2AlC matrix, which are likely impurities from the sintered product. For the sample oxidized 24 hours at 1400°C in steam, the oxide scale delaminated and became loose as shown in Figure 3.12, indicating that the oxide scale lost its protective effect at prolonged exposure time. This is in agreement with the variation of oxidation kinetics from a sub-parabolic law to a linear law with increasing oxidation time.

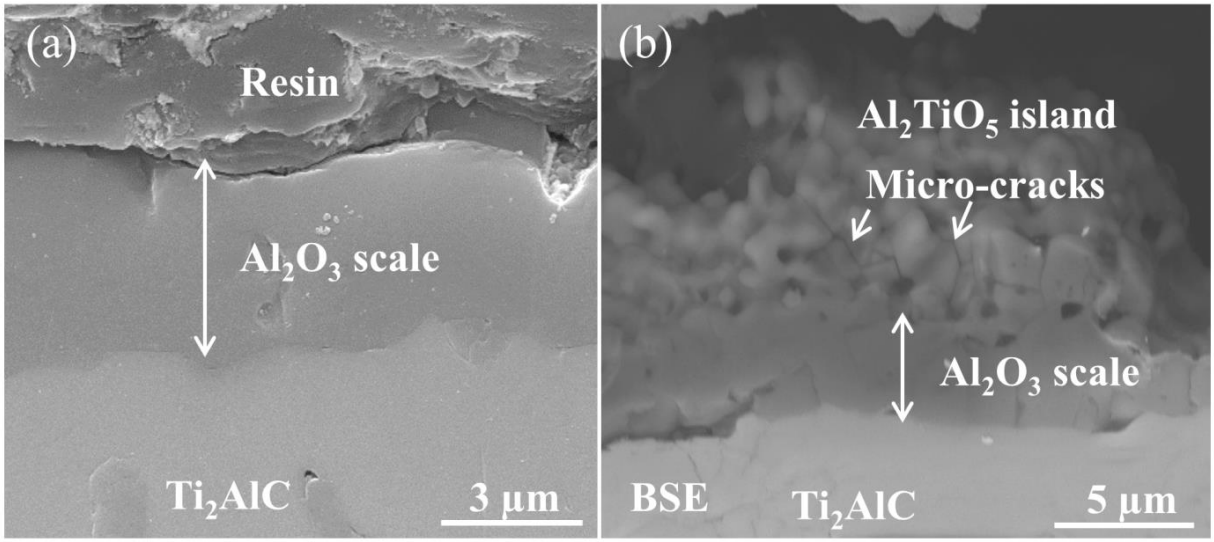

Figure 3.10 SEM micrographs of typical cross-sectional morphologies of Ti_2AlC after oxidation at 1400°C in steam for 1 hour: (a) the SE image shows alumina scale in general, and (b) the BSE image displays an isolated Al_2TiO_5 island on top of the alumina scale.

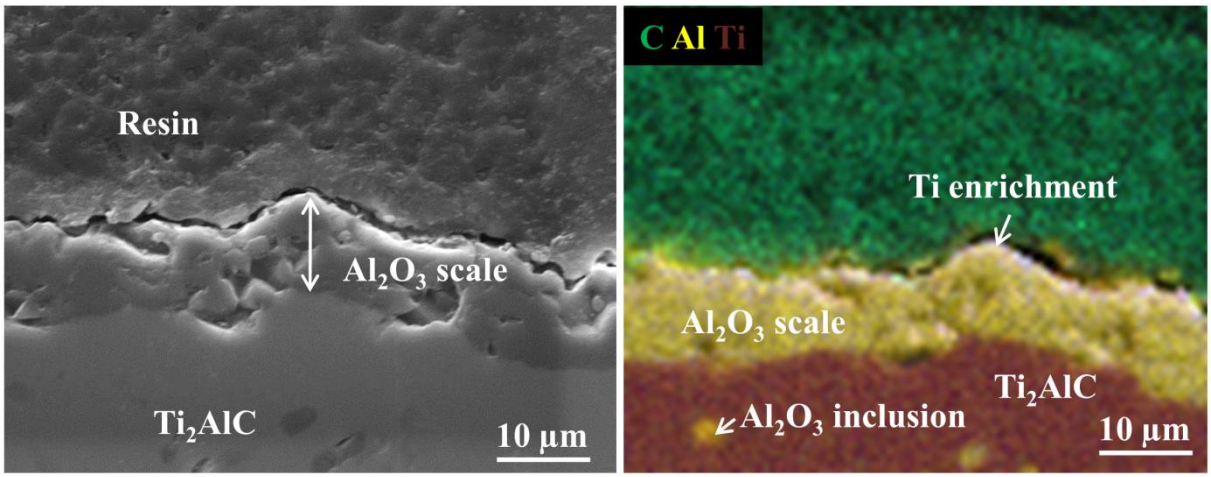

Figure 3.11 SEM micrographs of typical cross-sectional morphologies of Ti_2AlC after oxidation at 1400°C in steam for 12 hours and corresponding EDS mapping (C in green, Al in yellow and Ti in dark red).

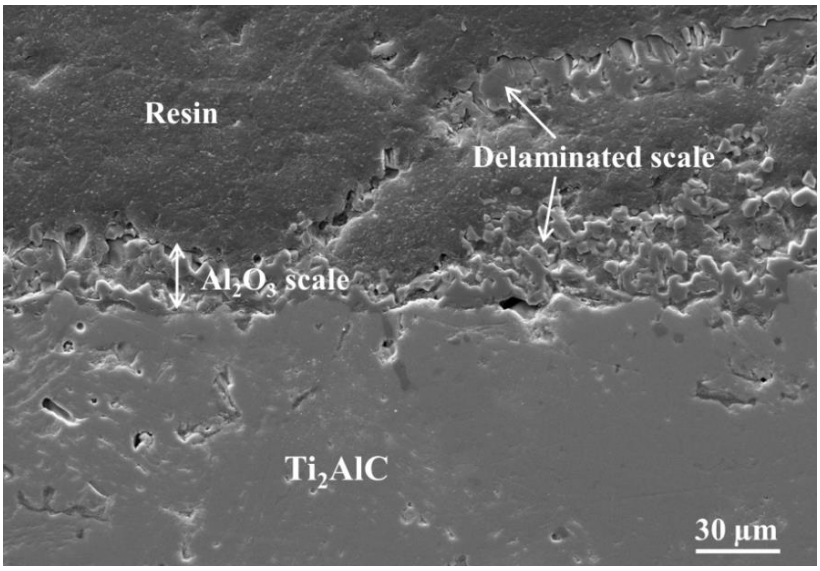

Figure 3.12 SEM micrographs of a typical cross-sectional morphology of Ti_2AlC after oxidation at 1400°C in steam for 24 hours showing a porous and delaminated oxide scale.

Figure 3.13 presents SEM micrographs of samples after oxidation at 1500°C in steam for 1, 12 and 24 hours. A relatively rough surface was revealed for the sample oxidized at 1500°C in steam for just 1 hour (Figure 3.13(a)). The scale was dense; micro-cracks observed on the surface (Figure 3.9(a)) did obviously not penetrate the alumina scale. Delamination and spallation of the oxide scale appeared with increasing exposure time (Figure 3.13(b) and (c)). Moreover, the oxide scales became porous and coarser. Two oxide layers separated by resin and fracture of the upper oxide scale are seen (Figure 3.13(c)). The structure of the α-Al_2O_3 grains was confirmed as columnar. Enrichment of Ti at the grain boundaries of alumina grains and on the superficial layer was occasionally observed by EDS, similar to Figure 3.11, indicating outward diffusion of Ti during the oxidation process, followed by oxidation and reaction with α-Al_2O_3 to form Al_2TiO_5. In addition, titanium oxides segregated at the grain boundaries of α-Al_2O_3 grains.

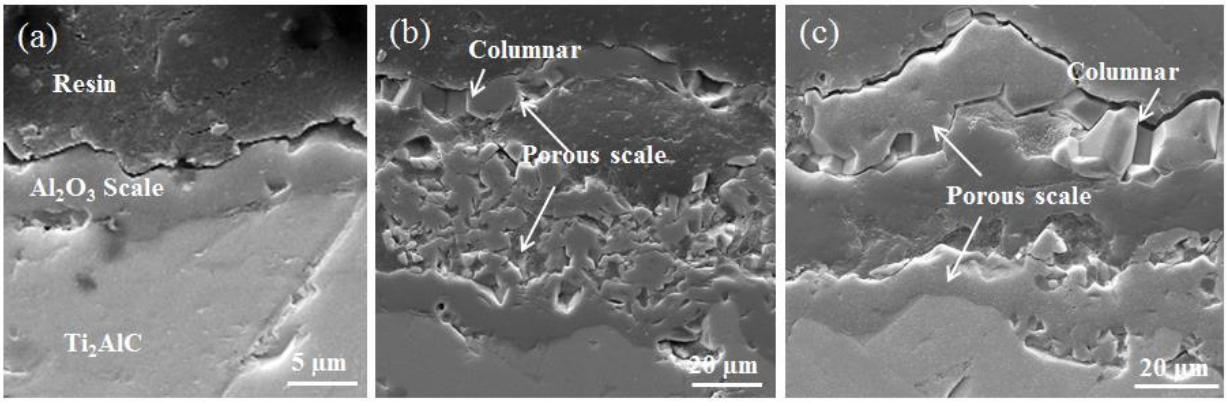

Figure 3.13 SEM micrographs of typical cross-sectional morphologies of Ti_2AlC after oxidation at 1500°C in steam, (a) 1, (b) 12 and (c) 24 hours.

3.3.2 Isothermal and transient oxidation at 1600°C

An isothermal oxidation test at 1600°C in steam resulted in a catastrophic oxidation of the Ti_2AlC sample. Therefore, a transient oxidation test starting from 500°C with a heating rate of 10 K/min up to 1600°C was conducted to figure out the highest tolerant temperature of the bulk Ti_2AlC MAX phase in steam. Figure 3.14 and Figure 3.15 show the flow rates of several species in the off-gas and XRD patterns of the surface of the Ti_2AlC samples after the isothermal test and the transient test, respectively. As can be seen in Figure 3.14(a), the flow rates of H_2 and CO_2 in the off-gas were driven up to extremely high levels compared to those measured for oxidation at 1400°C (more than one hundred times higher), and then decreased quickly. After examination of the morphology and mass change of the sample (around 35 wt.% mass gain and corresponding 170 mg/cm^2), it is suggested that the sample was quickly and completely consumed, i.e. catastrophic oxidation occurred. The corresponding XRD results (Figure 3.15) showed that the surface contained only two phases after the isothermal test, i.e. TiO_2 and Al_2TiO_5, indicating that Ti_2AlC failed to form a protective alumina scale at 1600°C in steam. The overall reaction of Ti_2AlC and steam at 1600°C can be written as

$$Ti_2AlC + 15/2H_2O = 3/2TiO_2 + 1/2Al_2TiO_5 + CO_2 + 15/2H_2 \quad (3\text{-}1)$$

The standard enthalpy of formation and heat capacity of Ti_2AlC were reported previously [145,146]. The enthalpy of this reaction at 1600°C is calculated to be around -940 kJ/mol, and slightly lower at 1500°C and 1400°C. This demonstrates that a large amount of hydrogen and heat will be released once Ti_2AlC is exposed to catastrophic oxidation in high-temperature steam.

During the transient test, the flow rates of all gases, except for H_2, remained small and nearly constant, as shown in Figure 3.14(b). The release rate of H_2 increased gradually up to around 1555°C, then accelerated and the slope of the curve became much pronounced. Hence, catastrophic oxidation of Ti_2AlC may occur at about 1555°C in steam without pre-oxidation. However, the flow rate of H_2 at 1600°C was several times lower in the transient test than that in the isothermal test, and the mass gain after the test was only around 2.27 mg/cm^2. XRD results (Figure 3.15) indicated that an α-Al_2O_3 scale formed on the surface of the sample, which protected the sample from fast consumption. Therefore, it can be predicted that the maximum tolerant temperature of Ti_2AlC in steam can be extended via a tailored pre-oxidation process.

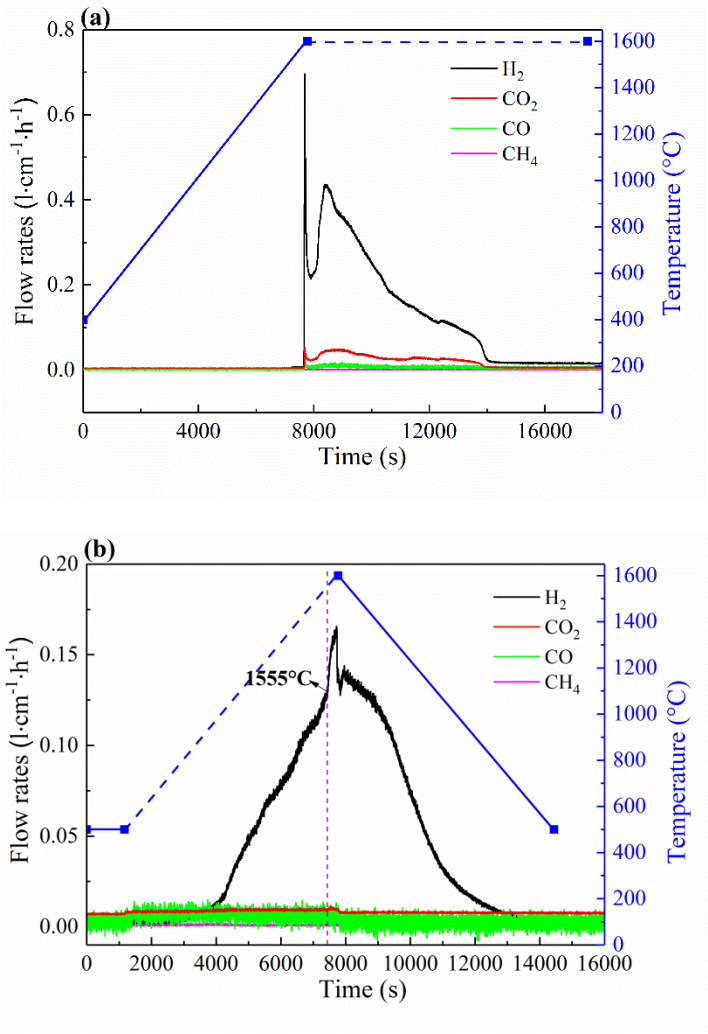

Figure 3.14 Flow rates of H_2, CO_2, CO, and CH_4 in the off-gas as a function of time for the Ti_2AlC samples oxidized at 1600°C: (a) isothermal test and (b) transient test. The blue solid line and blue dashed line of the temperature curves represent atmosphere of pure argon and of a mixture of steam and argon, respectively.

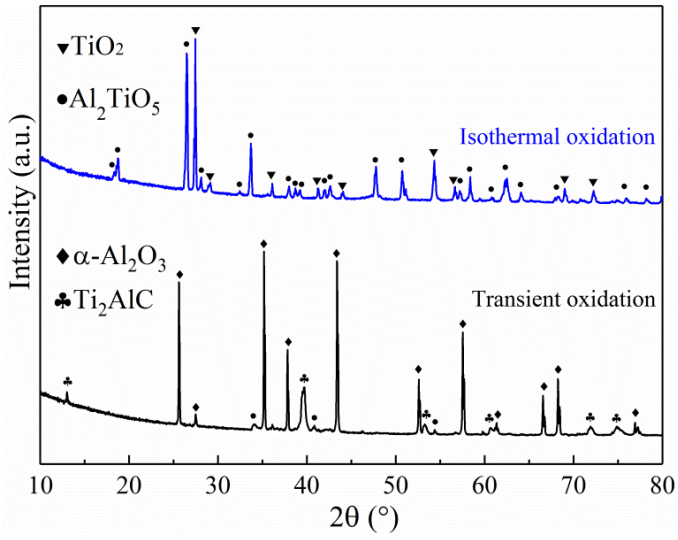

Figure 3.15 X-ray diffraction patterns of the surface of Ti_2AlC oxidized at 1600°C in steam for the isothermal test (top) and the transient test (bottom).

3.4 Discussion

Oxidation tests of the Ti_2AlC ceramic, despite not phase pure, at elevated temperatures revealed its superb oxidation resistance up to 1400°C and its ability to withstand temperature up to around 1550°C in steam. Compared with previous studies conducted in air [97,141], water vapor has been found to have only little effect on the oxidation kinetics of this alumina-forming material but the scale adhesion is reduced.

The microstructural evolution of the thermally grown oxide scale over oxidation time can be understood as described in the following. Generally, a transient oxidation stage emerges before the appearance of a protective alumina scale due to competitive and selective oxidation of Al and Ti atoms in the Ti_2AlC matrix as a function of oxidant chemical potential (or partial pressure) at the oxide/substrate interface [140]. Upon exposing the Ti_2AlC sample to elevated temperatures in oxidizing conditions, a thin oxide layer corresponding to the initial surface that contains a high concentration of base elements, in this case Ti, is supposed to develop first on the surface. The structure of this layer is usually loose and contains structural defects depending on the surface conditions, volume changes and CTEs mismatch of the matrix and the forming oxides [147]. Hence, the steam partial pressure at the oxide scale/substrate interface is high enough to promote both oxidation of Ti and Al. Even though growth of Al_2O_3 is thermodynamically favorable, however, it was proved that growth of TiO_2 is much faster [140]. Further oxidation therefore leads to the fast diffusion of Ti through this layer and rapid growth of TiO_2 grains at the oxide scale/ambient interface, leaving randomly Ti-enriched isolated islands on the surface during the initial stage of oxidation. Simultaneously, alumina starts to nucleate at the oxide scale/substrate interface. At temperatures higher than 1200°C, TiO_2 and Al_2O_3 react to form Al_2TiO_5. After this transient oxidation stage, the decrease of oxidant partial pressure at the interface prompts the selective oxidation of aluminum and the thickening and roughing of the protective α-Al_2O_3 scale. The oxidation rate will be mainly dominated by the inward diffusion of oxidant after a continuous alumina scale has established. Fast outward diffusion of Ti and growth of Al_2TiO_5 on the surface are suppressed. The oxidation kinetics is close to a cubic law, similar to previous findings on oxidation of Ti_2AlC and FeCrAl(RE) alloys at 1200°C, which is attributed to a grain coarsening effect of the alumina scale [45]. The decrease in grain-boundary diffusion paths over time limits the inward diffusion of oxidizing species during oxidation.

Randomly distributed Ti-enriched isolated islands grow during the initial stage of oxidation as mentioned above. The reduction of the dimensions and eventually disappearance of these Ti-enriched isolated islands with prolonged exposure time can be explained by the formation and evaporation of gaseous Ti-containing species. The generation of gaseous Ti-containing species, especially $TiO(OH)_2$ through the following reaction

$$TiO_2(s) + H_2O(g) = TiO(OH)_2(g) \quad (3\text{-}2)$$

was confirmed for Ti_2AlC oxidized in steam at 1300°C [138] and exposed in a high-pressure burner rig [142], as well as for hot-pressed TiO_2 in high-temperature steam [148]. The formation of volatile Ti-containing compounds/species in steam is supposed to become more pronounced at higher oxidation temperature.

The loss of the protective capability of the alumina scale after long exposure at 1400°C and directly from the beginning of oxidation at 1500°C is mainly associated with stress generation and relief during oxidation. Generally, stress can generate and accumulate at the oxide scale/substrate interface and within the scale during the oxidation process via different mechanisms [120]. The oxidation process mainly induces two types of stresses, thermal stresses and growth stresses. The thermal stresses arise from the different thermal expansion or contraction between the substrate and the scale. Growth stresses, which are a result of the oxidation process itself and thus occur during isothermal exposures, can be induced via various origins, like the volume difference between the oxidized element and its oxide, compositional or phase changes in the oxide and substrate, oxide segregation within the scale and so on. The differences of coefficients of thermal expansion between the Ti_2AlC matrix and the Al_2O_3 scale are small in magnitude, which typically ensures low thermal stresses at the interface [141]. However, the growth stresses can reach high level at such high temperatures. Once the stress accumulated within the scale/substrate system exceeds a critical value, it will trigger the stress relaxation process by cracking of the oxide scale and/or by creep of the substrate or oxide. The delamination and fracture, and finally spallation of the oxide scale along with high porosity illustrates mechanical disruption of the oxide scale to relief the high stresses built up in the α-Al_2O_3 scale. These defects provide short-circuit diffusion pathway for steam and result in breakaway oxidation at 1400°C and loss of protective effect from the early beginning of oxidation at 1500°C. Obviously, a higher oxidation temperature triggers higher values of stresses, which makes the scale more susceptible to failure.

Delamination of the scale appeared after oxidation in steam at 1400°C for 24 hours in this study, but the scale remained adherent during oxidation in air up to 25 hours at the same temperature [141]. The reduced scale adherence in steam is partially related with the impact of water vapor, which usually decreases the α-Al_2O_3 scale/substrate interfacial toughness and the α-Al_2O_3 intergranular toughness, and hence contributes to increasing cracking and spalling of the oxide scales [103,149].

As stated before, the samples are not pure Ti_2AlC MAX phase, but a mixture of Ti_2AlC, Ti_3AlC_2 and Ti-Al intermetallics, etc. Oxidation of Ti_3AlC_2 at elevated temperatures results in formation of an outer layer of TiO_2 and an inner layer of continuous α-Al_2O_3 [96]. Furthermore, due to lower Al content compared to Ti_2AlC, the Ti_3AlC_2 MAX phase is more susceptible to breakaway oxidation due to depletion of Al. Oxidation of Ti-Al intermetallics are typical fast, with non-protective oxide scales which are composed of both Al_2O_3 and TiO_2 [150]. These impurities have proved to deteriorate the oxidation resistance of MAX phases and increase their oxidation rate during high-temperature exposure [67]. Thus, the impurities (Ti_3AlC_2, Ti-Al intermetallics, etc) in the samples can enhance and accelerate the loss of protective effect of the alumina scale as they oxidize much faster with lower oxidation resistance.

At higher oxidation temperature (1600°C), the diffusion rate of oxidizing species in the oxide scale will increase significantly, and the interaction of steam and the material is much more intense. Hence, the steam can easily penetrate the matrix during the isothermal oxidation at 1600°C, oxidizing the samples rapidly and completely without the formation of an alumina scale. Transient oxidation starting from low

temperature results in growth of an alumina scale by pre-oxidation and avoids catastrophic oxidation as the temperature reaches 1600°C. The maximum tolerant temperature of Ti_2AlC in steam reaches up to approximate 1555°C, which can be attributed to its unique nanolaminated structure where relatively weak bonding of Ti - Al and stronger bonding of Ti - C leads to a high migration rate of aluminum in Ti_2AlC [61,72].

3.5 Summary and conclusions

The oxidation kinetics of bulk Ti_2AlC MAX phase ceramic (Maxthal 211®) followed a sub-parabolic law at the early stage of oxidation, then transferred to a linear law beyond 18 hours at 1400°C, and obeyed a linear law from the beginning of oxidation at 1500°C. The sample was rapidly and completely consumed during isothermal oxidation at 1600°C accompanied by large heat and hydrogen release. The maximum tolerant temperature of Ti_2AlC in steam was approximately 1555°C determined by a ramp test, which can be extended via a tailored pre-oxidation process.

The oxide scale formed at 1400°C and 1500°C was rough and consisted of randomly distributed Al_2TiO_5 isolated islands with large elongated grains embedded in a continuous coarse α-Al_2O_3 scale with small irregular grains. The dimensions of Al_2TiO_5 isolated islands gradually decreased with prolonged exposure time and increasing oxidation temperature due to generation and evaporation of gaseous Ti-containing species. The scale adhesion in steam is reduced compared to that in air. Stress generation and relief during oxidation resulted in loss of protective capability of the alumina scale. The mechanical disruption of the oxide scale through delamination, cracking and spallation contributes to the breakaway oxidation of Ti_2AlC at 1400°C and to the non-protective effect at 1500°C. The impurities (Ti_3AlC_2 and Ti-Al intermetallics) in the specimens are supposed to accelerate the failure of the protective alumina scale during oxidation. Short-circuit diffusion governs the growth of the α-Al_2O_3 scale with longer oxidation time at 1400°C and from the initial stage of oxidation at 1500°C.

Oxidation of Ti_2AlC ceramic at elevated temperatures herein reveals its superb oxidation resistance up to 1400°C and its ability to withstand temperature up to around 1550°C in steam. The oxide scale thickening rate of Ti_2AlC at 1400°C is more than three orders of magnitude lower than that of Zircaloy-4. Therefore, these findings offer great potential of Ti_2AlC as a promising oxidation-resistant coating on Zr-based alloy with respect to nuclear application.

4 Synthesis, characterization and steam oxidation of Ti_2AlC MAX phase coatings

The results presented in the previous chapter prove that bulk Ti_2AlC MAX phase exhibits superb oxidation resistance up to 1400°C in steam. Therefore, Ti_2AlC thin films will be first evaluated as potential high-temperature oxidation resistant coatings on Zr-based alloy claddings. Synthesis of high purity, particularly phase-pure polycrystalline MAX phase coatings on technically relevant substrates often remains a challenge. A new approach, i.e. Ti-C-Al elemental nanoscale multilayer stacks deposited by non-reactive magnetron sputtering followed by *ex-situ* annealing, is endeavored to prepare phase-pure Ti_2AlC coatings on researching SiO_2/Si and Al_2O_3 substrates. Then, the optimum parameters identified are used to fabricate coatings on practical Zircaloy-4 substrates.

Microstructural evolution and phase transformation during annealing of the as-deposited multilayer stacks were systematically investigated by e.g. classical and *in-situ* high-temperature X-Ray diffraction (HTXRD), Raman spectroscopy and transmission electron microscopy (TEM). The observations confirmed that the nanoscale multilayer guaranteed a short diffusion length and offered the advantage of more flexible controlling of each elemental concentration. Phase-pure, i.e. single-phase Ti_2AlC coatings were successfully obtained after 800°C annealing in argon for 10 min. The overall coating thickness deposited on Zircaloy-4 substrates was around 5.5 μm with or without a 500 nm thick TiC interface layer acting as diffusion barrier. The adhesion and mechanical properties of the coatings were evaluated using scratch tests and nanoindentation. The oxidation performances of the coated samples in high-temperature steam from 800°C to 1200°C were examined and compared to uncoated Zircaloy-4 and bulk Ti_2AlC ceramic. The coated Zircaloy-4 samples confirmed significant improvement of oxidation resistance compared to bare Zircaloy-4 at 800°C. The TiC barrier layer can suppress the rapid diffusion of Al into the substrate, contributing to better oxidation performance and longer life of Ti_2AlC/TiC coatings. However, both coatings demonstrated a low protective effect from oxidation at 1000°C in steam.

4.1 Introduction

In recent two decades, MAX phase thin films have been increasingly explored and synthesized for a variety of potential applications, like oxidation and corrosion resistant coatings, low friction surfaces, electrical contacts, sensors and others [63,73,151]. A large part of pioneering work on the synthesis of MAX phase thin films was performed using PVD processes, primarily by sputtering techniques, as well as cathodic arc evaporation, pulsed laser deposition [63].

Thin-film synthesis of MAX phases using sputtering techniques can be categorized into three main approaches: co-sputtering with 3 elemental targets, sputtering with compound targets and solid-state reaction synthesis via sputtering amorphous or an (artificial) multilayer [63]. Sputtering from M, A, and graphite targets represents the most common method for laboratory-scale synthesis of the MAX carbide thin films. The main advantageous feature of using three elemental targets is the flexibility in the individual

control of the elemental fluxes [63]. The initial values of the deposition parameters are based on some estimations or calibrations, and then a routine optimization procedure is thus performed to achieve the desired MAX phase stoichiometry [151]. A wide range of MAX phases, such as MAX phases in the Ti-Al-C system [79,152,153], Ti-Si-C system [82,154], V-Al-C system [155], etc. in thin films have been successfully demonstrated via this approach. In case of MAX nitrides, reactive sputtering in a N_2/Ar mixed atmosphere from co-sputtering with 2 elemental targets, i.e. M and A, is generally the method of choice [156,157]. Only very few attempts have been reported on employing reactive sputtering for synthesis of MAX carbides [158]. Reactive sputter deposition is relatively less explored, for synthesis of both MAX phase carbides and nitrides, mainly due to the process window (with respect to reactive gas partial pressure) for deposition of single-phase or high-purity MAX phases is extremely narrow [63]. Sputtering from compound targets is sometimes preferred for reasons of simplicity and repeatability [159,160]. However, a general problem confronting compound-target sputtering is that the film composition may deviate strongly from the nominal target composition. For instance, attempts to deposit the Ti_2AlC from one single compound target often resulted in chemical composition of the produced films that deviated significantly from the composition of the target; both loss of Al [84] and Ti [161] were observed. A separate plasma source was introduced to compensate the loss of an element (i.e. to achieve the desired thin film composition) during deposition from a compound target. This effect was typically enhanced with increasing deposition temperature and was attributed to a wide range of process phenomena, such as gas-phase scattering, A-element evaporation, and differences in angular distribution among the target elements [63]. The aforementioned two approaches involve directly nucleation of MAX phase films on the substrate by heating and maintaining the substrate at elevated temperatures. The solid-state reaction synthesis mainly deposits a film in a metastable state, such as amorphous or an (artificial) multilayer containing the three elements M, A, and X in the appropriate composition, at normal or low temperatures [162,163]. The as-deposited films are followed by annealing at certain temperature to trigger the transformation to MAX phase. Examples include annealing of magnetron-sputtered Ti/AlN [164] and Ti/Si/C [165] multilayers to corresponding Ti_2AlN and Ti_3SiC_2 MAX phases.

Apart from chemical composition within the thin films, another crucial parameter enabling the growth of MAX phase films is the selection of substrate temperature or annealing temperature. The nucleation of MAX phase structure requires significant thermal activation to enable sufficient mobility and energy of atoms for the desired atomic arrangement [63,79,86,152,166–168]. Lower deposition temperatures usually result in the formation of corresponding carbides and/or intermetallic phases. For instance, Wilhelmsson et al. attempted to synthesize Ti_2AlC and Ti_3AlC_2 MAX phases after co-deposition of three elemental targets on α-Al_2O_3 (0001) substrates [79]. They found that the deposition at 700°C and 800°C resulted in the formation of cubic (Ti,Al)C and perovskite carbide Ti_3AlC phases, respectively [79,169]. Epitaxial MAX phase thin films crystallized at 800°C, and they were grown at 900°C with high crystalline quality. It suggests that the order of the MAX phase (211, 312, or 413) is vital in determining the growth temperature [63]. Larger unit cells require higher formation temperature because of the longer diffusion

length. Previous work on sputter-deposition of MAX phases has demonstrated that the nucleation of Cr_2AlC [170] and V_2GeC [171] can be realized at a relatively low temperature (450°C), whereas other 211, 312 and 413 phases typically require synthesis temperatures at or higher than 800°C [166]. The relatively high processing temperature restricts the sputtering of MAX phase films on temperature-sensitive substrates.

Initial intensive studies on synthesis of MAX phase thin films were carried out using single crystal substrates, such as MgO(111) and Al_2O_3(0001), to enable the epitaxial growth of MAX phases [63,90,153,154,156,160,166,171–173]. A buffer/seed layer is occasionally grown on the substrate as a result of the close correlation between its specific lattice plane and the *a*-lattice parameter of the MAX phase [79,152,174]. This layer is typically preferred as the corresponding binary carbide to the MAX phase carbides, for instance TiC(111) in the case of Ti_2AlC(0001) and Ti_3AlC_2(0001) [152]. Later investigations also demonstrated that the MAX phase thin films generally can directly nucleate on the single crystal substrate in spite of some lattice mismatch [63,90]. However, synthesis of consistently high-quality MAX phase thin films often remains a challenge due to the stringent requirements of the optimal deposition conditions [151]. More recently, studies start to focus on deposition of thick, polycrystalline MAX phase coatings on structural material substrate for potential applications in specific situations. The oxidation behavior, thermal and chemical stability of these coatings is occasionally investigated. In the case of Ti_2AlC, Wang et al. synthesized thin films on polycrystalline Al_2O_3 specimens at 800°C, which were composed mainly of a Ti_2AlC phase with Ti_3AlC and TiC secondary phases [175]. During oxidation in air, the films were quickly oxidized at temperatures higher than 700°C, most likely due to their phase impurity. Garkas et al. successfully prepared high purity Ti_2AlC MAX phase coatings in an industrial-size coater at 800°C. They demonstrated that the coatings were unstable and completely decomposed during annealing at 1200°C for 1 h in vacuum due to out-diffusion followed by evaporation of Al [176]. Reactive magnetron sputtering with a compound Ti50Al50 (at.%) target in Ar/CH_4 atmosphere was also used to produce Ti_2AlC protective coatings on stainless steel substrates. However, these coatings were not phase-pure and contained through-cracks after annealing [158,177]. The scaling behavior of the Ti_2AlC MAX phase coatings in air and steam at 750°C were investigated, and the coatings were quickly oxidized without obvious oxidation resistance improvement.

High velocity oxy-fuel spray [92,178,179] and cold spray processes [48,93], using Ti_2AlC powders, were also adopted to deposit thick Ti_2AlC coatings as oxidation resistant coatings. However, the obtained coatings usually displayed a loose structure and contained impurity phases of Ti_3AlC_2, TiC and Ti-Al intermetallics. Oxidation of these coatings usually produce a discontinuous alumina scale with a significant amount of titania incorporated [179]. The coating performances are generally reduced during service and further investigations to overcome these limitations are required.

In summary, it can be concluded that a number of critical challenges, like deposition of thick, phase-pure coatings on technologically relevant substrates and further reduction of the processing temperature (particular using PVD processes), still exist regarding the synthesis of Ti_2AlC as well as other MAX phase

coatings [88]. This chapter is dedicated to, for the first time, elaborating the potential of synthesizing polycrystalline phase-pure Ti_2AlC coatings via ex-situ thermal annealing of nanoscale elemental multilayer stacks. This approach offers the possibility to control the stoichiometry of the films precisely and easily, and may reduce the crystallization temperature of the MAX phase due to chemical energy stored in such reactive multilayers [180]. In the first section, microstructural evolution and phase transformation during annealing of the as-deposited multilayer stacks on SiO_2/Si and Al_2O_3 substrates were systematically investigated. The mechanisms of reaction paths and crystallization of polycrystalline Ti_2AlC MAX phase during annealing are presented. In the second section, phase-pure polycrystalline Ti_2AlC MAX phase coatings were fabricated on polished Zircaloy-4 substrates by the same approach via annealing the multilayer stacks at 800°C for 10 min in argon. The microstructure, adhesion strength and mechanical properties of the coatings were evaluated and the oxidation performance of the coatings in high-temperature steam from 800°C to 1200°C was examined.

4.2 Experimental arrangement

4.2.1 Coating deposition

A facile, two-step process was adopted to synthesize the Ti_2AlC MAX phase coatings, namely magnetron sputtering of nanoscale elemental Ti-C-Al multilayer stacks and subsequent *ex-situ* thermal annealing. The Ti-C-Al multilayer stacks were deposited by non-reactive magnetron sputtering from three elemental targets, in a sequence of titanium, graphite and aluminum, using a laboratory PVD equipment (Leybold Z 550 coater). The schematic representation of the elemental nanoscale multilayer stacks and arrangement of the targets and substrates during deposition are shown in Figure 4.1. The thicknesses of each elemental layer are around 8 nm for titanium, 2 nm for carbon and 4 nm for aluminum, calculated according to the stoichiometric ratio of these three elements (2:1:1) in Ti_2AlC and considering their theoretical densities. These low values for the thicknesses of each elemental layer are selected in order to guarantee a short diffusion distance during annealing.

The substrates were cleaned in an ultrasonic bath in acetone for 10 min before they were placed in the vacuum chamber. Inside the deposition chamber, they were mounted on a rotating sample holder at a vertical distance of around 7 cm to the sputtering target. Prior to deposition, the chamber was evacuated to a base pressure of around 1×10^{-4} Pa. The substrates were plasma-etched at 500 W RF power in pure Ar atmosphere at 0.5 Pa for 10 min. For the deposition of the Ti-C-Al multilayer stacks, the working pressure of Ar was maintained at 0.5 Pa and the substrates were grounded. The magnetron power was set at 200 W for all three targets with RF power for Ti and Al targets and DC power for graphite target. These settings were used in separate experiments to deposit individual titanium, carbon, and aluminum single layer films on Si substrates, dedicated to the determination of individual deposition rates. The measured deposition rates were approximately 0.6 nm/s for Ti, 0.2 nm/s for C and 1.1 nm/s for Al. During multilayer deposition, the PVD equipment run in a stop-and-go mode, i.e. the sample holder rotated from one target position to another one and stayed for various holding times at each individual target position (Figure 4.1). A shutter was installed between the target and the substrate holder to only allow the deposition of one

element at each position. Furthermore, the substrates were not additionally heated during deposition. The periodical stack (with a thickness of 14 nm) has been repeated until a total film thickness of ~ 3 μm on Si, SiO_2/Si and Al_2O_3 substrates. The overall coating thickness was around 5.5 μm on Zircaloy-4 substrates with another design of coatings consisting of a 500 nm thick Ti (8nm)-C (4nm) intermediate layer. The Ti-C layer was deposited by switching off the Al target power and doubling the dwell time at C target position. This Ti-C layer reacts and changes to TiC after thermal annealing (see details in section 4.4), which is intended to serve as diffusion barrier during oxidation. The two main sides of the Zircaloy-4 substrates were coated. Note that only the two main sides of the Zircaloy-4 substrates were coated and four edges were not able to cover under present deposition configurations.

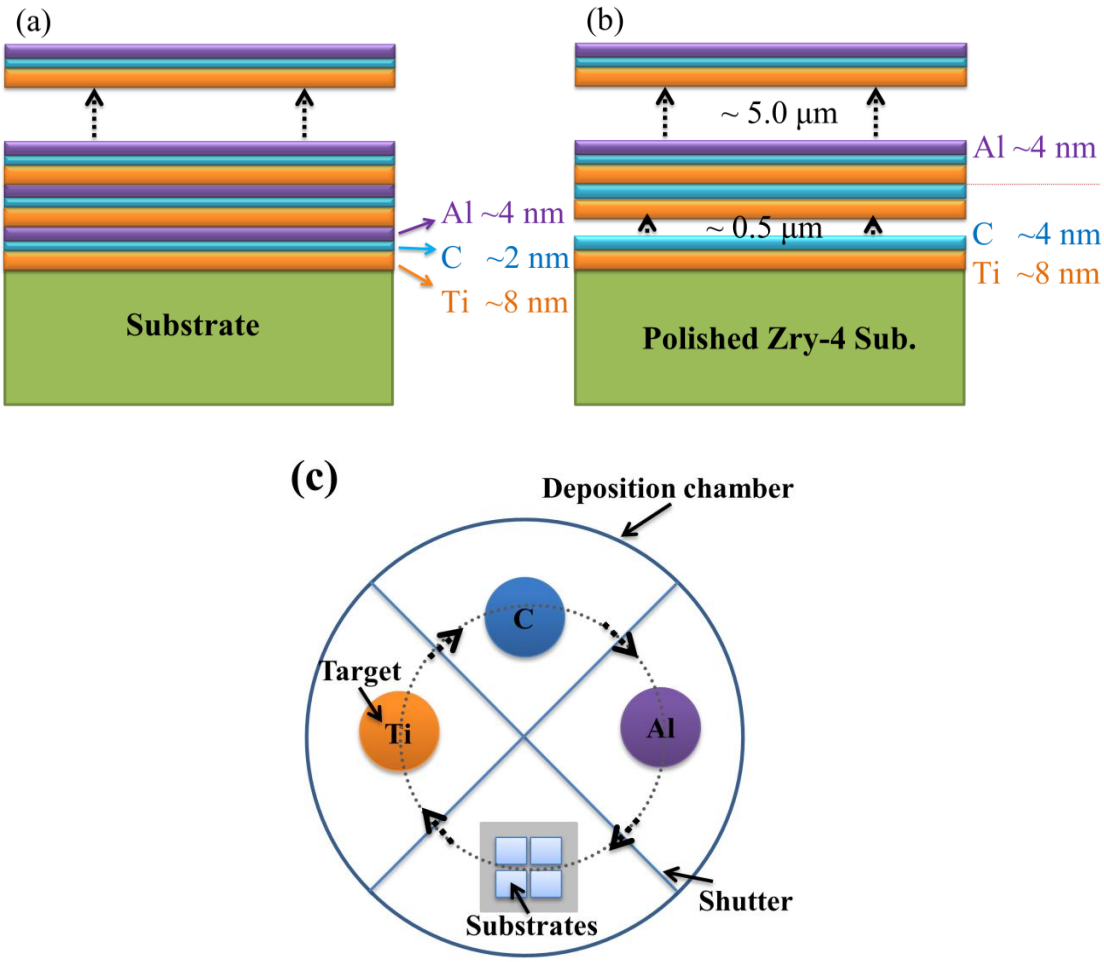

Figure 4.1 Schematic representation of (a) the elemental nanoscale multilayer stacks, (b) a second design of coatings with diffusion barrier on Zircaloy-4 substrates, and (c) arrangement of the targets and substrates during deposition.

4.2.2 Thermal annealing and high-temperature steam oxidation

After deposition, the coated specimens were *ex-situ* annealed in pure Ar (99.9999%) at atmospheric pressure using a commercial thermal balance (NETZSCH STA-449 F3 Jupiter) to facilitate the growth of MAX phases by solid reaction of the elemental multilayers. The balance consists of two furnaces: a silicon carbide furnace with the capability of heating up to 1600°C in dry atmosphere; a water vapor furnace that

can heat up to 1250°C and is designed for use in steam atmosphere. Annealing of the as-deposited coatings was conducted using the silicon carbide furnace. Figure 4.2 displays the schematics of the furnace. An oxygen trap system (OTS®) with zirconium getter ring was used to remove traces of residual oxygen in the gas atmosphere inside the instrument. The chamber was evacuated twice to 1.0×10^{-2} Pa before filling with Ar. Then a steady flow of Ar was maintained during annealing process. The samples were positioned vertically in the furnace using an alumina sample holder. The heating and the cooling rates were fixed at 10 K/min and the isothermal holding time was 10 min. The annealing temperature was varied from 600°C to 900°C for coatings on SiO_2/Si and Al_2O_3 substrates, but was selected at 800°C for coatings on Zircaloy-4 substrates.

The oxidation performance of the coatings in high-temperature steam from 800°C to 1200°C was examined using the water vapor furnace (NETZSCH STA-449/409). The steam flow rate was 3 g/h produced by a steam generator. The steam was injected directly into the reaction tube from the top to prevent contamination of the balance and to ensure a nearly pure steam atmosphere at the sample position. The temperature was stabilized for several minutes to reach equilibrium at the beginning of the isothermal period before injecting the steam. Other parameters (heating and cooling rates) were identical to the annealing test.

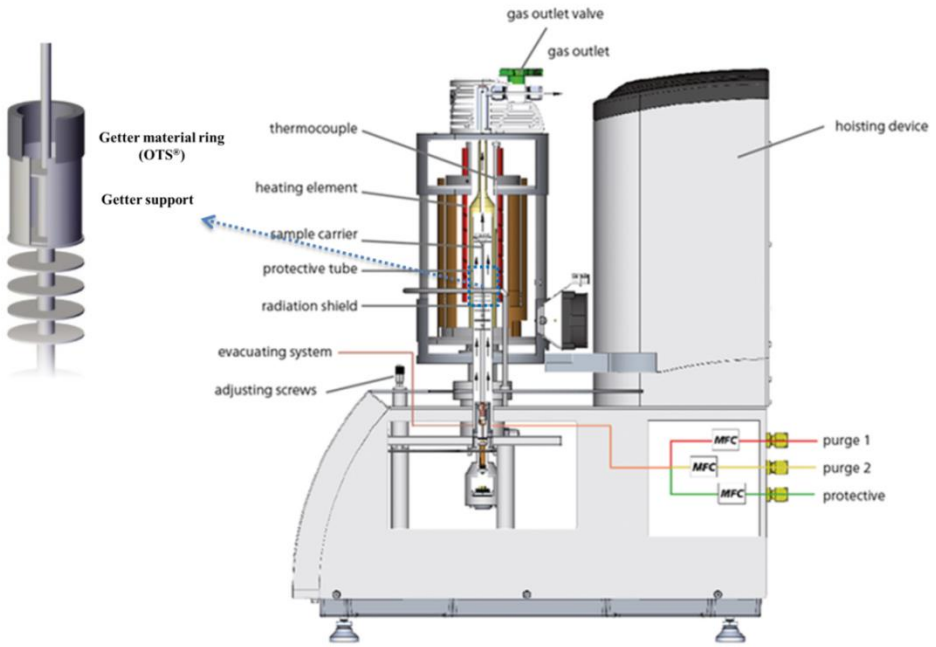

Figure 4.2 Schematic view of simultaneous thermal analyzer NETZSCH STA-449 F3 Jupiter of a silicon carbide furnace equipped with the oxygen trap system (OTS®).

4.2.3 Coating characterization

The overall chemical composition of the as-deposited coatings was determined by a JEOL JXA-8530F Field Emission Electron Probe Microanalyzer (EPMA) with 10 kV acceleration voltage and 100 nA probe current. An average value based on four measurements located in different regions was given. The

elemental depth profiles, both of the as-deposited and annealed coatings, were measured by depth-resolved Auger Electron Spectroscopy (AES) using a PHI 680 Xi Auger Nanoprobe system. An Ar ion beam with accelerating voltage 2 keV and ion current 500 nA was used for sputter etching. The electron beam for analysis was accelerated with a voltage of 10 KeV and a beam size of 24 nm.

The phase composition and crystalline structure of the coatings were analyzed by *ex-situ* X-Ray diffraction (XRD, Seifert PAD II diffractometer) and *in-situ* high-temperature X-Ray diffraction (HTXRD, Bruker D8). In case of *ex-situ* XRD measurement, a classical θ-2θ diffraction experiment was applied as before. The HTXRD measurements were conducted from 300°C to 1000°C in Ar (6N) with a temperature step of 20 K and a heating rate of 30 K/min using an Anton Paar HTK1200N high temperature stage. The CuKα_1 radiation with power 40 kV and 40 mA was used for HTXRD measurements. The recorded 2θ range was 8 to 50° with a step size of 0.04°, and a scan duration of approximately 5 min. Raman spectroscopy analysis was also conducted on some specific samples. The Raman spectra were collected and recorded for wavelengths between 160 and 2000 cm^{-1} with a Renishaw 1000 micro spectrometer using an argon ion laser at 514.5 nm (Modu-Laser, Type Aries-163) and power 2~3 mW on the sample surface.

The morphology of both surfaces and cross-sectional fracture surfaces was examined by scanning electron microscopy (SEM, Philips XL30S), and high-resolution transmission electron microscopy (HRTEM, FEI Tecnai 20 FEG). The cross-sectional lamellas for HRTEM analyses were prepared by focused ion beam in situ lift-out technique (FE-REM/FIB AurigaTM-Crossbeam System/Cobra FIB-Column, ZEISS Inc.). TEM imaging, including bright field and dark field modes, and selected area electron diffraction (SAED) were performed with 200 kV acceleration voltages of electron beam. High-resolution, high-angle annular dark field (HAADF) scanning-TEM was also applied for imaging. Compositional analysis was performed in the STEM mode using an energy dispersive X-ray (EDX) detector (production of EDAX Inc.).

The indentation hardness and reduced Young's modulus of the coatings were measured with a Berkovich nano-indenter (UMIS 2000). During the indentation test, the indentation depth was adjusted to be significantly higher than the surface roughness but less than 1/10 of the total film thickness to avoid substrate effects. The values reported herein represent the average based on at least ten indentations per sample. The commercial Ti_2AlC ceramic (Maxthal 211®) was used as reference for Raman spectroscopy analyses and hardness measurements. The coating-substrate adherence was evaluated by scratch tests (CSM Revetest) applying an increasing load of 20 N/cm up to 80 N. The indenter's sliding speed is 10 mm/min. Further determinations of the critical load of failure are from the micrographs of the scratches. The test has been repeated three times to obtain an average and accurate result.

The surface and cross-sectional morphology of Ti_2AlC coated Zircaloy-4 before and after oxidation were analyzed by an optical microscope (OM, Reichert-Jung MeF), as well as by SEM. For cross-sectional examination, the samples were first embedded in epoxy resin, then ground using SiC paper from 800 down to 2400 grit, and finally polished with a sequence of 15, 6 and 3 μm diamond pastes. The surfaces of coated Zircaloy-4 samples after oxidation at 800°C for 5 min were additionally examined by X-Ray

Photoelectron Spectroscopy (XPS). The measurements have been carried out using an IR/XPS–UHV system (Prevac) equipped with a VG Scienta R4000 electron energy analyzer. A monochromatic Al Kα X-ray source (1486.6 eV) was used as incident radiation. The energy scale has been calibrated to the reference peaks $Au4f_{7/2}$ (84.00 eV) and $Ag3d_{5/2}$ (368.26 eV). Prior to the data acquisition, the surface was sputter etched using an Ar^+ ion beam (1.5 keV, 10 mA) for around 5 mins to remove residual surface contamination. A CasaXPS Processing Software was used to treat the XPS spectra with a mixed Gaussian-Lorentzian function and Shirley background subtraction.

4.3 Coatings on Si, SiO_2/Si and Al_2O_3 substrates

4.3.1 Chemical composition

The chemical composition at four different regions of the as-deposited Ti-C-Al coating on Si(110) substrate determined by EPMA is shown in Table 4-1. The distribution of each element is homogeneous on macro scale and the coating consists of 50.5 ± 0.16 % Ti, 22.7 ± 0.40 % C and 26.8 ± 0.31 % Al (at.%). The results indicate that the overall chemical composition of the films is overall very close to the ideal stoichiometry of Ti, C, Al (2:1:1) in bulk Ti_2AlC; the concentration of carbon is however slightly lower than the theoretical value. This can be explained by the density of the deposited (amorphous) carbon layer which usually is slightly lower than the theoretical density of (crystalline) graphite which was adopted here to calculate the single layer thickness [181]. The periodical nanoscale multilayer stacks of the as-deposited coatings are proved by both following AES depth profiles and HRTEM images that will be shown later. Annealing of the coatings on pure Si substrate resulted in significant interdiffusion between the coatings and the substrates as identified by SEM-EDS, indicating a diffusion barrier is needed for the synthesis of MAX phase coatings on Si (or some metallic substrates) [45]. Therefore, annealing and characterization were mainly focused on coatings deposited on SiO_2/Si and Al_2O_3 substrates.

Table 4-1 Chemical composition of the as-deposited Ti-C-Al coating on Si substrate determined by EPMA.

Point	Ti (at.%)	C (at.%)	Al (at.%)
1	50.7	22.3	27.0
2	50.3	22.8	26.8
3	50.5	23.2	26.3
4	50.4	22.7	26.9
Average	50.5	22.7	26.8

Figure 4.3 shows the AES depth profiles of the four elements, Ti, Al, C, O in the as-deposited and 700°C and 800°C annealed samples on SiO_2/Si substrates. The as-deposited coating demonstrated clearly a periodical laminated structure with relatively sharp interface between the Ti, C, and Al elemental layers. The coating surface was contaminated by oxygen (due to exposure of the sample to the ambient) and was also rich in aluminum (as the top layer of the multilayer coating is aluminum). Further, the as-deposited

coating was barely contaminated by oxygen or other elements (i.e. the oxygen content was about 1.5 at.%). The deposition at ambient temperature resulted in a low desorption rate of oxygen from the residual gas and consequently in a minor oxygen incorporation in the coatings during growth [152]. The elemental layers completely diffused, and the distribution of each element became uniform at 700°C and 800°C annealing for 10 min, as demonstrated in Figure 4.3(b) and (c). There was no obvious difference between these two samples whereas the thickness of the surface oxide layer was significantly increased compared to the as-deposited coatings (by around 50 nm). The diffusion of Al toward the surface, driven by surface oxidation, became more pronounced with the increasing annealing temperature. Due to the outward diffusion, the Al content shifts to a slightly lower concentration than that of C after annealing at 800°C compared to slightly higher concentration for the as-deposited and the 700 °C annealed coatings. This surface oxidation was a result of residual air trapping in the annealing oven or trace oxygen impurity in the argon gas that was not captured by the zirconium trap during annealing treatments.

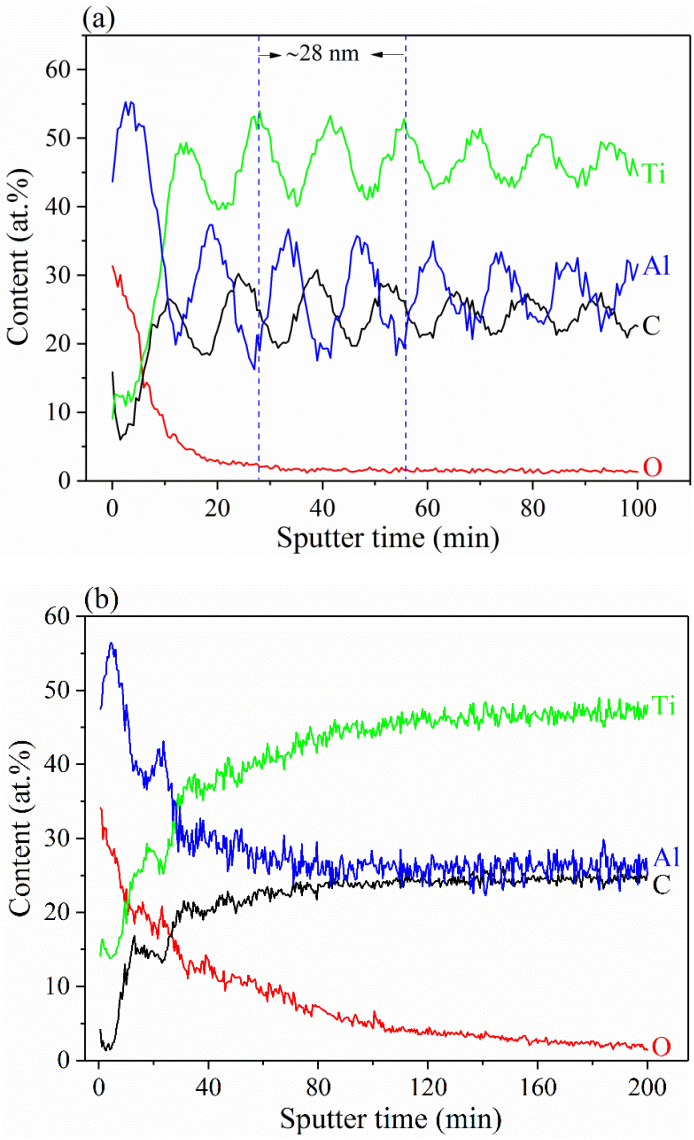

(Continued)

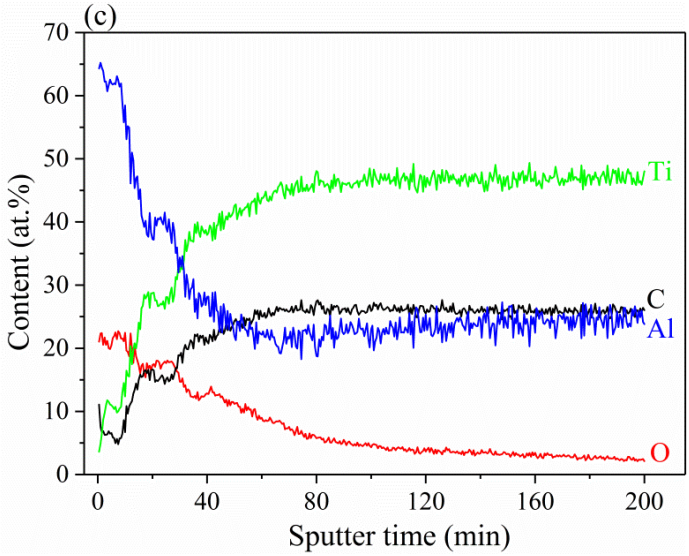

Figure 4.3 AES elemental depth profiles of coatings deposited on SiO_2/Si substrate. (a) as-deposited, (b) annealed at 700°C, (c) annealed at 800°C.

4.3.2 Phase crystallization and evolution

The *ex-situ* X-ray diffraction patterns of the as-deposited and annealed coatings from 600°C to 900°C on SiO_2/Si substrates of individual samples are presented in Figure 4.4. Figure 4.4(a) shows the XRD pattern for the as-deposited coating. A relatively broad diffraction peak is observed at around 38°, close to the theoretical position of Ti (002) (JCPDS #44-1294) and Al (111) (JCPDS #04-0787) reflexes. The diffraction pattern demonstrates that the titanium and aluminum layers are grown in a nanocrystalline structure. The carbon layers, as expected, are grown in an amorphous network. After annealing at 600°C (Figure 4.4(b)), the XRD pattern shows a different character: nanocrystalline titanium and aluminum phases are not observed anymore, while the formation of the intermetallic compound Al_3Ti (JCPDS #37-1146) and potentially titanium carbide TiC_x (JCPDS #32-1383) are observed. The diffraction intensity originating from the titanium carbide reflex is however relatively weak and the signal is broad, suggesting that some carbon remains in an amorphous state within the coating. In addition, transition binary carbides frequently exhibit wide homogeneity ranges with carbon vacancy [182]. For example, TiC has a stoichiometry ranging from approximately $TiC_{0.5}$ to $TiC_{0.98}$. It was therefore indicated as TiC_x here.

As the annealing temperature increases to 700°C, the diffraction intensity of Al_3Ti increases significantly probably because the diffusion of aluminum becomes extremely fast once the temperature reaches or exceeds the melting temperature of Al (around 660°C). Meanwhile, a Ti_2AlC MAX phase begins to crystallize and reflexes of the Ti_2AlC (002) and (006) lattice planes (JCPDS #29-0095, $P6_3/mmc$ space group with a=0.304 nm and c=1.360 nm) [67] are clearly visible. The crystallization onset temperature of the Ti_2AlC phase synthesized by this method is in the range of 600°C-700°C. The sample annealed at 800°C displays the formation of pure Ti_2AlC MAX phase only. The formation of common competing binary and ternary phases in the Ti-C-Al system, like Ti-Al intermetallics, TiC, Ti_3AlC and Ti_3AlC_2

described in previous published work [79,84,158], during the deposition of Ti_2AlC MAX phase are not observed. The crystallinity of the Ti_2AlC MAX phase is enhanced at 800°C compared to that at 700°C, which means the crystallinity of the MAX phase is significantly dependent on thermally activated processes. The sharp and strong diffraction peaks at 13.01° and 39.74° generated by the (002) and (006) lattice planes, respectively, demonstrate a (00l) basal plane preferred orientation in the Ti_2AlC MAX phase coatings. For the sample annealed at 900°C, the highest temperature in this study, the diffraction pattern is on a first view similar to that annealed at 800°C. However, some slight modification is visible: the diffraction intensity of the (002) plane decreases; the originally observed (006) lattice plane signal seems to overlap with a (103) lattice plane signal and a tiny shift of these to lower diffraction angles is noticed. This is probably due to the increasing diffusion rates at higher temperature enabling the fast growth of Ti_2AlC grains along with the loss of oriented growth.

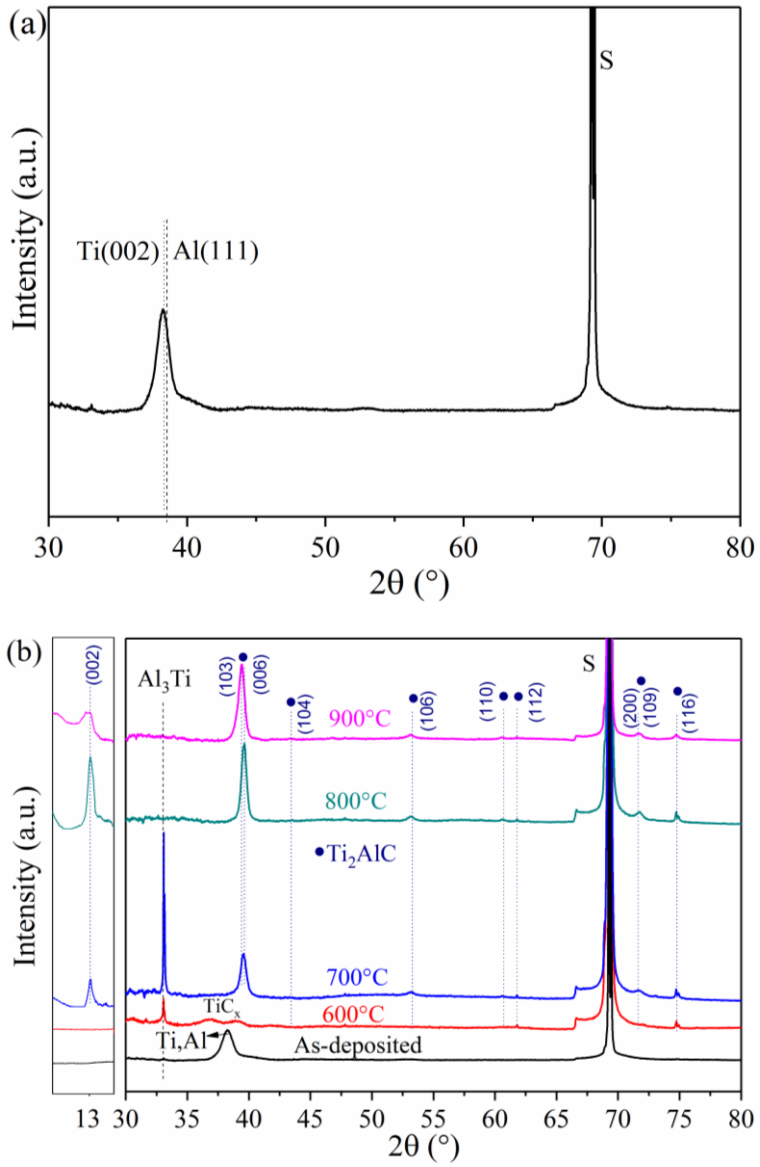

Figure 4.4 XRD patterns of coatings on SiO_2/Si substrate. (a) as-deposited coating, (b) individual annealed coatings from 600°C to 900°C in argon. Signals characteristic of Ti_2AlC are marked by black circles (•), S marks signals assigned with the substrate.

The phase crystallization in dependence of the annealing temperature examined by *in-situ* HTXRD is shown in Figure 4.5. Due to the observation of significant cracking and spallation for the coatings on SiO_2/Si substrate during annealing (shown later), the HTXRD measurements were carried out on coatings grown on Al_2O_3 substrates. The evolution of diffraction peaks and signal intensities during annealing from low to high temperature can be clearly seen (Figure 4.5(a)). The nucleation and growth of Ti_2AlC MAX phase crystals is confirmed by checking the specific diffraction reflection of (002) lattice plane at 2θ of 13.01°. Figure 4.5(b) and (c) display the selected enlarged views of the data from 300°C to 500°C at 2θ of 30 – 50° and 520°C to 800°C at 2θ of 10 – 50°, respectively. As displayed in Figure 4.5(b) at low temperatures (below 400°C), apart from the reflection assigned with the substrate, only diffraction peaks belonging to Ti and Al phases are observed. In addition, the position and intensity of their reflection remains barely unchanged from 300°C to 420°C. It is suggested that the nanoscale elemental multilayers thus retain stable up to around 420°C. The relatively broad diffraction peak at around 38° (reflection of Ti and Al existing at low temperatures) gradually shifts to lower diffraction angles at higher temperatures above 440°C. This broad diffraction peak positioned at around 35.5° can be assigned to the reflection from the (111) lattice plane of TiC_x phase ($0.47<x<1$, denoted as TiC_x since the stoichiometry may deviate from the perfect stoichiometry as a shift of the reflection is shown compared to the theoretical value [182]). The formation of a poorly crystallized TiC_x phase via diffusion reaction starting from 460°C up to 700°C is in good agreement with the results obtained for the annealed coatings on SiO_2/Si substrates (Figure 4.4). The absence of reflection from Ti-Al intermetallic compounds at temperatures below 800°C can be attributed to their very small nanocrystals or even completely amorphous structure during *in-situ* annealing. The crystallization onset temperature of the Ti_2AlC MAX phase is identified at a narrow temperature interval, i.e. 640 - 660°C, as shown in Figure 4.5(c). This information provides a useful criterion to select the suitable annealing temperature to fabricate Ti_2AlC coatings by this method on temperature-sensitive substrates. The intensities of the two diffraction peaks corresponding to Ti_2AlC (002) and (004) lattice planes are progressively enhanced with increasing temperatures up to 800°C, indicating the improved crystallinity as well as the formation of a highly textured or ordered MAX phase coating. HTXRD pattern at 800°C confirms that single-phase Ti_2AlC coatings are successfully produced and no impurity phases are identified. It is worthwhile mentioning that the intensities originated from the MAX phase decrease at temperatures higher than 900°C. This observation is considered to arise from relatively low stability of the MAX phase coatings due to their nano-grains that make them vulnerable to oxidation or decomposition at high temperatures [81].

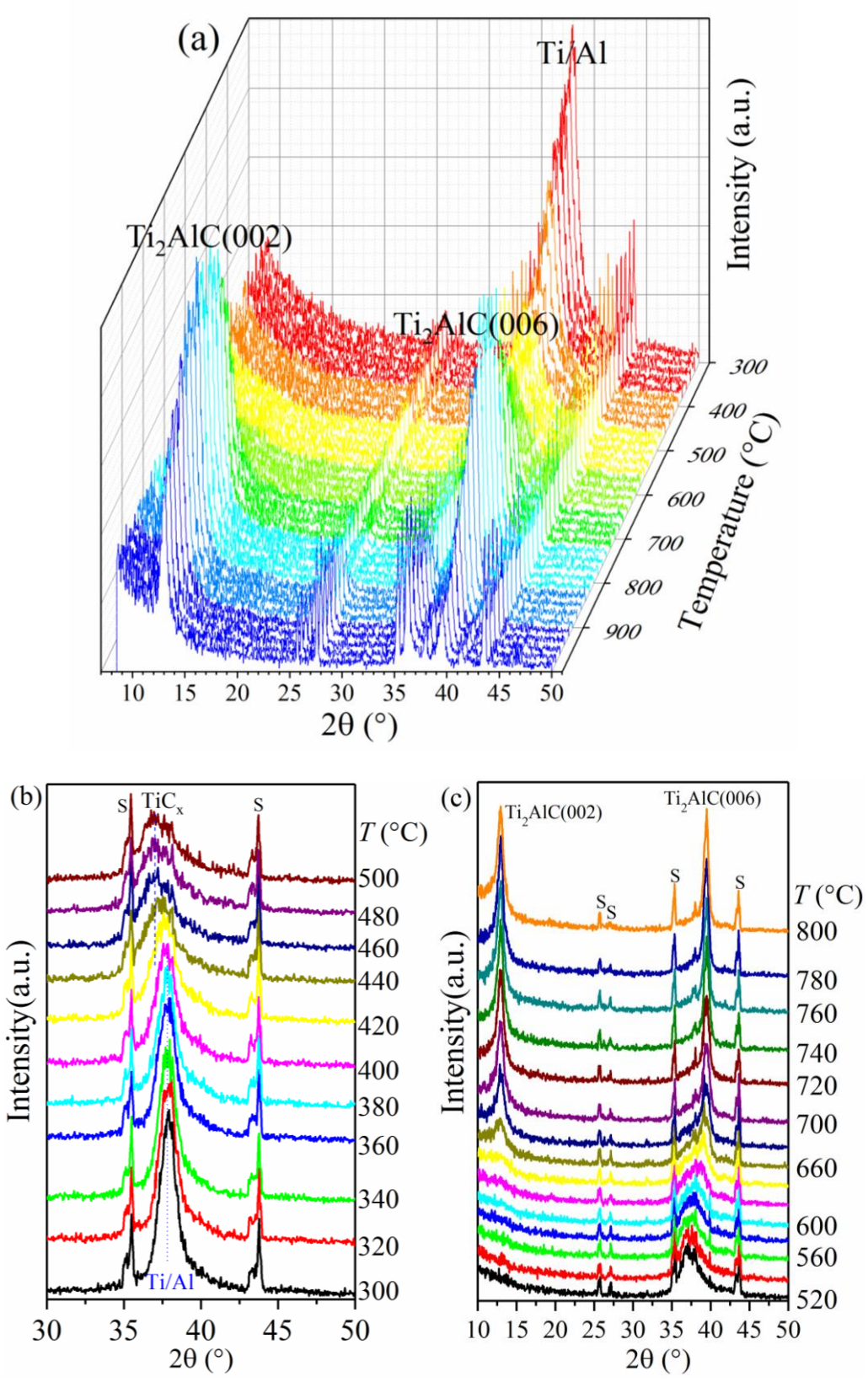

Figure 4.5 *In-situ* HTXRD patterns of Ti-C-Al coatings on Al_2O_3 substrate during annealing in argon with temperature step 20 K. (a) Waterfall plot of full temperature range from 300°C to 1000°C; selected enlarged views of the patterns: (b) from 300°C to 500°C, and (c) from 520°C to 800°C showing the phase crystallization as a function of annealing temperature. S marks signals assigned to the substrate.

Raman spectroscopy analyses were further performed to further confirm the interpretations of phase evolution and crystallization of Ti_2AlC MAX phase during annealing at successively increasing temperatures. Figure 4.6 shows the Raman spectra of the commercial Ti_2AlC bulk ceramic, as-deposited and annealed coatings on SiO_2/Si substrates in the range of 160 cm^{-1}-2000 cm^{-1}. The theoretical Raman vibration modes of Ti_2AlC, i.e. E_{1g}&E_{2g} and A_{1g} (vibrational direction parallel or perpendicular to the basal plane, respectively [145]), are located at 266 cm^{-1} and 365 cm^{-1}, respectively.

The Raman shift signals of the commercial Ti_2AlC bulk ceramic in the low wavenumber range agree well to the theoretical values of its vibration modes. Amorphous carbon thin films and materials containing amorphous carbon phases are characterized by the vibration modes of the so-called D and G bands, which are usually located at around 1350 cm^{-1} and 1580 cm^{-1} [183]. Such spectral features are not observed at this region for the bulk Ti_2AlC samples used in this study. However, the intensity of these two bands is significant in the as-deposited Ti-C-Al coatings, indicating the magnetron sputtered carbon layers are grown in an amorphous state. With respect to the coatings annealed at 700°C, the D and G band intensities decrease dramatically. Simultaneously, the Raman active modes attributed to the Ti_2AlC MAX phase begin to become visible in the Raman spectra. For the 800°C and 900°C annealed coatings, the amorphous carbon character completely disappears as shown in the Raman spectra. The Raman shift peaks belonging to Ti_2AlC become sharp and strong, and the location of these observed signals fits quite well with the theoretical values as mentioned above [184]. Table 4-2 lists the Raman active modes of the Ti_2AlC MAX phase reported previously and observed in this study. These results further support the statement that Ti_2AlC crystallizes already at 700°C, and a pure Ti_2AlC MAX phase is obtained at 800°C.

Broader bands of lower intensity located in the range of 500 - 750 cm^{-1} were observed in most samples, but not in case of the as-deposited coatings. These bands are all supposed to be assigned with thin surface oxide and/or oxycarbide layers [185,186] after annealing, as demonstrated by above AES depth profiling measurements. The surface oxidation of the coatings becomes more pronounced with increasing annealing temperatures as indicated in Figure 4.6.

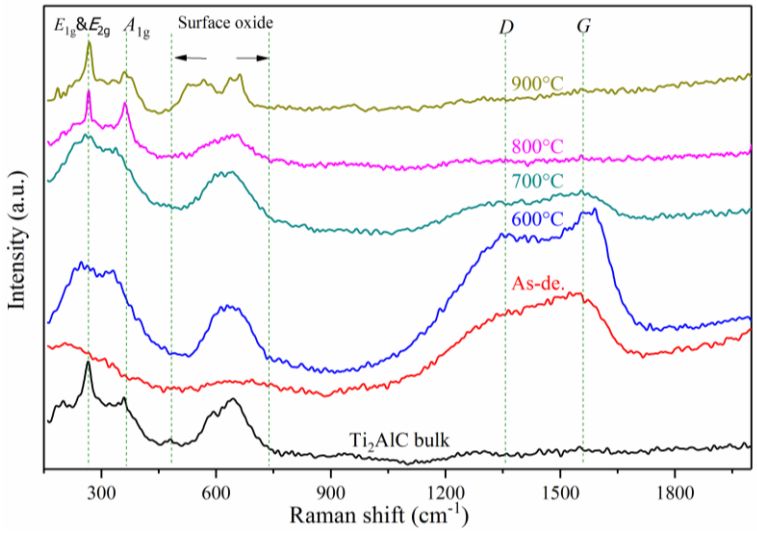

Figure 4.6 Raman spectra for commercial bulk Ti_2AlC ceramic, as-deposited and annealed coatings on SiO_2/Si substrates.

Table 4-2 Raman active modes (cm^{-1}) of the commercial bulk Ti_2AlC and coatings obtained in this study.

	E_{1g}&E_{2g}	A_{1g}	Ref.
Calculated	266	365	[184]
Experimental	260.9	370.3	[187]
Ti_2AlC bulk	264.6	358.7	This work
700°C annealed coating	261.5	342.2	This work
800°C annealed coating	266.8	362.9	This work
900°C annealed coating	269.0	359.7	This work

4.3.3 Morphology and microstructural evolution

The surface and cross-sectional morphology of the as-deposited and 800°C annealed coatings on SiO_2/Si substrates investigated by SEM are displayed in Figure 4.7. The as-deposited coating is uniform and dense, free of pinholes, pores or other defects at this length scale. The coating thickness is ~ 3.2 μm, in accordance with the predicted values calculated by the deposition rates of each individual target. However, the coating annealed at 800°C shows a large quantity of cracks; and cracks are also observed for coatings annealed at other temperatures. The linear coefficients of thermal expansion (CTE) of Si, amorphous SiO_2 and Ti_2AlC are 2.6 × 10^{-6} K^{-1}, 0.55 × 10^{-6} K^{-1} and ~8.7 × 10^{-6} K^{-1}, respectively [67,188,189]. The large CTE mismatch between the substrate and the coating contribute to cracking of the coatings during annealing at high temperature. It is therefore suggested that a more suitable substrate or adhesive interlayer should be applied on significant CTE mismatch substrates for practical application of Ti_2AlC coatings synthesized by this method.

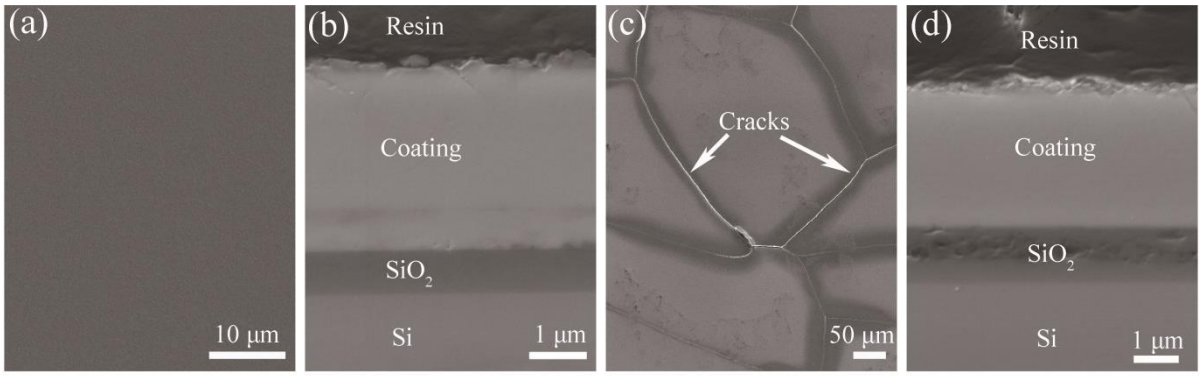

Figure 4.7 SEM images of the coatings on SiO_2/Si substrates. (a) Surface top view and (b) cross section view of as-deposited coating, (c) surface top view and (d) cross section view of 800°C annealed coating.

The as-deposited, 700°C and 800°C annealed coatings on SiO_2/Si substrates were further characterized by TEM in order to gather more insights into the microstructural evolution of the coatings during annealing.

The cross-sectional bright-field TEM image of an as-deposited Ti-C-Al coating is displayed in Figure 4.8. The layered stacks are obviously confirmed by the different material related contrasts and the thickness of each layered stack is around 14 nm as planned. The enlarged image below shows a detail of this nanoscale multilayer structure in higher magnification. It is clearly visible that the design follows the sequence of the titanium, –carbon, and –aluminum with titanium as the initial layer deposited on the substrate. The thickness of each layer is consistent with the estimated values according to the pre-determined deposition rates of individual materials, and the interfaces between each layer are sharp. The carbon layer is amorphous and the other two metal layers are nanocrystalline. Figure 4.9 shows a typical HRTEM image of the coating after annealing at 700°C. In full agreement with the previously described XRD results and further determined by lattice parameters and fast Fourier transform (FFT) analysis, three different nanocrystalline phases are confirmed: TiC_x, Al_3Ti, and the MAX phase Ti_2AlC. No manifest amorphous phase is seen. The crystallization of the Ti_2AlC MAX phase is shown without doubt, despite its volume content is low.

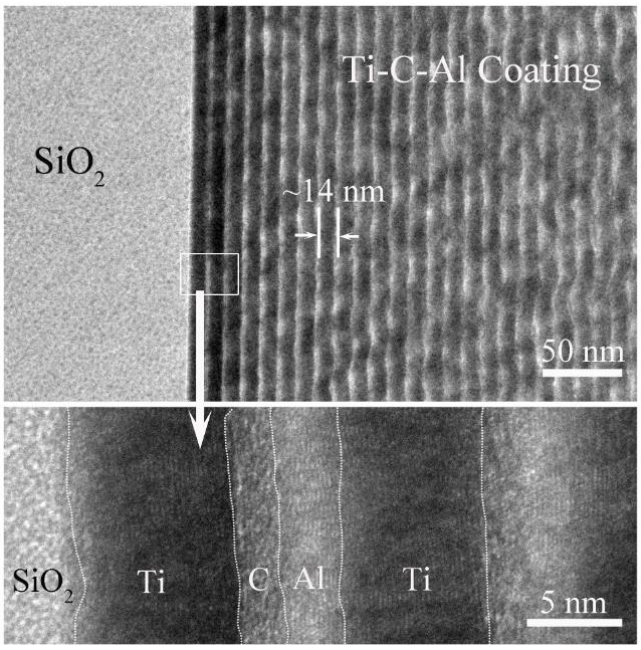

Figure 4.8 Bright-field TEM images of an as-deposited multilayer Ti-C-Al coating on SiO_2/Si substrate.

Figure 4.10 illustrates the plan-view bright field TEM images and the corresponding FFT image of the coating annealed at 800°C. As shown in Figure 4.10(a), the coating fully crystallizes to single Ti_2AlC phase with grain sizes around 20 nm. The strong overlapping of these nano-sized grains in the image plane prevents their clear TEM imaging. The typical nanolaminated crystal structure of MAX phase is shown. The coating shows a preferred orientation of (00l) basal planes as demonstrated in the inserted FFT image. The measured d-spacing of 0.68 nm in Figure 4.10(b) is quite consistent with the theoretical value of the (001) lattice plane of the Ti_2AlC MAX phase. No secondary amorphous or glass phases in the grain boundaries and no evident impurity phases are detected. Figure 4.10(c) shows the fast-Fourier transformed image of area B, which is indexed as [1-210].

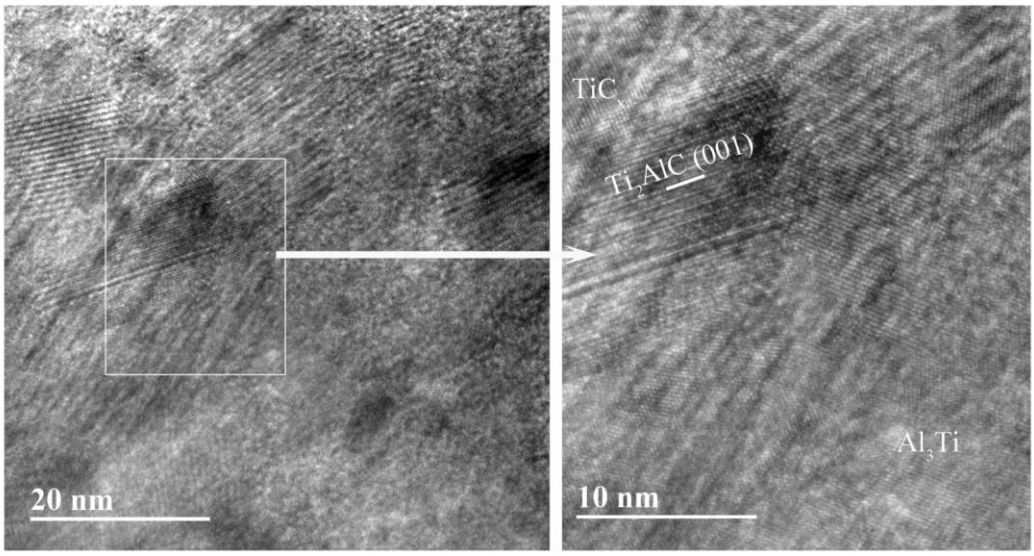

Figure 4.9 Bright-field TEM images of a coating on SiO_2/Si substrate after annealing at 700°C.

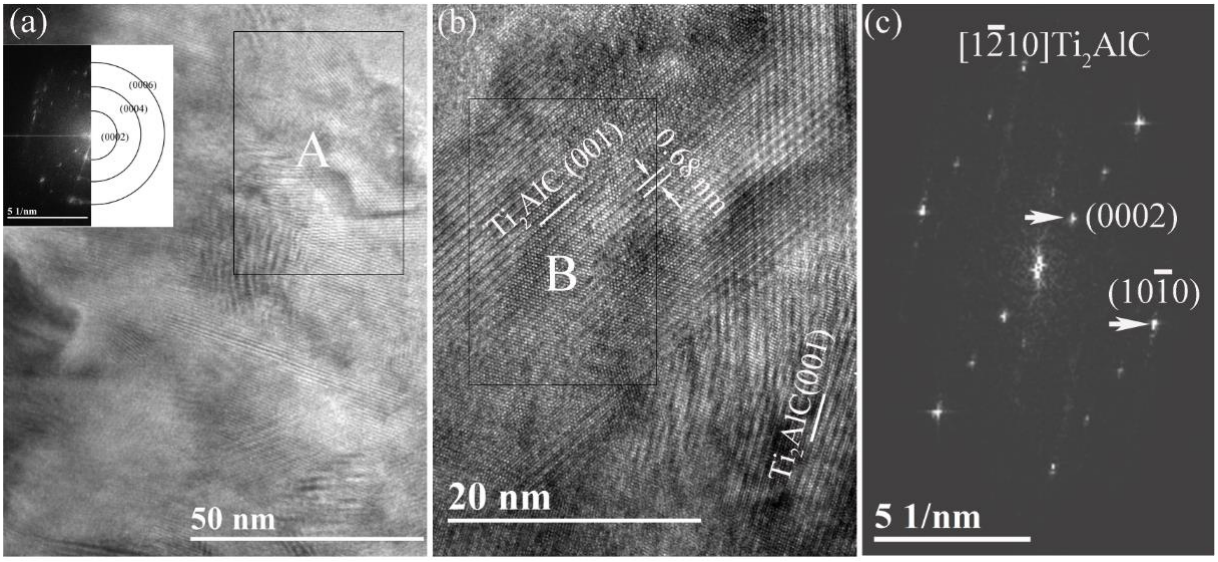

Figure 4.10 TEM images of coating on SiO_2/Si substrate after annealing at 800°C. (a) Plan-view of bright-field image with FFT image inserted on upper left corner, (b) HRTEM image of area A in (a), (c) FFT image of area B in (b).

The interface between the amorphous SiO_2 layer and the coatings was also investigated by TEM. A HAADF image and a HRTEM image of the interface is shown in Figure 4.11 for the coating annealed at 800°C. A thin interdiffusion zone, around 20 nm thick, is clearly visible. Figure 4.11(b) shows the HRTEM image of the interface. The SiO_2 substrate is amorphous, whereas, the diffusion layer displays rather a nanocrystalline structure. The interface between the coating and the diffusion layer is uniform, however, the interface between the diffusion layer and the amorphous SiO_2 substrate layer shows a more irregular shape. No intergrown phases were observed between the coating and the diffusion layer. The EDS line-scanning results, the line indicated in Figure 4.11(a) from A to B, are given in Figure 4.11(c). The profiles reveal that mainly the coating elements diffuse into the substrate and the principle diffusion

species is Al. A small amount of Ti in the coating also diffuses into the substrate. The reaction kinetics is generally extremely fast in nanoscale reactive multilayers at elevated temperatures and previous investigations have proved that MAX phase can grow with only few seconds annealing via diffusion reaction of magnetron-sputtered multilayer [80]. Thus, interdiffusion at coating/substrate interface probably proceeds predominantly in the form of Ti_2AlC phase, rather than multilayers or intermediate phases, during annealing at 800°C. The Al-enriched interdiffusion zone is associated with the unique layered structure contributing to higher mobility of A element in MAX phases.

Characterization of the coatings on both SiO_2/Si and Al_2O_3 substrates suggests that crystallization of the Ti_2AlC MAX phase starts at ~660°C and single phase Ti_2AlC coatings directly nucleate and grow at 800°C with a (00l) basal plane preferred orientation, independent of the (oxide) substrate, via diffusion reaction.

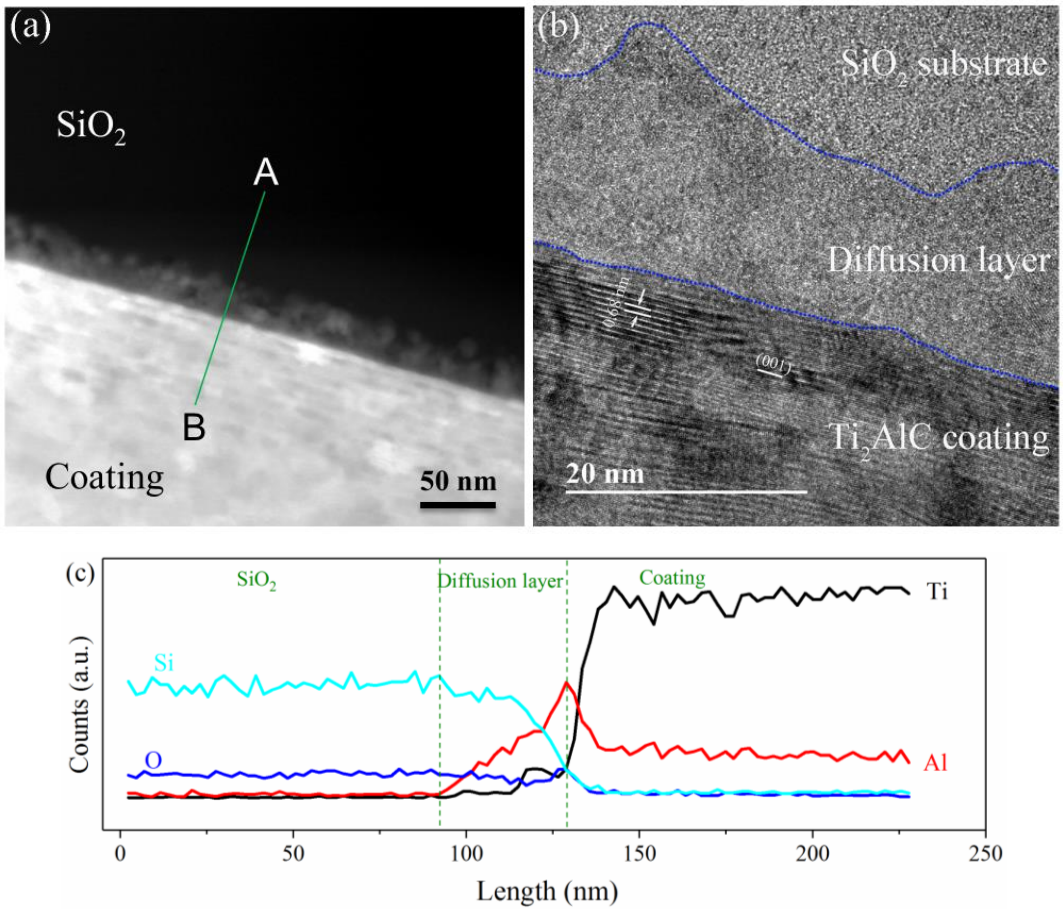

Figure 4.11 TEM images and EDS line scanning of the coating-substrate interface after annealing at 800°C. (a) a HAADF image, (b) a plan-view bright-field HRTEM image, (c) EDS elemental profiles along the line in (a) from A to B.

4.3.4 Mechanical properties

The hardness and reduced Young's modulus with the standard deviation of the bulk Ti_2AlC ceramic and the Ti_2AlC coatings measured by nanoindentation are displayed in Figure 4.12. The measured indentation hardness and reduced Young's modulus of bulk Ti_2AlC are 4.3 ± 1.1 GPa and 158.7 ± 28.3 GPa, respectively. These values are in accordance with previous literature data [67]. The low hardness of the

MAX phase ceramic is attributed to the relatively weak bonds between TiC slabs and Al layers causing easy basal plane slip upon deformation [73]. The relatively large scattering of measured data can be explained by the phase purity of the samples as shown in Chapter 3. For the as-deposited coating, the indentation hardness and reduced Young's modulus are around 7.6 GPa and 124.1 GPa. The measured values of hardness of the annealed coatings from 700°C to 900°C are in the range of 13 – 18 GPa, approximately 3 – 5 times higher than the value of bulk Ti_2AlC, and are similar to values reported for MAX phase coatings deposited by magnetron sputtering [12,16,29]. The highest level of indentation hardness is observed at 800°C with a value of 17.2 GPa. The reduced Young's modulus gradually increased in the whole range of annealing temperature, reaching 270.3 GPa at 900°C.

Considering the hardness is the response of a material's ability to resist deformation upon loading, it is significantly affected by the composition and the microstructure of the materials. Moreover, compared to polycrystalline bulk materials, thin films often show anisotropic hardness due to preferred orientation and low grain sizes. Based on the microstructure evolution of the coatings annealed at different temperatures, it is possible to understand the trend in change of the indentation hardness and reduced Young's modulus. Due to the formation of the nanocrystalline Ti_2AlC MAX phase and its enhanced crystallinity upon annealing from 700°C to 800°C, the indentation hardness and reduced Young's modulus gradually increase. The measured values scatter considerably at 700°C due to the formation of metallic and ceramic mixture phases. The decreasing hardness of the coatings after annealing at 900°C can be explained by the coalescence of the Ti_2AlC grains, elimination of preferred orientation, and probably removal of some growth defects [83].

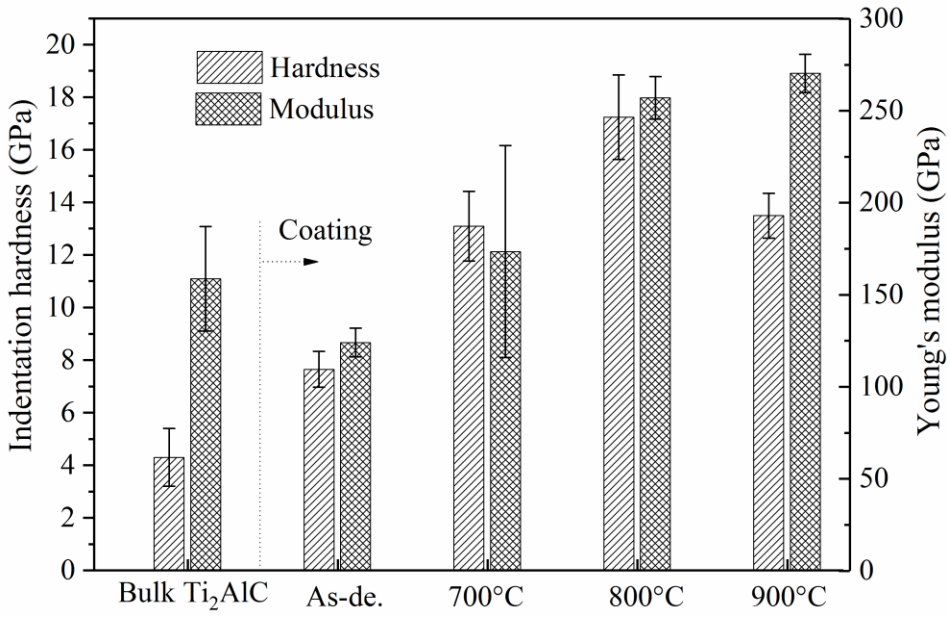

Figure 4.12 Indentation hardness and reduced Young's modulus of bulk Ti_2AlC ceramic and coatings synthesized in this study.

4.4 Coatings on Zircaloy-4 substrates

The high-temperature oxidation resistance of Ti_2AlC MAX phase relies on the growth of an alumina scale on the surface; results presented in the previous section proved that significant diffusion of Al from the coating into the substrate occurred during annealing. In order to suppress the fast diffusion of Al into the substrate and retain the Al reservoir to form alumina scale during high-temperature oxidation, two designs of coatings on Zircaloy-4 substrate were developed, i.e. without or with a 500 nm thick intermediate TiC layer as diffusion barrier [190]. Selection of TiC as diffusion barrier is considering the high stability and low diffusivities of transition metal carbides [191], and utilization of compounds in Ti-C-Al ternary system allowing easy fabrication during deposition. The coatings were synthesized following the identical two-step procedure, i.e. deposition and *ex-situ* annealing, with respect to the coatings on Si/SiO_2 and alumina substrates. The TiC barrier was realized via annealing the magnetron-sputtered Ti-C multilayer stacks as mentioned in experiment section.

4.4.1 Coating characterization

4.4.1.1 Phase composition

Figure 4.13 shows the XRD patterns of the as-deposited and 800°C annealed coatings with and without diffusion barrier. The XRD patterns are composed of similar diffraction peaks for both as-deposited coatings. Apart from the diffraction signals generated by the Zircaloy-4 substrates and similar to findings reported for as-deposited coatings on SiO_2/Si substrates, in the Ti-C-Al (coating) or Ti-C (diffusion barrier) multilayer stacks, the titanium and/or aluminum layers consist of nanocrystalline grains with relatively low crystallinity and the carbon layers, as expected, are grown in an amorphous state. After annealing, the XRD patterns display different features. Growth of phase-pure Ti_2AlC MAX phase is confirmed in Figure 4.13(c) for the coatings without diffusion barrier after annealing. In case of as-deposited coatings with barrier, additional diffraction signals assigned to TiC phase are distinguished after annealing (Figure 4.13(d)). The diffraction peak located at around 35.9° corresponds to the TiC (111) lattice plane. It suggests that the Ti-C-Al and Ti-C elemental multilayer stacks react and crystallize to corresponding Ti_2AlC and TiC phases during annealing at 800°C for 10 min. The grain size of the Ti_2AlC MAX phase coatings after annealing was calculated based on the Scherrer's equation using the XRD reflex [88]. The results suggest the grain size is in the range of 15 - 20 nm, consistent with results presented in the previous sections and determined by TEM.

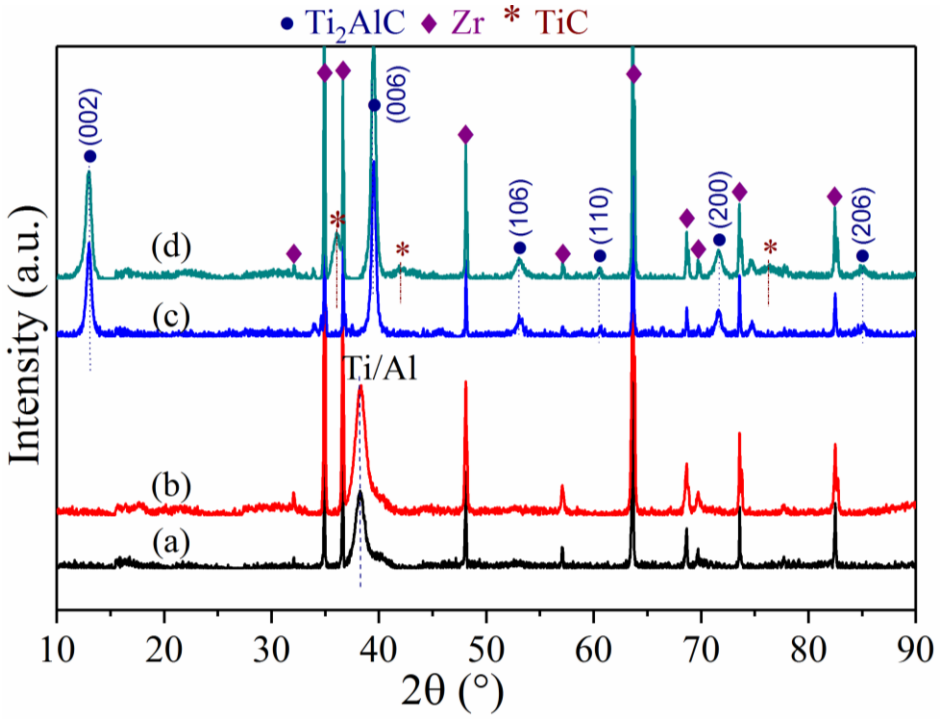

Figure 4.13 XRD patterns of coatings on Zircaloy-4 substrates. As-deposited Ti-C-Al coating (a) without and (b) with diffusion barrier, coatings (c) without and (d) with diffusion barrier annealed at 800°C in argon for 10 min.

Figure 4.14 shows the Raman spectra of the as-deposited and the 800°C annealed coatings with and without diffusion barrier. Curves (a) and (b) in Figure 4.14 demonstrate that there are no distinguishable sharp peaks except one broad hump corresponding to D and G bands, characteristic of amorphous carbon, for both as-deposited coatings. For coatings without barrier after annealing at 800°C, the Raman active modes attributed to Ti_2AlC can be clearly seen as shown in Figure 4.14(c). The signals of E_{1g}&E_{2g} and A_{1g} modes are located at 265.7 and 361.8 cm^{-1}, respectively, which agrees quite well with the theoretical values [184]. The signals are sharp with high intensity, indicating that the coatings are well-crystallized after annealing. Furthermore, no signals are detected anymore in the region of D and G bands. These findings support the claim that a phase-pure Ti_2AlC coating was obtained after 800°C annealing. However, in case of curve (d) of coatings with barrier after annealing, additional signals were recorded. The D and G bands still exist with better resolution, and a sharp signal appears at 200 cm^{-1}. XRD results have indicated that the as-deposited Ti-C barrier layer reacts to form TiC during annealing. Consequently, these signals can be assigned to TiC. Stoichiometric TiC has no Raman vibration modes but the introduction of disorder due to carbon vacancies make them Raman active [192]. It suggests that the as-deposited Ti-C barrier layer changes to sub-stoichiometric TiC_x ($0.47<x<1$) because of carbon deficiency. The broad peaks located at the region of 500-750 cm^{-1} for both annealed coatings is caused by a thin surface oxide layer formed on the surface of coatings during annealing as explained in previous section.

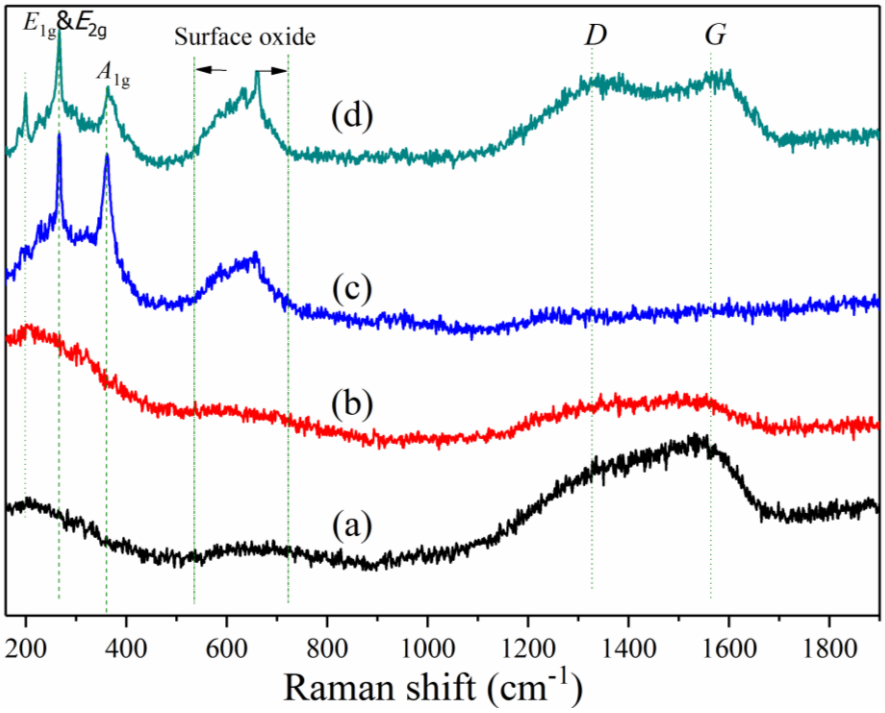

Figure 4.14 Raman spectra of coatings on Zircaloy-4 substrates. As-deposited Ti-C-Al coating (a) without and (b) with diffusion barrier, coatings (c) without and (d) with diffusion barrier annealed at 800°C in argon for 10 min.

4.4.1.2 Morphology and microstructure

Figure 4.15 are surface and cross-sectional SEM images of the as-deposited coatings with and without barrier layer on Zircaloy-4 substrates. Both coatings are uniform and dense, free of any visible defects at this length scale. As predicted, the coating thickness is around 5.5 μm. In case of coating with barrier, the 500 nm thick Ti-C barrier layer can be clearly identified from the cross-sectional image of Figure 4.15(d).

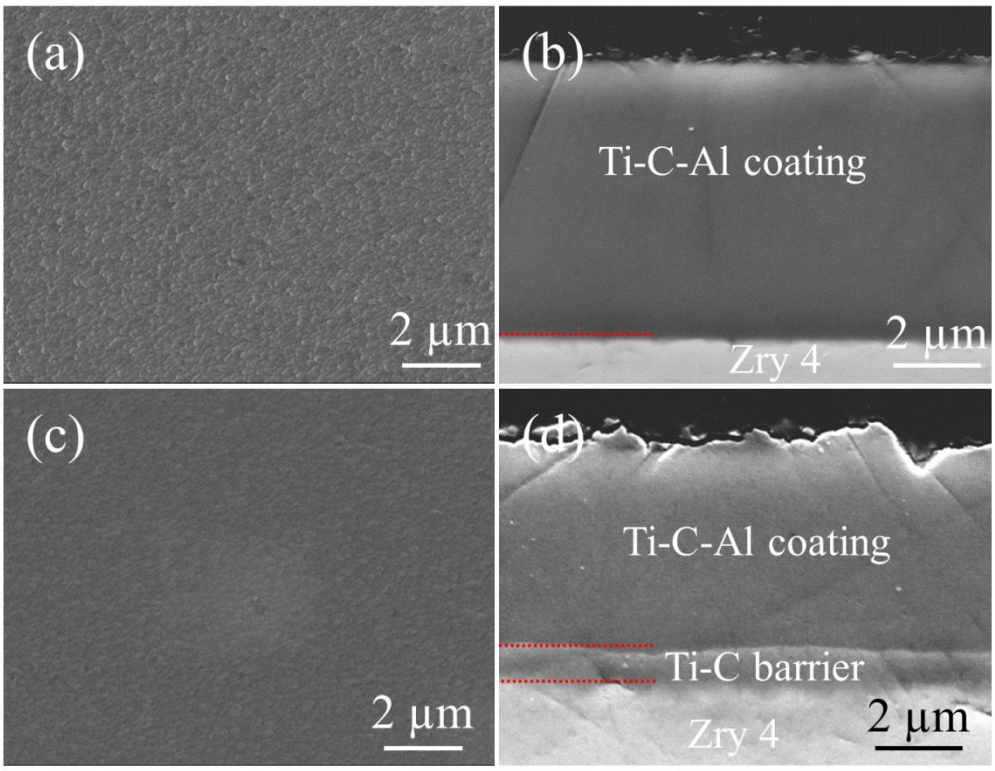

Figure 4.15 SEM images of as-deposited coatings with and without barrier layer on Zircaloy-4. (a) Surface top view and (b) cross section view of coating without barrier layer, (c) surface top view and (d) cross section view of coating with barrier layer.

Figure 4.16 and Figure 4.17 show the SEM images of the surface and cross section together with EDS mapping of the coatings without and with 500 nm TiC barrier after 800°C annealing, respectively. As shown in surface top view images, both coatings remain uniform, dense and free of voids and micro-cracks after annealing. A thin interdiffusion zone, mainly diffusion of Al from the coating into the Zircaloy-4 substrate, was observed for the coating without TiC barrier, and the thickness of the diffusion layer is around few hundred nanometers as identified by the EDS mapping (Figure 4.16(c)). In case of coating with barrier (Figure 4.17(b), the Ti_2AlC coating and the TiC barrier layer can be easily distinguished. The TiC layer can effectively prevent the fast inward diffusion of Al into the substrate during annealing as no apparent Al interdiffusion layer at the interfaces was observed as shown by EDS mapping of Figure 4.17(c).

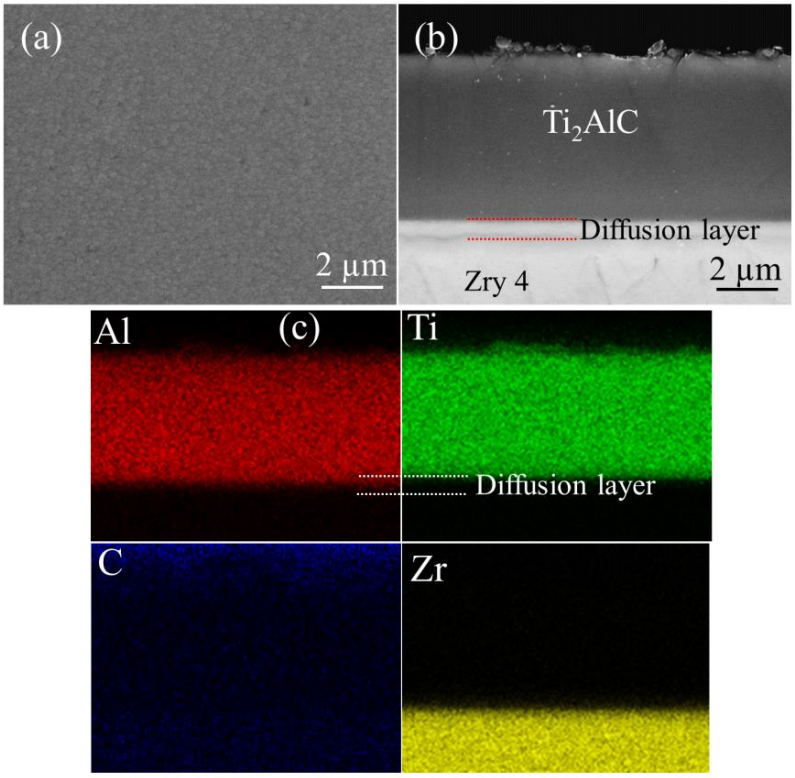

Figure 4.16 SEM images of the Ti_2AlC coating without TiC barrier layer on Zircaloy-4 after 800°C annealing. (a) Surface top view, (b) cross section view and (c) EDS elemental mapping of cross section.

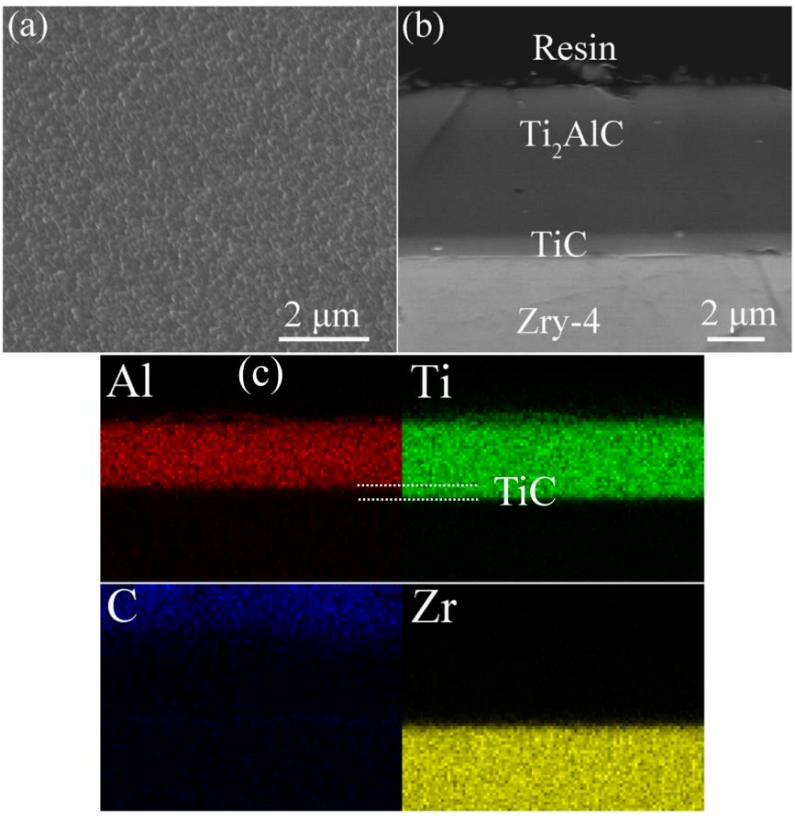

Figure 4.17 SEM images of the Ti_2AlC/TiC coating on Zircaloy-4 after 800°C annealing. (a) Surface top view, (b) cross section view and (c) EDS elemental mapping of cross section.

4.4.1.3 Mechanical properties

Figure 4.18 shows the indentation hardness and reduced Young's modulus with the standard deviation of the uncoated substrate and coated and annealed specimens. The Zircaloy-4 substrate is relatively soft, and the indentation hardness and reduced Young's modulus are 2.8 ± 0.2 GPa and 70.1 ± 7.1 GPa, respectively. The coatings, both the as-deposited and the annealed ones are much stiffer than the substrate. The as-deposited coatings with or without diffusion barrier exhibit similar values; the indentation hardness and reduced Young's modulus are about 8.5 GPa and 120 GPa, respectively. After annealing, both the hardness and modulus roughly doubled, to around 15 GPa for the hardness and 200 GPa for the modulus. The tendency and values were in accordance with those obtained for the annealed coatings on SiO_2/Si substrates.

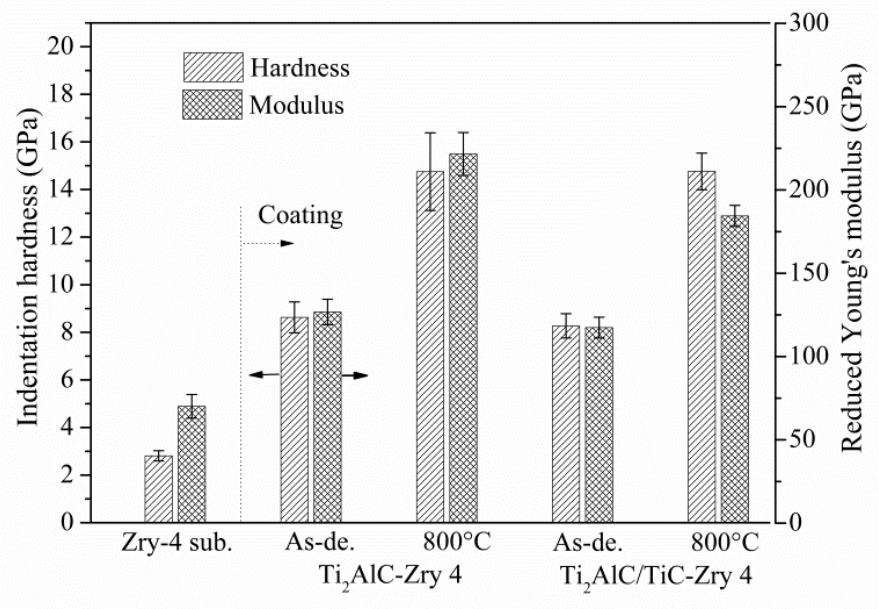

Figure 4.18 Indentation hardness and reduced Young's modulus of bare Zircaloy-4 substrate, coated and annealed samples with and without TiC barrier layer.

Figure 4.19(a) displays the surface morphology SEM images of the coatings after the scratch tests and Figure 4.19(b) shows the critical loads of failure of the coatings in the scratch test. The average minimum scratch load at which the coating is removed and the substrate becomes continuously visible, by adhesive failure, defines the critical load of failure (L_{C2}) [133]. Significant tensile cracking was observed for both coatings, with and without barrier, around the initial failure area. Once the load exceeded the critical value, extensive spallation and delamination of the coatings were observed, demonstrating a brittle failure mode. The average critical load of failure of the Ti_2AlC coatings without TiC barrier was about 50 N, around 20 N higher than that of Ti_2Al/TiC coating (Figure 4.19(c)). The better adherence of Ti_2AlC coatings without diffusion barrier can be attributed to the diffusion of Al from the coating into the substrate resulting in the formation of a strong metallurgical bond at the coating/substrate interface, therefore increasing the interfacial adhesion between the coating and the substrate.

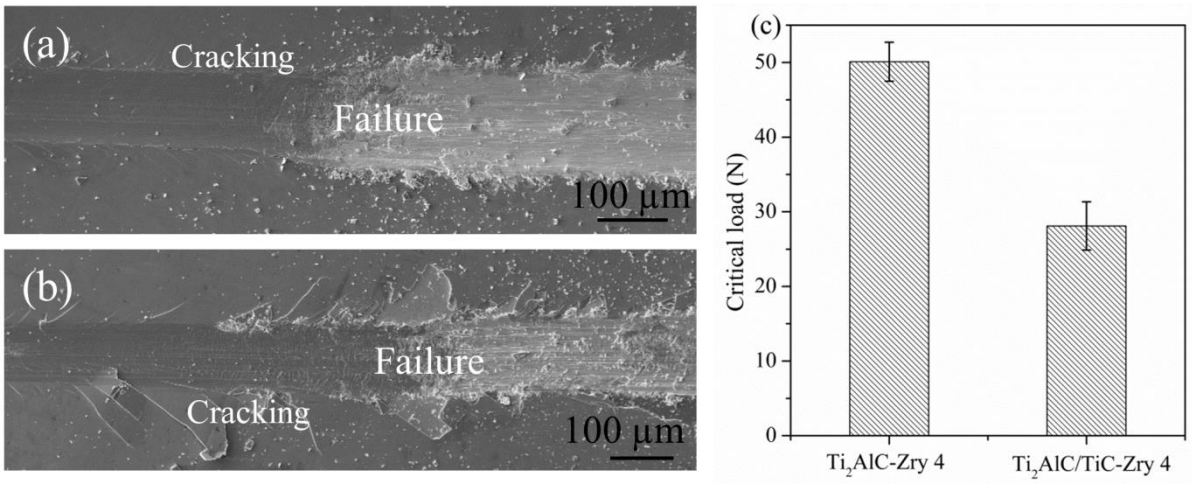

Figure 4.19 Results of scratch tests of Ti_2AlC and Ti_2AlC/TiC coated Zircaloy-4 after annealing. SEM images of surface top views: (a) Ti_2AlC coating, (b) Ti_2AlC/TiC coating, and (c) critical loads of failure of the coatings in the scratch test.

4.4.2 High-temperature oxidation in steam

Isothermal oxidation tests from 800°C to 1200°C in steam of bare Zircaloy-4, coated Zircaloy-4 with or without diffusion barrier after 800°C annealing, and Ti_2AlC bulk ceramic were conducted to investigate their oxidation behavior. Their oxidation performances were evaluated and compared.

4.4.2.1 Post-test appearance

Figure 4.20 presents the general post-test appearance of the coated samples after isothermal oxidation in steam at 800°C for 5 and 250 min, 1000°C for 5 min, and 1200°C for 15 min, respectively. It could be distinguished that 800°C-5 min oxidation of Ti_2AlC coatings and 800°C-5 and -250 min oxidation of Ti_2AlC/TiC coating had not fully consumed the coatings, whereas all other coatings were completely oxidized. The Ti_2AlC coatings with TiC barrier demonstrated obvious better oxidation resistance than those of without TiC barrier. The coatings were quickly consumed, even with just 5 min oxidation, once the temperature reached or exceeded 1000°C as shown in the Figure 4.20. Widespread cracks, spallation and delamination were observed in case of fully oxidized coatings.

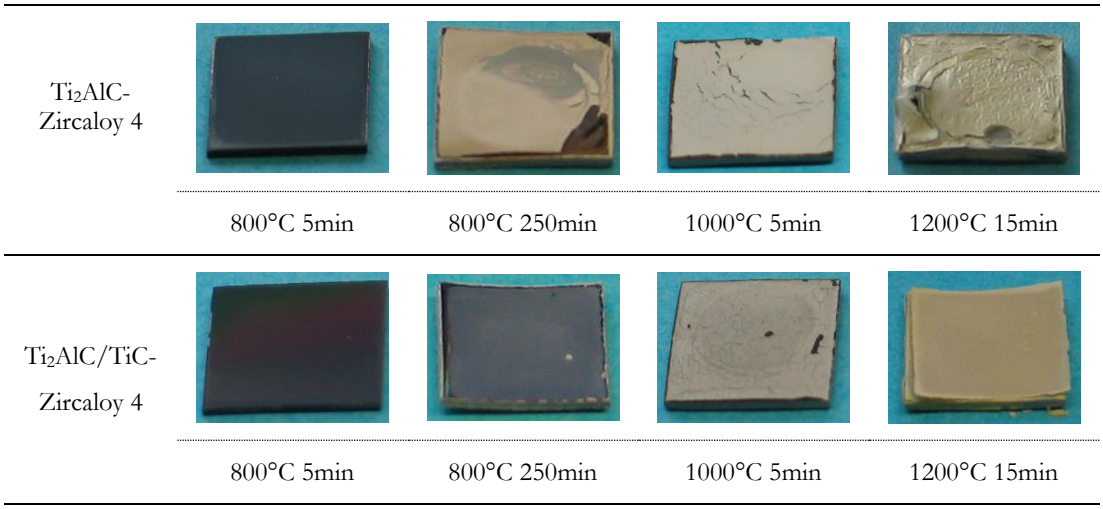

Figure 4.20 Digital images showing post-test appearance of the coated samples after isothermal oxidation in steam at different temperatures and times.

4.4.2.2 Oxidation kinetics

Figure 4.21 shows the oxidation kinetics of the polished Zircaloy-4 substrate, Ti_2AlC and Ti_2AlC/TiC coated Zircaloy-4 and bulk Ti_2AlC at 800°C up to 250 min in steam. The dashed lines display the fitting results of the mass gain versus oxidation time curves using two different oxidation rate laws, i.e. cubic and parabolic, within selective time intervals. Generally, the oxidation kinetics of uncoated Zircaloy-4 obeyed a cubic law during the whole exposure up to 250 min. Parabolic kinetics were found for the coated Zircaloy-4 during initial oxidation and for the bulk Ti_2AlC ceramic as shown by the fitting dashed lines. The mass gains of the coated Zircaloy-4 were significantly lower during the initial stage of exposure compared to uncoated samples. However, the oxidation rate of Ti_2AlC coated Zircaloy-4 was about two times faster than that of Ti_2AlC/TiC coated Zircaloy-4 before the exposure time reached 100 min. The Ti_2AlC/TiC coated Zircaloy-4 exhibited a mass gain rate very similar to that of bulk Ti_2AlC up to around 150 min. Then the oxidation kinetics shifted to a much faster rate for both coatings with and without barrier. The initial period with slower oxidation rate was significantly shorter and the oxidation rate after the turning point was obviously faster for the Ti_2AlC coated Zircaloy-4 than for that with TiC barrier. This difference is caused by the quick consumption of the coatings without TiC barrier exposing the fresh surface of the Zircaloy-4 substrates and faster oxidation rate of the uncovered edges of the samples with TiC barrier, respectively, which will be explained later. The Ti_2AlC/TiC coated Zircaloy-4 showed significantly improved oxidation resistance during oxidation at 800°C for 250 min in steam with several times lower mass gain than that of bare Zircaloy-4.

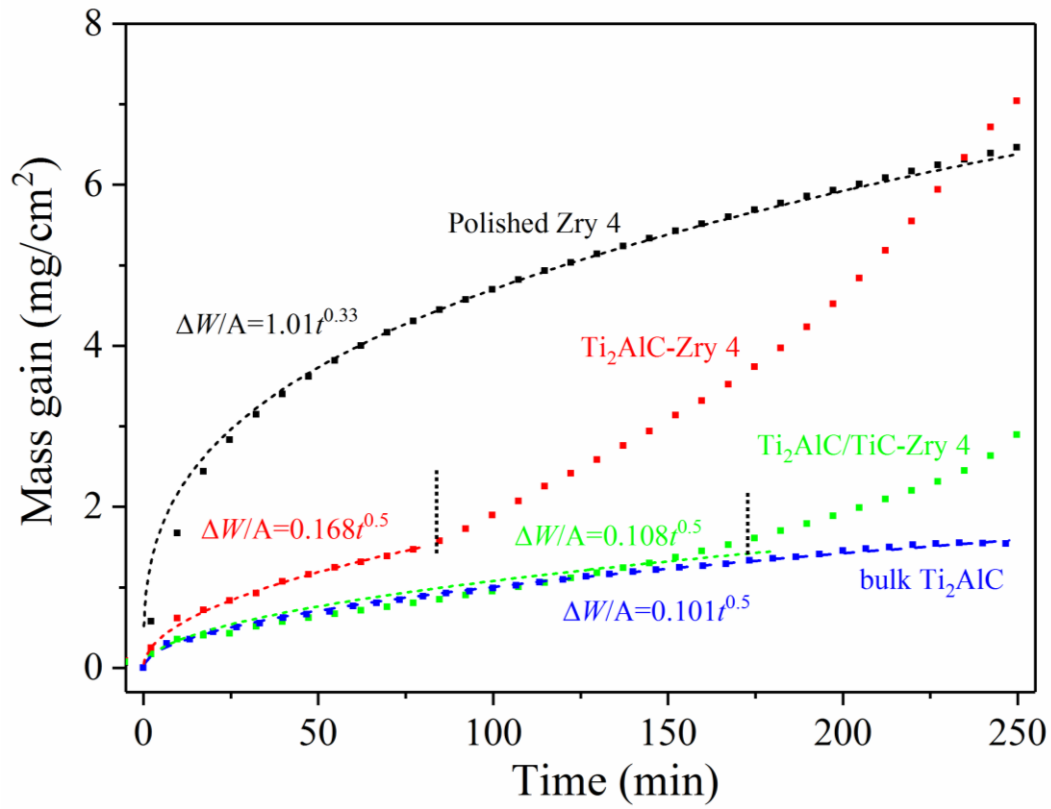

Figure 4.21 Oxidation kinetics of bulk Ti_2AlC, polished Zircaloy-4 substrates, and Ti_2AlC and Ti_2AlC/TiC coated Zircaloy-4 at 800°C in steam. The dashed lines are fitting results of the oxidation rate. The vertical dotted lines indicate the turning point of oxidation rate of the coated Zircaloy-4 samples during oxidation and the fitting limits.

The oxidation kinetics of the bare and coated Zircaloy-4 samples at 1000°C and 1200°C in steam are shown in Figure 4.22. The oxidation rate of the coated Zircaloy-4 samples, either with Ti_2AlC or Ti_2AlC/TiC coatings, did not show any noticeable reduction compared to the uncoated samples. Their initial oxidation rates are comparable or even a little bit higher for coated samples. This reflects that the coatings were rapidly consumed at a temperature reaching and beyond 1000°C. At 1000°C, the oxidation kinetics of polished Zircaloy-4 first obeyed a parabolic law, and then changed to a linear law at around 150 min. The transition is caused by so called breakaway oxidation (due to cracking of ZrO_2 scale), which is well known for zirconium alloys at temperatures below 1050°C [24]. The sample was observed to be fully oxidized at around 240 min (Figure 4.22(a)) and the mass gain remained then constant. The oxidation kinetics of coated Zircaloy-4 samples roughly followed a parabolic law during the whole exposure up to 250 min. However, the coated samples were not completely oxidized and exhibited slightly lower mass gains at the end of exposure. This improvement seems mainly due to the delay or the absence of the transition to breakaway oxidation of coated Zircaloy-4 samples. Oxidation at 1200°C resulted in a parabolic law for both the bare and coated Zircaloy-4 samples. The mass gain of the coated sample with TiC barrier was slightly lower than that of the sample without barrier. Different from the coatings, bulk Ti_2AlC demonstrated an extremely low mass gain (1.06 mg/cm^2 - 250 min oxidation at 1200°C), almost two magnitudes lower than those of coated Zircaloy-4 samples. The mass gain at 1200°C was even lower

than that at 1000°C (1.47 mg/cm² - 250 min), suggesting that high-temperature oxidation of bulk Ti_2AlC promoted the selective oxidation of Al to form a protective α-Al_2O_3 scale [45].

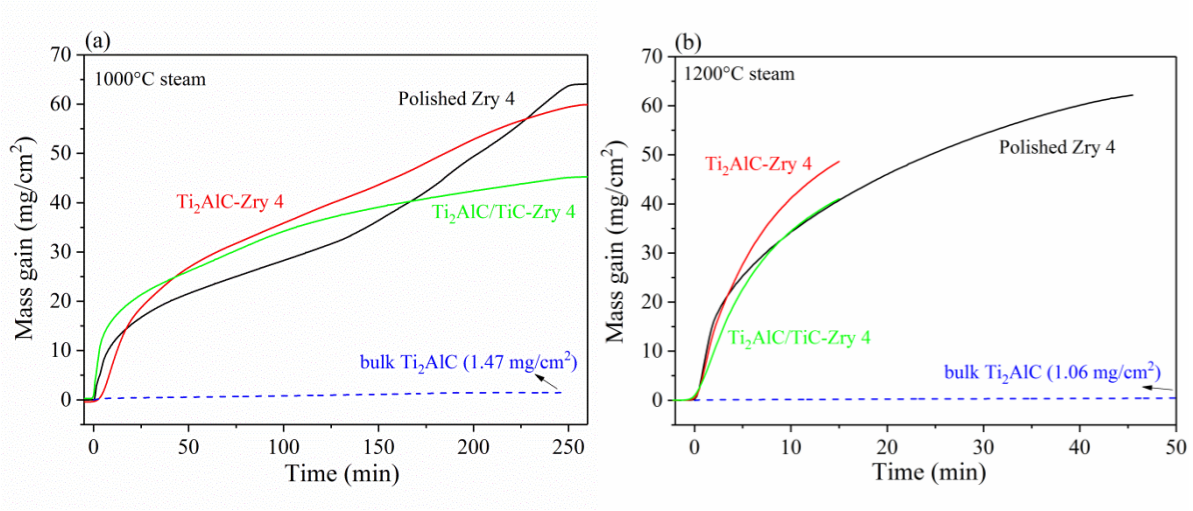

Figure 4.22 Oxidation kinetics of bulk Ti_2AlC, polished Zircaloy-4 substrates, and Ti_2AlC and Ti_2AlC/TiC coated Zircaloy-4 at (a) 1000°C and (b) 1200°C in steam.

4.4.2.3 Phase composition of the oxide scale

Phase composition of the oxide scales formed on the surface of coated Zircaloy-4 substrates after 800°C oxidation for different times identified by XRD is shown in Figure 4.23. The diffraction signals originated from the substrate (Zr) and un-reacted Ti_2AlC coating were clearly seen after 5 min oxidation for both coated samples. Two different oxidation products were detected: rutile (TiO_2) and metastable alumina (θ-Al_2O_3). The intensities of diffraction peaks correlated to rutile decreased for the Ti_2AlC coatings with oxidation time from 5 to 250 min, and monoclinic ZrO_2 phase was additionally observed after 250 min oxidation. Correspondingly, the Ti_2AlC phase disappeared. This was due to the complete consumption of the Ti_2AlC coating during long-term oxidation followed by partial spallation (confirmed by cross-sectional examination later). The intensities of diffraction peaks correlated to rutile increased considerably for the Ti_2AlC/TiC coatings with increasing oxidation time, and the signals assigned to Ti_2AlC still existed with high intensity at 250 min. Thus, the Ti_2AlC/TiC coatings have not been completely oxidized after exposure at 800°C for 250 min.

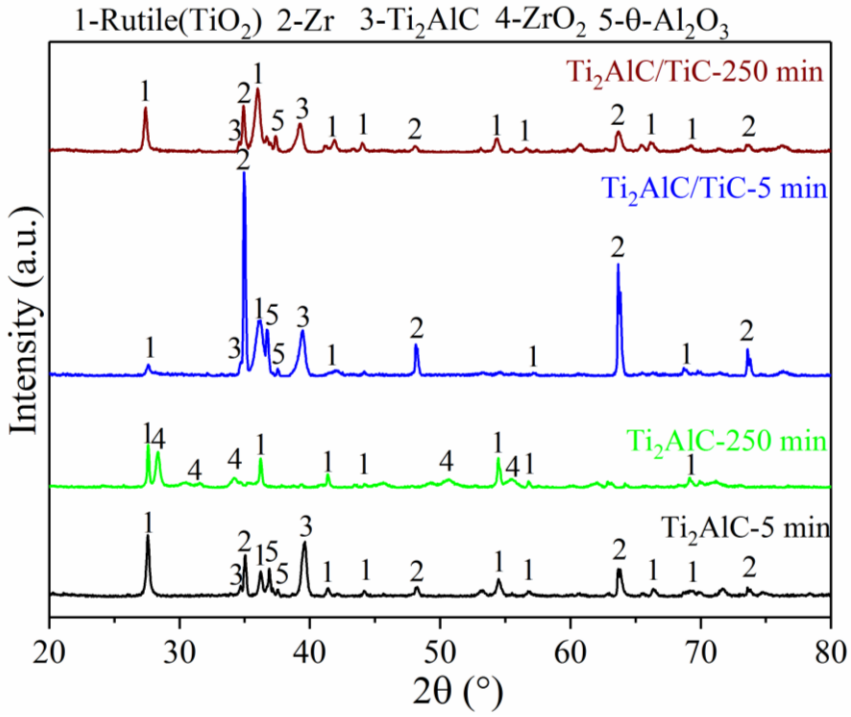

Figure 4.23 XRD patterns of oxide scales formed on the surface of Ti_2AlC and Ti_2AlC/TiC coated Zry-4 samples after oxidation at 800°C in steam for 5 and 250 min.

To further confirm the oxidation products on the surface of the coatings, XPS measurements were conducted on the coatings after oxidation at 800°C for 5 min. The XPS spectra of Ti, Al and O binding energies of the Ti_2AlC/TiC coatings are displayed in Figure 4.24. The peak fitting results for the various species are shown in the figure. Two different states of Ti and Al were found, corresponding to the oxidation products and the beneath Ti_2AlC coating. The Ti $2p_{1/2}$, Ti $2p_{3/2}$ and Al 2p peaks located at around 465.0 eV, 458.8 eV and 73.8 eV, respectively, are identified as binding energies of oxidation products rutile (R-TiO_2) and metastable θ-Al_2O_3 compared with the values reported in the literature [193]. The absence of bonds characteristic of anatase (A-TiO_2) and α-Al_2O_3 is coincident with previous reports, i.e. one is stable at low temperature (<700°C) and the other one usually starts to grow beyond 900°C [135]. The signals of Ti $2p_{1/2}$ at 460.1 eV and Al 2p at 71.0 eV with a substantially lower intensity are attributed to unoxidized Ti_2AlC coating. Therefore, the O1s band can be deconvoluted into two parts, indicating a peak at 530.0 eV (characteristic of the binding energy of O in rutile) and another peak at 530.8 eV (characteristic of the binding energy of O in θ-Al_2O_3). The intensity of the signals of O and Al in the alumina-type curve is several times higher than that of O and Ti in the rutile-type curve. The observations suggest that the surface is composed of a mixture of rutile and θ-Al_2O_3 phases with the θ-Al_2O_3 being as the main component at the initial stage of oxidation.

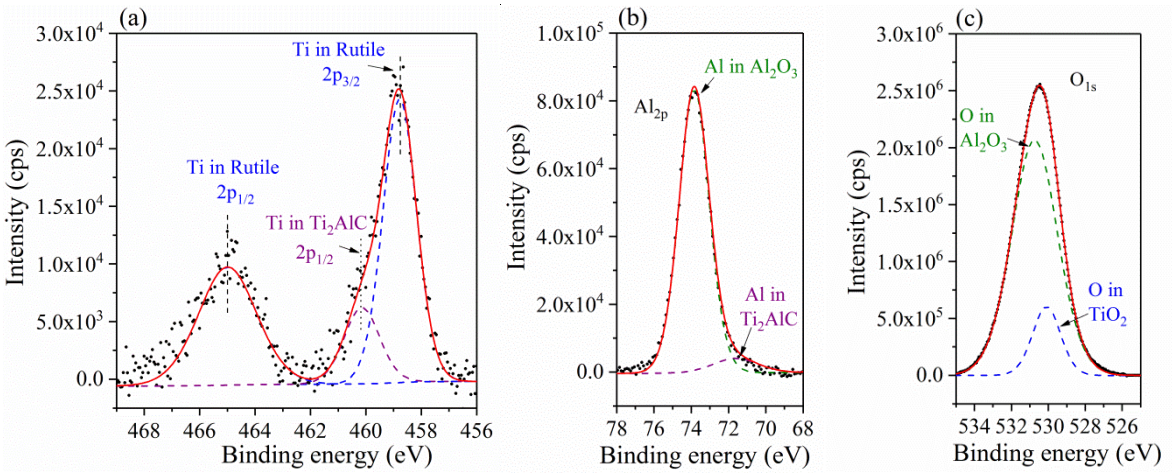

Figure 4.24 XPS spectra of Ti_2AlC/TiC coating on Zircaloy-4 substrate after oxidation at 800°C for 5 min in steam. (a) Ti, (b) Al, (c) O. The dark points are original data. The red solid curves are overall fitting results. The dashed lines are fitting peaks corresponding to different states of various species.

4.4.2.4 Microstructural evolution during oxidation

Figure 4.25 shows the SEM images of typical surface morphologies of Ti_2AlC and Ti_2AlC/TiC coated Zircaloy-4 together with bulk Ti_2AlC after oxidation at 800°C in steam for different periods. The surface morphologies were similar for the coated samples after short time oxidation (Figure 4.25(a) and (c)). Two different types of grains, fine whiskers and angular plates, were observed, and the volume content of each type of grains changed in dependence of the oxidation time. Based on the XRD results and previous studies [103,135], the whisker and angular plate grains can be assigned as θ-Al_2O_3 and rutile, respectively. A higher volume content of whisker grains, on the surface of Ti_2AlC coatings was observed than that on Ti_2AlC/TiC coatings. The Ti_2AlC coating was fully consumed after 250 min oxidation and partially spalled off (Figure 4.25(b)). The underneath Zircaloy-4 substrate was exposed showing a smoother surface with granular grains. On the contrary, the Ti_2AlC/TiC coating persisted adhesive after 250 min oxidation and many round-shaped crystals appeared on the surface. The coatings retained their integrity without spallation or formation of cracks before being completely oxidized; however, the surface oxide layer was porous, and some voids and pores existed. Concerning the bulk Ti_2AlC, it can be seen in Figure 4.25(e) that the size of the fine whisker and angular plate grains on the surface was considerably smaller than that on the coatings.

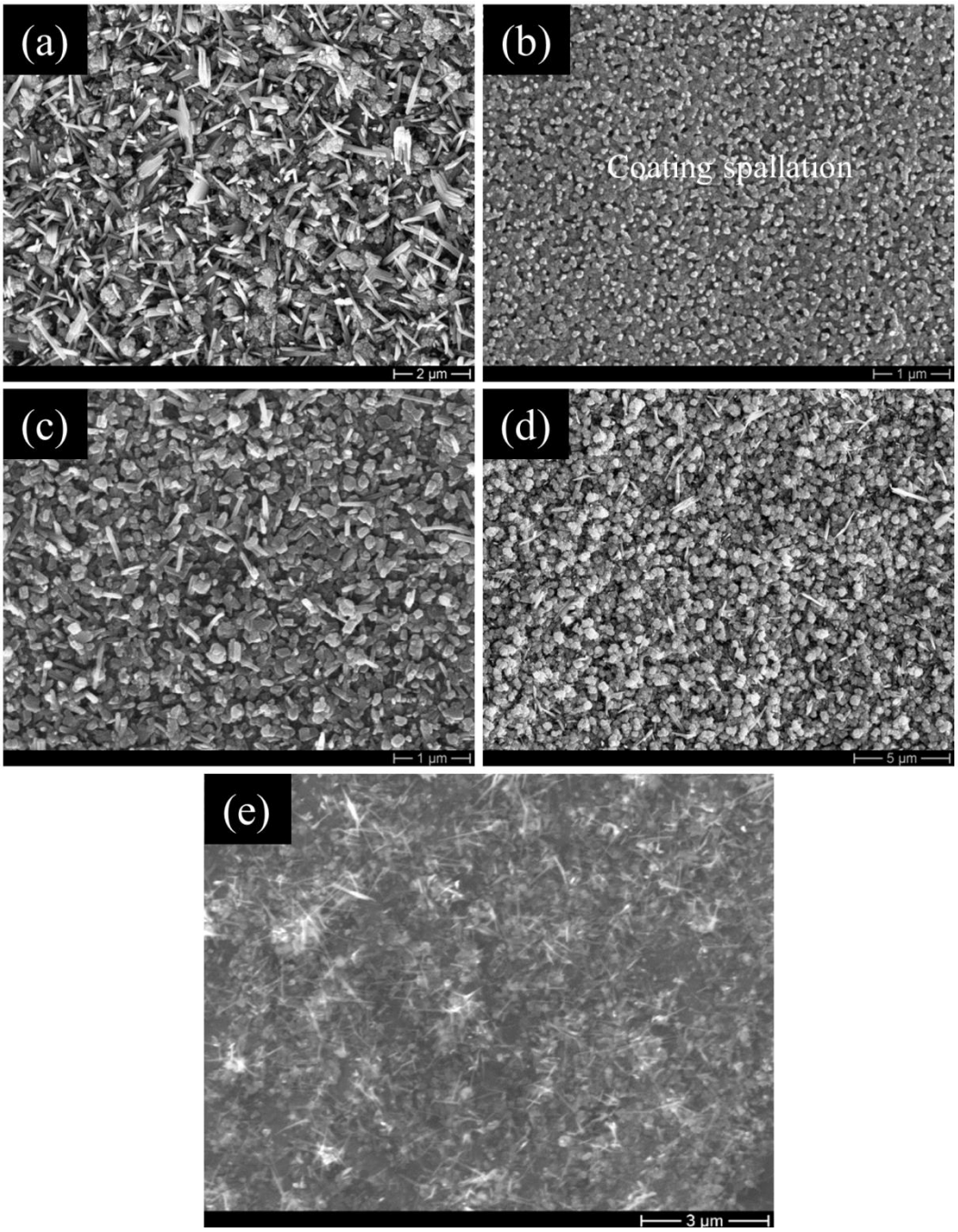

Figure 4.25 SEM images of typical surface morphologies of coated Zircaloy-4 and bulk Ti_2AlC after oxidation at 800°C in steam. Ti_2AlC coated Zircaloy-4 after oxidation for (a) 5 and (b) 250 min, Ti_2AlC/TiC coated Zircaloy-4 after oxidation for (c) 5 and (d) 250 min, (e) bulk Ti_2AlC after oxidation for 250 min. The surface of bulk Ti_2AlC is shown here as reference.

Figure 4.26 shows the cross-sectional SEM images with corresponding EDS elemental mapping of the coatings after oxidation at 800°C in steam for 5 min. Dissimilar oxide layer arrangements were observed for the coatings with and without TiC barrier. For the coatings without barrier, the oxide scale demonstrated a double-layered structure. The external oxide layer was an Al_2O_3-rich layer with certain amount of TiO_2; the internal oxide layer was a TiO_2 layer with trace of Al_2O_3 as shown in Figure 4.26(a). The Al_2O_3-rich layer was relatively dense compared to the TiO_2 layer which contained micropores. Only

one Al_2O_3-rich layer was observed for the coating with TiC barrier (Figure 4.26(b)). The total thickness of the oxide layer on the Ti_2AlC coating was around 3 times thicker than that on the Ti_2AlC/TiC coating. Diffusion of Al from the coatings into the Zircaloy-4 substrate was seen for both coatings as illustrated by the dashed lines in the EDS mapping images; however, only limited diffusion was shown for the coating with TiC barrier, while the diffusion for the coating without TiC barrier was substantially more pronounced.

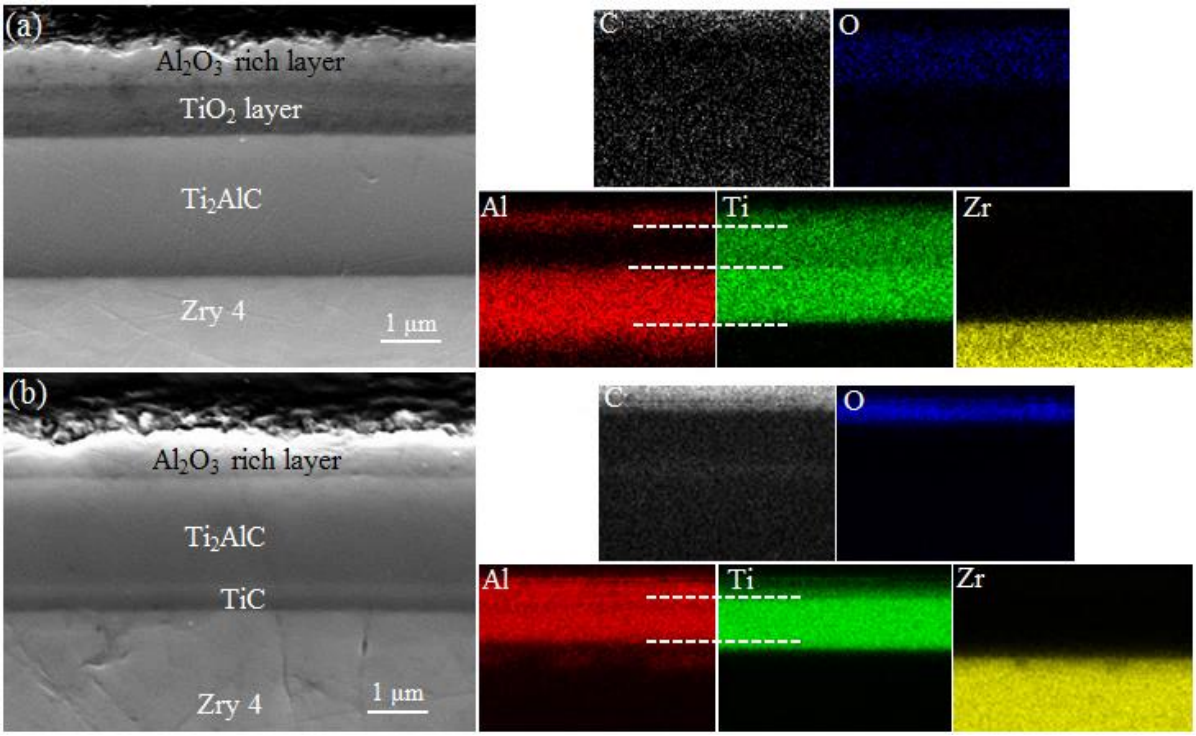

Figure 4.26 Cross-sectional SEM images and corresponding individual EDS elemental mapping after oxidation at 800°C in steam for 5 min. (a) Ti_2AlC and (b) Ti_2AlC/TiC coated Zircaloy-4.

After 250 min oxidation at 800°C, the uncoated Zircaloy-4 sample was oxidized forming an oxide layer of around 60 μm thick as shown in Figure 4.27(a). The Ti_2AlC coating was fully consumed at these conditions (Figure 4.27(b)). Partial spallation of the fully oxidized coating occurred. The underneath substrate was oxidized on both sides; the oxide layer was significantly thicker (~40 μm) for the side where the coating spalled off than that of the other side (~10 μm) where the coating was loosely adherent. The thinner oxide layer on the undetached area implied that the fully consumed coating could still act as a diffusion barrier to suppress the fast penetration of oxidizing gas into the substrate. An important finding is that the Ti_2AlC/TiC coatings away from the edge maintained intact and adhesive; it was only partially consumed after 250 min oxidation at 800°C as shown in Figure 4.27(c). On the other hand, it can be obviously observed that the uncoated edges of Zircaloy-4 substrate were aggressively oxidized. The steam penetrated the matrix of the substrate along the edges, leading to the premature failure of the coating at this region (Figure 4.27(c)). It can be assumed that the slightly faster oxidation rate of Ti_2AlC/TiC coated Zircaloy-4 compared to bulk Ti_2AlC after 150 min in Figure 4.21 is largely due to the fast oxidation of edge areas.

The cross section of samples after oxidation at 800°C for 250 min were also checked by SEM and the images with the EDS elemental mapping are shown in Figure 4.28. The completely oxidized Ti_2AlC coatings resulted in a triple-layered oxide structure (Figure 4.28(a)): relatively dense Al_2O_3-rich layers located at the gas/coating interface and the coating/substrate interface, which was separated by a porous TiO_2 layer in the middle, indicating two-directional diffusion of the Al in the coating. The oxide layer formed on the Ti_2AlC/TiC coating was similar to that of the Ti_2AlC coating after oxidation for 5 min shown in Figure 4.26(a). The surface was an Al_2O_3-rich layer followed by a porous TiO_2 layer beneath. However, there was a slight difference observed, i.e. a nearly pure Al_2O_3 layer emerged between the Al_2O_3-rich layer and TiO_2 layer as shown by the mapping. Nearly 2.5 μm thick Ti_2AlC remained after 250 min oxidation. Both the gas/coating interface and the coating/substrate interface became rough, illustrating the outward diffusion of cations and inward diffusion of anions occurred simultaneously. The Al in the Ti_2AlC coating penetrated through the TiC diffusion barrier generating a thick diffusion zone during the long exposure, and no obvious diffusion of Ti and Zr was confirmed (Figure 4.28(b)).

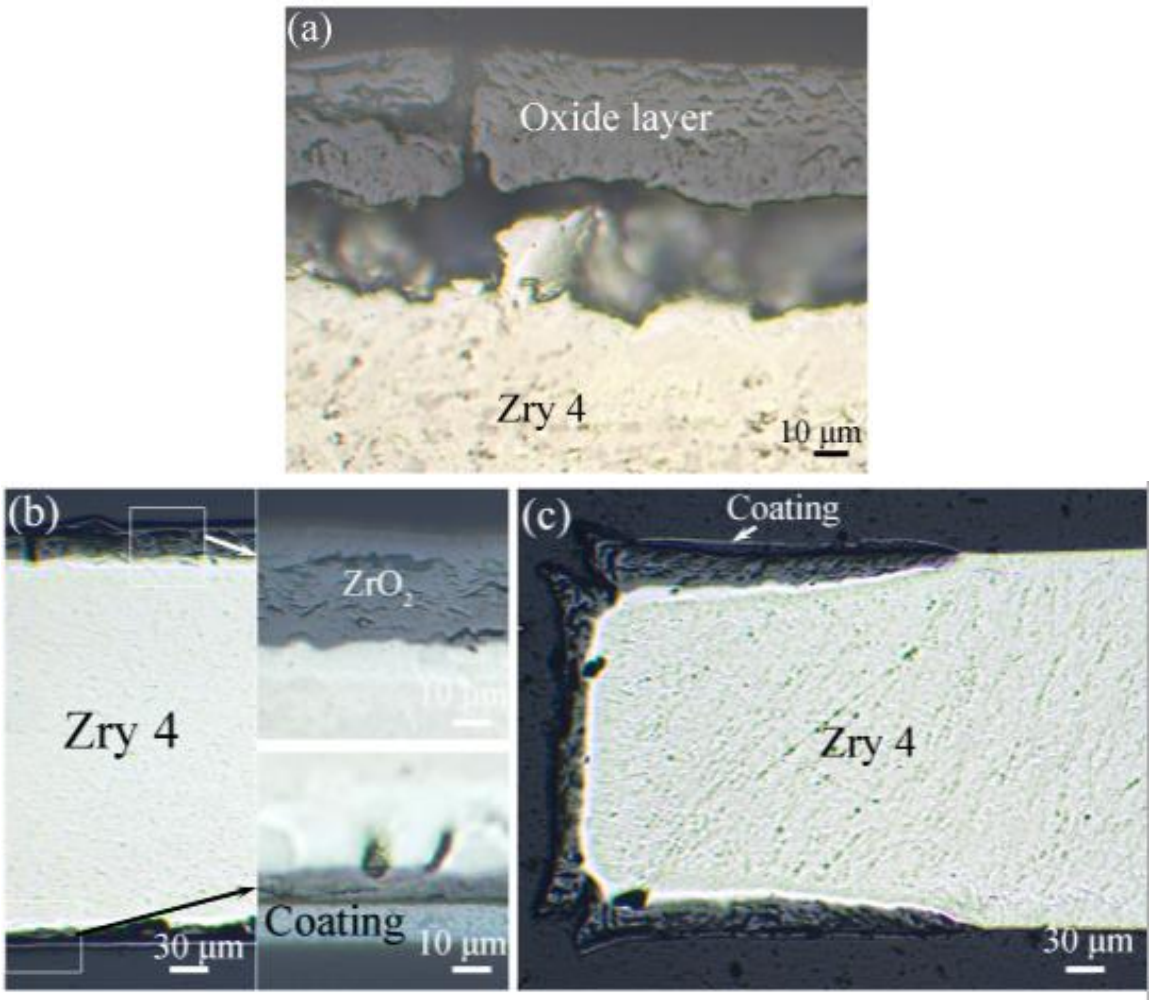

Figure 4.27 Optical images of typical cross sections after oxidation at 800°C in steam for 250 min, (a) uncoated Zircaloy-4 substrate, (b) Ti_2AlC and (c) Ti_2AlC/TiC coated Zircaloy-4 samples.

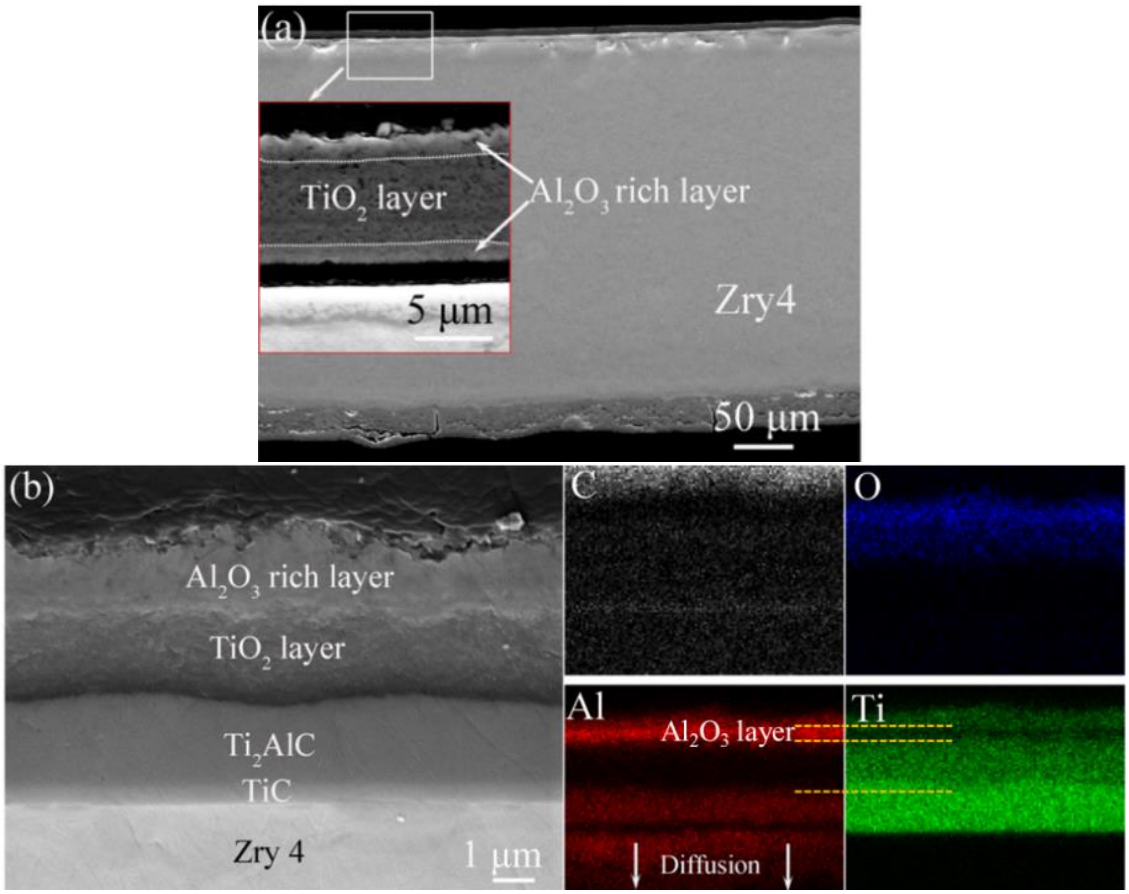

Figure 4.28 SEM images of typical cross sections after oxidation at 800°C in steam for 250 min. (a) Ti_2AlC and (b) Ti_2AlC/TiC coated Zircaloy-4 with corresponding EDS elemental mapping.

Similar microstructures were observed for the coatings oxidized at higher temperatures, 1000°C and 1200°C; a typical example is shown in Figure 4.29. Even after oxidation at 1000°C for just 5 min, complete oxidation of the coatings was confirmed. The coatings underwent severe cracking and delamination. Consequently, the underneath Zircaloy-4 substrates were seriously attacked by steam resulting in a porous, cracked and hence non-protective ZrO_2 layer.

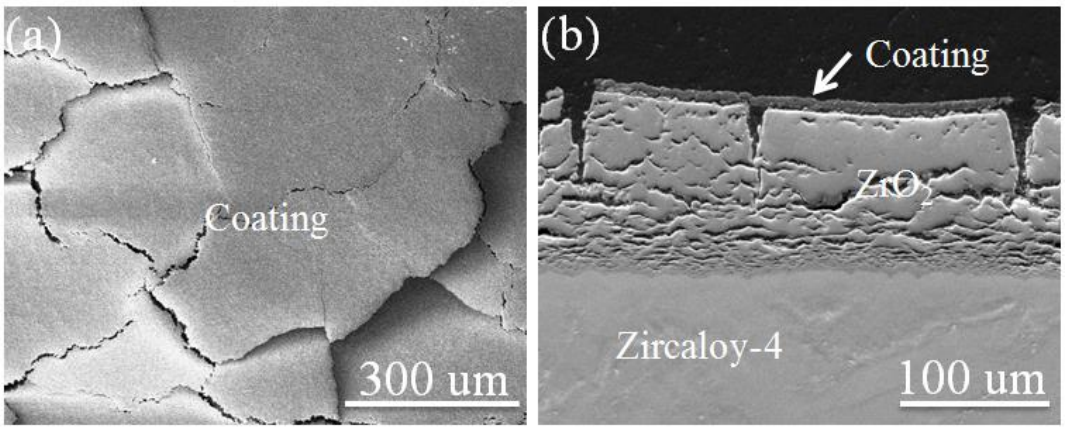

Figure 4.29 SEM images of Ti_2AlC/TiC coated Zircaloy-4 after oxidation at 1000°C in steam for 5 min. (a) Top surface view and (b) cross-sectional view.

4.5 Discussion

4.5.1 Synthesis of Ti_2AlC MAX phase coatings

The crystal structure of MAX phases can be described as nearly-close-packed M layers with the X atoms filling the octahedral sites which are periodically interleaved by group-A elemental layers [61]. The large unit cells determine their long *c*-axis characteristic, being around 13 Å for M_2AX phases [73]. Hence, it has been well acknowledged that sputter-growth of MAX phase films requires significant thermal activation to enable sufficient mobility and energy for the desired atomic arrangement [63,67,83,152,170]. Lower deposition temperatures usually result in the formation of competing carbides and/or intermetallic phases. When it comes to Ti_2AlC coatings deposited by PVD, the most common temperature reported previously for the formation of MAX phase was equal to or higher than 800°C [79,152,153,158,176], by depositing from one target or simultaneously from multiple targets. This work demonstrates that the crystalline transition from the non-MAX competing phases to Ti_2AlC MAX phase formation can be reduced to temperature of approximately 660°C through the adoption of elemental nano-layered stacks and subsequent thermal annealing. This lower crystallization temperature of the MAX phase is likely attributed to nanoscale effects, such as higher surface activity and shorter diffusion length in nanoscale and nanocrystalline materials. In addition, the as-deposited reactive multilayer thin films are a form of energetic material that consists of a well-defined, heterogeneous structure and stored chemical energy [180]. The stored chemical energy can be released to prompt a self-propagating exothermic reaction via stimulation by an external source, e.g thermal annealing. Thus, the required annealing temperature to form MAX phase can be further reduced. The relatively lower-temperature synthesis realized in this work appeals for synthesis of Ti_2AlC MAX phase onto temperature-sensitive substrate materials.

In this study, a reaction path for the formation of Ti_2AlC MAX phase coating has been demonstrated similar to the synthesis of bulk Ti_2AlC ceramic using a stoichiometric mixture of Ti, Al and graphite powder [194–196]. As shown by the XRD and TEM observations, first Al reacts with Ti to form intermetallic phases, and the diffusion and reaction between the residual Ti and C produces non-stoichiometric TiC_x. In a second step (starting from around 660°C), the reaction between the intermetallic and the TiC_x results in the formation of the Ti_2AlC MAX phase. It is necessary to note that the reaction path for the formation of the Ti_2AlC MAX phase by annealing of elemental layers in our study shows distinct deviation from previous investigations on deposition synthesis of Ti_2AlC through *in-situ* heating of the substrates. Deposition with *in-situ* heating at elevated temperature can successively lead to the formation of cubic (Ti,Al)C, then perovskite carbide Ti_3AlC, and finally the Ti_2AlC MAX phase with increasing substrate temperature [79,152,176]. Maintaining the substrate temperature at a certain level during deposition allows for a sufficient diffusion of each element to form the corresponding stable phase. However, in this study an annealing was applied after the deposition process and the annealing period is considerably shorter. The specific arrangement of the elemental multilayer stacks can support the thermodynamically preferred reaction of Al with Ti to form the Ti-Al intermetallic phase. Adjusting the

multilayer nanoscale architecture according to the desired stoichiometry of the final MAX phase and taking into account mutual diffusion of the individual elements (as well as the heat of formation of the various phases and compounds) offers a new tool for tailor-made synthesis of MAX phase materials. One challenging issue during the synthesis of MAX phase coatings is to obtain high purity MAX phases. A relatively narrow window of the composition close to the stoichiometry is a prerequisite for the synthesis of a homogenous MAX phase, where a small deviation from the stoichiometry results in impurity phases or even unwanted third phases. A small amount of impurity phases, often binary carbides, have been proved to reduce the performance of the coatings, such as oxidation resistance [175] and electrical conductivity [79]. Sputtering from one compound target usually results in off-stoichiometric composition of the films, often deviating strongly from that of the target. The use of three elemental targets to deposit elemental multilayers has advantages of providing more flexible and powerful control of each elemental flux. Phase pure MAX phases can be obtained by subsequent annealing of this elemental multilayer system.

Previous studies on magnetron sputtering of MAX phase coatings mainly focused on epitaxial growth of MAX phase thin films on the single crystal substrates, like MgO(111) [154,160,174,197] and Al_2O_3(0001) [79,152,172]. Basal-plane-oriented growth of MAX phase films is typically obtained due to the small mismatch of lattice parameters between the film and the substrate. Growth of MAX phases on amorphous or polycrystalline substrates usually leads to coatings with non-oriented polycrystalline microstructure [158,161]. It is worth to mention that the Ti_2AlC MAX phase coatings after annealing at 800°C in this study show a (00l) basal plane preferred-orientation. It is well-accepted that at the initial stage of crystallization nuclei of randomly distributed orientation form; however, the morphology is determined by the relative growth rates of all possible orientations [112]. The crystallographic face with the lowest growth rate will determine the orientation of the grains. It has been demonstrated that the growth rate along the *c*-axis is much lower than that of *a*-axis for the MAX phases [198]. Another possible explanation is that the (00l) surface may have the lowest surface energy, which appeals to terminate on the grain surface [199]. Additionally, the specific nanoscale multilayer architecture seems to play a crucial role in the induction of a preferential texture of the MAX phase coatings. The shorter diffusion lengths in longitudinal direction as well as a spatial elemental composition close to the ideal stoichiometry within each multilayer stack allow a higher growth rate in the lateral direction. Thus, the MAX phase grains align with their *c*-axis, i.e., the [00l]-direction, perpendicular to the sample surface. Above effects result in the growth of the Ti_2AlC grains with *c*-axis normal preferred orientation, and similar behavior has been observed sometimes in the preparation of bulk MAX phase ceramics [63,73].

4.5.2 Oxidation of Ti_2AlC MAX phase coatings in steam

Despite phase-pure and dense Ti_2AlC coatings were successfully obtained in this study, however, the coatings presented distinctive and more complex oxidation behavior compared to bulk MAX phase materials. In addition, the superior oxidation resistance of bulk Ti_2AlC was not inherited by the magnetron-sputtered Ti_2AlC coatings herein.

Oxidation of bulk Ti_2AlC at temperature below 700°C leads to an anomalous oxidation with relatively high oxidation rate due to the formation of non-protective scales consisting of anatase and rutile [135]. At elevated oxidation temperatures, the oxide scale consists of a double-layer structure: an outer discontinues TiO_2 (rutile) layer and an inner alumina layer. Metastable polymorphs of alumina (like γ-, θ- Al_2O_3) mainly grow at temperature lower than 900°C; higher temperatures promote the growth of a dense, adherent α-Al_2O_3 layer. The oxidation mechanism for the growth of a double-layer scale on the surface of bulk Ti_2AlC can be explained by initial transient oxidation, and subsequent selective oxidation of Al [45,140].

The Ti_2AlC coatings without TiC barrier in this study also form a scale with two sub-layers before being completely consumed after oxidation at intermediate temperature (800°C). However, contrary to the scale formed on the bulk, the surface layer is a metastable Al_2O_3-rich layer mixed with TiO_2 and the inner porous layer is TiO_2 (rutile) with traces of Al_2O_3. A similar structure but with slight differences of the oxide scale in the case of coatings with TiC barrier, i.e. a nearly pure alumina layer is detected between these two layers after oxidation at the same temperature. Compared with bulk Ti_2AlC, the dissimilar scaling behavior of the coatings can be attributed to various factors, like microstructure and thickness of the coatings as well as the interaction between the coating and the substrate. At the initial stage of oxidation, both TiO_2 and Al_2O_3 can simultaneously nucleate on the surface of the samples. Even though the formation of Al_2O_3 is thermodynamically favored, it has been proved that the growth kinetics of TiO_2 is much faster than that Al_2O_3 at low temperature and high oxidant partial pressure [140]. The grains are usually coarse in Ti_2AlC bulk ceramic. On the contrary, it has been demonstrated that the coatings obtained in this study are nanocrystalline with an abundance of grains and boundaries. As a result, TiO_2 will grow preferentially on the surface of bulk Ti_2AlC as Ti represents the main constituent. In terms of coatings, the outward diffusion of Al is supposed to be considerably enhanced due to the numerous grain boundaries as well as the unique layered structure of MAX phases resulting in fast migration rate of the A elements [200]. Therefore, an Al_2O_3-rich layer grows on the surface of the coatings during initial transient oxidation stage.

Continued oxidation will decrease the oxidant chemical potential (or partial pressure) at the oxide scale/substrate (Ti_2AlC bulk or coating) interface, promoting the selective oxidation of Al due to a much lower oxygen pressure needed for the formation of alumina. The Ti_2AlC bulk ceramic can act as a huge Al reservoir to provide adequate aluminum for producing a continuous Al_2O_3 layer. For alumina-forming materials, breakaway oxidation occurs once the Al content is below the critical minimum aluminum content due to the continuing consumption of the Al, resulting in a catastrophic breakaway oxidation by formation of non-protective matrix-based scales. This phenomenon has been well documented for FeCrAl-based alloys [201]. Recently the breakaway oxidation of Ti_3AlC_2 MAX phase (Ti_2AlC counterpart) at 1100°C in air has been investigated, and the corresponding critical Al content is proved to be around 6% lower than the initial content [202]. The specimen thickness has a profound effect on the time to breakaway oxidation; longer lifetime can be achieved by increasing the thickness to supply more Al. The coatings investigated here are only 5 μm thick; hence, only a limited amount of Al can be supplied. Fast diffusion of Al from the Ti_2AlC coatings without TiC diffusion barrier into the substrate quickly depletes

the Al content in the coatings, probably leading rapidly to Al content lower than the corresponding critical value. Consequently, further oxidation also produces mixed oxides of Al_2O_3 and TiO_2. For the Ti_2AlC/TiC coatings, even though the diffusion of Al into the substrate is unavoidable, the diffusion rate is suppressed by the presence of the TiC barrier. The relatively high Al content in the Ti_2AlC/TiC coatings enables successful establishment of a pure Al_2O_3 layer beneath the transient oxide layer, resulting in a better oxidation resistance compared to that of Ti_2AlC coatings without TiC barrier layer. The formation of an inner porous TiO_2 layer can be understood by two steps: (1) outward diffusion of Al from the coatings in two directions first leaves a Ti_2C layer beneath the oxide scale; (2) inward diffusion of oxidant through the Al_2O_3-rich layer oxidizes the Ti_2C layer to first form probably a TiC_xO_{1-x} phase [190,203], then TiO_2 and carbon oxide gases by following overall equations:

$$Ti_2C(s) + 5H_2O(g) = 2TiO_2 \text{ (rutile, s)} + 5H_2(g) + CO(g) \quad (4\text{-}1)$$

$$Ti_2C(s) + 6H_2O(g) = 2TiO_2 \text{ (rutile, s)} + 6H_2(g) + CO_2(g) \quad (4\text{-}2)$$

The Al-depleted hexagonal unit can shrink accompanied by a large reduction of volume and the Ti_2C slabs can relax to form stable TiC_x ($0.47<x<1$) before oxidation as observed during the decomposition of Ti_3SiC_2 thin films [82]. Oxidation of TiC at high temperature also produces a porous TiO_2 scale [204], hence, it can be expected that the TiO_2 layer contains a large quantity of pores. It seems that the aluminum cations can diffuse through this porous TiO_2 layer, and then precipitate as alumina beneath the scale formed during the transient oxidation stage. Similar behavior has been reported previously during oxidation of bulk Ti_3AlC_2, $Ti_2AlC_{0.5}N_{0.5}$ [205], and Ti_2AlN [206]. One explanation is that the relatively low oxidation temperature (800°C here) decreases the reaction kinetics between the outward diffusion of aluminum cations and inward diffusion of oxidant anions providing the aluminum cations time to migrate out [200]. With the oxidation temperature increasing to 1000°C, both the oxidation rate and the diffusion of Al into the substrate become much faster. Thus, both coatings are supposed to be rapidly consumed due to the low thickness together with growth of a porous oxide scale. Another factor leading to the fast failure of the coatings is probably associated with the phase transformation of TiO_2 and Al_2O_3. Both Al_2O_3 and TiO_2 have several different polymorphs; two common polymorphs of TiO_2 are anatase and rutile. Only α-Al_2O_3 is thermodynamically stable, while other alumina polymorphs are metastable. Metastable phases can grow at the initial stage of oxidation, and their transformation to more stable polymorphs associates with volume change and stress accumulation within the oxide scale. Consequently, the phase transformation makes the scale more susceptible to cracking and delamination especially at high temperatures.

4.6 Summary and conclusions

A two-step process, i.e. Ti-C-Al nanoscale elemental multilayer stacks deposited by non-reactive magnetron sputtering followed by *ex-situ* annealing, was adopted to prepare Ti_2AlC MAX phase coatings. The high-temperature oxidation behavior of Ti_2AlC coated Zircaloy-4 in steam was examined to evaluate its potential as protective coatings in such applications.

Annealing of as-deposited coatings at 440–660°C resulted in the formation of a mixture of Ti-Al intermetallics and titanium carbide. The crystalline transition from the competing non-MAX phases to Ti_2AlC MAX phase was found at around 660°C. Phase-pure Ti_2AlC coatings were obtained after 800°C annealing for 10 min with an average grain size around 20 nm. The 800°C annealed coating also displayed a preferred orientation of (00l) basal plane perhaps because of lower growth rate along *c*-axis, the lowest surface energy of the (00l) surface in MAX phases as well as specific as-deposited nanoscale multilayer architecture.

The same approach was adopted to deposited Ti_2AlC coatings on Zircaloy-4 substrates by selecting an annealing temperature of 800°C. The overall coating thickness was around 5.5 μm with or without a 500 nm thick TiC diffusion barrier. The coatings, with a hardness of around 15 GPa and a modulus of 200 GPa after annealing, were much stiffer than the Zircaloy-4 substrate. Scratch tests observed a brittle failure mode and the critical load of failure was about 50 N and 30 N for the Ti_2AlC and Ti_2AlC/TiC coatings, respectively. During oxidation at 800°C in steam, the oxide scales demonstrated different structural characteristics for coatings with and without TiC barrier. Coatings without TiC barrier formed a duplex-layered scale: an outer θ-Al_2O_3 rich layer mixed with TiO_2 and an inner porous TiO_2 layer; correspondingly, a triple-layered scale (θ-Al_2O_3+TiO_2/θ-Al_2O_3/TiO_2) grew on coatings with TiC barrier at 800°C. The TiC barrier suppressed the rapid diffusion of Al from the coatings into the substrate, contributing to different scale structure, better oxidation performance and longer life of Ti_2AlC/TiC coatings. The coated Zircaloy-4 demonstrated significant improvement of oxidation resistance compared to uncoated samples at 800°C in steam. However, both coatings were quickly consumed with a weak or non-protective effect from around 1000°C. The fast failure of the coatings at 1000°C was associated with the low thickness of the coatings, higher interdiffusion rates between coating and substrate and potential phase transformation of the oxide products.

5 Synthesis, characterization and steam oxidation of Zr-C-Al coatings

In this chapter the deposition, characterization and evaluation of coating materials in the Zr-C-Al system, with a focus of the potential formation of Zr_2AlC and Zr_3AlC_2 MAX phases and other layered ternary carbides, as oxidation resistant coatings on Zircaloy-4 are described. No MAX phase formation, but growth of a ternary Zr(Al)C carbide phase was observed after annealing the nanoscale elemental Zr-C-Al multilayers in argon at temperatures from 600°C to 1200°C. Coatings with three different Zr/Al ratios, corresponding to stoichiometries of 2Zr/C/Al, 3Zr/5C/3Al, 2Zr/5C/4Al (potential formation of a Zr_2AlC MAX phase, and two other layered ternary carbides $Zr_3Al_3C_5$ and $Zr_2Al_4C_5$), were deposited on polished Zircaloy-4 substrates, and their high-temperature oxidation behavior in steam was examined.

5.1 Introduction

Materials in the Zr-C-Al system are of specific interest in terms of application in nuclear reactors. All three elements (Zr, C and Al) exhibit low thermal neutron absorption cross sections without impairing the neutron economics in the core. The forming ZrO_2 scale is stable with slow growth rate during normal operation in hot-water aqueous corrosion. Al_2O_3 represents one of the most effective diffusion barriers during high-temperature steam or air oxidation scenarios. Therefore, ternary compounds in the Zr-C-Al system could be very promising as oxidation resistant coatings to improve the accident tolerance of the Zr-based alloy fuel claddings. A number of layered ternary carbides in the Zr-C-Al systems have been synthesized and characterized. These carbides can be mainly divided into two categories based on their crystal structure. One category is with the general formula of $(ZrC)_nAl_3C_2$ and $(ZrC)_nAl_4C_3$, like $Zr_2Al_3C_4$, $Zr_3Al_3C_5$, $Zr_2Al_4C_5$, etc [207–209]. The crystal structures of these compounds are described as ZrC blocks being interleaved by Al_3C_2 or Al_4C_3 units. Oxidation of these ternary compounds at high temperatures produce an oxide scale composed of both ZrO_2 and Al_2O_3; their oxidation resistances progressively improve with increasing Al concentration. Another class of ternary Zr-C-Al carbides is formed within the family of MAX phases, including recently synthesized Zr_2AlC [210] and Zr_3AlC_2 [211]. Due to their specific nanolaminated structure leading to a high migration rate of the A element, both Zr_2AlC and Zr_3AlC_2 MAX phases are potentially alumina-forming materials, like Ti_2AlC, during high-temperature oxidation.

Actually, Al-containing Zr-based MAX phases are assumed to be unstable with respect to their competing phases, mainly ZrC, in the Zr-C-Al system [212–214]. A majority of studies attempting to synthesize Zr_2AlC and Zr_3AlC_2 MAX phases were unsuccessful, resulting mostly in the formation of only ZrC, combined with diverse Zr-Al alloys [65,212,215]. Only non-Al containing Zr-based MAX phases or Al containing solid solutions, like Zr_2SC [216], Zr_2InC [217] and $(Nb_{0.8}, Zr_{0.2})_2AlC$ [74], were identified. Recently, Lapauw et al. experimentally synthesized Zr_2AlC [210] and Zr_3AlC_2 [211] MAX phases, but the samples contained significant amounts of secondary phases ZrC and Zr-Al intermetallics. The criteria for

growth of these two MAX phases are still unclear and their oxidation resistance has not yet been studied. In addition, no reports associated with synthesis of Zr_2AlC and Zr_3AlC_2 MAX phases as thin films are found up to now.

The synthesis, characterization and evaluation of coating materials in the Zr-C-Al system, with a focus of the potential formation of layered ternary carbides, as oxidation resistant coatings on Zircaloy-4 are presented in this chapter. The coatings were deposited by non-reactive magnetron sputtering using three elemental targets applying a nanoscale elemental multilayer design with a multiple stacking sequence of zirconium, carbon and aluminum layers like described in the previous chapter [218]. However, no MAX phases, but Zr(Al)C carbide, formed after annealing in argon at temperatures from 600°C to 1200°C. Coatings with three different Zr/Al ratios, corresponding to stoichiometries of 2Zr/C/Al, 3Zr/5C/3Al, 2Zr/5C/4Al, were deposited on polished Zircaloy-4 substrates. The overall coating thickness was around 5.5 μm including a 500 nm thick ZrC diffusion barrier. The oxidation behavior of coated Zircaloy-4 in high-temperature steam was examined in the temperature range of 700°C to 1000°C, and compared to bare Zircaloy-4 samples.

5.2 Experimental arrangement

Two designs of multilayer coatings, with the individual thickness of each nanoscale elemental layers ~Zr 10 nm/C 2.2 nm/Al 4 nm and ~Zr 9 nm/C 2.4 nm/Al 2 nm based on the stoichiometries of Zr_2AlC and Zr_3AlC_2, respectively, were deposited on SiO_2/Si substrates and polycrystalline alumina substrates. The coating thickness was around 3 μm on these two substrates. The thickness of each individual elemental layer was calculated based on the stoichiometric ratio of the three elements with respect to their theoretical density of zirconium (6.51 g/cm^3), graphite (2.26 g/cm^3) and aluminum (2.70 g/cm^3).

Coatings with three different Zr/Al concentration ratios, corresponding to stoichiometries of 2Zr/C/Al, 3Zr/5C/3Al, 2Zr/5C/4Al, were deposited on polished Zircaloy-4 substrates. The selection of these three stoichiometries aims at potential formation of a Zr_2AlC MAX phase, and two other layered ternary carbides $Zr_3Al_3C_5$ and $Zr_2Al_4C_5$. Another purpose is to investigate the influence of Zr/Al concentration ratio on oxidation performance of the coatings. The coating with stoichiometry of 3Zr/2C/Al (Zr_3AlC_2) was not deposited on Zircaloy-4 substrates considering its low Al content. The coating thickness is around 5.5 μm on Zircaloy-4 substrates with a 500 nm thick Zr/C interlayer as diffusion barrier. Figure 5.1 shows schematically the design of the as-deposited multilayer stacks on alumina and Zircaloy-4 substrates. In addition, the thickest elemental layer for the as-deposited coatings on Zirclaoy-4 substrates was also limited to around 10 nm of zirconium layer or aluminum layer.

All experimental procedures related with deposition, thermal annealing, characterization and high-temperature oxidation were carried out using the similar setup as reported in subchapter 4.2 for the Ti_2AlC coatings. The Ti target was replaced by a 75 mm diameter, cylindrical Zr target. The measured deposition rate was around 0.9 nm/s for Zr at 200 W RF power. The annealing temperatures were changed from 600°C to 1200°C for the as-deposited coatings, and the oxidation tests in steam were conducted at 700°C, 800°C and 1000°C.

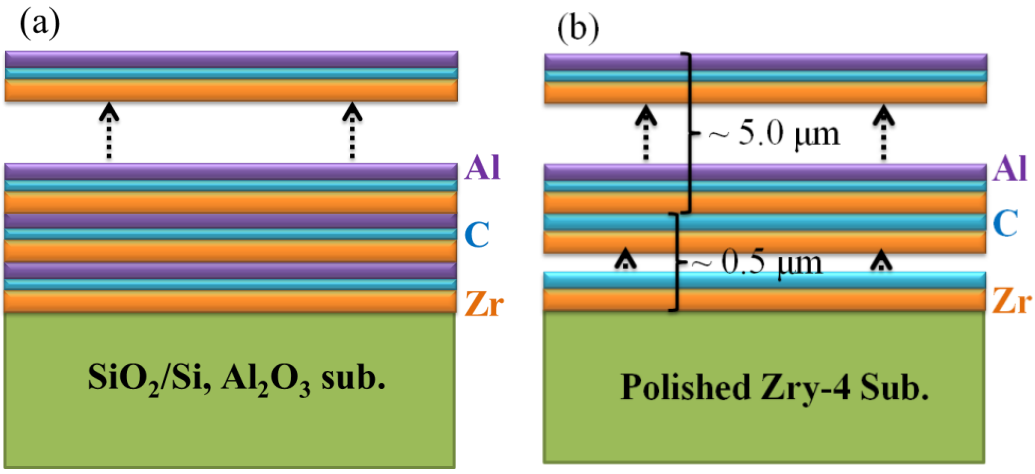

Figure 5.1 Schematic representations of the as-deposited elemental multilayer stacks on (a) SiO_2/Si and alumina substrates, and (b) Zircaloy-4 substrates.

5.3 Coatings on SiO_2/Si and alumina substrates

The overall chemical composition of the as-deposited coatings on SiO_2/Si substrate measured by EPMA and the corresponding theoretical values are shown in Table 5-1. The contents of Zr and Al for both coatings are nearly equal to the theoretical values of these two elements in Zr_2AlC and Zr_3AlC_2 MAX phases. The C contents in both coatings are slightly lower than the theoretical values. The level of O impurities is around 6 at.%. The relatively high level of oxygen is most likely due to some signal originating from the SiO_2/Si substrate also collected by the detector. Surface contamination by oxygen when the coatings are exposed to the ambient or trapping some oxygen in the coatings during deposition may also increase the level of O impurities in the as-deposited coatings (i.e. Zr is a strong oxygen getter). The level of O impurities could be reduced once the vacuum chamber is heated or cleaned before starting a new process – i.e. more/improved cleaning efforts may be required when depositing pure Zr-based coatings. Overall, the chemical composition of the as-deposited multilayer coatings is reasonably close to the nominal stoichiometries of the two MAX phases.

Table 5-1 Chemical composition of the as-deposited coatings on SiO_2/Si substrate in comparison with the theoretical values.

Coating design	**Chemical composition (at.%)**			
	Zr	C	Al	O
2Zr/C/Al	50.5	18.9	24.9	5.7
Theoretical	50	25	25	-
3Zr/2C/Al	52.3	24.9	16.7	6.0
Theoretical	50	33.33	16.67	-

In order to induce the potential formation of Zr_2AlC and Zr_3AlC_2 MAX phases, the as-deposited coatings on Al_2O_3 substrates were annealed in Ar at atmospheric pressure from 600°C to 1200°C with temperature interval of 100°C for 10 min (using individual samples). Higher annealing temperatures (above 1200°C) are unfavorable in case of practical application and also cause significant oxidation of the coatings due to residual oxygen in the furnace. XRD analysis showed that there were no MAX phases, but instead a ZrC carbide phase formed, during annealing at all different temperatures. Figure 5.2 displays the representative XRD patterns for the as-deposited, 800°C and 900°C annealed coatings. In case of the as-deposited coatings, the zirconium and aluminum layers are characterized by a nanocrystalline structure, while the carbon layers are amorphous [88]. After annealing, apart from the diffraction signals stemming from the alumina substrate, all the other XRD signals can be attributed to the ZrC phase (JCPDS #35-0784) for both coatings. The degree of crystallinity of the coatings improved with increasing annealing temperature since the peaks became sharper and stronger. The ZrC (111) plane was located at 2θ of 33.525°, slightly shifted to higher diffraction angles compared to the theoretical value (33.041°); this suggests that the presence of Al in the coatings results in the formation of a cubic rock salt (Zr,Al)C solid solution structure. The dissolved oxygen (Table 5-1) in the coatings may also partially contribute to the shift of diffraction peaks.

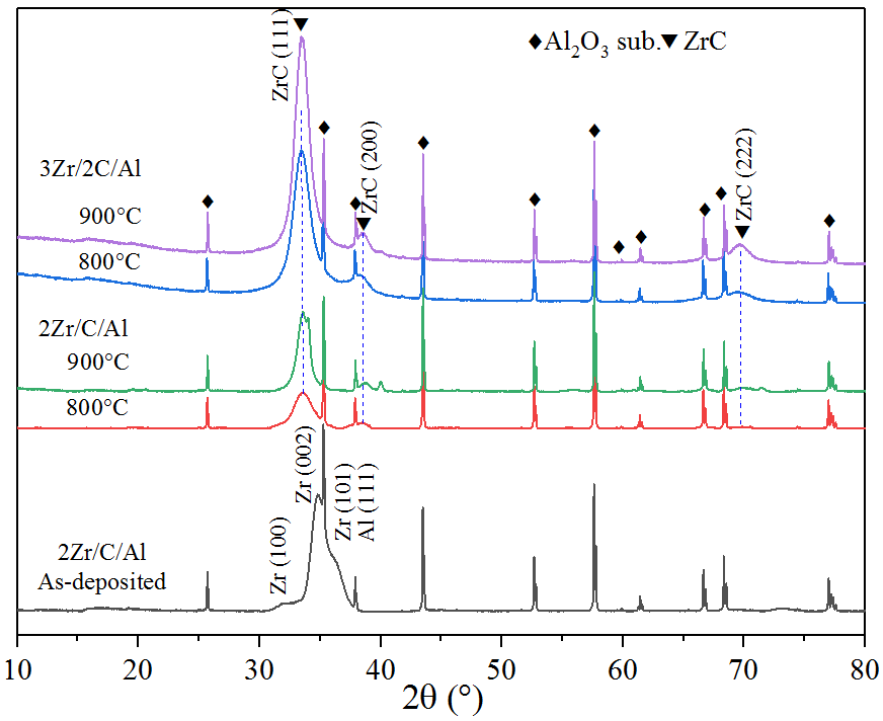

Figure 5.2 XRD patterns of as-deposited 2Zr/C/Al coating, 2Zr/C/Al and 3Zr/2C/Al coatings after 800°C and 900°C annealing in argon for 10 min on Al_2O_3 substrates.

5.4 Coatings on Zircaloy-4 substrates

5.4.1 Characterization

XRD analyses show that the phase constituents of all three as-deposited or annealed coatings on the Zircaloy-4 substrates are similar. The as-deposited coatings are composed of nanocrystalline zirconium and aluminum layers and amorphous carbon layers. No MAX phase or other layered ternary carbide formation was identified after the heat treatment; see for example in Figure 5.3 the typical XRD patterns after annealing at 600°C (similar up to 1200°C). All annealed coatings crystallized to a cubic ZrC phase with a B1 NaCl crystal structure, in consistence with observations for samples with Al_2O_3 substrates.

Figure 5.4 presents representative plan-view (as-deposited) and cross-sectional (600°C annealed) SEM micrographs of the 2Zr/C/Al coatings on the Zircaloy-4 substrates. The coatings display a uniform and smooth surface before and after annealing without indication of delamination or spallation. The coatings are dense and free of voids or cracks after annealing as shown in Figure 5.4(b). The 500 nm thick ZrC barrier can be easily distinguished due to the different contrast. No noticeable differences in surface topography and cross-sectional microstructure are identified for the other two designs of coatings.

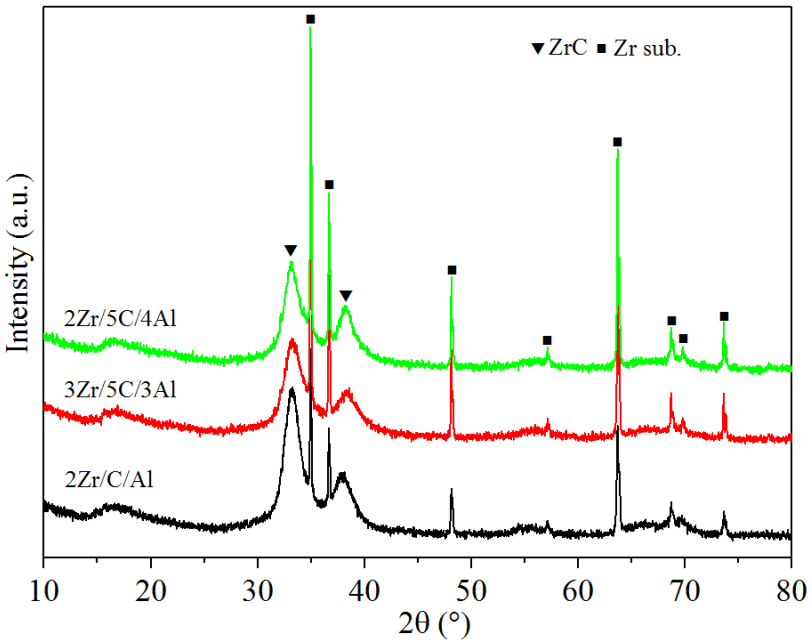

Figure 5.3 XRD patterns of 2Zr/C/Al, 3Zr/5C/3Al and 2Zr/5C/4Al coatings on Zircaloy-4 substrates after 600°C annealing in argon for 10 min.

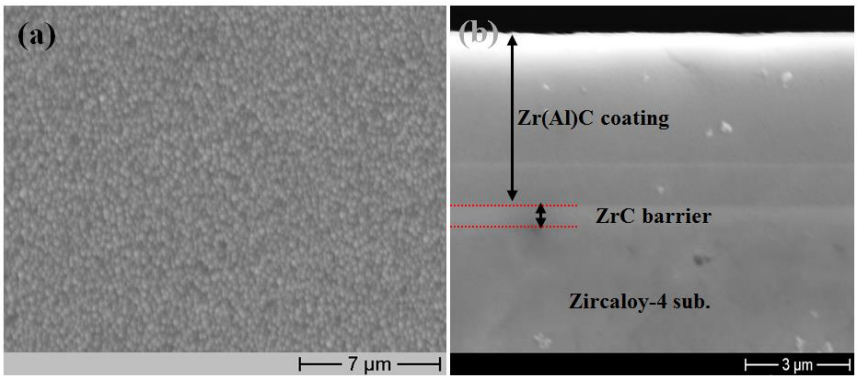

Figure 5.4 SEM images of 2Zr/C/Al coatings on polished Zircaloy-4 substrates. (a) Surface view of as-deposited coatings, (b) cross-sectional view of 600°C annealed coatings.

5.4.2 High-temperature oxidation

Coated coupons of Zircaloy-4 and uncoated Zircaloy-4 coupons as reference were oxidized in steam at temperatures of 700°C, 800°C up to 250 min and at 1000°C up to 60 min in order to evaluate the oxidation resistance of the coatings as a function of the three stoichiometries.

5.4.2.1 Oxidation kinetics

Figure 5.5 shows the mass gain (per unit surface area) of the coated and uncoated Zircaloy-4 during oxidation at 700°C. Similar to previous studies [12,24], the oxidation kinetics of bare Zircaloy-4 at 700°C in steam can be summarized into two stages. During the initial stage of oxidation, the oxidation followed a cubic or sub-cubic oxidation kinetics, and the oxidation rate was controlled by the diffusion of the steam through the oxide scale. The oxidation rate changed to a linear kinetics, called breakaway oxidation, due to loss of the protective properties of the oxide scale with prolonged exposure. The transition time between the two stages of the bare Zircaloy-4 was found to be around 70 min in this study. Oxidation of the coated Zircaloy-4 at the same temperature essentially obeyed as well a two-stage oxidation kinetics, like uncoated Zircaloy-4, as shown in Figure 5.5. However, all three coated samples revealed lower oxidation rates compared to the uncoated Zircaloy-4. In particular, the two coatings with higher Al content (i.e., 3Zr/5C/3Al and 2Zr/5C/4Al) displayed the best oxidation resistance and similar lowest oxidation rate at least before the transition point. The final mass gain is around 2.8 mg/cm^2 for 3Zr/5C/3Al coating and around 3.2 mg/cm^2 for both 2Zr/C/Al and 2Zr/5C/4Al coatings, about 40% and 30% lower compared to the bare Zircaloy-4, respectively. It is necessary to point out that the transition times are quite similar for both coated and uncoated coupons; therefore, the oxidation of uncoated edges probably resulted in the mass gain curves with similar tendency. The accelerated oxidation rate of the 2Zr/5C/4Al coating, after around 80 min which became comparable to the behavior of the 2Zr/C/Al coating, was likely attributed to the cracking and spallation of the coatings (see following SEM characterization).

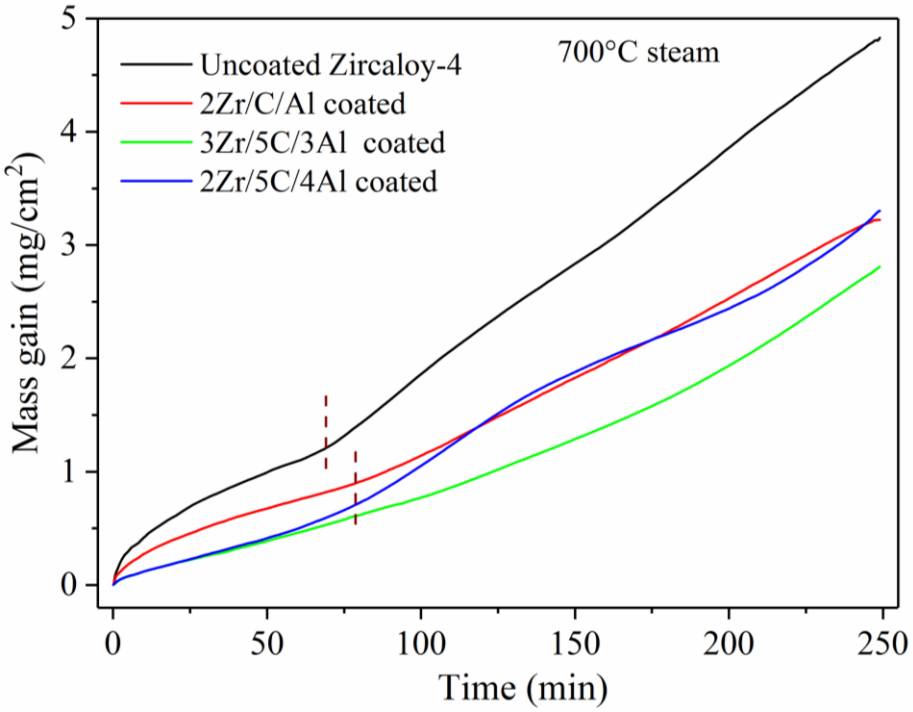

Figure 5.5 Mass gain per unit surface area of the coated and uncoated Zircaloy-4 coupons during oxidation in steam at 700°C. The vertical dashed lines indicate where the transition of the oxidation kinetics occurs.

Figure 5.6 shows the mass gain of the coated and uncoated Zircaloy-4 coupons during oxidation at 800°C and 1000°C in steam. Similar to oxidation at 700°C, coatings with higher Al content displayed somehow lower mass gains of the three stoichiometries during oxidation. The oxidation kinetics is different from that at 700°C, and all samples essentially follow a parabolic oxidation rate. However, all coatings showed weak protection at both temperatures, resulting in comparable or just slightly lower mass gains of coated coupons compared to uncoated one from the beginning of exposure.

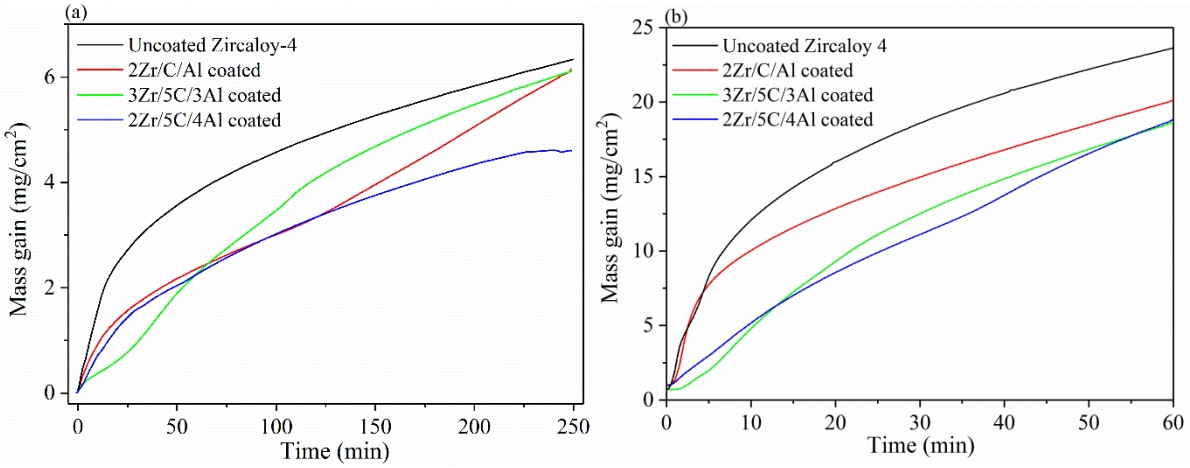

Figure 5.6 Mass gain per unit surface area of coated Zircaloy-4 (coatings with three different stoichiometries) and uncoated Zircaloy-4 during oxidation in steam at (a) 800°C for 250 min and (b) 1000°C for 60 min. Note the different scales for mass gain at different temperature.

5.4.2.2 Microstructural evolution during oxidation

In order to gain more insights into the oxidation behavior of the coatings, the surfaces and cross-sections of the coated coupons were examined by SEM. Figure 5.7 displays the plan-view and cross-sectional SEM micrographs including EDS mapping of the 2Zr/C/Al coated coupon after oxidation at 700°C. As shown in Figure 5.7(a), the coating exhibited good adhesion to the substrate with no indications of cracking or spallation after oxidation. The formation of an oxide scale on the surface was confirmed by the cross-sectional SEM micrograph. EDS mapping analysis suggested that the thickness of the oxide scale is around 2.9 μm. The residual coating of 2.2 μm thick retains non-oxidized under this condition. In addition, the oxide scale obviously consisted of two sublayers: a mixed Al_2O_3-rich and ZrO_2 outer layer, and a ZrO_2 inner layer (Figure 5.7(d)). Oxidation of the uncoated edges led to growth of a ~30 μm thick ZrO_2 layer (Figure 5.7(c)) with Zr(O) layer beneath. The differential oxide scale thickness between the coatings and the uncoated areas revealed that the coatings provide much better oxidation resistance improvements as is reflected by the mass gain curves at 700°C. The calculated mass gain based on the oxide scale thickness on the coatings was around 0.5 mg/cm^3, one magnitude lower than uncoated one. The major mass gain of the 2Zr/C/Al coated sample during exposure was attributed to the oxidation via uncoated edges.

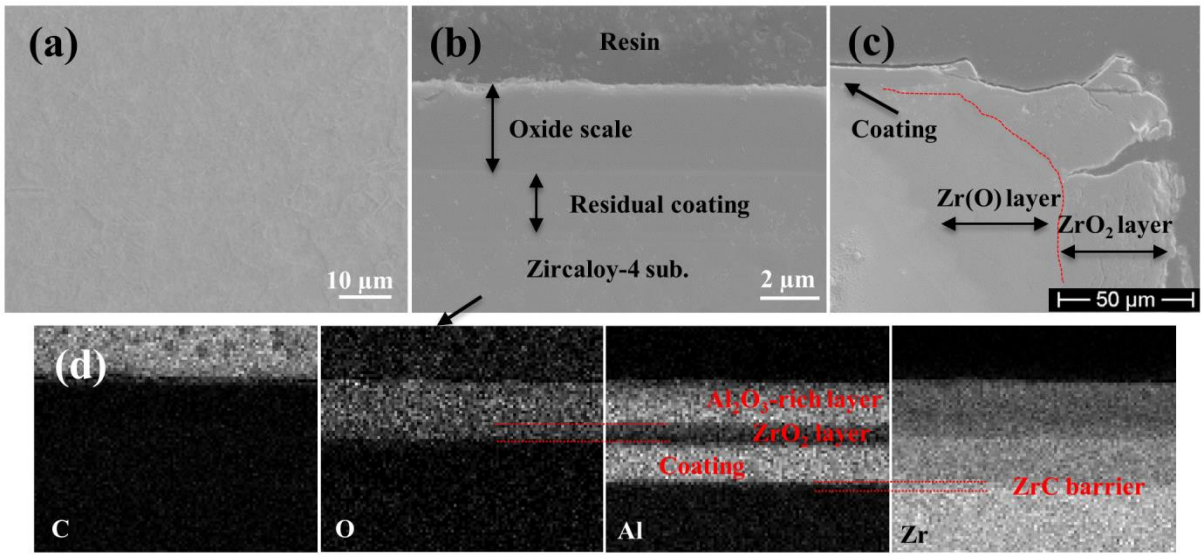

Figure 5.7 SEM images of 2Zr/C/Al coatings on polished Zircaloy-4 substrates after oxidation in steam at 700°C for 250 min. (a) plan view, (b) and (c) cross-sectional view, (d) EDS mapping of cross section of (b).

Figure 5.8 and Figure 5.9 present the plan-view and cross-sectional SEM micrographs of 3Zr/5C/3Al and 2Zr/5C/4Al coated coupons after oxidation at 700°C. In contrast to the 2Zr/C/Al coating, these two coatings demonstrated low adhesion to the substrate, and widespread cracks and spallation of the coatings were observed after oxidation as clearly seen in Figure 5.8(a) and Figure 5.9(a). The underneath substrate was severely attacked by steam where the coatings cracked or peeled off. In addition, more pronounced peeling off was observed for coatings of lower Zr and higher Al content (2Zr/5C/4Al coatings). Oxidation of these two coatings resulted in the growth of an oxide scale featured with single layer

structure, as revealed by the EDS mapping in Figure 5.8(c) and Figure 5.9(c). The oxide scales are composed of predominant Al_2O_3 with some amount of ZrO_2. No delamination was observed between the oxide scale and the coatings. The oxide layer microstructure and thicknesses on the three types of coatings after oxidation were determined from the cross-sectional SEM images, and the results are compared in Table 5-2. The oxide scale thickness gradually decreased from ~2.20 μm, then ~1.43 μm to ~0.83 μm with increasing Al concentration in the coatings, i.e. the ratio between Zr and Al in the three types of coatings changed from 2:1, 1:1 to 1:2.

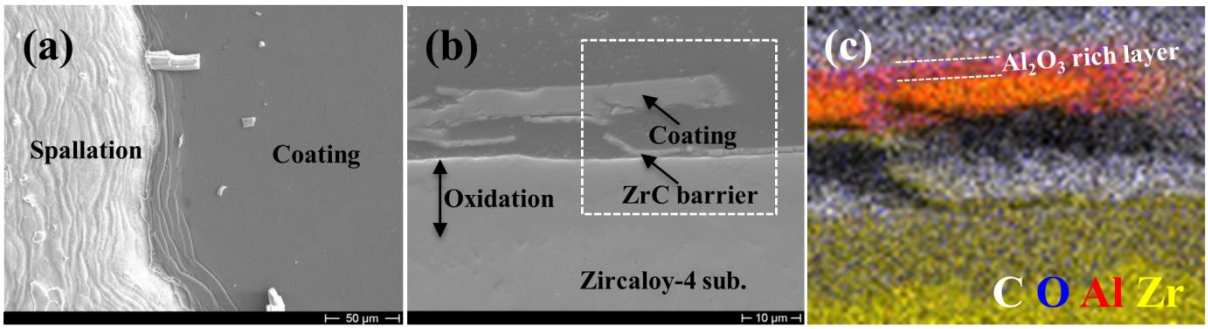

Figure 5.8 SEM images of 3Zr/5C/3Al coatings on Zircaloy-4 substrate after oxidation at 700°C in steam for 250 min. (a) Plan view, (b) cross-sectional view, (c) EDS mapping of the selected dashed rectangle area in (b).

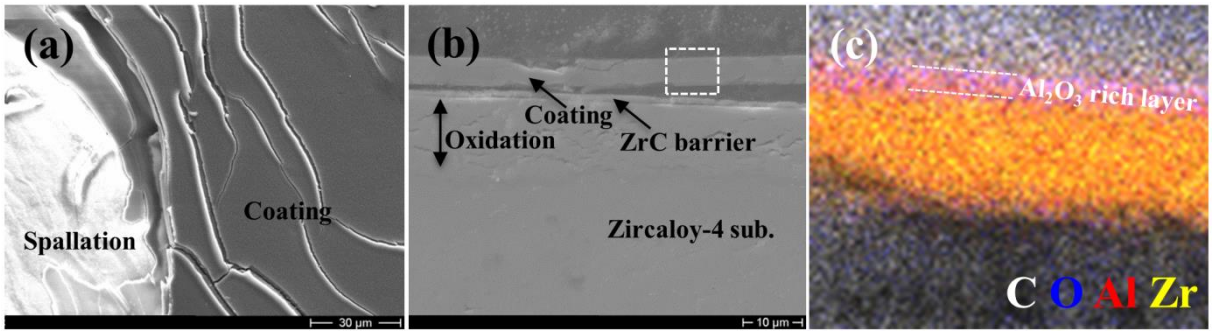

Figure 5.9 SEM images of 2Zr/5C/4Al coatings on Zircaloy-4 substrate after oxidation at 700°C in steam for 250 min. (a) Plan view, (b) cross-sectional view, (c) EDS mapping of the selected dashed rectangle area in (b).

Table 5-2 Microstructure and thickness of the oxide scales grown on the coatings during oxidation at 700°C in steam for 250 min.

	Coatings design		
	2Zr/C/Al	3Zr/5C/3Al	2Zr/5C/4Al
Oxide scale structure	A mixed Al_2O_3-rich+ZrO_2 outer layer, and a ZrO_2 inner layer	A single Al_2O_3-rich+ZrO_2 layer	A single Al_2O_3-rich+ ZrO_2 layer
Oxide scale thickness	~ 2.20 μm	~ 1.43 μm	~ 0.83 μm

Figure 5.10 shows the plan-view and cross-sectional SEM micrographs of the three coated coupons after oxidation at 800°C for 250 min. Even though no or rare spallation, significant cracking of the 2Zr/C/Al coating after exposure was observed at this higher oxidation temperature, Figure 5.10(a). These cracks served as short-circuit diffusion paths for steam into the Zircaloy-4 substrate beneath. Therefore, the Zircaloy-4 substrate also underwent considerable oxidation, and growth of a porous ZrO_2 layer with thickness around 40 μm was confirmed as shown in Figure 5.10(a'). In case of the 3Zr/5C/3Al coating, both significant cracking and spallation of the coatings occurred after oxidation as in Figure 5.10(b). For the coating with the highest Al concentration, i.e. 2Zr/5C/4Al, nearly the complete coating peeled off and the surface displayed a different but relative smooth topography in Figure 5.10(c). The cross-sectional micrograph in Figure 5.10(c') revealed that delamination occurred at the coating and the ZrC barrier interface, as the ZrC barrier was still attached to the substrate while the outer 2Zr/5C/4Al layer was completely gone. Regarding the coated coupons after oxidation at highest temperature 1000°C for 60 min, a visual check found that all three coatings are lost from the surface after the exposure. Therefore, they were not further examined.

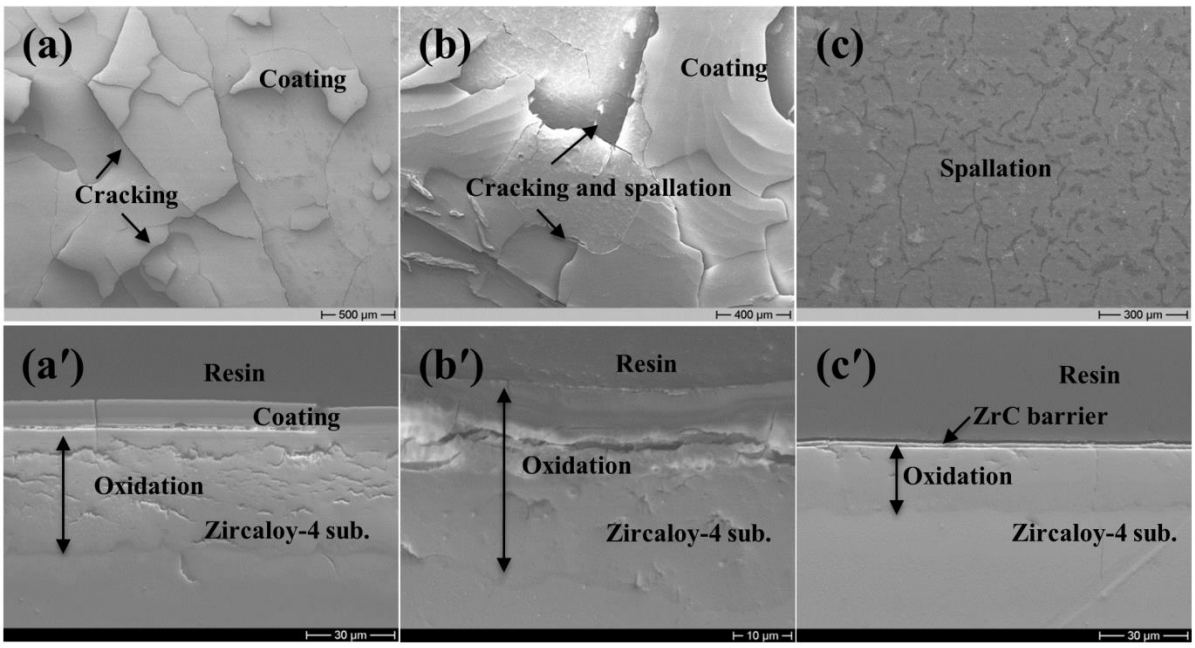

Figure 5.10 SEM images of (a) and (a') 2Zr/C/Al coating, (b) and (b') 3Zr/5C/3Al coating, (c) and (c') 2Zr/5C/4Al coating on Zircaloy-4 substrates after oxidation in steam at 800°C for 250 min. First row: plan view and second row: cross-sectional view.

5.5 Discussion

5.5.1 Deposition of coatings in the Zr-C-Al system

Annealing of the nanoscale elemental multilayers with a multi-stacking sequence of zirconium, carbon, and aluminum layers corresponding to the stoichiometries of Zr_2AlC and Zr_3AlC_2 from 600°C to 1200°C resulted in formation of Zr(Al)C carbide, rather than Zr-based MAX phases in this study. In fact, Al-containing Zr-based MAX phases are often assumed to be unstable or metastable with respect to their

competing phases in Zr-C-Al ternary system. Initial work conducted by Nowotny and collaborators [65,212] and the majority of works performed recently [74,215] on the exploration of layered ternary carbides in the Zr-C-Al system found no layered ternary compounds belonging to MAX phases as reflected in Figure 5.11, presenting the phase diagram of the system Zr-C-Al at 1000°C adopted from [212]. Several ternary carbides, like $Zr_2Al_3C_5$ and $Zr_3Al_3C_5$, which are classified into other categories, have been successfully produced.

Regarding the bulk form of Zr-based MAX phases, Lapauw et al. recently experimentally produced them by means of reactive hot pressing of a ZrH_2, Al and C powder mixture at a temperature of around 1500°C and a pressure of 20 MPa [210,211]. However, a relatively narrow temperature window was found for the synthesis of MAX phases and ZrC was always present as a secondary phase [211]. The maximum yield reported of the Zr_2AlC product synthesized at 1525°C was only 48.9 mol.%, with the residue of 51.1 mol.% ZrC_x [210]. Further investigations suggest that the key for successful synthesis of Zr-based MAX phases is to surpass the nucleation free energy barrier without favoring competitive phase formation (like ZrC). Si impurities or deliberate additions promoting the formation of Zr-Si intermetallic phases which presumably act as a nucleation substrate for the MAX phase can support the growth or improve the quality of a MAX phase in the final products [219]. Furthermore, self-propagating high-temperature synthesis (SHS) of Zr-C-Al elemental powder mixtures with Al content from 0 to 40 wt.% revealed that the final products only contained the stable ZrC phase and the metallic Al phase. Recently Lai et al. explored the synthesis of ternary carbide thin films in the Zr-C-Al system by pulsed cathodic arc evaporation on four different single-crystal substrates (α-Al_2O_3(001), MgO(111), 4H-SiC(001), and yttria-stabilized-zirconia (YSZ) (111)) [220]. Growth of $Zr_2Al_3C_4$ thin films was confirmed only on 4H-SiC(001) and α-Al_2O_3(001) substrates where a stringent criteria (i.e. optimum deposition temperature and elemental flux) was required. In most cases, formation of ZrC was verified. In addition, this group attempted to deposit films corresponding to the Zr_3AlC_2 MAX phase composition, but no trace of this phase was observed on all substrates [220].

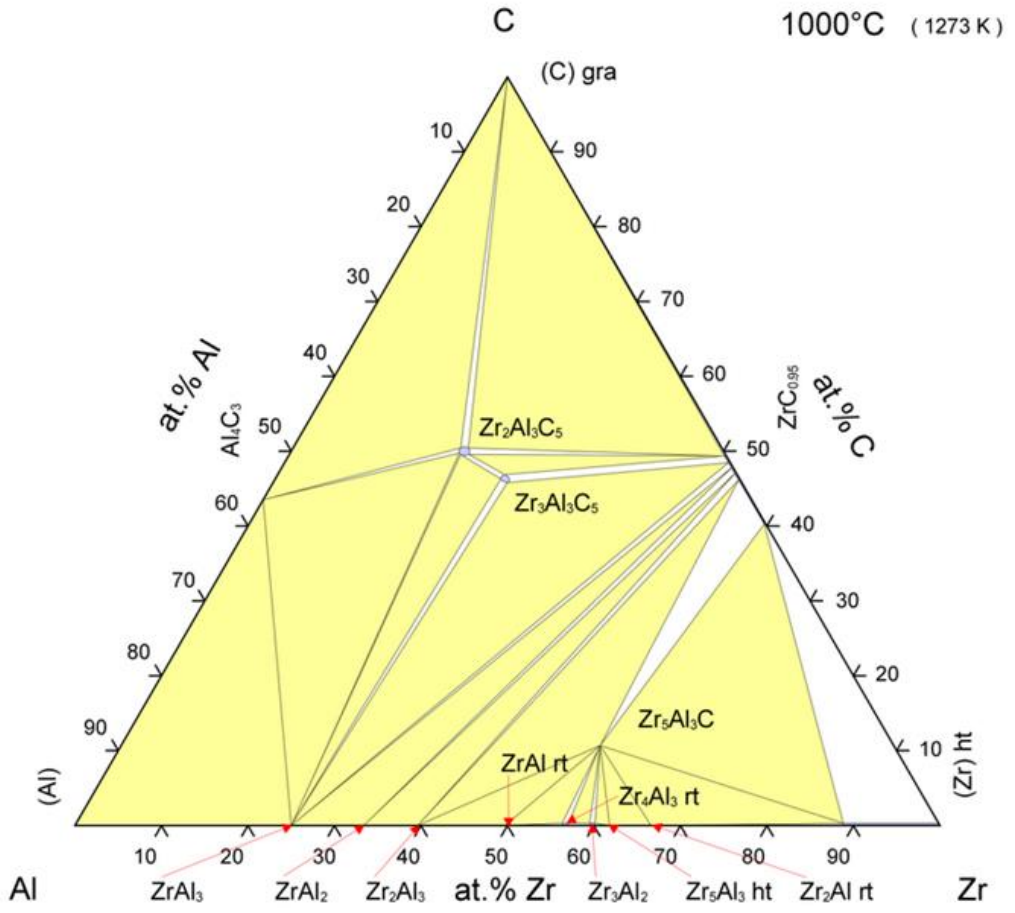

Figure 5.11 Isothermal section of phase diagram of Zr-C-Al system at 1000°C [212].

Based on above literature findings, it can be seen that ZrC always presents as intermediate phase and/or competing phase during synthesis of higher ordered ternary Zr-based carbides. Furthermore, ZrC remains highly thermodynamically stable in the Zr-C-Al system. Thus, annealing of the elemental Zr-C-Al multilayers between 600°C and 1200°C in this study leading to the formation of ZrC could be expected before. Even though the phase diagram shows a low solubility of Al in the ZrC, we assume that Al in the annealed coatings occupy the lattice position of Zr atoms metastably because of a shift of the diffraction peaks of the ZrC phase compared to the theoretical values (Figure 5.2). Similar phenomena have been observed for the deposition of transition metal (TM) aluminum nitride coatings, like TiAlN and ZrAlN coatings [221,222]. These compound coatings generally crystallize into cubic rock salt structures, the stable configuration of binary transition metal nitrides (TMN), at Al concentrations lower than a critical value due to the metastable conditions during PVD. Transition metal atoms in the TMN lattice are substituted by the Al atoms with smaller atomic radius, leading to shrinkage of the lattice constant and hence a shift in the 2θ value in the XRD signals of such phases (in comparison to the pure binary phases) [221,222].

5.5.2 Oxidation of coatings in steam

The three types of Zr-C-Al coatings displayed better oxidation resistance than the Zircaloy-4 substrate but showed low adherence especially at temperatures higher than 800°C. Variations of the microstructure and thickness of the oxide scales grown on the coatings after oxidation at low temperature, 700°C, can be explained by their different stoichiometries. The ratio between Zr and Al in the three types of coatings are 2:1, 1:1 and 1:2, respectively. In addition, the Gibbs free energy (⊿G) for the reaction of Al with steam is lower than that of Zr (-787.8 kJ/mol for Al and -526.2 kJ/mol for Zr at 700°C). Thus, Al preferably reacts with steam during oxidation. It is reasonable that an Al_2O_3-rich layer mixed with ZrO_2 grows on the surface during oxidation of the coatings since Zr also has a high affinity to steam and/or oxygen at high temperature. The oxidation mechanism for the growth of a double-layer oxide on the 2Zr/C/Al coating seems to be simultaneously outward diffusion of Al toward the gas/oxide interface and inward diffusion of oxidizing species to the oxide/coating interface. Due to the relatively low concentration of Al in the 2Zr/C/Al coatings, Al in the top surface of the coating is presumably quickly consumed via diffusing out to oxidize, consequently leaving a ZrC_x layer beneath. Growth of metastable alumina phases, like γ-, θ-Al_2O_3, have been widely confirmed for alumina-forming materials during oxidation at relatively low temperatures (usually below 900°C) [223]. Results presented in the previous chapter also confirmed that no stable α-Al_2O_3 phase but metastable θ-Al_2O_3 formed after oxidation at 800°C in steam of Ti_2AlC coatings. The metastable alumina phases obviously provide less protective effects than the stable α-Al_2O_3. Additionally, the oxide scale also contains a certain amount of ZrO_2, which is featured by a much higher defect density and growth rate compared to Al_2O_3 at elevated temperatures. Hence, it suggests that steam can readily penetrate the outer Al_2O_3-rich scale to oxidize the remaining ZrC_x. Increasing the Al content in the coatings supposes to simultaneously raise the alumina concentration within the scale, which can in turn improve the protective nature of the scale. Similar observations were made for example for TiAlN coatings: increasing the Al content in such TiAlN coatings resulted in an increase of its high-temperature oxidation resistance due to the formation of an Al_2O_3-rich scale [224]. The oxidation onset temperatures for ternary Zr-C-Al ceramics or coatings are also much higher than that for ZrC [207]. Therefore, the oxidation resistance of the Zr-C-Al coatings investigated in this study gradually improved and the oxide scale thickness successively became thinner with increasing Al concentration (Table 5-2).

The distinct adherence of those three types of coatings exhibited during oxidation is most likely due to the thermal expansion mismatch between the coatings and the substrate. The coefficients of thermal expansion (CTE) for Zircaloy-4 substrate, ZrC, Zr, Al are 6.0, 6.2, 5.8, and 24.0 ($\times 10^{-6}$ K^{-1}), respectively. The CTE for Al is almost four times higher than that of the other three materials. Increasing the Al content in the coatings will certainly drive up the CTE mismatch between the coating and the Zircaloy-4 substrate as well as between the coating and the ZrC barrier, making the coating more susceptible to peel off during temperature changes. Therefore, the 2Zr/C/Al coatings exhibited better adherence on Zircaloy-4 than the 3Zr/5C/3Al and 2Zr/5C/4Al coatings. In addition, the main delamination of the 3Zr/5C/3Al and 2Zr/5C/4Al coatings during oxidation at 700°C was observed between the coating and

the ZrC barrier, instead of between the ZrC barrier and the substrate. This phenomenon is consistent with the discrepancy of above reported CTE values.

At oxidation temperatures higher than 800°C, faster oxidation rate associated with various stresses induced by, for instance, growth and phase transformation of oxides, interaction between the coating and substrate will accelerate the degradation process of the coatings. Tremendous cracking and spallation appeared for all three coatings after oxidation at 800°C and 1000°C. This implies that the protective effect of the three coatings is limited to around 800°C in steam.

5.6 Summary and conclusions

Various elemental multilayers with a nanoscale architecture and a multiple stacking sequence of zirconium, carbon, and aluminum layers based on the stoichiometries of Zr_2AlC and Zr_3AlC_2 were deposited on Al_2O_3 substrates. No MAX phase formation, but growth of a ternary Zr(Al)C carbide phase, was observed after annealing in argon at temperatures from 600°C to 1200°C.

Coatings with three different Zr/Al ratios, corresponding to stoichiometries of 2Zr/C/Al, 3Zr/5C/3Al, 2Zr/5C/4Al, were deposited on Zircaloy-4 substrates. All three annealed coatings crystallized to a cubic, solid solution ZrC phase with a B1 NaCl crystal structure, and Al is suggested to occupy the lattice position of Zr atoms. The coated samples revealed lower oxidation rates compared to the uncoated Zircaloy-4 at 700°C. In particular, the two coatings with higher Al content (i.e., 3Zr/5C/3Al and 2Zr/5C/4Al) displayed better oxidation resistance. The oxide scale consisted of two sublayers for the 2Zr/C/Al coatings: a mixed Al_2O_3-rich and ZrO_2 outer layer, and a ZrO_2 inner layer. Oxidation of the other two coatings led to the growth of oxide scales featured by a predominant Al_2O_3 single layer. However, these two coatings with higher Al content demonstrated low adhesion to the Zircaloy-4 substrates. Widespread cracks and spallation of the coatings were observed after oxidation due to the discrepancy in thermal expansion coefficients between the coatings and the substrate. All coatings showed weak or no protection effect at higher oxidation temperatures 800°C and 1000°C with tremendous cracking and spallation.

6 Synthesis, characterization and steam oxidation of Cr_2AlC MAX phase coatings

Cr_2AlC, one of the alumina-forming MAX phases, is further synthesized and examined as potential protective coating on Zircaloy-4 substrates at temperatures higher than 1000°C. Similar to the Ti_2AlC coatings, the Cr_2AlC coatings are synthesized by magnetron sputtering using elemental nanoscale multilayer stacks, and subsequent *ex-situ* thermal annealing in argon. Crystallization of the Cr_2AlC MAX phase starts from 480°C and formation of a single Cr_2AlC MAX phase at 550°C is confirmed. Two designs of coatings are realized on Zircaloy-4 substrates, without or with a 1.5 µm thick Cr overlayer. The Cr overlayer aims to eliminate potential fast hydrothermal dissolution of Al during normal operation. The total thickness of the coatings is around 6.5 µm with a 500 nm thick Cr interlayer as bonding layer and diffusion barrier. The high-temperature oxidation tests evidence high adherence, excellent oxidation resistance up to at least 1200°C and autonomous self-healing capability via the growth of a protective Al_2O_3 scale for Cr_2AlC/Cr coatings and of a protective Al_2O_3 scale beneath Cr_2O_3 for Cr/Cr_2AlC/Cr coatings. Thus, Cr_2AlC-based coatings on Zr alloys have promising application prospects as one type of ATF claddings in terms of migrating fast oxidation of cladding with steam during accidental scenarios.

6.1 Introduction

In the Cr-C-Al system, only one ternary compound, namely the Cr_2AlC MAX phase, is identified up to now [61]. Like other MAX phases, Cr_2AlC shares the unique combination of the merits of both metals and ceramics stemming from its distinctive nanolaminated structure. Cr_2AlC also represents one of the most deeply investigated MAX phases since chromium is a common alloying element with easy access [225]. Additionally, alloys with a higher Cr concentration generally display better high-temperature oxidation and corrosion resistance what makes Cr_2AlC a highly promising candidate for diverse applications. Therefore, the synthesis, microstructure, mechanical properties, electrical properties, high-temperature oxidation and hot corrosion resistance and tribological behavior of bulk Cr_2AlC have been systematically studied in recent decades [45,99,226–231]. Like Ti_2AlC, Cr_2AlC is elastically stiff (Young's modulus of 278 GPa, shear modulus of 116 GPa) and relatively soft (Vickers hardness of ~5 GPa) [228]. The theoretical density of Cr_2AlC is 5.24 g/cm^{-3} [232] and its coefficient of thermal expansion (CTE) lies in the range of 11~13.3 × 10^{-6} K^{-1} [225,228]. Cr_2AlC is electrically and thermally conductive with a electrical conductivity of 1.4 × 10^6 $\Omega^{-1}\cdot m^{-1}$ and thermal conductivity of approximately 22 $W\cdot m^{-1}\cdot K^{-1}$ at room temperature [233]. Cr_2AlC also displays good high-temperature oxidation resistance up to 1300°C, self-healing behavior with respect to the high migration rate of Al and its subsequent selective oxidation in an oxidizing atmosphere [98,99,230,234,235], and excellent hot corrosion resistance against molten Na_2SO_4 salt [98,231].

Bulk Cr_2AlC ceramic was first synthesized by Jeitschko et al. in the 1960s [64] using hot pressing of elemental powders at 1500°C. Recent investigations on the synthesis of bulk materials concentrated on

reducing the impurity content of final products for experimental tests of its intrinsic properties. High purity bulk Cr_2AlC with less than 5 vol.% impurities has been successfully fabricated as reported by Li et. al. [236]. The high-temperature oxidation mechanism and oxidation kinetics of Cr_2AlC have been well understood and documented [98,99,234,235]. In 2007, Lin et al. [98] carried out primary work on the high-temperature oxidation of Cr_2AlC in the 800–1300°C range in air. Their findings confirmed that selective oxidation of aluminum took place during the high-temperature oxidation of Cr_2AlC due to its unique crystal structure and bonding characteristics. A continuous Cr_7C_3 sub-layer formed between the protective alumina layer and the Cr_2AlC substrate, due to consumption of Al by forming an Al_2O_3 scale. The oxidation kinetics were fitted to be parabolic with rate constants of 1.08×10^{-12} and 2.96×10^{-9} $kg^2\cdot m^{-4}\cdot s^{-1}$ at 800°C and 1300 °C up to 20 h, respectively. The overall parabolic rate constants are on the same order of magnitude but slightly higher than that of Ti_2AlC and Ti_3AlC_2 at same temperatures. However, the presence of a chromium carbide layer beneath the alumina scale is quite problematic for the Cr_2AlC MAX phase. The oxidation of the underlying carbide at high temperature deteriorates the oxidation resistance, via formation of voids and inducing cracking and spallation of the protective alumina scale. Another issue limiting the operating temperature of Cr_2AlC is the relatively high mismatch of CTE between this compound and the protective alumina layer that forms. The alumina scale is susceptible to cracking and spalling once the oxidation temperature reaches 1300°C. Similar behavior has been observed by subsequent studies. For instance, Lee et al. [99] reported that the cyclic oxidation resistance of Cr_2AlC in air to be excellent at 1000°C, good at 1100°C, intermediate at 1200°C, but poor at 1300°C. The cyclic oxidation resistance of Cr_2AlC at 1300 °C decreased significantly due to the formation of voids and the spallation of the scales. Furthermore, Li et al. investigated the influence of grain size on the oxidation behavior of Cr_2AlC at 1100°C and 1200°C using fine-grained (2 μm) and coarse-grained (60 μm) samples [235]. The oxidation rate of the fine-grained sample is relatively faster than that of the coarse-grained samples with respect to grain boundaries providing a rapid diffusion path during oxidation. Furthermore, the crack-healing capability of the Cr_2AlC MAX phase by surface oxidation at elevated temperatures has been intensively investigated [94,230,237]. It was confirmed that the crack healing of Cr_2AlC is an oxidation process where the crack gap is filled essentially by Al_2O_3; one example in Figure 6.1 shows healing of a crack area in Cr_2AlC after oxidation at 1200°C in air for 4 h [230]. The existence of impurity Cr particles locally accelerated the healing process by providing Cr_2O_3 nucleation sites. Overall, Cr_2AlC can endure temperature up to 1200°C for long time exposure and possible to 1400°C for short time service in oxidizing atmospheres with autonomous crack healing or self-healing capability.

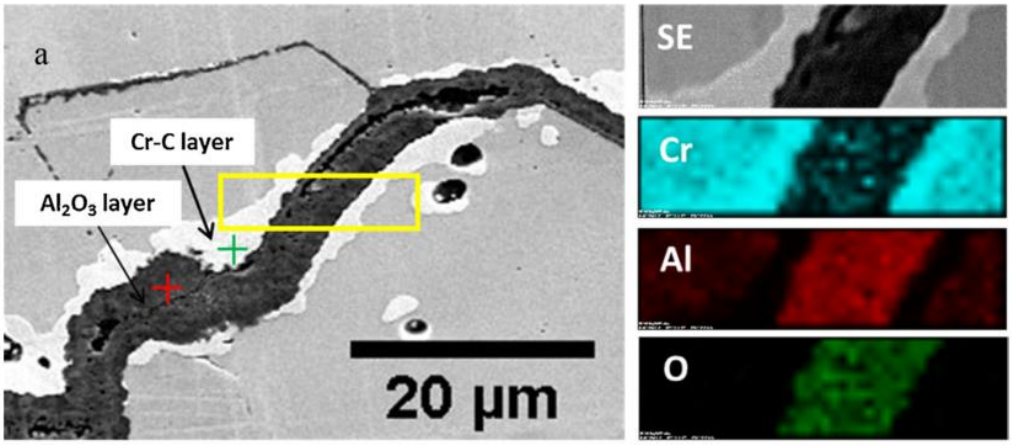

Figure 6.1 SEM image and corresponding elemental maps showing healing of a crack area in Cr_2AlC after oxidation at 1200°C in air for 4 h [230].

The remarkable chemical and physical properties of Cr_2AlC MAX phase offer a huge potential for high-temperature protective coating applications and stimulated numerous works recently on the synthesis of Cr_2AlC thin films [80,87,159,170,185,238–248]. Similar to other MAX phase films, the fabrication of Cr_2AlC coatings was also mainly carried out by PVD processes using either individual elemental targets or compound targets, by means of directly heating the substrates or heat treatment after deposition. Literature indicated that the Cr_2AlC MAX phase coatings can crystallize at lower deposition temperatures in contrast to other MAX phase coatings, like Ti_2AlC and Ti_3SiC_2 [63]. The typical crystallization temperature of Cr_2AlC MAX phase coatings was reported to be around 500°C. The lower deposition temperatures offer the advantage for deposition on heat-sensitive substrates. In addition, deposition of high-purity Cr_2AlC coatings seems to be easier than other MAX phase coatings, such as Ti_2AlC. Schneider et al. reported that a deviation from the stoichiometric composition of up to 6.3 at.% Al still led to formation of single-phase Cr_2AlC [244]. One interpretation suggests that Cr_2AlC lattice can dissolve some Al metastably by replacing Cr, as proved by ab initio calculations [249]. Walter et al. [245] also demonstrated the possibility of an industrially applicable large-scale deposition of Cr_2AlC films on steel. Cr_2AlC MAX phase coatings have been investigated as potential protective coatings on titanium alloys [246] and superalloys [238] against high-temperature oxidation in air. Compared with bulk Cr_2AlC, the Cr_2AlC coatings possessed similar oxidation behavior, forming a dense, continuous α-Al_2O_3 oxide scale on Cr carbides. The significant improvement of the oxidation resistance of the substrates at least up to 1100°C was confirmed. Recently, Berger et al. found that small Y addition within Cr_2AlC coatings promoted the α-Al_2O_3 phase formation relative to the other metastable alumina, retarded the scale growth and improved the adhesion between the α-Al_2O_3 layer and the Cr_2AlC film [242]. Shang et al. [159] reported that alloying Cr_2AlC with Si caused an increase in Al_2O_3 scale thickness by increasing the nucleation density of Al_2O_3. Therefore, Cr_2AlC provides great potential for utilization as protective coatings at high temperatures, and its high-temperature oxidation resistance can be further improved by tailoring the deposition process and by doping with appropriate elements.

Even though the synthesis and high-temperature oxidation behavior of Cr_2AlC coating in air have been explored, there is no work focusing on the evaluation of Cr_2AlC as protective coatings on zirconium-based alloys and the examination of its high-temperature oxidation behavior in humid atmosphere. In this chapter, synthesis, characterization and high-temperature oxidation in steam of Cr_2AlC-based coatings on Zircaloy-4 substrates are described.

6.2 Experimental arrangement

All experimental procedures related with deposition, thermal annealing, characterization and high-temperature steam oxidation of Cr_2AlC coatings herein were carried out using the similar setup as reported in subchapter 4.2 for the Ti_2AlC coatings. The Ti target was replaced by a 75 mm diameter, cylindrical Cr target. The nanoscale multilayer approach was maintained for as-deposited Cr-C-Al coatings. The thicknesses of each elemental layer were changed to around 7 nm for chromium, 2 nm for carbon and 4 nm for aluminum, calculated according to the stoichiometric ratio (i.e. 2:1:1) in Cr_2AlC and considering their theoretical densities. The measured deposition rate was about 0.8 nm/s for Cr at 200 W RF power. All the deposition parameters were the same except the holding time at each individual target was slightly adjusted. First, Cr-C-Al multilayer coatings with around 3 μm thickness were deposited on Si(100) wafer and polished alumina substrates. The coatings on Si(100) wafers were used to determine the chemical composition, and coatings on alumina substrates were subjected to heat treatment in pure argon for XRD and *in-situ* HTXRD measurements to identify the phase evolution. Based on previous literatures, the annealing temperatures of individual sample were selected below 600°C [185,248]. The HTXRD measurement was implemented as before from 300°C to 1000°C with a temperature step of 20 K.

Coatings on the Zircaloy-4 substrate consisted of two designs and their schematic views are depicted in Figure 6.2. In the previous chapters, it was demonstrated that the adherence of the coatings was reduced when using a binary carbide interlayer as diffusion barrier. Therefore, for the coatings in the Cr-C-Al system, both designs utilized a pure Cr interlayer aiming as bonding layer and diffusion barrier layer. A thin metallic layer acting as bonding layer has been used in numerous applications to improve the adherence of hard nitride coatings [50,52]. The thickness of the Cr interlayer was around 500 nm, which was deposited by only switching on the Cr target power without rotating the substrate holder. In the first design, the periodical stack has been repeated with a thickness of ~ 6 μm. Hence, the total film thickness was about 6.5 μm. To avoid the potential fast dissolution of Al within the coatings during reactor normal operation (Figure 1.5 in section 1.3), in the second design the periodical stack was reduced to ~ 4.5 μm thick and a Cr overlayer with a thickness of ~ 1.5 μm was deposited on the top. Both as-deposited coatings were subjected to heat treatment in argon, and then their high-temperature oxidation behavior at 1000°C in steam was examined. Transient oxidation tests from 300°C to 1000°C or 1200°C in steam using as-deposited coatings without additional annealing were also performed. The heating and cooling rates were kept at 10 K/min.

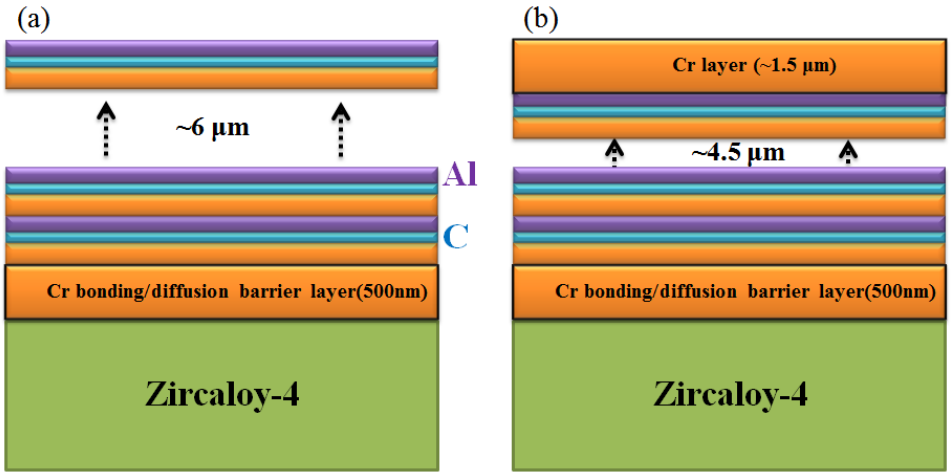

Figure 6.2 Schematic representations of two designs of the as-deposited Cr-C-Al multilayer coatings on Zircaloy-4 substrate. (a) without and (b) with a 1.5 µm Cr overlayer.

6.3 Coatings on Si and alumina substrates

6.3.1 Composition and phase evolution

The as-deposited coatings on Si and alumina substrates only consisted of the Cr-C-Al multilayer stacks without the Cr barrier layer or Cr overlayer. The overall chemical composition of the as-deposited coating on Si(100) wafer determined by EPMA is: Cr: 54.5 at.%, Al: 26.1 at.%, C: 19.2 at.%, and O: 0.3 at.%. Similar as reported previously for the Ti-C-Al coatings, the C content of the Cr-C-Al coating is slightly lower related to desired value (25 at.%). Overall, the composition agrees relatively well with the ideal stoichiometry of the desired Cr:C:Al ratio of 2:1:1 in the Cr_2AlC MAX phase.

Figure 6.3 shows the XRD patterns of the as-deposited Cr-C-Al coating and the annealed ones at 450°C, 500°C and 550°C in argon for 10 min on polished alumina substrates of individual samples. All the diffraction peaks attributed to Al_2O_3 phase belong to the substrate. As expected, the as-deposited coating was mainly composed of nanocrystalline Cr (JCPDS #06-0694) and Al (JCPDS #04-0787) layers as well as amorphous C layers. After annealing at 450°C, the evolution of various diffraction peaks was clearly visible in the diffractograms. The elemental multilayers transformed to a mixture of Cr-Al intermetallic compounds and chromium carbides. The broad signals at 2θ about 41.5° and 43.7° most probably originated from the Al_9Cr_4 (330) reflection (JCPDS #44-1294) and the Cr_7C_3 (151) reflection (JCPDS #44-1294), respectively. The broad feature indicated the weak degree of crystallinity or even amorphous structure considering the low annealing temperature. Annealing at 500°C already triggered the crystallization of the Cr_2AlC MAX phase. The specific diffraction peak at 13.6° could be unambiguously assigned to the Cr_2AlC (002) reflection (JCPDS #29-0017). Therefore, it could be deduced that the growth of Cr_2AlC MAX phase was due to diffusion reactions among Cr-Al intermetallic compounds and chromium carbides. Coatings annealed at 550°C resulted in the formation of phase-pure Cr_2AlC MAX phase. No competing or metastable phases like binary chromium carbides were detected. Furthermore, all major signals detected after annealing at 550°C coincided with the peak positions of (00l) basal planes of

Cr_2AlC. This observation indicated that the coatings possessed a preferred (00l) texture where the basal planes of the Cr_2AlC crystal were aligned parallel to the substrate surface and the previously as-deposited nanoscale multilayers. The relatively broad feature of the diffraction peaks revealed that the Cr_2AlC grains are very fine.

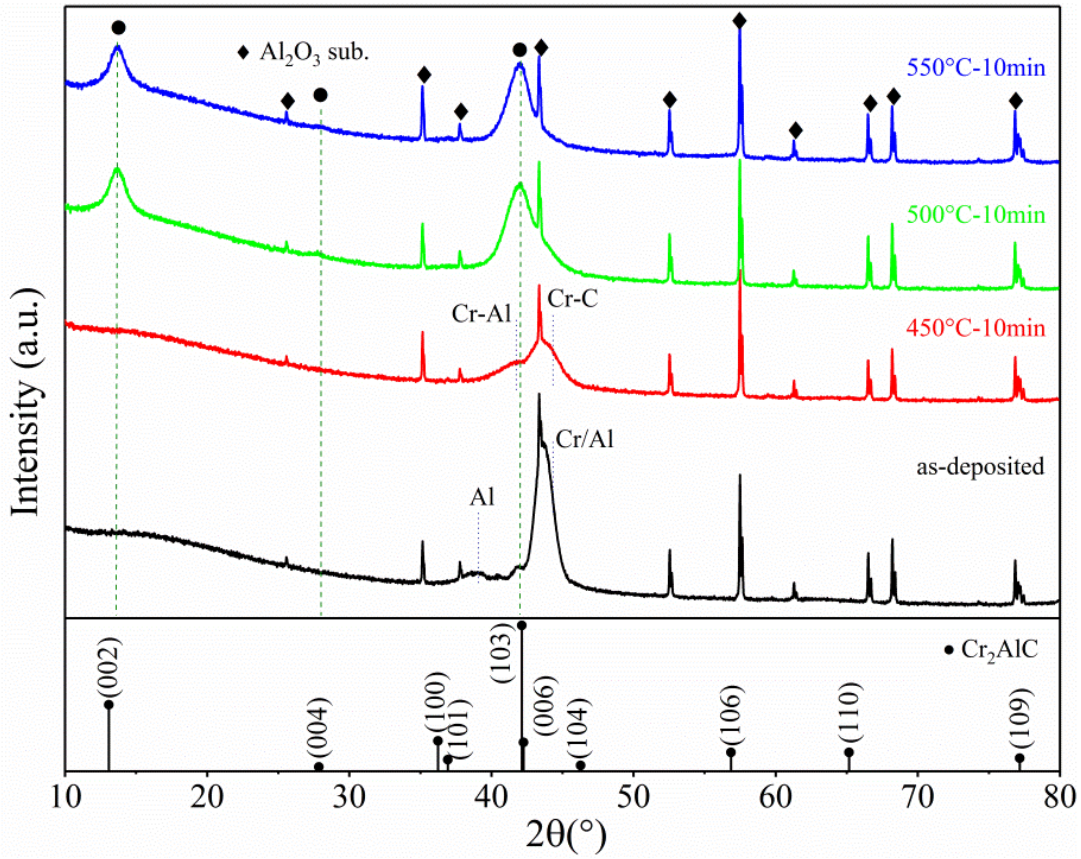

Figure 6.3 XRD patterns of as-deposited Cr-C-Al coating and 450°C, 500°C and 550°C 10 min annealed coatings in argon on alumina substrates.

Figure 6.4 illustrates the *in-situ* HTXRD patterns of the Cr-C-Al coating on Al_2O_3 substrate, showing the evolution of diffraction peaks and signal intensities as a function of annealing temperature. As shown in Figure 6.4(a), the crystallization and growth of Cr_2AlC MAX phase crystals was confirmed. The high intensities of the (002) and (006) lattice planes further identified the preferred (00l) orientation of the Cr_2AlC crystals, as observed in the individually annealed samples. Both peaks became sharper and stronger with increasing annealing temperature, showing improved degree of crystallinity and high stability of the Cr_2AlC coating. It is worthwhile mentioning that at temperatures higher than around 800°C lower intensity peaks at 2θ of around 36.4° and 42.1° that could be assigned to the Cr_2AlC (100) and (103) planes appeared and grew. This observation suggested that high-temperature annealing activated grain growth and/or coalescence in other directions apart from the *c*-axis. Figure 6.4(b) shows selected enlarged views of the patterns from 300°C to 500°C. By comparing the patterns, it reveals that the nanoscale elemental multilayer retained largely stable up to around 420°C. Higher annealing temperatures led to mutual reaction as shown by the gradual shift of reflection position at 2θ of around 44°. The onset

crystallization temperature of Cr_2AlC MAX phase was found to be around 480°C. This finding is consistent with the results obtained from individually annealed samples (below 500°C).

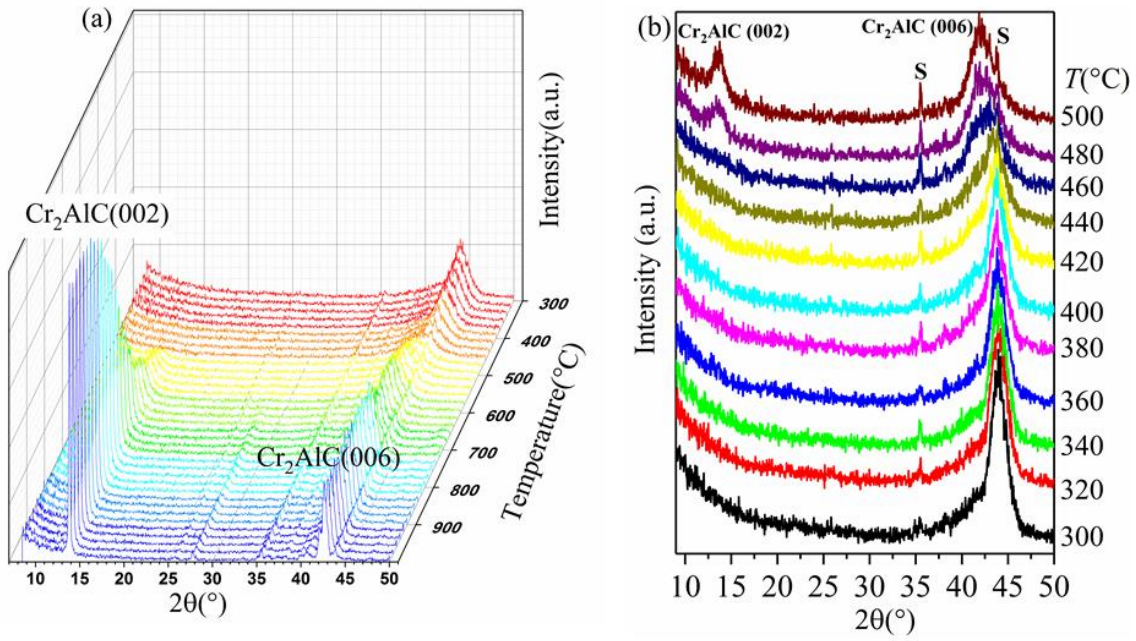

Figure 6.4 *In-situ* HTXRD patterns of the Cr-C-Al coating on Al_2O_3 substrate during annealing in argon with a temperature step of 20 K: (a) waterfall plot of full temperature range from 300°C to 1000°C, and (b) selected enlarged view of the patterns from 300°C to 500°C showing the evolution of diffraction signals and intensities as a function of annealing temperature. S stands for alumina substrate.

6.3.2 Mechanical properties

The hardness and reduced Young's modulus with the standard deviation of the coatings on alumina substrates before and after annealing measured by nanoindentation are displayed in Figure 6.5. The measured indentation hardness and reduced Young's modulus of the as-deposited Cr-C-Al coating were 12.9 ± 1.8 GPa and 204.2 ± 19.4 GPa, respectively. The hardness value was nearly two times higher than that of the as-deposited Ti-C-Al coating. The higher hardness of the as-deposited Cr-C-Al coating could be interpreted in terms of extremely brittle nature and high hardness of pure Cr at room temperature [250]. Both the hardness and the modulus were almost unchanged after annealing at 450°C. The hardness slightly increased to 16.9 GPa at 500°C, and decreased to 14.6 GPa at 550°C. The reduced Young's modulus gradually increased reaching around 247.8 GPa at annealing temperature 550°C. These values are similar to those published in literature for Cr_2AlC MAX phase coatings deposited by magnetron sputtering [251].

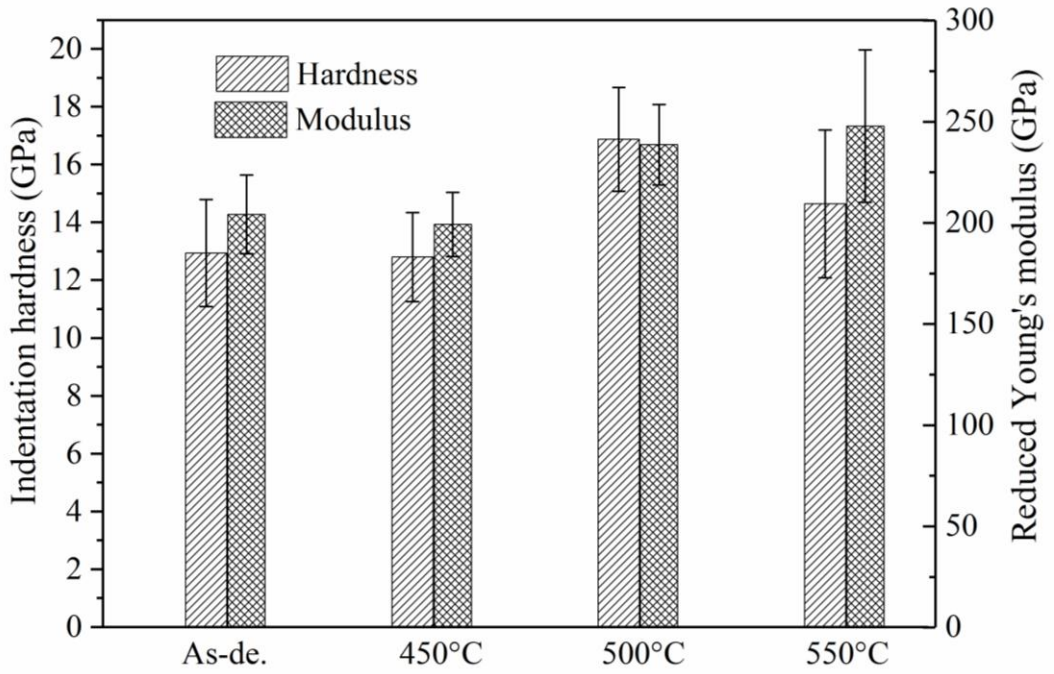

Figure 6.5 Indentation hardness and reduced Young's modulus of the Cr-C-Al coatings on alumina substrates before and after annealing at different temperatures.

6.4 Coatings on Zircaloy-4 substrates

6.4.1 Characterization

Figure 6.6 shows the XRD patterns of the two designs of coatings without and with a surface Cr overlayer on Zircaloy-4 substrates before and after annealing in argon at 550°C for 10 min. In case of as-deposited coatings without the surface Cr layer, a broad signal at around 44° and another one with much lower intensity at 38° exist that could be assigned to Cr (110) reflection and Al (111) reflection, respectively. As expected and similar to the coatings on alumina substrate, the chromium and aluminum layers consisted of nanocrystalline grains with relatively low crystallinity and the carbon layers were grown in an amorphous state for the as-deposited coatings. However, an additional diffraction signal corresponding to Cr (200) reflection appeared for the coatings with the surface Cr layer. It suggests that the nanoscale multilayer stacks restrict the growth of the chromium nanolayers with specific preferential orientation, i.e. Cr (110). The thick Cr overlayer can grow randomly without any preferential orientation.

After annealing, the XRD patterns displayed the formation of phase-pure Cr_2AlC MAX phase for coatings without the surface Cr layer. Both Cr_2AlC and Cr phases were identified, but no other competing phases were observed for coatings with the surface Cr layer after annealing. The diffraction peaks belonging to Cr became sharper and were slightly shifted to higher diffraction angles, which indicated grain growth of the Cr overlayer and a reduction of the internal stresses within the coatings by thermal annealing effect.

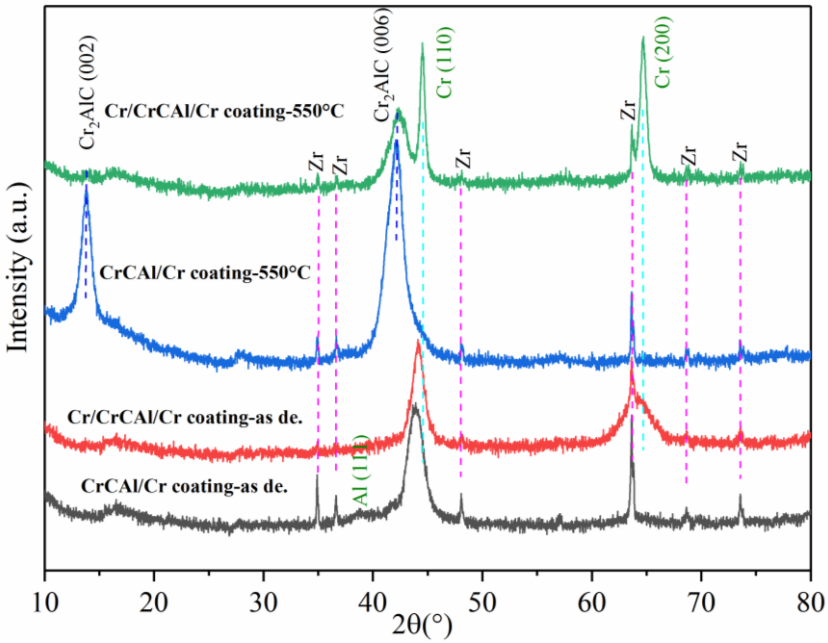

Figure 6.6 XRD patterns of coatings without or with a surface Cr overlayer on Zircaloy-4 substrates before and after annealing in argon at 550°C for 10 min.

Figure 6.7 and Figure 6.8 display the typical surface micrographs of the coatings before and after annealing at 550°C, respectively. As seen in Figure 6.7, both as-deposited coatings are dense, smooth and crack free. The enlarged surface view indicate d that the coatings are composed of very fine grains. Even though the coatings remained adherent and uniform without spallation as depicted in Figure 6.8, parallel micro-cracks were observed on both coating surfaces after annealing. The high mismatch of CTEs between the Cr_2AlC coating (11~13.3 × 10^{-6} K^{-1}) and the Zircaloy-4 substrate (~6 × 10^{-6} K^{-1}) likely change the internal stresses from compression state before annealing to tensile state after annealing, making the coatings prone to cracking.

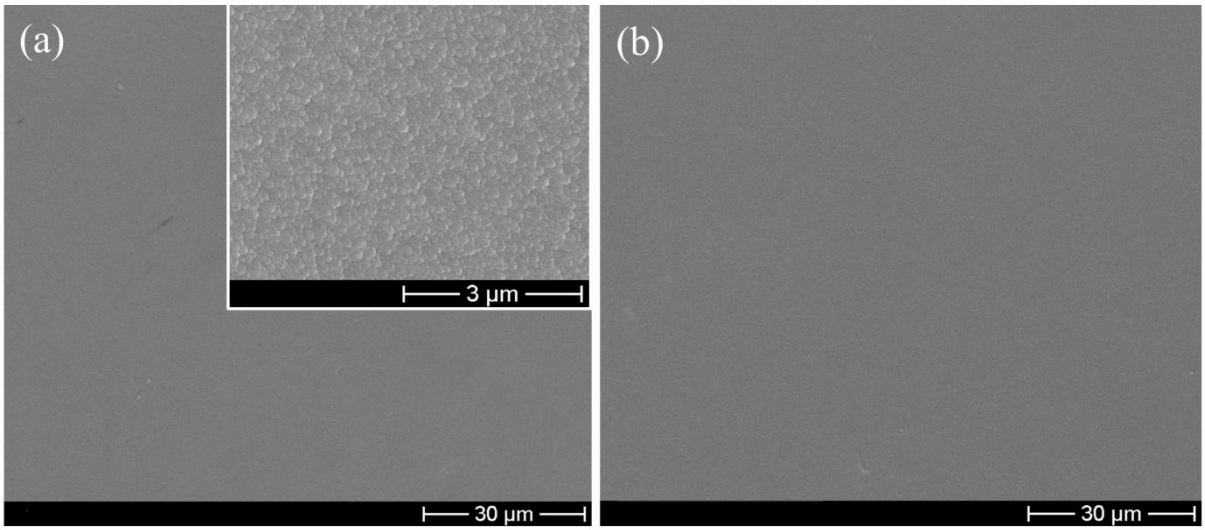

Figure 6.7 Surface top view SEM images of the as-deposited coatings on Zircaloy-4 (a) without and (b) with a surface Cr overlayer. The inserted image in (a) shows a higher magnification view.

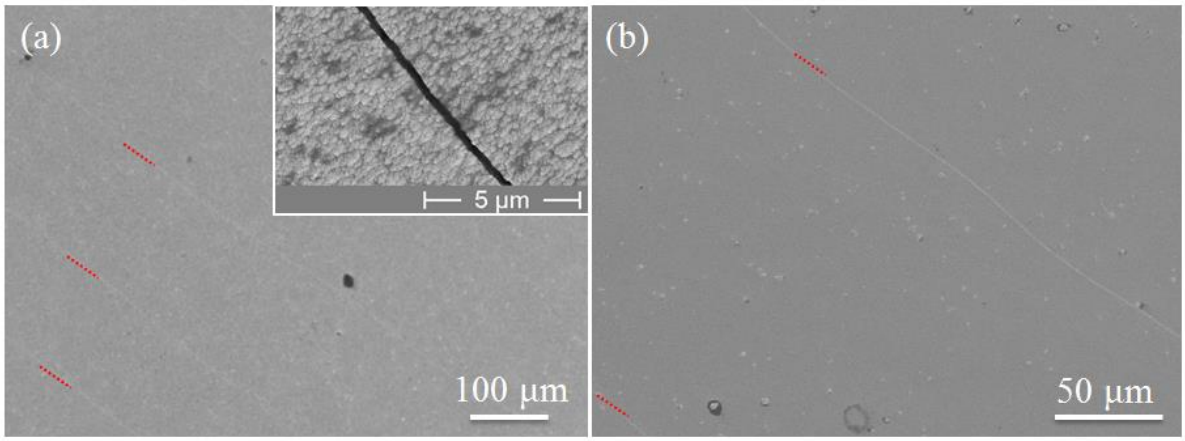

Figure 6.8 Surface top view SEM images of the 550°C annealed coatings on Zircaloy-4 (a) without and (b) with a surface Cr overlayer. Red dotted lines are guidance for micro-cracks; the inserted image in (a) shows a higher magnification view of a micro-crack.

Figure 6.9 presents cross-sectional SEM images of the two designs of coatings after annealing at 550°C. The sublayers could be easily distinguished via different contrasts and the interfaces were sharp and clear. The overall coating thicknesses including each individual sublayer are consistent with the predicted values based on measured deposition rates as depicted in Figure 6.9. The coatings remained dense, free of voids after annealing. The micro-cracks seem to have not penetrated through the coatings and are partially blocked by the multilayer structure.

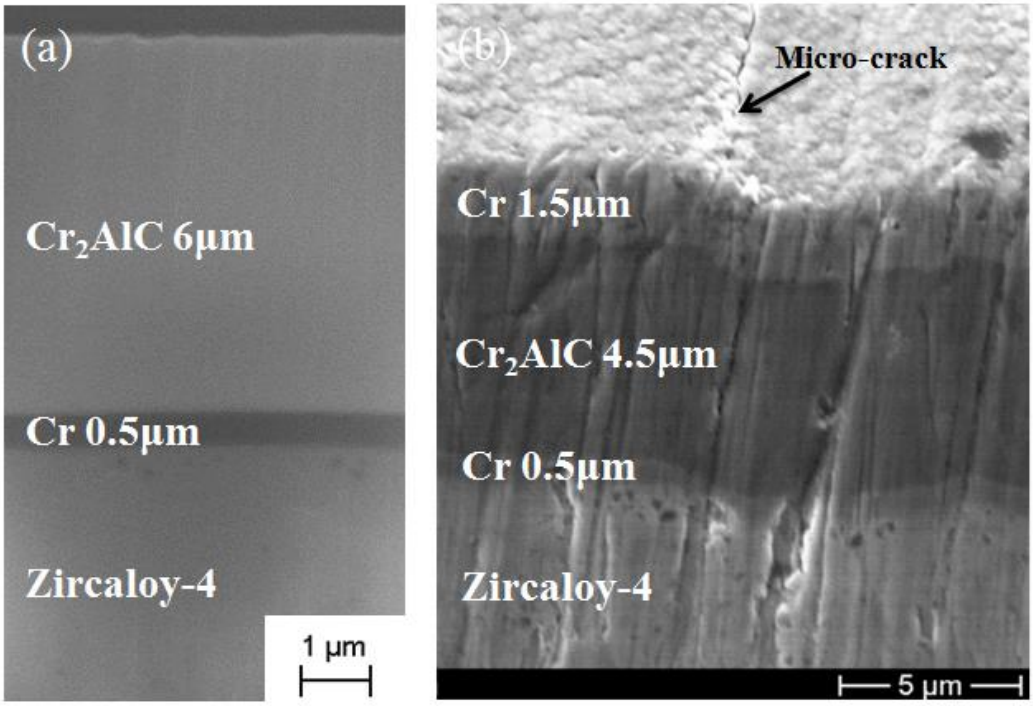

Figure 6.9 Cross-sectional SEM images of the 550°C annealed coatings on Zircaloy-4 (a) without and (b) with a surface Cr overlayer. Note sample (a) and (b) are prepared by FIB and cutting, respectively; sample (b) is slightly titled during imaging.

In order to identify the phase evolution and interface microstructure after annealing, the annealed coatings were additionally characterized by TEM. Figure 6.10 shows the typical overview bright-field TEM image and HRTEM images at two interfaces and in the middle of the coating without a surface Cr overlayer on Zircaloy-4. A columnar microstructure along the growth direction of the Cr interlayer was evident from the cross-sectional overview TEM image at a low magnification. On the other hand, the Cr_2AlC layer was composed of nanocrystallites. The thickness of the Cr bonding layer was confirmed to be around 500 nm and the outer Cr_2AlC coating was around 6.2 μm thick. The HRTEM image (number 1) revealed that a thin interdiffusion/reaction layer, around 10 nm thick, developed at the Zircaloy-4 substrate/Cr bonding layer interface during annealing as indicated by the black arrows. No apparent interdiffusion layer was found at the Cr bonding layer/Cr_2AlC coating interface (number 2). Transformation of the nanoscale elemental multilayers to the Cr_2AlC MAX phase was unquestionably proved by the unique layered structure and the inserted FFT image. However, the image (number 3) revealed a relatively low degree of crystallinity and the sizes of the Cr_2AlC grains were only approximately 10 nm. The low annealing temperature combined with the short dwell time here, i.e. 550°C 10 min, limited the growth and coalescence of the crystallites.

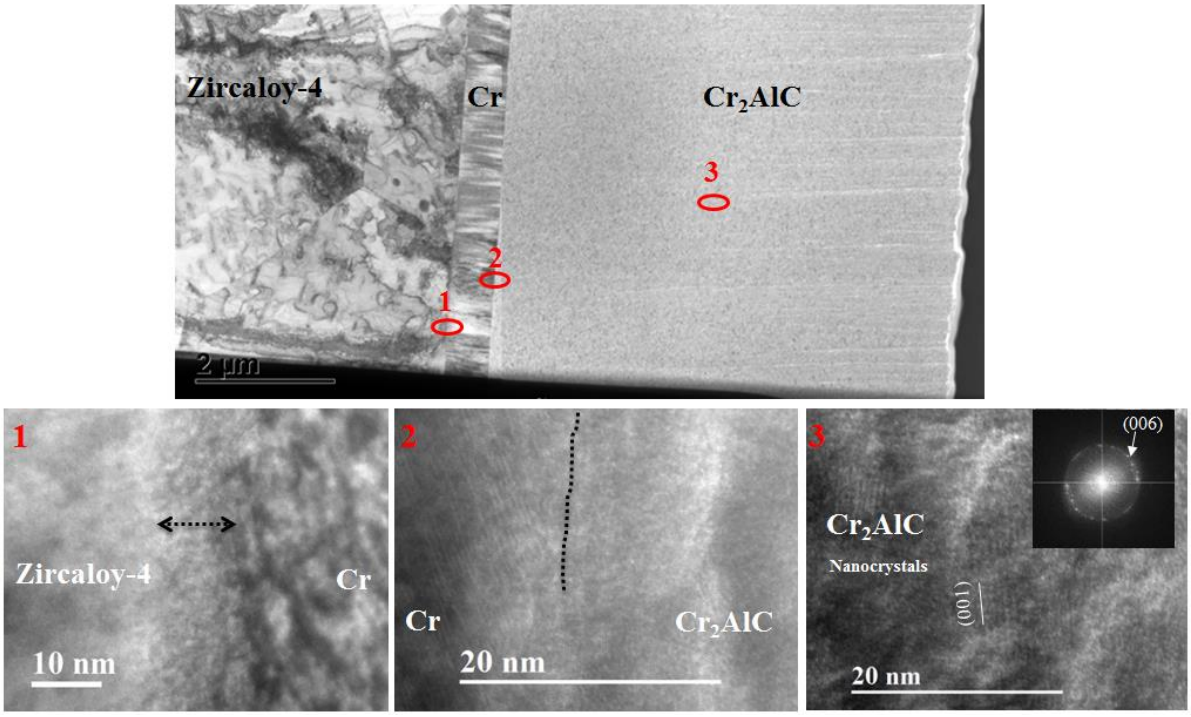

Figure 6.10 Bright-field TEM images of the coating without a surface Cr overlayer on Zircaloy-4 after annealing at 550°C for 10 min. The upper image is a general view and the images below are detailed views at two interfaces and in the middle of the coating as marked by different numbers. The inset in image number 3 describes the corresponding FFT of the image.

EDS mapping at the Cr/Cr_2AlC interface was conducted to examine the diffusion behavior during annealing and the images are displayed in Figure 6.11. The mapping results demonstrated that the distribution of Cr and Al at the Cr/Cr_2AlC interface was uniform and no apparent inward diffusion of Al

from the Cr_2AlC coating into the Cr bonding layer was observed. The findings confirmed that the Cr layer could serve to some extent as diffusion barrier during annealing and/or oxidation.

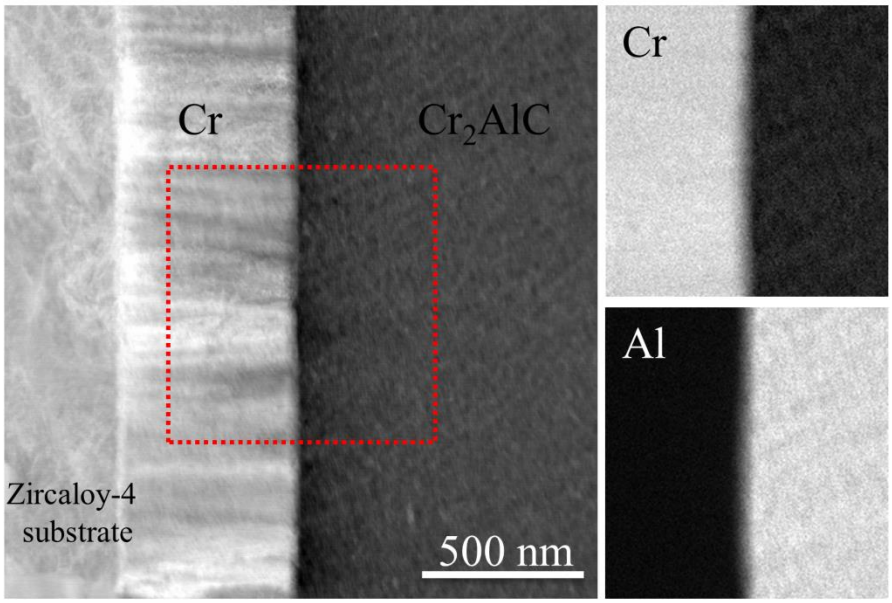

Figure 6.11 STEM images at the Cr_2AlC/Cr interface and corresponding EDS mapping at the red rectangle area of Cr and Al of the coating without a surface Cr overlayer after annealing at 550°C for 10 min.

6.4.2 High-temperature oxidation in steam

High-temperature oxidation tests up to 1200°C in steam of the coated Zircaloy-4 samples were conducted to investigate the oxidation behavior of the two types of coatings. Two kinds of tests were performed, namely isothermal oxidation tests of annealed samples and transient oxidation tests of as-deposited coated samples without additional annealing.

6.4.2.1 Isothermal oxidation of annealed samples

Figure 6.12 shows the oxidation kinetics, i.e. the mass gain per unit area as a function of oxidation time, of the coated and annealed samples at 1000°C in steam for 1 hour. For comparison, the data of an uncoated Zircaloy-4 sample is also included. The oxidation kinetics of polished Zircaloy-4 obeyed a parabolic law and the weight gain reached 25.06 mg/cm^2 after oxidation. The high-temperature oxidation resistance of both types of coated Zircaloy-4 was remarkably improved over the uncoated Zircaloy-4 and the weight gains were only around 3.77 mg/cm^2 under same condition. The mass gains of the coated specimens are about 1/8 of that of the uncoated one. In addition, on the specimen edges, severe oxidation occurred as observed for the coatings presented in previous chapters. The majority of the mass gains were attributed to the fast oxidation of improper or uncoated four edges of the Zircaloy-4 substrate at this high temperature. Thus, the mass gain values cannot exactly reflect the oxidation behavior and one may underestimate the actual oxidation resistance improvements of the coatings. Overall, the coated specimens exhibited extremely slow weight gain rates without accelerated oxidation during the whole exposure. Both coatings provide outstanding performance against steam oxidation at 1000°C.

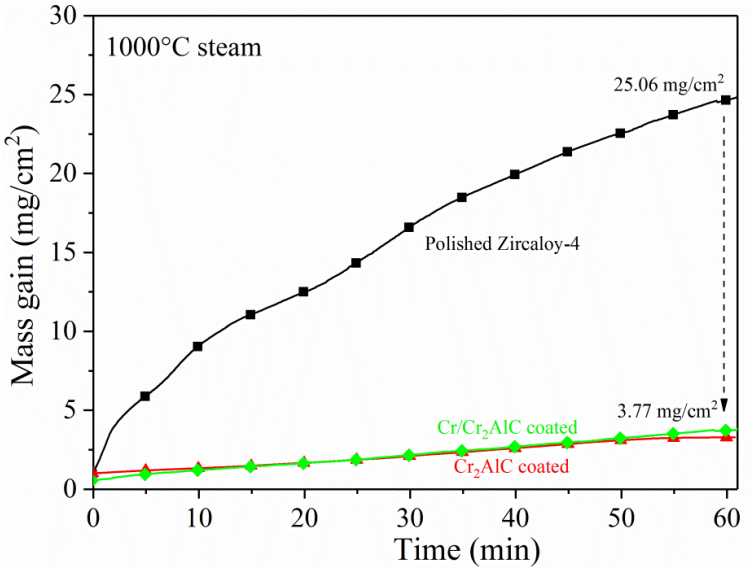

Figure 6.12 Oxidation kinetics of the coated and uncoated Zircaloy-4 samples at 1000°C in steam for 1 hour.

XRD analyses was performed to identify the oxide scale growth on the surface of both coatings after oxidation and the results are displayed in Figure 6.13. The principal phase found was the Cr_2AlC MAX phase for the coatings without the Cr overlayer and Cr_2O_3 for the coatings with the Cr overlayer, respectively. Additionally, minor contributions of phases including α-Al_2O_3 and binary chromium carbides (most likely Cr_7C_3 and/or Cr_3C_2) also existed for coatings without the Cr overlayer. This indicated that a thin alumina oxide scale grew on the surface of the Cr_2AlC coating and the outward diffusion of Al toward the surface to oxidize decomposed a small amount of Cr_2AlC MAX phase grains to binary chromium carbides. In comparison, oxidation of the Cr overlayer led to growth of a thick Cr_2O_3 scale on the surface. Due to the probing depth of the X-ray, the beneath Cr_2AlC sublayer probably could not be detected.

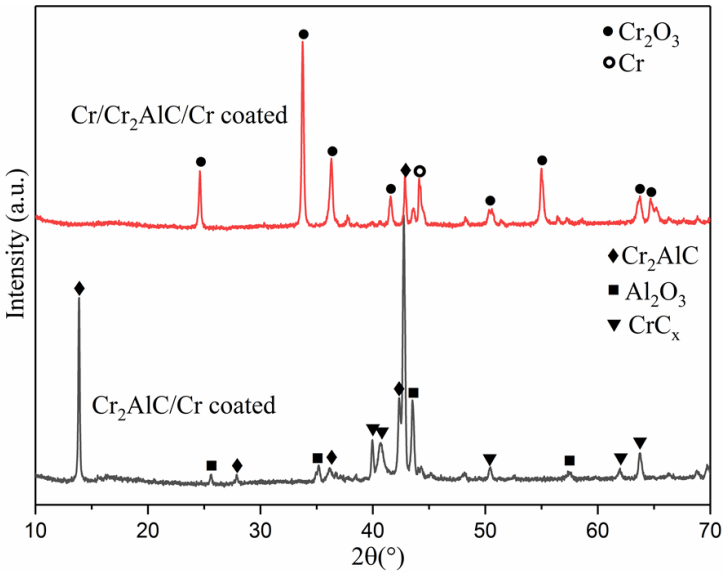

Figure 6.13 XRD patterns of the coated surfaces after oxidation at 1000°C in steam for 1 hour. Top: coating with Cr overlayer, bottom: without Cr overlayer.

Figure 6.14 shows overview and high-magnification SEM images of typical surface morphologies of the coated Zircaloy-4 after oxidation at 1000°C in steam for 1 hour. As shown in Figure 6.14(a) and (b), both coatings remained adherent without delamination or spallation; the oxide scales were smooth, and free of nodules. Additional micro-cracks appeared on the surface of the Cr_2AlC/Cr coating after oxidation and the cracks intersected forming a network. Only original parallel cracks induced by annealing were observed on the surface of Cr/Cr_2AlC/Cr coating. The enlarged surface views in Figure 6.14(a') and (b') indicated that the oxide scale was mainly composed of very fine oxide crystals for the Cr_2AlC/Cr coating, while needle-like oxide grains and equiaxed oxide grains grew on the surface of Cr/Cr_2AlC/Cr coating. As identified by XRD in Figure 6.13, the oxide scales were presumed to be α-Al_2O_3 and Cr_2O_3, respectively. The α-Al_2O_3 scale (Figure 6.14(a')) displayed a much denser surface morphology compared to that of Cr_2O_3 scale (Figure 6.14(b')), which consisted of small voids.

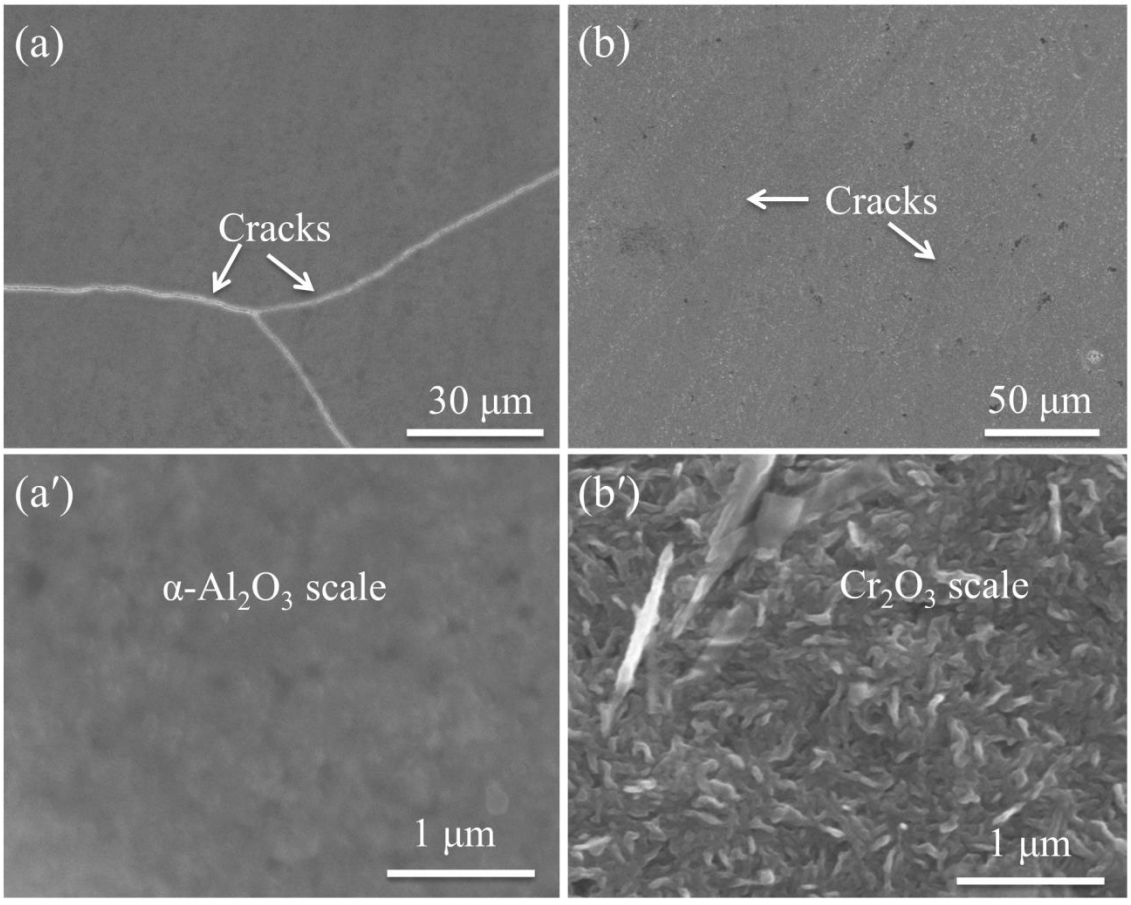

Figure 6.14 SEM images of typical surface morphologies of coated Zircaloy-4 after oxidation at 1000°C in steam for 1 hour. (a) and (a') Cr_2AlC/Cr coated, (b) and (b') Cr/Cr_2AlC/Cr coated.

Cross-sectional SEM images of coated Zircaloy-4 and uncoated Zircaloy-4 after oxidation are presented in Figure 6.15. As shown in Figure 6.15(a), a thin and dense α-Al_2O_3 scale grew on the Cr_2AlC/Cr coating surface and the major part of the coating was not oxidized. The thickness of the α-Al_2O_3 scale was around 0.6 μm and the calculated weight gain according to this scale thickness was just 0.12 mg/cm^2. Oxidation of the Cr/Cr_2AlC/Cr coating resulted in formation of an interesting multilayer structure consisting of

several sublayers. Nearly 80% of the Cr overlayer was oxidized and growth of Cr_2O_3 was apparently much faster than that of α-Al_2O_3 as in shown Figure 6.15(b). But the Cr overlayer can act as a corrosion resistant layer since the Cr_2O_3 scale has proved to be stable and slow growing during PWR normal operation (see section 1.3). However, an autoclave corrosion test under simulated normal operation is needed to prove this claim. One important finding is that steam can penetrate through the Cr_2O_3 scale and the unconsumed Cr layer to oxidize the Cr_2AlC coating beneath. It can be clearly seen that a thin α-Al_2O_3 scale forms at the Cr/Cr_2AlC interface. The relatively porous structure and a high gas diffusion rate in the Cr_2O_3 scale as well as a higher equilibrium oxygen/steam partial pressure of Cr_2O_3 in comparison to that of α-Al_2O_3 (Ellingham diagram in Section 2.2) are responsible for the appearance of this thin α-Al_2O_3 layer beneath the Cr overlayer. Obviously, the α-Al_2O_3 scale can provide better high-temperature oxidation resistance than the Cr_2O_3 scale. In comparison, oxidation of uncoated Zircaloy-4 under the same condition led to growth of a porous, non-protective ZrO_2 layer with significant pores and cracks, Figure 6.15(c). The thickness of the ZrO_2 layer was about 135 µm, more than 200 times thicker than the oxide scales on the coatings.

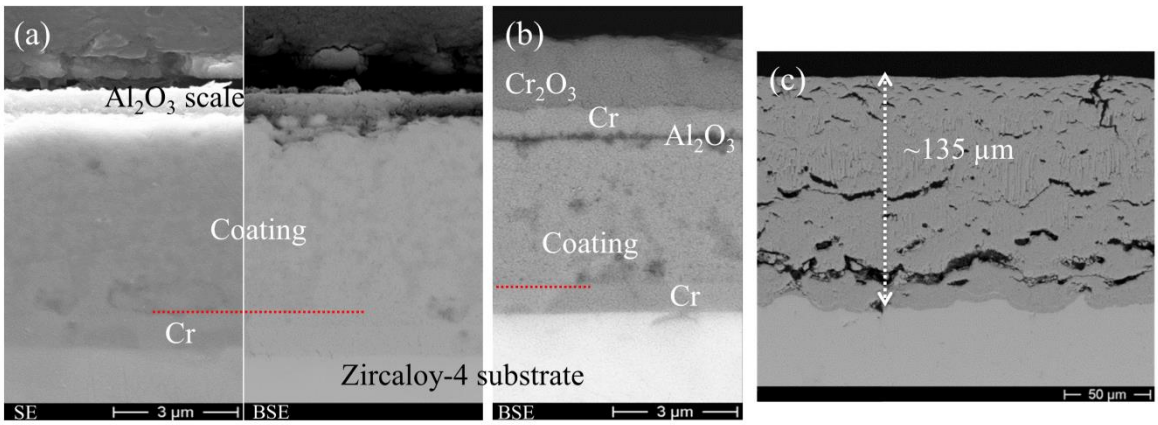

Figure 6.15 Cross-sectional SEM images of coated and uncoated Zircaloy-4 after oxidation at 1000°C in steam for 1 hour. (a) Cr_2AlC/Cr coated, (b) Cr/Cr_2AlC/Cr coated and (c) uncoated Zircaloy-4.

Figure 6.16 and Figure 6.17 show the EDS mapping of the Cr_2AlC/Cr and Cr/Cr_2AlC/Cr coated Zircaloy-4 after oxidation at 1000°C in steam for 1 hour, respectively. The EDS mapping revealed that the oxide scale formed on Cr_2AlC/Cr coatings was composed of nearly pure alumina, presumably with minor chromia solution. Locally fast diffusion of Al from the Cr_2AlC coating into the Cr bonding layer was shown in Figure 6.16 EDS mapping, most probably after the columnar grain boundaries of the Cr layer. However, no significant mutual diffusion between the Cr layer and the Zircaloy-4 substrate was confirmed. EDS mapping of Cr/Cr_2AlC/Cr coated Zircaloy-4 proved the sublayer structure as identified by SEM-BSE in Figure 6.15(b). A Cr_2O_3 scale formed on the surface due to oxidation of the Cr overlayer and a thin alumina layer grew at the Cr/Cr_2AlC interface. Clusters with different brightness, i.e. rich or poor in Al within the Cr_2AlC layer for both coatings, appeared. The residual Al content in the Cr_2AlC layer was obviously higher for the Cr/Cr_2AlC/Cr coating than that of the Cr_2AlC/Cr coating due to less oxidation.

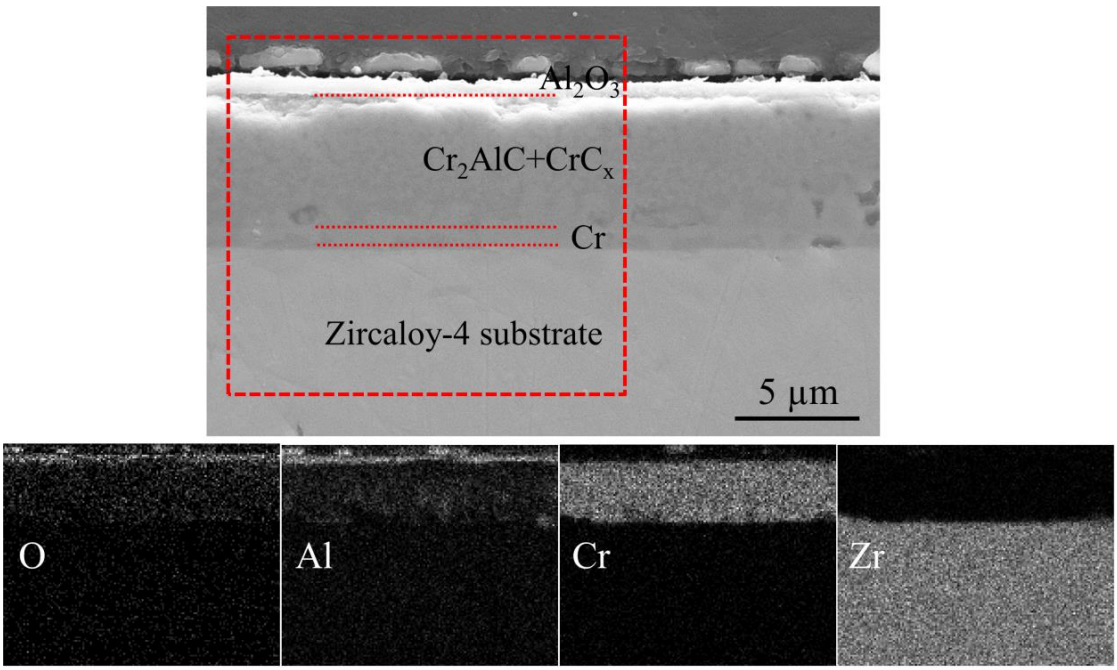

Figure 6.16 Cross-sectional SEM images of Cr_2AlC/Cr coated Zircaloy-4 and corresponding EDS mapping at the red rectangle area after oxidation at 1000°C in steam for 1 hour.

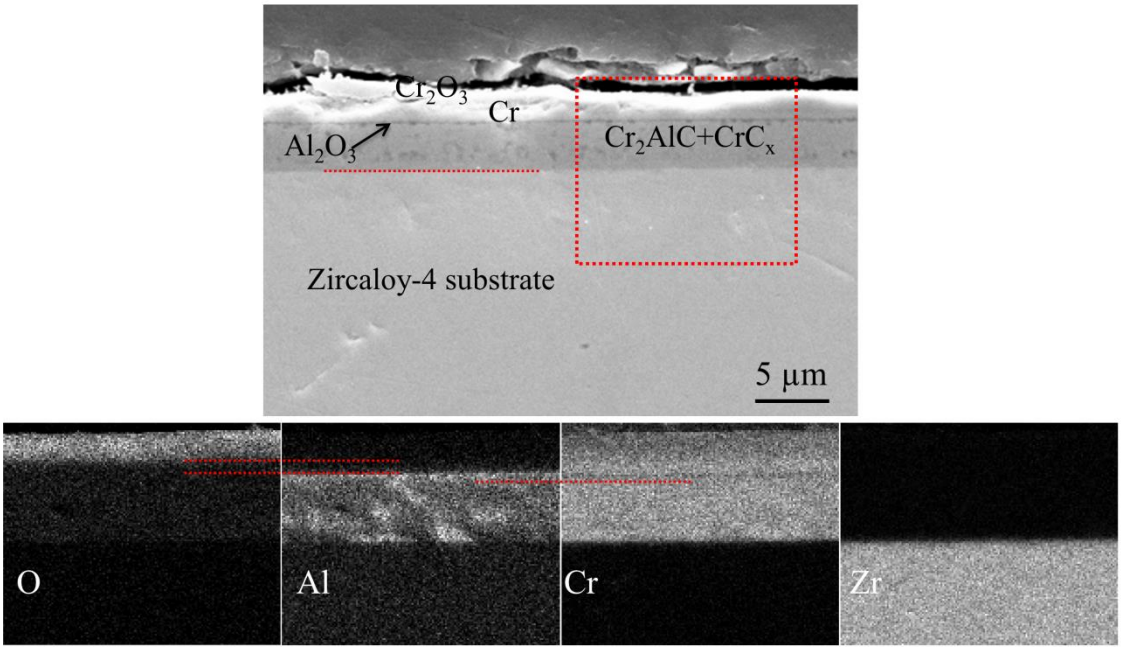

Figure 6.17 Cross-sectional SEM images of Cr/Cr_2AlC/Cr coated Zircaloy-4 and corresponding EDS mapping at the red rectangle area after oxidation at 1000°C in steam for 1 hour.

Cracks are obviously undesirable for thin coatings since they act as fast diffusion channels, which are detrimental to the coating integrity and durability. The influence of the micro-cracks on the performance of the coatings was examined by SEM, and Figure 6.18 shows the cross-sectional SEM-BSE images of typical crack areas of the coated Zircaloy-4 after oxidation. Similar to bulk Cr_2AlC, both coatings possess a

crack-healing capability by fast growth of alumina filling the crack gap. As shown in Figure 6.18, the cracks were completely healed after oxidation at 1000°C for 1 hour and the dense alumina scale suppressed further oxidation of regions adjacent to the cracks and oxidation of the Zircaloy-4 substrate. No apparent attack of Zircaloy-4 substrate by steam around the crack region was confirmed. Two contrasts of white and gray within the Cr_2AlC sublayer, especially in Figure 6.18(a) for the Cr_2AlC/Cr coating, were distinguished. The two phases were virtually uniformly distributed, except slightly high density of the grains with brighter color underneath the scale and adjacent to the scale/coating interface were found. These grains with brighter color were deficient in Al and enriched in Cr and C, presumably to be the Cr_7C_3 and/or Cr_3C_2 phases as shown in the XRD results. The other more gray phase represents originally Cr_2AlC grains.

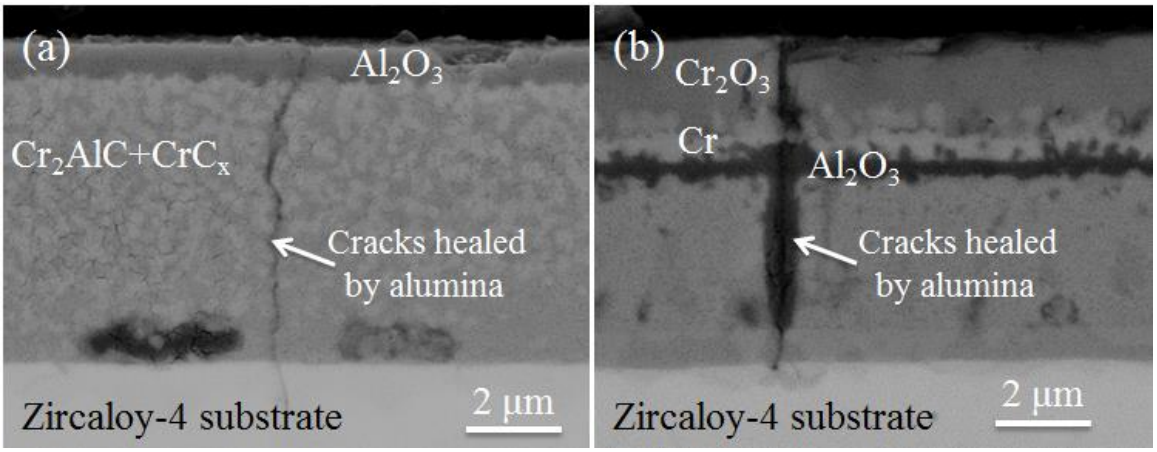

Figure 6.18 Cross-sectional SEM-BSE images of coated Zircaloy-4 after oxidation at 1000°C in steam for 1 hour showing the crack healing capability by growth of alumina. (a) Cr_2AlC/Cr coated, (b) Cr/Cr_2AlC/Cr coated.

6.4.2.2 Transient oxidation of as-deposited coated samples

Even though the micro-cracks within the coatings after annealing are completely healed during high-temperature oxidation, they can be a detrimental factor during hydrothermal corrosion under normal operation. One solution to solve this problem is to use the as-deposited coatings, which also offer the benefit to avoid potential altering the microstructure of Zircaloy-4 substrate by heat treatment. Therefore, transient oxidation tests simulating a typical loss-of-coolant (LOCA) scenario using as-deposited coated samples were performed.

Figure 6.19 shows the mass gain per unit area as a function of time during the transient tests from 300°C to 1000°C and 1200°C with 10 K/min heating rate in steam with a following 10 min holding period. Data of both types of coated samples and an uncoated sample as well as temperature profiles are included. The oxidation rate of uncoated Zircaloy-4 was obviously much faster than that of the coated ones; furthermore, the oxidation rate of uncoated Zircaloy-4 accelerated from approximately 900°C associated with strongly increased mass gain. Both coated samples had similar mass gain during the tests, but clearly lower values, ten times lower at 1000°C and around 4 times lower at 1200°C. All three curves displayed

similar upward tendency during transient oxidation up 1200°C as in Figure 6.19(b), indicating the mass gain of the coated samples was mainly caused by the edge effect. Cross-sectional SEM images shown later will support this claim.

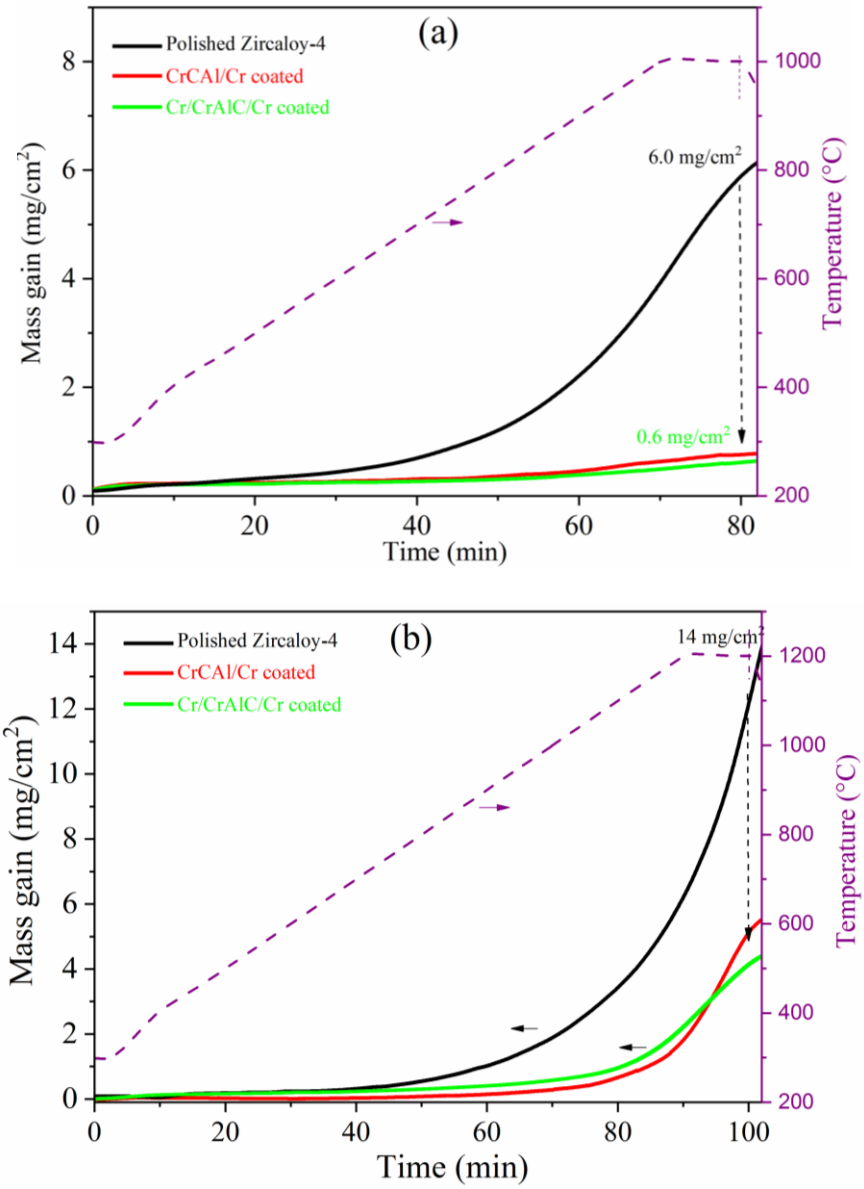

Figure 6.19 Mass gains per unit area vs. time for as-deposited CrCAl-based coated and uncoated Zircaloy-4 samples during the transient tests from 300°C to (a) 1000°C and (b) 1200°C in steam with following 10 min holding time.

XRD patterns of the coated surfaces after transient tests to 1000°C are presented in Figure 6.20; inserted images are appearance of the coated samples after the test. Similar to the annealed samples after isothermal oxidation at 1000°C for 1 hour, the major phase was identified to be the Cr_2AlC MAX phase for the CrCAl/Cr coating and Cr_2O_3 for the Cr/CrCAl/Cr coating after the transient tests. This indicated that the nanoscale elemental multilayers in the as-deposited coatings were transformed to the Cr_2AlC MAX phase during the ramp-heating period. This could be excepted since the onset crystallization temperature for Cr_2AlC was below 500°C and the elemental multilayers are supposed to undergo limited

oxidation before completely converting to the MAX phase. Growth of an α-Al_2O_3 scale during high-temperature oxidation then is guaranteed even though utilization of as-deposited coatings. A thin α-Al_2O_3 scale grew on the surface of the CrCAl/Cr coating as shown by its low diffraction intensity, while a thick Cr_2O_3 scale formed on the Cr/CrCAl/Cr coating. The inserted images revealed that both coatings were adherent without spallation but showing different colors due to growth of different oxide scales. Premature failure of the coatings occurred at the edges/corners of the coated specimens due to severe oxidation of Zircaloy-4 substrate as displayed by the fringes in the inserted images showing sample appearance.

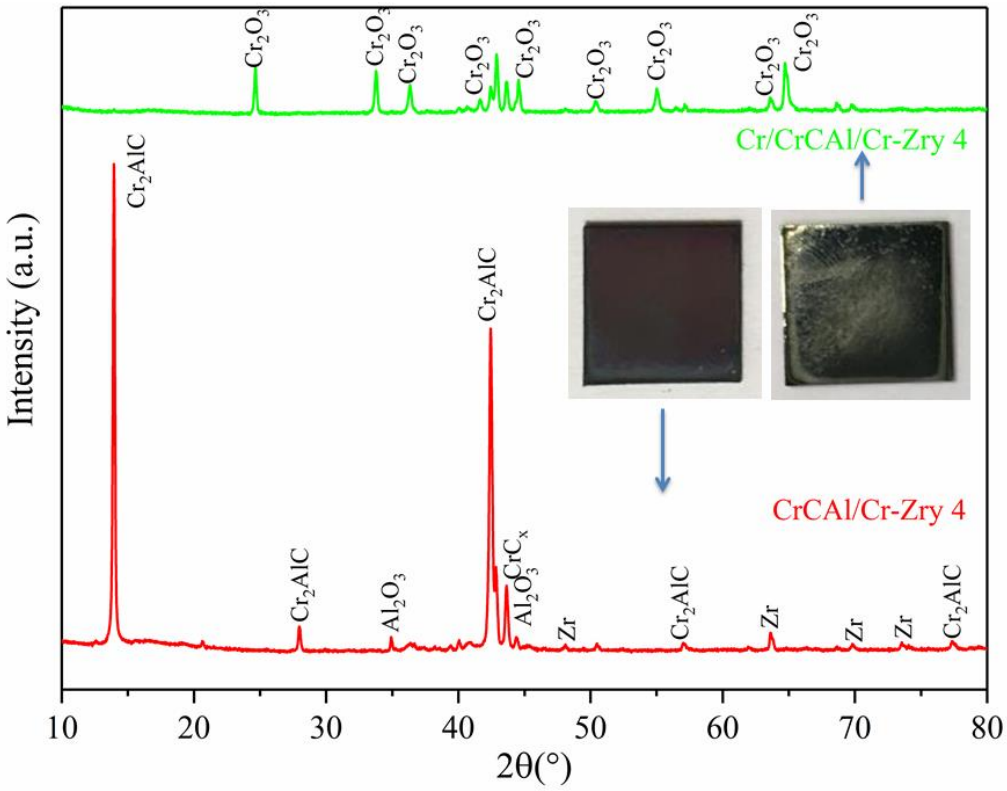

Figure 6.20 XRD patterns of the coated surfaces after transient tests from 300°C to 1000°C in steam with following 10 min holding time. Inserted are digital images of the coated samples after test.

The surface and cross section of the coated Zircaloy-4 samples after the transient tests to 1200°C were examined by SEM, and the typical images are shown in Figure 6.21 and Figure 6.22, respectively. Both coatings remained uniform, smooth without delamination or spallation after the test, but significant cracking of the CrCAl/Cr coating while no cracking of the Cr/CrCAl/Cr coating was observed as shown in Figure 6.21. A thicker CrCAl or Cr_2AlC sublayer in CrCAl/Cr coating likely induced higher stresses within the coating during oxidation due to large CTE mismatch between Cr_2AlC and Zircaloy-4 substrate, leading to the cracking of the CrCAl/Cr coating. However, Cr and Zircaloy-4 have quite similar CTEs, i.e. ~6.8 × 10^{-6} K^{-1} for Cr and ~6.0 × 10^{-6} K^{-1} for Zircaloy-4, which should make the Cr/CrCAl/Cr coating more tolerant to cracking. A thin, dense α-Al_2O_3 scale, less than 1 μm thick, was observed on the CrCAl/Cr coating in Figure 6.22(a). In case of the Cr/CrCAl/Cr coating, the Cr overlayer was completely

oxidized and the oxide scale was composed of two sublayers: an outer Cr_2O_3 layer due to oxidation of the Cr overlayer and an inner α-Al_2O_3 layer due to oxidation of the CrCAl or Cr_2AlC coating beneath. The thickness of the Cr_2O_3 layer was several times larger than that of the α-Al_2O_3 layer. The two oxide layers exhibited good adherence without delamination. Due to the higher oxidation temperature (1200°C here), the volume content of the Al-rich grey areas decreased significantly within the coatings as compared to Figure 6.18 (1000°C). Less grey areas could be detected in Figure 6.22(a) and (b), which corresponded to a significant outward diffusion of Al and consumption of the Cr_2AlC phase through the growth of an α-Al_2O_3 scale. The brighter domains are presumably Cr_7C_3 and/or Cr_3C_2 phases as identified by XRD before. Moreover, the thin Cr bonding layer at the substrate/coating interface could hardly be distinguished and displayed a similar contrast to upper regions of the coatings. The substrate/coating interface is still clearly visible. It is reasonable to assume that significant reaction and interdiffusion occurred between the Cr layer and the CrCAl layer within the coatings due to higher temperature. Oxidation of uncoated Zirclaoy-4 at identical conditions resulted in the formation of a thick ZrO_2 layer (nearly 100 μm thick) as in Figure 6.22(c).

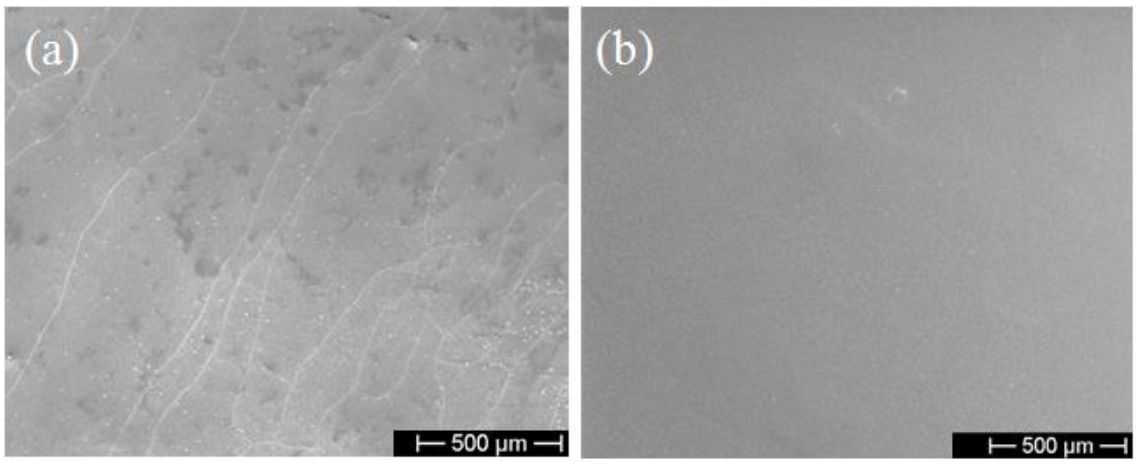

Figure 6.21 SEM images of typical surface morphologies of coated Zircaloy-4 after transient tests from 300°C to 1200°C in steam with 10 min holding time. (a) CrCAl/Cr coated, and (b) Cr/CrCAl/Cr coated Zircaloy-4.

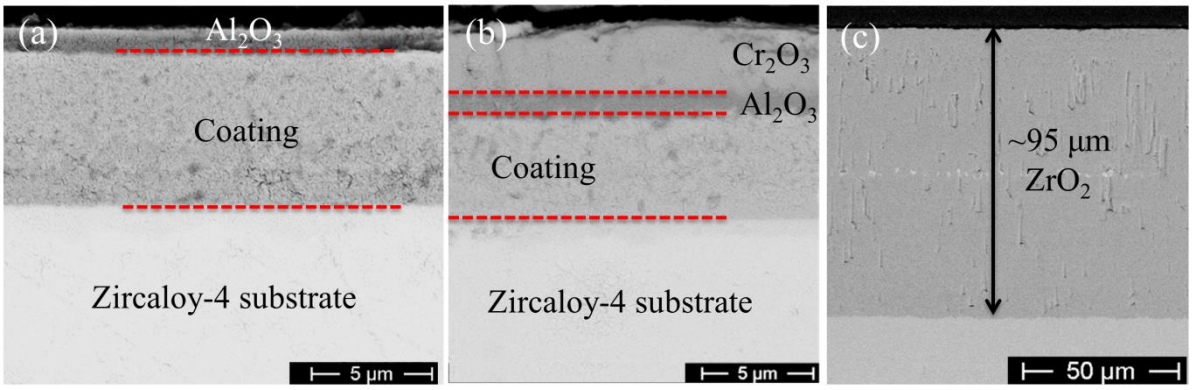

Figure 6.22 Cross-sectional SEM-BSE images of coated and uncoated Zircaloy-4 after transient tests from 300°C to 1200°C in steam with 10 min holding time. (a) CrCAl/Cr coated, (b) Cr/CrCAl/Cr coated and (c) uncoated Zircaloy-4.

Figure 6.23 presents an additional cross-sectional SEM-BSE image at low magnification of CrCAl/Cr coated Zircaloy-4 after the transient test to 1200°C. Obviously, the uncoated edges were severely attacked by the steam and a thick ZrO_2 scale formed. Steam penetrated deeply into the matrix at the corners. Thus, the major part of the mass gain recorded during the tests in Figure 6.19 was attributed to oxidation of the uncoated edges. The coating possesses high adherence without spallation even on the ZrO_2 layer, and only limited local failure of the coatings near the corners was observed. In all other regions, the coating protected the underneath Zircaloy-4 substrate from oxidation.

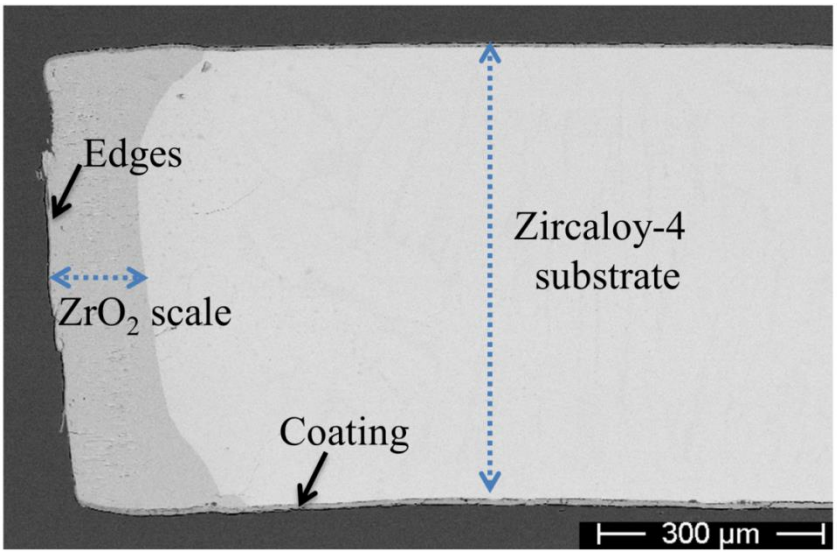

Figure 6.23 Cross-sectional SEM-BSE image at low magnification of CrCAl/Cr coated Zircaloy-4 after transient tests from 300°C to 1200°C in steam with 10 min holding time.

6.5 Discussion

6.5.1 Synthesis of Cr_2AlC MAX phase coatings

One crucial issue of the synthesis of MAX phase thin films using PVD technique either by *in-situ* heating of the substrate or *ex-situ* heat treatment of as-deposited samples is the selection of the processing temperature. Even though the processing temperatures are generally several hundred degrees lower for MAX phase coatings than the typical ranges used for bulk MAX phase synthesis, however, the majority of the 211 MAX phase coatings, like Ti_2AlC and Nb_2AlC, require deposition temperatures higher than 700°C using magnetron sputtering. This relatively high-temperature restricts their utilization on temperature-sensitive substrates. Previous studies suggest that the synthesis of Cr_2AlC MAX phases via sputter deposition could be realized at a relatively low temperature of around 500°C [80,170], which offers the possibility for widespread applications. This study confirms similar findings, i.e. the formation of crystalline Cr_2AlC by solid reaction from initially nanoscale elemental multilayer is located at approximately 480°C. Eklund et al. explain that the M-C bonding energy in MAX phases decreases when M is altered from group 4 to 6 (e.g., from Ti to Cr) and that should kinetically favor M and C surface diffusion successively [63]. Thus, MAX phases with group 5 and 6 transition metals, for instance Cr_2AlC

and V_2AlC, require the lowest synthesis temperatures among the MAX phase carbides. In addition, M-A intermetallics and binary carbides always exist as intermediate phases or competing phases during the synthesis of MAX phase thin films. The formation mechanism of 211 MAX phases proposed previously is based on mutual reactions between the intermetallics and the binary carbides at high temperatures. The reaction path for Cr_2AlC as well as for Ti_2AlC (presented in Chapter 4) follows a similar sequence. As proved by HTXRD measurement, the diffusion and reaction between the elemental multilayers first lead to the formation of Cr-Al intermetallic phases and CrC_x; with increasing annealing temperature the reaction between the intermetallics and CrC_x results in the formation of the Cr_2AlC MAX phase starting from around 480°C.

Figure 6.24 compares the enthalpy and Gibbs free energy of formation for three types of transition metal carbides involved in this study. Lower values mean higher stability of the carbides. Results presented in previous chapters have shown that the onset crystallization temperature of Ti_2AlC MAX phase is approximate 660°C, while no MAX phase formation in the Zr-C-Al system is confirmed within the annealing temperature up to 1200°C. This suggests that the critical temperature of MAX phase growth, at least partially, is associated with the thermodynamic stability of their counterpart binary carbides. The stability increases in the sequence of CrC_x ($Cr_{23}C_6$, Cr_7C_3 and Cr_3C_2), TiC and ZrC. In addition, Cr_2AlC and Ti_2AlC are highly thermodynamically stable and Zr_2AlC is metastable. Therefore, it becomes successively harder converting the binary carbides from Cr to Zr to corresponding high-ordered MAX phase through reaction with other intermediate phases. Moreover, it brings more challenges to produce phase-pure MAX phase products in both bulk form and coatings following this sequence.

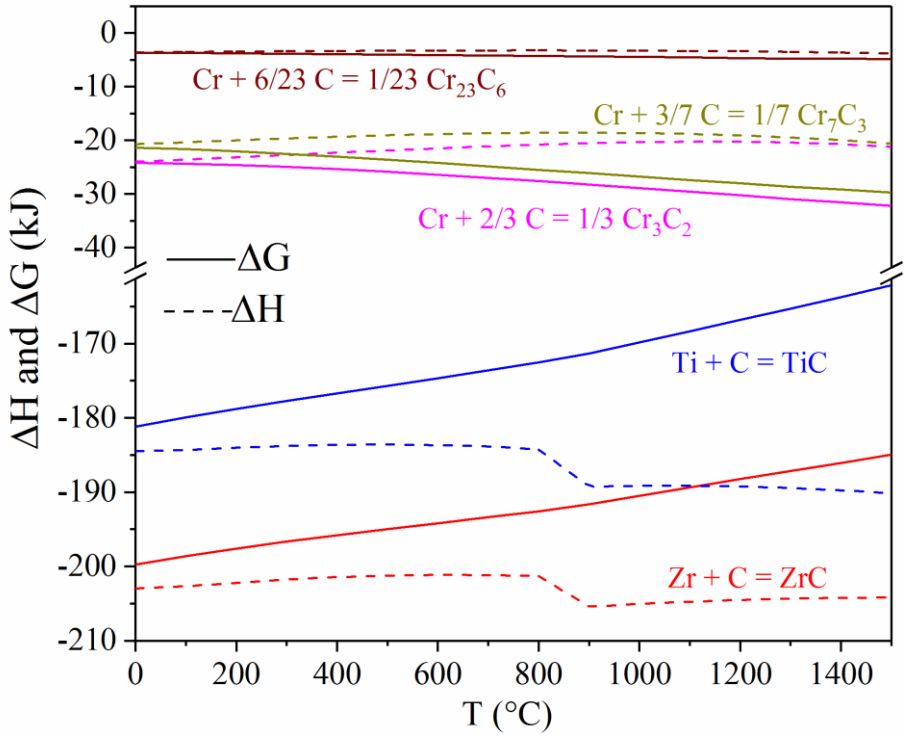

Figure 6.24 Calculated enthalpy and Gibbs free energy (using HSC Chemistry 9) of formation for three types of transition metal carbides involved in this study [252].

Similar to the Ti_2AlC coatings, the Cr_2AlC coatings synthesized here also display a basal plane preferred orientation with the *c*-axis perpendicular to the sample surface and the multilayer stacks. As discussed before, the lower growth rates along *c* compared to the growth along *a*-axis for MAX phase grains combined with the specific nanoscale multilayer architecture in the as-deposited coatings result in textured growth of MAX phases during annealing. This approach offers a universal method for potential tailor-made synthesis of phase-pure and basal plane textured MAX phase films.

6.5.2 Oxidation of Cr_2AlC MAX phase coatings in steam

The oxide scaling behavior of the Cr_2AlC coatings in steam investigated here is similar with respect to the oxidation of bulk ceramic and sputtered coatings in air atmosphere reported before. The coatings exhibit an excellent oxidation resistance up to at least 1200°C even though only few microns thick. The weak M–A bonding compares to the strong directional covalent M–X bonds resulting in higher migration rate of the A element in the MAX phase structure. Thus, in case of Cr_2AlC coatings herein, selective oxidation of Al occurs and growth of a thin α-Al_2O_3 scale on the surface at high temperature is confirmed. In general, depletion of Al adjacent to the scale/coating interface leaves a Cr-C layer mainly made of Cr_7C_3 and/or Cr_3C_2 beneath the alumina scale. This can be clearly understood from the Cr-C-Al phase diagram of the isothermal section at 1273 K in Figure 6.25, in which a loss of Al leads to dissociation of the Cr_2AlC MAX phase into Cr_7C_3 and Cr_3C_2 phases. However, a slight difference for the Cr_2AlC coatings investigated here is that after oxidation the CrC_x grains are comparatively uniformly distributed within the coatings. The origin of this may be that the Cr_2AlC coatings herein are composed of textured nanocrystalline grains and that typical large columnar grains are absent by adopting a two-step synthesis process. Therefore, these features enable fast outward diffusion of Al from the inner region of the Cr_2AlC coatings leaving isolated CrC_x crystallites (Figure 6.16). Besides, columnar grain boundaries can act as short-circuit diffusion paths allowing the fast diffusion of oxidizing gas along the boundaries into the substrate. Internal oxidation was often observed for MAX phase coatings showing typical columnar microstructure [238,247]. No internal oxidation of the coatings or the substrates is shown for the Cr_2AlC coated samples herein due to the unique microstructure, which favors their potential high-temperature application.

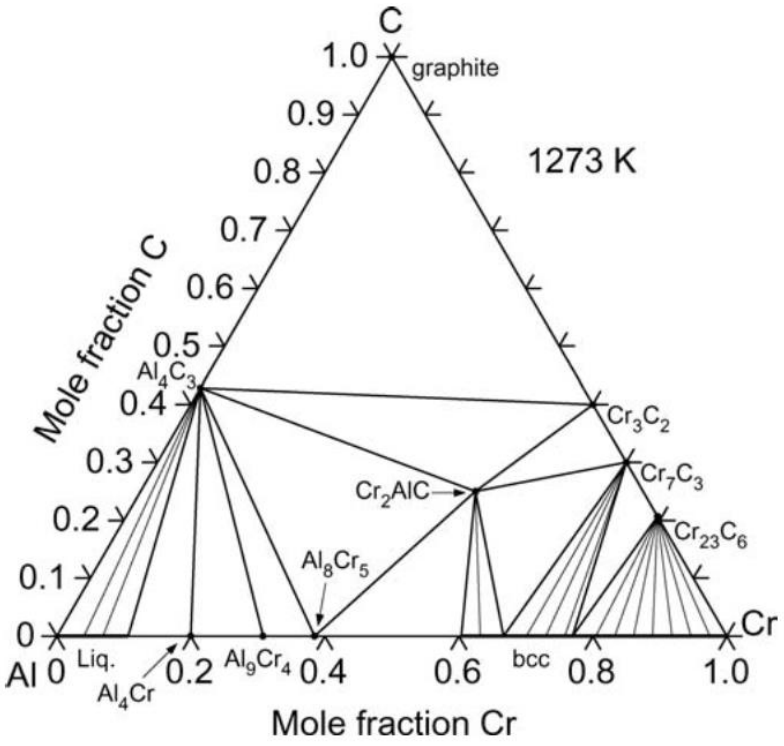

Figure 6.25 Phase diagram of Cr-C-Al system of isothermal section at 1273 K [249].

An oxide scale consisting of both alumina and MO_2 (TiO_2 or ZrO_2) rather than pure alumina forms on the surface of the Ti_2AlC and Zr(Al)C coatings during high-temperature oxidation as presented in previous chapters. However, growth of a nearly pure alumina scale is confirmed on the Cr_2AlC coatings. Cr_2O_3 is believed to act as nucleation sites for α-Al_2O_3 because they share a same crystal structure (rhombohedral) with similar lattice parameters and can form a solid solution over the entire composition range (at high temperature) as shown in Figure 6.26. Formation of Cr_2O_3 nuclei at the surface of Cr_2AlC during the initial stage of oxidation also occurs, and these nuclei are supposed to serve as nucleation sites for the α-Al_2O_3. Therefore, growth of α-Al_2O_3 grains will be accelerated on Cr-based coatings compared to that on Ti-based and Zr-based coatings, enabling the growth of a nearly pure alumina scale. A solid solution of $(Cr, Al)_2O_3$ probably grows on the thin top surface of the Cr_2AlC coating during the initial stage of oxidation, followed by growth of pure alumina due to the continuously decreasing partial pressure of the oxidizing gas at scale/coating interface [159,238]. The low diffusion rate of gas through the α-Al_2O_3 scale renders better oxidation resistance and higher tolerant temperature of Cr-based coatings, i.e. Cr_2AlC here.

One main issue confronting the Cr_2AlC-based coatings for long time service at high temperatures is the consumption of the Al-reservoir with subsequent oxidation of the Cr-C layer beneath, similar to the behavior of bulk Cr_2AlC ceramic. Depletion of Al within the Cr_2AlC coatings generally not only leaves a Cr-C layer beneath but also induces cavity/void formation at the scale/coating interface. Once the supply of Al is suspended due to its full consumption, oxidation of the carbide layer via inward diffusion of steam will result in formation of Cr_2O_3 and CO or CO_2 gas. Cr_2O_3 is known to easily evaporate especially in

humid atmosphere at elevated temperatures via formation of hydroxide gas species. Both oxidation and evaporation will result in cavity formation. Therefore, the adherence of the oxide scale is reduced with progressively increasing exposure time. In general, Cr_2AlC coatings can provide good protection at 1200°C and their performance is highly challenged once the temperature reaching 1300°C as found in literature [159].

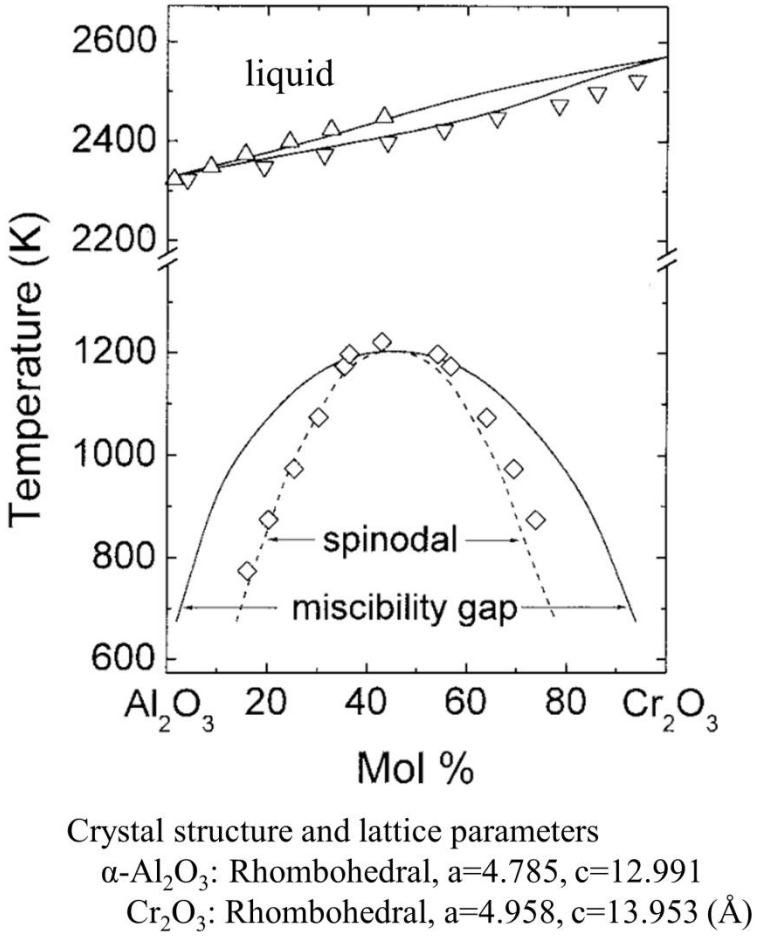

Figure 6.26 Calculated and experimental quasi-binary section Al_2O_3 - Cr_2O_3 of the Al-Cr-O phase diagram adopted from [253] with inserted crystallographic data of the two oxides.

6.6 Summary and conclusions

Cr_2AlC MAX phase coatings were synthesized via a two-step approach, i.e. magnetron sputtering of elemental nanoscale multilayer thin films, and subsequent *ex-situ* thermal annealing in argon. The mutual diffusion and reaction within the elemental multilayers first lead to the formation of Cr-Al intermetallic phases and CrC_x; the reaction between the intermetallics and the CrC_x results in the crystallization of the Cr_2AlC MAX phase starting from around 480°C. The low annealing temperature needed for synthesis of Cr_2AlC offers the possibility for widespread applications. The Cr_2AlC coatings display a basal plane preferred orientation with the *c*-axis perpendicular to the sample surface and the multilayer stacks as observed for the Ti_2AlC coatings. The lower growth rates along *c* than along *a*-axis for MAX phase grains

combined with the specific nanoscale multilayer architecture in the as-deposited coatings mostly response for the textured growth of the MAX phase grains during annealing.

The Cr_2AlC coatings were then examined as high-temperature protective coatings on Zircaloy-4 substrates. Two designs of coatings were used for deposition on Zircaloy-4 substrates. The coatings were around 6.5 μm thick with a 500 nm Cr interlayer as bonding layer and diffusion barrier. One design of coatings replaces the top 1.5 μm Cr-C-Al multilayers with same thickness of a pure Cr layer to eliminate potentially fast hydrothermal dissolution of Al during normal operation. Annealing of the as-deposited coatings on Zircaloy-4 substrate at 550°C for 10 min resulted in the formation of Cr_2AlC MAX phase but triggered the appearance of parallel micro-cracks due to mismatch of CTEs. Growth of a protective α-Al_2O_3 scale for the Cr_2AlC/Cr coatings and of a protective α-Al_2O_3 scale beneath Cr_2O_3 for the Cr/Cr_2AlC/Cr coatings during high-temperature oxidation were confirmed. The growth rate of Cr_2O_3 scale was much faster than that of α-Al_2O_3 scale and oxidation induced depletion of Al caused transformation of the Cr_2AlC layer to a mixture of Cr_2AlC and binary CrC_x. The micro-cracks were self-healed due to growth of alumina associated with corresponding volume expansion via oxidation of Cr_2AlC. Transient oxidation of the *as-deposited* coatings revealed a similar oxidation mechanism compared to the annealed coatings and an excellent oxidation resistance up to at least 1200°C, which provided one solution to avoid cracks induced by annealing. Thus, Cr_2AlC-based coatings show excellent application prospects as protective coatings on zirconium alloy claddings to improve the accident tolerance of water-cooled nuclear reactors.

7 H_2 permeation behavior of Ti_2AlC and Cr_2AlC coated Zircaloy-4 by neutron radiography

Hydrogen absorption of nuclear fuel claddings during normal operations as well as accidental scenarios has high safety relevance because hydrogen dramatically degrades the mechanical properties of zirconium alloys. Therefore, an ideal protective coating on zirconium alloy cladding should be a good hydrogen diffusion barrier and the hydrogen permeation through the coating is an important parameter ensuring cladding integrity and safety. In this chapter, the hydrogen permeation of two MAX phase coatings, namely Ti_2AlC and Cr_2AlC, on Zircaloy-4 is investigated by means of neutron radiography. Hydrogen permeation experiments through non-oxidized and pre-oxidized coatings have been performed. Both coatings have been confirmed as robust hydrogen diffusion barriers that effectively suppress hydrogen permeation into the matrix.

7.1 Introduction

The presence of hydrogen within a material's microstructure can result in a severe loss of ductility, catastrophic and unpredictable failure of structural components in service [254]. Hydrogen embrittlement is a serious concern for a variety of materials, for instance Zr-based alloy claddings [255] and advanced high-strength steels [256]. As explained in Chapter 1, zirconium alloy claddings absorb hydrogen significantly during both normal and accidental conditions. Hydrogen can dissolve or precipitate as brittle hydrides in the matrix. Hydrogen absorption dramatically degrades the mechanical properties of zirconium alloy claddings, limiting nuclear fuel to high burnup and challenging the integrity of the cladding tube especially during off-normal conditions.

One solution to mitigate hydrogen embrittlement usually involves applying barrier coatings on the surface to minimize further ingress of hydrogen from external sources [257,258]. In an ideal case, the protective coatings that should improve the high-temperature oxidation resistance of zirconium alloys in steam can also serve as a diffusion barrier for hydrogen. Therefore, an important property of the coatings is the permeability of hydrogen at operation temperature (~ 350°C) and at high temperatures during accident scenarios. The MAX phase materials are being intensively investigated for potential nuclear application, but there are no experimental reports on their hydrogen permeation behavior yet. Phase-pure Ti_2AlC and Cr_2AlC MAX phase coatings have been successfully fabricated on Zircaloy-4 substrate as presented before, thus it is of specific interest and essential to check their performance as protective barriers for hydrogen diffusion [259].

Generally, the hydrogen concentration in materials can be measured by hot vacuum extraction [260] or neutron radiography [261]. The hot vacuum extraction is a destructive method which determines the hydrogen concentration in the extracted gas using mass spectrometry. It typically provides an average

hydrogen content of segments. Neutron radiography technique uses polychromatic neutron beams, either in the cold or thermal energy range, to probe the specimens. The radiography image contrast varies locally based on neutron attenuation depending on hydrogen content and thickness of the specimens. Neutron radiography allows determining the hydrogen content non-destructively with a spatial resolution in the order of tens of micrometers. Hydrogen uptake in zirconium alloy has been studied quantitatively by means of neutron imaging as shown by various groups [261–264]. This chapter reports the first neutron radiography investigations of the hydrogen permeability through Ti_2AlC and Cr_2AlC MAX phase coatings on Zircaloy-4. Hydrogen permeation experiments at several temperatures, including 800°C, 700°C, 500°C and 350°C, were carried out for non-oxidized and pre-oxidized coatings.

7.2 Experimental arrangement

7.2.1 Preparation of MAX phase coated samples

Solid cylinder Zircaloy-4 alloy specimens were used as substrates for coating deposition. In order to suppress fast hydrogen uptake of the fresh Zircaloy-4, the substrate specimens were pre-oxidized at 800°C and atmospheric pressure for 30 min in Ar-20 vol.% O_2 atmosphere using the BOX facility to produce a dense ZrO_2 oxide layer of around 30 µm thickness [265]. The pre-oxidized layer can effectively suppress the hydrogen uptake besides the uncoated area during hydrogen permeation experiments [265]. The oxide layer was removed at one base plane of the cylinders by mechanical grinding and polishing, allowing hydrogen uptake through this plane. The polishing followed the similar procedure as rectangular Zirclaoy-4 plates used before. Then the Ti_2AlC and Cr_2AlC MAX phase coatings, respectively, were deposited on this polished base plane following the two-step approach as before. No diffusion barrier or bonding layer were deposited between the MAX phase coatings and Zircaloy-4 substrates here. The annealing temperatures were 800°C and 550°C for Ti_2AlC and Cr_2AlC coatings and the dwell time was 10 min, which have been identified to be appropriate for the formation of single-phase crystalline MAX phase structures in previous chapters. Figure 7.1 depicts exemplarily the size and topography of one Ti_2AlC coated cylinder Zircaloy-4 alloy specimen. The phase composition and microstructure of the coatings were investigated and verified by XRD and SEM.

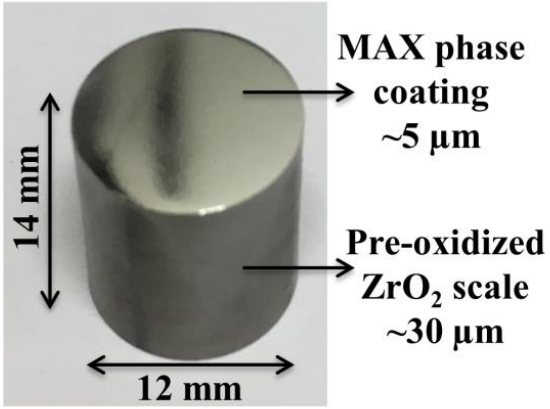

Figure 7.1 Ti_2AlC MAX phase coated Zircaloy-4 specimen for H_2 permeation experiments.

7.2.2 H_2 permeation experiments

The H_2 permeation experiments were conducted also using the BOX rig facility, except that 350°C experiments using the thermal balance (NETZSCH STA 409). The cylinder specimen was placed on an alumina boat positioned at the center of the furnace. The specimen was first heated in pure argon atmosphere (6N) with Ar flow rate of 20 l/h and heating rate of 10 K/min to the desired temperatures, then the atmosphere was changed to Ar-5 vol.% H_2 with the same flow rate for H_2 permeation. Following the isothermal annealing in Ar/H_2, the atmosphere was switched back to pure argon and the specimen was cooled down to room temperature in the furnace. The off-gas during hydrogen annealing was monitored by the mass spectrometer (Balzers GAM 300). The H_2 permeation experiments were conducted at several temperatures, including 800°C, 700°C, 500°C and 350°C. In principal, the coatings will undergo corrosion or oxidation during practical application. In order to determine the H_2 permeation behavior through oxidized coatings, some of the coated samples were pre-oxidized at 800°C under atmospheric pressure for 1 hour in Ar-20 vol.% O_2 atmosphere before H_2 permeation experiments. The mass of the specimens before and after test was measured. Uncoated Zircaloy-4 specimens were treated in the same way as reference.

7.2.3 Neutron radiography

Neutron radiography experiments were performed at the Imaging with Cold Neutrons (ICON) facility at the Swiss spallation neutron source (SINQ) at Paul Scherrer Institute (PSI) Villigen, Switzerland [266] using a cold neutron spectrum. The micro-tomography setup consists of an ANDOR detector with 13.5 μm pixel distance. A field of view of 28 mm × 28 mm and a beam collimation of L/D ≈ 340 were applied. The distance between the 20 μm thick Gadox scintillator screen and the sample was about 5 mm. In order to detect small hydrogen concentrations, the median of 11 to 166 images of 60 s individual acquisition times were determined using the ImageJ software. This procedure suppresses white spots in the image caused by high energetic γ quants. The ImageJ software was also used for the quantitative analysis of the median images.

The quantitative correlation between hydrogen concentration in terms of N_H/N_{Zr} atomic number ratio and total macroscopic neutron cross section Σ_{total} were determined by measuring of cladding tube segments with known hydrogen concentration as described in [261].

$$\Sigma_{total} = \frac{-ln\left(\frac{I-I_B}{I_0-I_B}\right)}{s}\sum_i N_i*\sigma_i = \Sigma_{total}(sample\ as\ received) + N_H*\sigma_H \quad (7\text{-}1)$$

I, I_0 and I_B are the neutron intensity with sample, without sample and the background intensity, respectively. S is the path length of the neutron through the specimen, N_i is the number density and σ_i is the total microscopic neutron cross section of the isotope i. Because $N_H*\sigma_H = \frac{N_H}{N_{Zr}}*N_{Zr}*\sigma_H$ the dependence of Σ_{total} on N_H/N_{Zr} can be written as a linear equation:

$$\Sigma_{total} = A + B*\frac{N_H}{N_{Zr}} \quad (7\text{-}2)$$

with $A = \Sigma_{total}$*(sample as received)* and $B = N_{Zr}*\sigma_H$.

Figure 7.2 plots the calibration curve measured in this beam time. The following correlation was determined:

$$\Sigma_{total} = 0.222 + 2.153*\frac{N_H}{N_{Zr}} \quad (7\text{-}3)$$

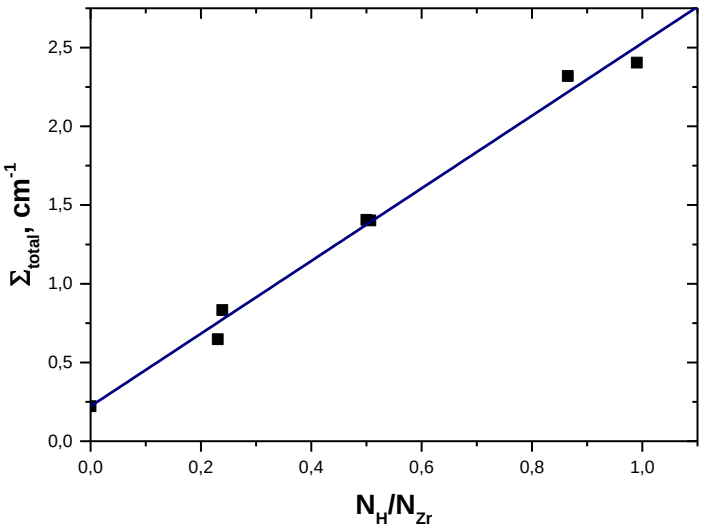

Figure 7.2 Calibration curve of the dependence of the total macroscopic neutron cross section Σ_{total} on the atomic number density ratio between hydrogen and zirconium N_H/N_{Zr}.

7.3 Results

7.3.1 Characterization of MAX phase coatings

Consistent with results obtained in the above chapters, single-phase and dense Ti_2AlC and Cr_2AlC MAX phase coatings have been synthesized following the two-step processes. Figure 7.3 shows the XRD patterns of the Ti_2AlC and Cr_2AlC MAX phase coatings on Zircaloy-4 substrates after annealing of the as-deposited elemental nanoscale multilayers at 800°C and 550°C, respectively, for 10 min in argon. Both type of samples show only XRD signals attributable to the Ti_2AlC or Cr_2AlC MAX phase and the Zircaloy-4 substrate. Common competing phases, like binary carbides and intermetallic, which could occur during preparation of the MAX phase coatings by magnetron sputtering and post-annealing were not detected by XRD. It is necessary to mention that the crystallinity of two MAX phase materials is slightly different. The relatively sharp peaks of the Ti_2AlC coatings indicate higher crystallinity and larger grains than those of the Cr_2AlC coatings. Both coatings have a basal-plane preferred orientation. Apart from high-intensity peaks originated from (002) and (006) basal planes, the Ti_2AlC coatings also show XRD signals of other various lattice planes. However, the Cr_2AlC coatings show mainly signals of basal-plane with highly textured structure. The significant differences in crystallite size probably stem from their different annealing temperatures as discussed in Chapter 6.

Figure 7.4 shows the cross-sectional SEM micrograph of the Ti_2AlC MAX phase coating. Similar to Chapter 4, the coating is dense and uniform, as well as free of micro-cracks and other large growth defects. Figure 7.5 are surface and cross-sectional SEM micrographs of the Cr_2AlC MAX phase coating. Consistent with the finding in Chapter 6, parallel micro-cracks were observed on the surface of the Cr_2AlC coatings after annealing. However, the cracks seem do not penetrate the coating and the coating shows a dense and uniform feature. The thicknesses of both coatings are around 5.1 μm without any diffusion barrier layer or bonding layer.

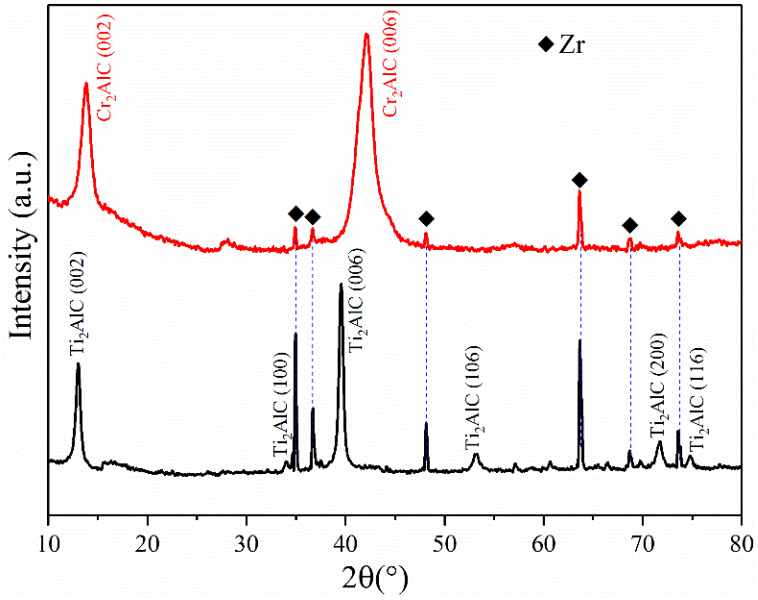

Figure 7.3 XRD patterns of Ti_2AlC (bottom) and Cr_2AlC (top) MAX phase coatings on Zircaloy-4 substrates by annealing of as-deposited elemental nanoscale multilayers.

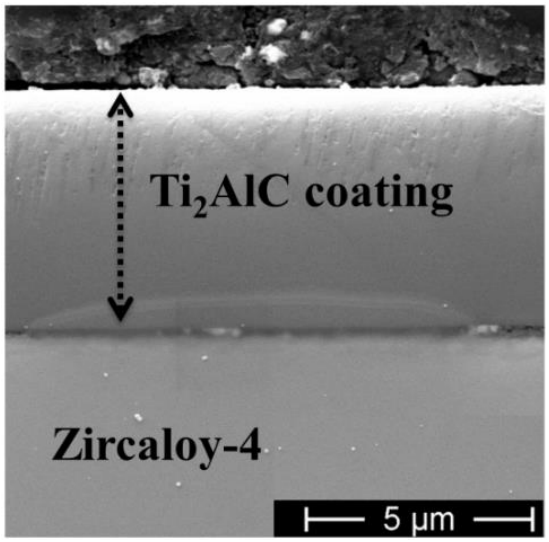

Figure 7.4 SEM image of cross-sectional view of the Ti_2AlC coating on Zircaloy-4 substrate.

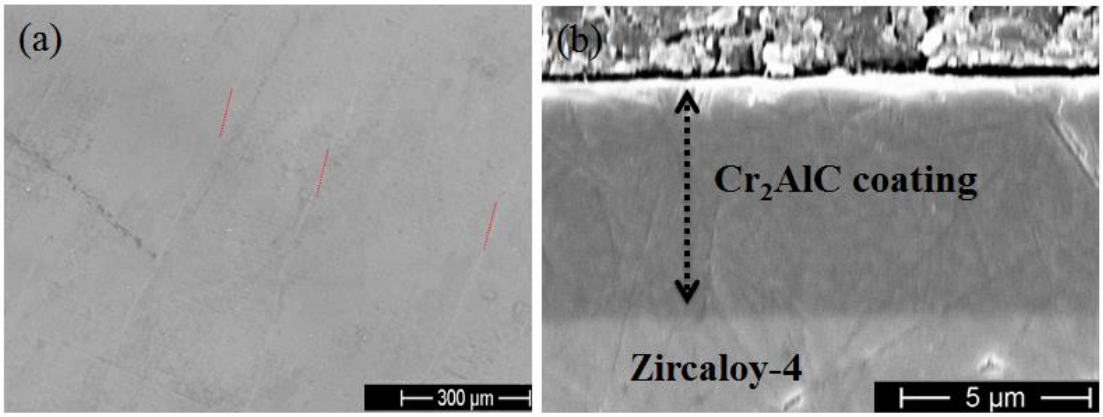

Figure 7.5 SEM images of (a) surface and (b) cross-sectional view of the Cr_2AlC coating on Zircaloy-4 substrate.

7.3.2 H_2 permeation of non-oxidized coatings

Uncoated Zircaloy-4 specimens, before and after hydrogen loading, were examined initially as reference, and the results are displayed in Figure 7.6. Figure 7.6(a) and (b) shows the neutron radiography images of the uncoated Zircaloy-4 specimens before and after hydrogen annealing at 700°C for 1 h, respectively. The same brightness and contrast settings were applied for all radiography images in order to give a straightforward visual inspection for comparing the hydrogen content. The pristine Zircaloy-4 specimen appears homogeneously bright due to the high neutron transmission. In contrast, after thermal annealing in hydrogen atmosphere, significant amount of hydrogen penetrated the cylinder through the polished plane and the hydrogen containing regions became much darker (Figure 7.6(b)). The diffusion front is clearly visible. Figure 7.6(c) illustrates the hydrogen distribution profile along the cylinder axis. The hydrogen concentration reached 5000 wppm at the gas/alloy interface. The lower regions of the cylinder loaded with hydrogen showed similar brightness compared to the pristine specimen. Thus, no obvious hydrogen penetration through the pre-oxidized ZrO_2 scale was detected.

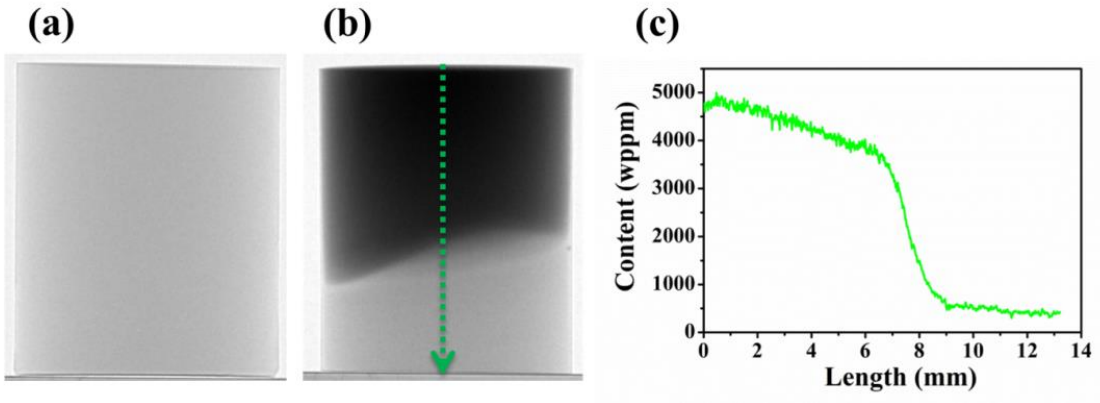

Figure 7.6 Neutron radiography images of the reference uncoated Zircaloy-4 specimens (a) before hydrogen loading and (b) after hydrogen permeation at 700°C for 1 h (hydrogen dark), (c) hydrogen distribution profile along cylinder axis from top to bottom in (b).

Figure 7.7(a) and (b) present the neutron radiography images of Cr_2AlC and Ti_2AlC coated Zircaloy-4 specimens after annealing in Ar/H_2 at 800°C for 1 h. Figure 7.7(c) plots the hydrogen distribution profiles along the cylinder axis. The images apparently reveal that both coatings are robust barriers against hydrogen permeation. The brightness of Figure 7.7(a) and (b) are on the same level compared to the pristine specimens (Figure 7.6(a)). The quantitative analysis given in Figure 7.7(c) shows a homogeneous hydrogen distribution profile along the cylinder axis without any gradients. The determined averaged hydrogen concentrations are very low, about 50 wppm for the Ti_2AlC coated and only about 10 wppm for Cr_2AlC coated Zircaloy-4. It has to be taken into account that the values are determined by Eq. (7-3) based on the model that only the hydrogen concentration is changed. Processes slightly increasing the total macroscopic neutron cross section, like the diffusion of oxygen from the oxide layer or atoms from the coating into the metal, are not considered. Therefore, the absence of a gradient in the hydrogen distribution proves that no hydrogen uptake through the coating occurred even the averaged value is not exactly zero. It has to be mentioned that the scattering of the values is not caused by the counting statistics in the neutron radiography experiment. The scattering cannot be reduced by re-binning of the detector pixels. It shows that the fluctuations in the hydrogen concentrations determined are attributed to the local material fluctuations. It can be concluded that the ~5 µm MAX phase coatings are just as effective as the pre-oxidized 30 µm ZrO_2 layer suppressing hydrogen uptake into the matrix.

The excellent performance of both coatings as hydrogen diffusion barrier was further confirmed by the evolution of hydrogen concentration in the off-gas during annealing as shown in Figure 7.8. The hydrogen concentration decreased gradually in the off-gas due to continuous absorption for the uncoated specimen (Figure 7.8(a)). The hydrogen concentration remained constant without any indication of decrease during the whole hydrogen exposure period for the coated specimens, Figure 7.8(b). This phenomenon revealed that no or negligible hydrogen penetrated through the coatings and the pre-oxidized ZrO_2 layer during annealing.

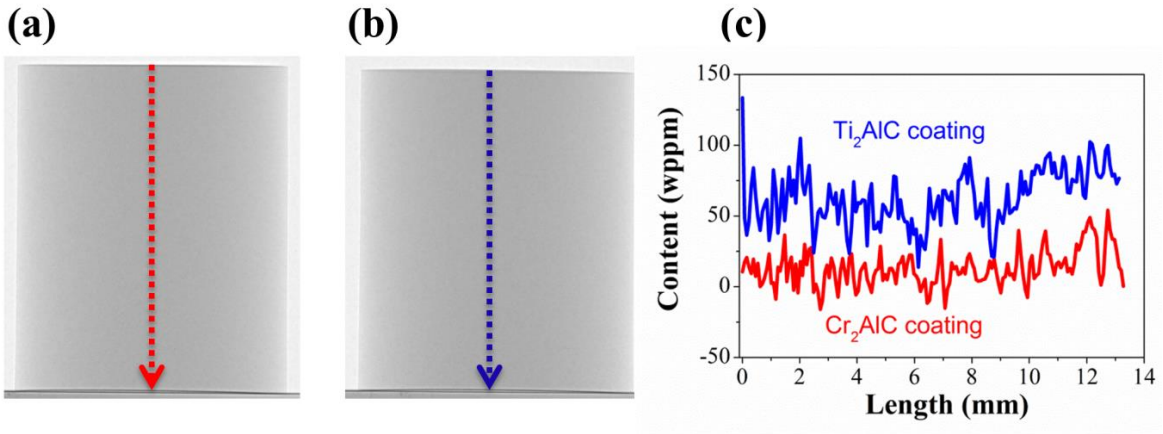

Figure 7.7 Neutron radiography images of (a) Cr_2AlC and (b) Ti_2AlC coated Zircaloy-4 specimens after hydrogen permeation at 800°C for 1 h. (c) Hydrogen distribution profiles along cylinder axis from top to bottom in (a) and (b).

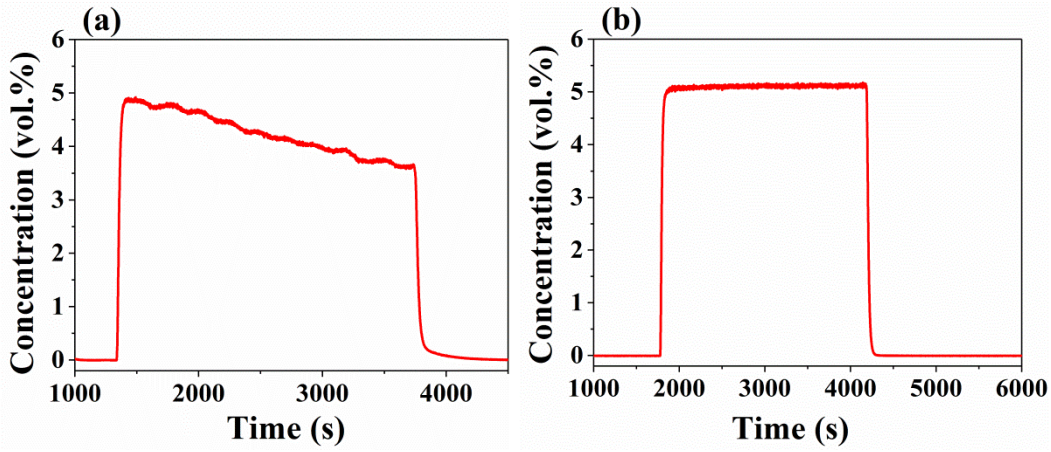

Figure 7.8 Hydrogen concentration in the off-gas during hydrogen annealing of (a) uncoated Zircaloy-4 at 700°C and (b) Ti_2AlC and Cr_2AlC coated Zircaloy-4 at 800°C for 1 h.

The hydrogen diffusion rate through the MAX phase coatings cannot be calculated based on Fick's diffusion law since no hydrogen concentration gradient was observed. The hydrogen permeation rate can be estimated by the following definition:

$$\emptyset = \frac{\Delta m}{S \cdot t} \tag{7-4}$$

$\emptyset$ is the hydrogen permeation rate at a certain temperature, Δm is the mass gain due to hydrogen absorption, S is the exposure area and t is the permeation time. Assuming that the hydrogen concentration is at the magnitude of 10^1 ppm for the MAX phase coated Zircaloy-4 specimens after hydrogen permeation at 800°C for 1 h, the hydrogen permeation rate through the uncoated and coated surfaces can be compared. The estimated rate is around 6.6×10^{-2} $g \cdot m^{-2} \cdot s^{-1}$ for uncoated Zircaloy-4 at 700°C; in contrast, it descends to around 10^{-4} $g \cdot m^{-2} \cdot s^{-1}$ for MAX phase coated specimens even at a higher temperature 800°C. It is necessary to mention that the maximal permeation rate estimated here is based on very low average values of the hydrogen concentrations being below their point-to-point scattering as shown in Figure 7.7(c). Hence, the ~5 μm MAX phase layer reduced the hydrogen permeation rate at least by about two orders of magnitudes or more. Experiments at 800°C for longer time were also performed, however, failure of the pre-oxidized ZrO_2 scale occurred (shown below) leading to unsuccessful evaluation of the coatings.

7.3.3 H_2 permeation of pre-oxidized coatings

Figure 7.9 displays the images of pre-oxidized Cr_2AlC coated Zircaloy-4 specimens after hydrogen permeation at two different temperatures (700°C and 500°C) for 1 hour. The neutron radiography images after annealing in hydrogen atmosphere at 700°C for 1 hour (Figure 7.9(a)) show similar brightness levels compared to the as-received specimen (Figure 7.6(a)) and the coated, non-oxidized one (Figure 7.7(a)). No obvious dark regions were observed. For the specimen after annealing at 500°C for 1 hour, localized failure of the ZrO_2 layer through crack and spallation was found (Figure 7.9(b)). Hydrogen penetrated through the failure areas and the hydrogen containing area appeared darker. The hydrogen distribution

profile proves that in the upper part of the specimens where the coating is located and less oxide layer failure exists, the hydrogen concentration is close to zero, just around dozens of wppm. Figure 7.10 shows the evolution of the hydrogen concentration in the off-gas during hydrogen permeation at 500°C. The hydrogen concentration remained constant, then decreased gradually after certain exposure time, which is associated with the localized failure of the ZrO_2 layer. The reason leading to the failure of the ZrO_2 layer perhaps is the diffusion of oxygen from the oxide into the metal. It seems to be enhanced by treatment during grinding and polishing and is accelerated by the local material swelling after first local hydrogen uptakes. In all permeation tests, during which the ZrO_2 layer survived, the hydrogen concentration in the off-gas flow always remained constant.

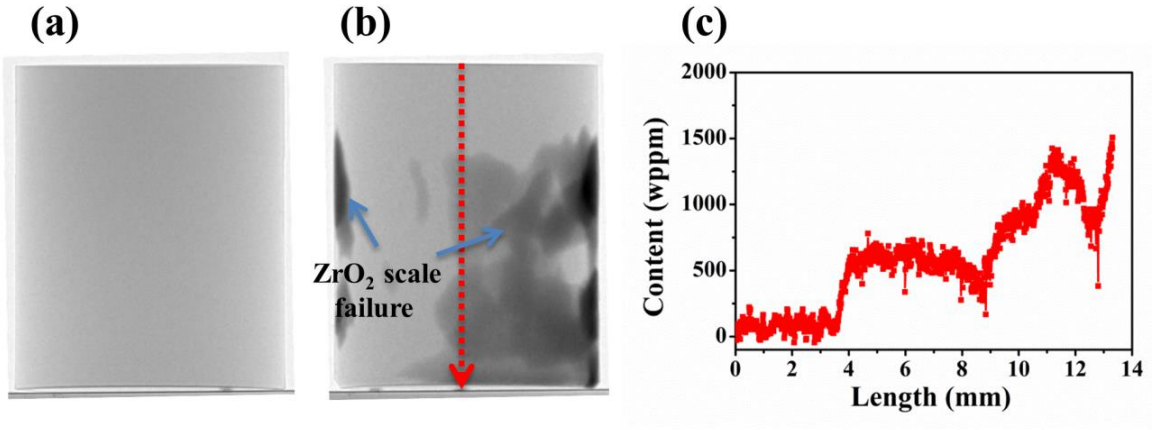

Figure 7.9 Neutron radiography images of pre-oxidized Cr_2AlC coated Zircaloy-4 specimens after hydrogen permeation at (a) 700°C and (b) 500°C for 1 h (hydrogen dark), (c) hydrogen distribution profile along cylinder axis from top to bottom in (b).

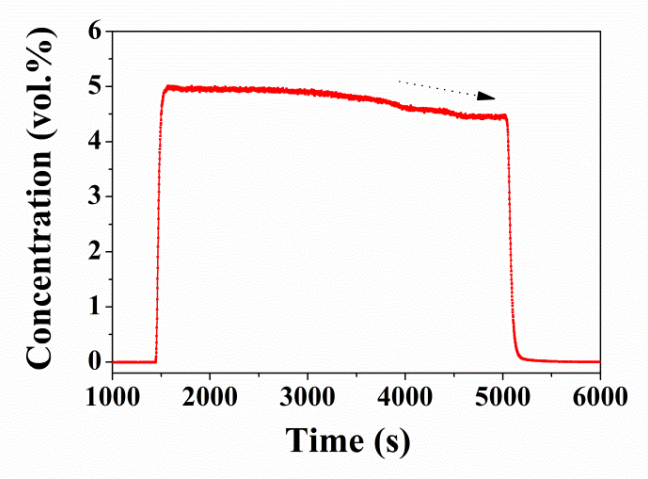

Figure 7.10 Hydrogen concentration in the off-gas during hydrogen permeation of pre-oxidized Cr_2AlC coated Zircaloy-4 specimens at 500°C for 1 h. A slight decrease of the hydrogen concentration was shown due to fast permeation through locally failed ZrO_2 scale.

The pre-oxidized Ti_2AlC coatings were proved as effective as the pre-oxidized Cr_2AlC coatings in limiting the hydrogen permeation as shown in Figure 7.11. No dark areas enriched in hydrogen were observed except for one small region after 500°C exposure where the ZrO_2 layer failed. It is hard to determine which coating suppresses the hydrogen uptake more efficiently. No hydrogen absorption of the substrate above the detection limits was observed for both coatings. Figure 7.12 shows the results of pre-oxidized Cr_2AlC and Ti_2AlC coated Zircaloy-4 specimens after hydrogen permeation at 350°C for 4 h. Annealing of both pre-oxidized coatings in hydrogen atmosphere at 350°C for 4 h revealed no indication of mass change, and the hydrogen concentration determined by quantitative analysis appeared below 1 wppm.

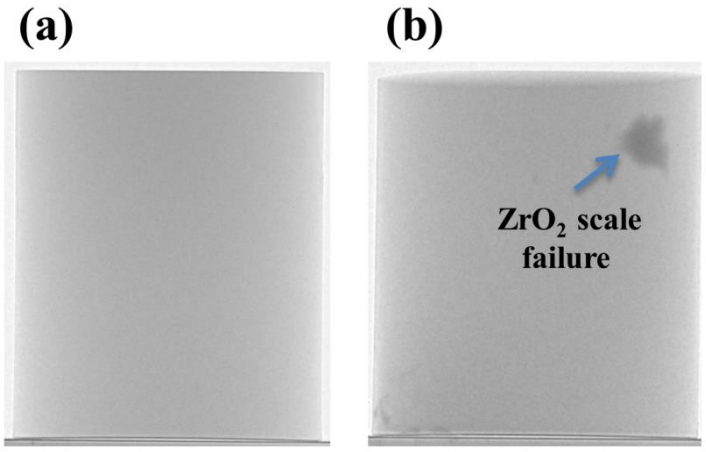

Figure 7.11 Neutron radiography images of pre-oxidized Ti_2AlC coated Zircaloy-4 specimens after hydrogen permeation at (a) 700°C and (b) 500°C for 1 h (hydrogen dark).

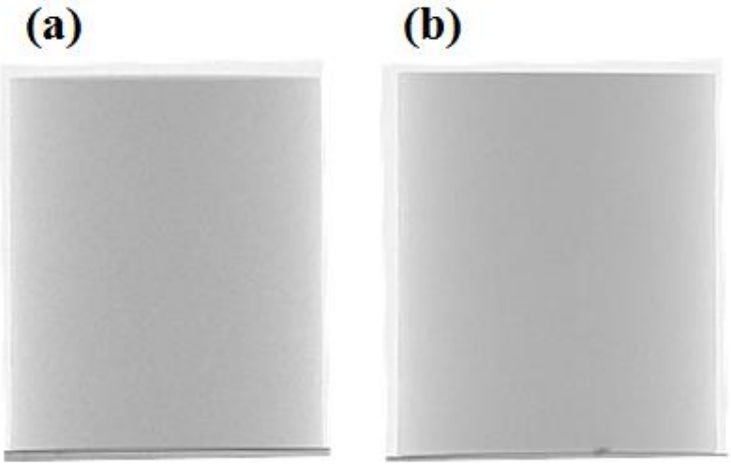

Figure 7.12 Neutron radiography images of pre-oxidized (a) Cr_2AlC and (b) Ti_2AlC coated Zircaloy-4 specimens after hydrogen permeation at 350°C for 4 h.

7.4 Discussion

A variety of coatings, mainly oxide, nitride and carbide ceramics, on structural components have been examined extensively as hydrogen permeation barriers [267]. These ceramics usually have very low

permeability for hydrogen isotopes caused by their low hydrogen solubility and diffusivity. Previous studies also confirmed that finely dispersed carbides in a steel matrix act as deep trapping sites to retain hydrogen, which might otherwise diffuse through [254,256]. Trapping of hydrogen fairly reduces the apparent hydrogen diffusion rates in the matrix; the hydrogen isotopes are restricted to the interior lattice structure of the carbides. Recent first-principle theoretical calculations demonstrated that hydrogen interstitial atoms are preferably and as readily to be incorporated into the interstitial sites of Ti-Al layers in stoichiometric Ti_3AlC_2 or C vacancies in C-deficient Ti_3AlC_2 MAX phase [268,269]. Due to MAX phases share similar lattice structure, above calculated configurations of hydrogen trapping sites are suggested also applying for the two 211-MAX phases, Ti_2AlC and Cr_2AlC. The trap of hydrogen atoms in interstitial or vacancy sites probably can drastically impede the permeation of hydrogen and reduce the hydrogen partial pressure at the MAX phase coating/substrate interface.

Another important factor determining the barrier efficiency is the microstructural integrity [267,270]. Thus, barriers that can provide a sufficient permeation reduction should be essentially free of various defects. In general, grain boundaries featured by the typical columnar structure of coatings deposited by PVD or other macroscale defects including cracks and voids that act as short-circuit diffusion path can significantly reduce the barrier efficiency. However, by adopting a two-step synthesis process, the MAX phase coatings in this study are dense, consisting of nano-crystalline grains without columnar growth [88]. Theoretical calculations showed that hydrogen diffusion along the basal plane is feasible with respect to Ti_2AlC [271] and Ti_2AlN [272] MAX phases, while the diffusion along the *c*-axis is difficult. It suggests that a dense, basal-plane textured MAX phase coating could act as a barrier against diffusion of interstitial H atoms. Both MAX phase coatings obtained in this study are characterized by a basal-plane textured microstructure with the *c*-axis perpendicular to the sample surface. The unique microstructural features of the coatings can improve the efficiency in limiting hydrogen permeation.

Oxidation of Ti_2AlC and Cr_2AlC coatings lead to the growth of oxide scale on the surface. The Ti_2AlC coated Zircaloy-4 grew a scale consisting of two sub-layers: an outer dense alumina-rich layer and an inner porous titania layer during oxidation at 800°C, as presented in Chapter 4. In general, the oxidation of Cr_2AlC coatings result in the formation of an alumina-rich scale at relatively low temperatures or a dense continuous oxide scale consisting of alumina on Cr carbides at high temperatures [159,247]. In line with literature, growth of a dense alumina scale was confirmed during oxidation of the Cr_2AlC coatings at 1000°C in steam in this study (Chapter 6); in addition, the micro-cracks were healed by alumina. Alumina, particularly the α-phase of aluminum oxide (corundum), and chromia are robust hydrogen permeation barriers that can reduce the permeation rate by three orders of magnitude in laboratory experiments [257,273]**.** Thus, it can be expected that both pre-oxidized MAX phase coatings can serve as satisfactory barriers for limiting hydrogen permeation.

7.5 Summary and conclusions

Neutron radiography investigations have been adopted to measure the hydrogen permeability of Ti_2AlC and Cr_2AlC MAX phase coatings on zirconium alloys. The uncertainty of the hydrogen permeation rate

through the coatings is given by the detection limit of hydrogen concentration in zirconium alloys using neutron radiography. In the case of the experiments of this study, it is in the order of magnitude of 10^{-4} $g \cdot m^{-2} \cdot s^{-1}$.

Both, the non-oxidized and pre-oxidized Ti_2AlC and Cr_2AlC MAX phase coatings suppress hydrogen uptake effectively and reduce the hydrogen permeation rate at least by about two orders of magnitudes compared to bare Zircaloy-4. Their permeation rate is below the detection limit given before. The ~5 µm MAX phase coatings are as effective as the pre-oxidized 30 µm ZrO_2 layer suppressing hydrogen permeation into the matrix. The unique microstructural features of the coatings, namely free of columnar growth and highly basal-plane textured grains, improve the efficiency in limiting hydrogen permeation as a barrier.

8 Conclusions and Outlook

Zirconium-based alloys, as state-of-the-art cladding material for current light water reactors (LWRs), show some crucial constraints concerning fast degradation, exothermic reaction with high-temperature steam associated with hydrogen generation in accident scenarios, which have drawn great attention to develop a more accident tolerant fuel (ATF) cladding especially after the Fukushima accidents. One strategy to improve the performance of the zirconium alloy claddings in accidental scenarios while preserving their excellent behavior under normal operating conditions is to modify the external surface via oxidation resistant coatings deposition. This dissertation work was initiated to deposit a coating with an inherently high temperature oxidation resistance on zirconium alloy claddings enabling drastically reduce the oxidation and degradation of the cladding during off-normal conditions. Al-containing MAX phase carbides (Ti_2AlC, Zr_2AlC and Cr_2AlC) were down selected as coating materials considering their unique attributes combination of both ceramics and metals together with excellent high-temperature oxidation resistance.

Oxidation of one commercial Al-MAX phase Ti_2AlC (Maxthal 211®) in steam in the temperature range of 1400–1600°C was performed to validate its high-temperature oxidation resistance and ascertain its potential as protective coatings. The results revealed that its oxidation kinetics followed a sub-parabolic law at the early stage of oxidation, then transferred to a linear law beyond 18 hours at 1400°C, and obeyed a linear law from the beginning of oxidation at 1500°C. The sample suffered catastrophic oxidation, i.e. rapidly and completely consumed, during isothermal oxidation at 1600°C accompanied by large heat and hydrogen release. The maximum tolerant temperature of Ti_2AlC in steam was approximately 1555°C determined by a ramp test. The oxide scale formed at 1400°C and 1500°C consisted of randomly distributed Al_2TiO_5 isolated islands with large elongated grains embedded in a continuous coarse α-Al_2O_3 scale. Oxidation of Ti_2AlC ceramic at elevated temperatures ascertain its superb oxidation resistance and the oxide scale thickening rate of Ti_2AlC at 1400°C is more than three orders of magnitude lower than that of Zircaloy-4.

A major issue confronting the synthesis of MAX phase coatings, especially thick polycrystalline coatings, is the retention of stable intermediate or competing phases, like binary carbides and intermetallics. A facile two-step approach was developed, i.e. first magnetron sputtering of nanoscale elemental multilayer stacks and subsequent thermal annealing in argon, for potential growth of phase-pure MAX phase coatings. Phase-pure Ti_2AlC and Cr_2AlC MAX phase coatings have been successfully fabricated, but formation of Zr(Al)C carbide rather than the Zr_2AlC MAX phase was confirmed in the Zr-C-Al system. The oxidation performances in high-temperature steam of the three types of coated zirconium alloys were evaluated to determine if they are qualified as an acceptable choice for ATF application.

In terms of synthesis of Ti_2AlC MAX phase coatings, Ti-C-Al elemental multilayer stacks with thicknesses of around 8 nm for Ti, 2 nm for C and 4 nm for Al were deposited by non-reactive magnetron sputtering using three elemental targets. Annealing of the coatings at 440–660°C resulted in the formation of a

mixture of Ti-Al intermetallics and titanium carbide. The crystalline transition from these competing non-MAX phases to Ti_2AlC MAX phase was found at around 660°C. Phase-pure Ti_2AlC coatings were obtained after 800°C annealing for 10 min with an average grain size of around 20 nm. The 800°C annealed coating also displayed a basal plane preferred orientation. Significant diffusion of Al from the coating into the substrate occurred during annealing. Therefore, Ti_2AlC coatings of two designs with and without a 500 nm thick TiC layer as diffusion barrier were synthesized on Zircaloy-4. The overall coating thickness was around 5.5 μm. The coatings, around 15 GPa of hardness and 200 GPa of modulus after annealing, were much stiffer than the Zircaloy-4 substrate. Scratch tests displayed a brittle failure mode for both coatings and the critical failure load was about 50 N and 30 N for the Ti_2AlC and Ti_2AlC/TiC coatings, respectively. The better adherence of the Ti_2AlC coatings without diffusion barrier can be attributed to the diffusion of Al from the coating into the substrate, increasing the interfacial adherence between the coating and substrate. During oxidation at 800°C, the Ti_2AlC coatings without TiC barrier formed an oxide scale with two sublayers: an outer metastable θ-Al_2O_3 rich layer mixed with TiO_2 (rutile) and an inner porous TiO_2 layer with traces of Al_2O_3. Correspondingly, a triple-layered scale (θ-Al_2O_3+TiO_2/θ-Al_2O_3/TiO_2) grew on coatings with the TiC barrier. The TiC barrier suppressed the rapidly diffusion of Al from the coatings into the substrate, contributing to different scale configuration, better oxidation performance and longer life of Ti_2AlC/TiC coatings. The coated Zircaloy-4 demonstrated significant improvement of oxidation resistance compared to uncoated samples at 800°C in steam. However, both coatings were quickly consumed with weak or non-protective effect from around 1000°C.

Coatings in the Zr-C-Al system, with a focus of the potential formation of Zr_2AlC and Zr_3AlC_2 MAX phases, were deposited and examined. The similar nanoscale elemental multilayer architectures with a multiple stacking sequence of zirconium, carbon, and aluminum layers based on the stoichiometries of Zr_2AlC and Zr_3AlC_2 were firstly deposited on Al_2O_3 substrates. No MAX phases formation, but the formation of Zr(Al)C carbide, was observed after annealing in argon at temperatures from 600°C to 1200°C. Coatings with three different Zr/Al ratios, corresponding to stoichiometric ratios of 2Zr/C/Al, 3Zr/5C/3Al, and 2Zr/5C/4Al, were deposited on polished Zircaloy-4 substrates. The coating thicknesses were 5.5 μm with a 500 nm thick ZrC layer between the coating and substrate as diffusion barrier. All annealed coatings crystallized to a cubic ZrC phase with a B1 NaCl crystal structure, and Al is suggested to occupy the lattice position of Zr atoms. All three coated samples revealed lower oxidation rate compared to the uncoated Zircaloy-4 at 700°C. In particular, the two coatings with higher Al content (i.e., 3Zr/5C/3Al and 2Zr/5C/4Al) displayed better oxidation resistance. The oxide scale consisted of two sublayers for the 2Zr/C/Al coatings: an outer Al_2O_3-rich and ZrO_2 mixed layer, and an inner ZrO_2 layer. Oxidation of the other two coatings led to growth of oxide scales characterized by a predominant Al_2O_3 single layer. However, the two coatings with higher Al content demonstrated low adhesion to the Zircaloy-4 substrates. Widespread cracks and spallation of the coatings were observed after oxidation due to the thermal expansion mismatch between the coatings and the substrate. All coatings showed weak or no protection at higher oxidation temperatures 800°C and 1000°C with tremendous cracking and spallation.

Cr_2AlC MAX phase coatings were successfully produced using the same two-step approach and were examined as protective coatings on Zircaloy-4. Crystallization of Cr_2AlC from 480°C and formation of phase-pure Cr_2AlC at 550°C is confirmed by annealing of the as-deposited elemental nanoscale multilayer stacks on alumina substrates. The Cr_2AlC coatings also display a basal plane preferred orientation. Two designs of coatings were deposited on Zircaloy-4 substrate. The total thickness of the coatings was around 6.5 μm with a 500 nm Cr interlayer as bonding layer and diffusion barrier. One design of coatings replaced top 1.5 μm Cr-C-Al multilayer with the same thickness of pure Cr layer to eliminate potential fast hydrothermal dissolution of Al during normal operation. Annealing of the as-deposited coatings on Zircaloy-4 substrate at 550°C for 10 min resulted in the formation of Cr_2AlC MAX phase but triggered the appearance of micro-cracks on the surface. Growth of a thin, dense and protective α-Al_2O_3 scale for the Cr_2AlC/Cr coatings and of a protective α-Al_2O_3 scale beneath Cr_2O_3 for the Cr/Cr_2AlC/Cr coatings during high-temperature oxidation were confirmed. The growth rate of Cr_2O_3 scale was much faster than that of α-Al_2O_3 scale and oxidation induced depletion of Al caused transformation of the Cr_2AlC layer to a mixture of Cr_2AlC and binary CrC_x. The cracks were self-healed due to growth of alumina associated with corresponding volume expansion via oxidation of Cr_2AlC. Transient oxidation of as-deposited coatings revealed their similar oxidation mechanisms compared to the annealed coatings and excellent oxidation resistance up to at least 1200°C, which provides one potential solution to avoid cracks induced by annealing.

The phase evolution during annealing of the as-deposited multilayer stacks, at least partially, can be interpreted by the thermodynamic stability of the corresponding MAX phases and their counterpart binary carbides. Ti_2AlC and Cr_2AlC are proved to be thermodynamically stable while Al-containing Zr-based MAX phases are often assumed to be unstable or metastable with respect to their competing phases. In case of binary carbides, the stability increases in the sequence of CrC_x ($Cr_{23}C_6$, Cr_7C_3 and Cr_3C_2), TiC and ZrC. Therefore, it becomes successively harder converting these binary carbides, from Cr to Zr, to their corresponding high-ordered MAX phases through reaction with other intermediate phases during annealing. Thus, it seems reasonable that Ti_2AlC and Cr_2AlC MAX phases were successfully obtained with lower crystallization temperature for Cr_2AlC, but Zr(Al)C was formed in the Zr-C-Al system. Both MAX phase coatings displayed a preferred orientation of (00l) basal plane perhaps because of lower growth rate along *c*-axis, the lowest surface energy of the (00l) surface in MAX phases as well as the specific as-deposited nanoscale multilayer architecture. The failure of the Ti_2AlC and Zr(Al)C coatings from around 1000°C in steam was associated with the low thickness of the coatings, high interdiffusion rate between coating and substrate, and potential phase transformation of the oxide products (TiO_2 and ZrO_2). Cr_2O_3 and α-Al_2O_3 show similar crystal structure and are completely miscible (at elevated temperatures). Therefore, Cr_2O_3 can act as nucleation sites for α-Al_2O_3, which promotes and accelerates the growth of an alumina scale during oxidation of Cr_2AlC coatings.

In addition, H_2 permeation behavior of Cr_2AlC and Ti_2AlC coated Zircaloy-4 was investigated by neutron radiography since hydrogen absorption dramatically degrades the mechanical properties of zirconium alloys. Both coatings were around 5 μm thick without any bonding layer or diffusion barrier. Both, the

non-oxidized and pre-oxidized Ti_2AlC and Cr_2AlC MAX phase coatings can suppress hydrogen uptake effectively and reduce the hydrogen permeation rate at least by about two orders of magnitudes compared to the uncoated zirconium alloys. The unique microstructural features of the coatings, namely free of columnar growth and highly basal-plane textured grains, improve their efficiency in limiting hydrogen permeation as a barrier.

The investigations performed in this dissertation imply that the Cr_2AlC-based coatings, featured by their outstanding oxidation resistance and autonomous self-healing capability, hold promising application prospects as protective coatings on Zr alloy claddings for further development. With the purpose of eventually enhancing the accident tolerance of fuel cladding under transient accident scenarios, one prerequisite for ATF coatings is that they must withstand the simultaneous occurrence of aqueous corrosion by hot water, irradiation damage, and various stresses during normal operations for a certain period, typically two to three fuel cycles, without failure. Thus, the performances of the Cr_2AlC-based coatings during normal operations need to be evaluated and validated. The coating campaigns have been implemented with flat rectangular coupons as underlying substrate, instead of tube shape used in nuclear reactors. Therefore, it is necessary to validate that the well-established two-step approach is capable to coat tube substrate, even full-length cladding tube, with desired microstructure and high reproducibility.

The reliability of functional thin coatings during service profoundly depends on their structural integrity. Micro-cracks are present on the Cr_2AlC coatings synthesized by the two-step approach stemming from the high CTE mismatch between the coating and the substrate. Even though these cracks are self-healed by alumina during high-temperature oxidation, they may act as a detrimental degradation issue during normal operation. Potential solutions to avoid the cracking of the coatings, for instance utilization of as-deposited coatings or searching for better bonding interlayer, should be pursued.

MAX phase, as intrinsic ceramic materials, are quantified by a limited ductility and/or low fracture toughness. When utilized as coatings, they are prone to crack or spallation when experiencing high stresses. The mechanical properties, especially the adhesive strength, of the coatings during in-core service and off-normal transient conditions still require assessment. Multilayer coatings with alternating metallic and ceramic sublayers generally possess superior mechanical properties compared to single-layer coatings. In the Cr-C-Al system, Cr/Cr_2AlC multilayer coatings with proper design are of specific interest and deserve to be further explored.

References

[1] S. Chu, A. Majumdar, Opportunities and challenges for a sustainable energy future, Nature. 488 (2012) 294–303.

[2] S.J. Zinkle, G.S. Was, Materials challenges in nuclear energy, Acta Mater. 61 (2013) 735–758.

[3] S.J. Zinkle, K.A. Terrani, J.C. Gehin, L.J. Ott, L.L. Snead, Accident tolerant fuels for LWRs: A perspective, J. Nucl. Mater. 448 (2014) 374–379.

[4] Z. Duan, H. Yang, Y. Satoh, K. Murakami, S. Kano, Z. Zhao, J. Shen, H. Abe, Current status of materials development of nuclear fuel cladding tubes for light water reactors, Nucl. Eng. Des. 316 (2017) 131–150.

[5] H.G. Kim, J.H. Yang, W.J. Kim, Y.H. Koo, Development Status of Accident-tolerant Fuel for Light Water Reactors in Korea, Nucl. Eng. Technol. 48 (2016) 1–15.

[6] C. Tang, M. Stueber, H.J. Seifert, M. Steinbrueck, Protective coatings on zirconium-based alloys as accident-tolerant fuel (ATF) claddings, Corros. Rev. 35 (2017) 141–166.

[7] International Atomic Energy Agency, IAEA Annual Report - GC(61)/3, Vienna, Austria, 2016: 1-146.

[8] Z. Hu, Developments of analyses on grid-to-rod fretting problems in pressurized water reactors, Prog. Nucl. Energy. 106 (2018) 293–299.

[9] K.A. Terrani, S.J. Zinkle, L.L. Snead, Advanced oxidation-resistant iron-based alloys for LWR fuel cladding, J. Nucl. Mater. 448 (2014) 420–435.

[10] C.R.F. Azevedo, Selection of fuel cladding material for nuclear fission reactors, Eng. Fail. Anal. 18 (2011) 1943–1962.

[11] A.T. Motta, A. Couet, R.J. Comstock, Corrosion of Zirconium Alloys Used for Nuclear Fuel Cladding, Annu. Rev. Mater. Res. 45 (2015) 311–343.

[12] M. Steinbrück, N. Vér, M. Große, Oxidation of advanced zirconium cladding alloys in steam at temperatures in the range of 600-1200 °C, Oxid. Met. 76 (2011) 215–232.

[13] M. Hirano, T. Yonomoto, M. Ishigaki, N. Watanabe, Y. Maruyama, Y. Sibamoto, T. Watanabe, K. Moriyama, Insights from review and analysis of the Fukushima Dai-ichi accident, J. Nucl. Sci. Technol. 49 (2012) 1–17.

[14] S. Bragg-Sitton, Development of advanced accident-tolerant fuels for commercial LWRs, Nucl. News. 53 (2014) 83–91.

[15] B.A. Pint, K.A. Terrani, Y. Yamamoto, L.L. Snead, Material Selection for Accident Tolerant Fuel Cladding, Metall. Mater. Trans. E. 2 (2015) 190–196.

[16] V.A. Avincola, M. Grosse, U. Stegmaier, M. Steinbrueck, H.J. Seifert, Oxidation at high temperatures in steam atmosphere and quench of silicon carbide composites for nuclear application, Nucl. Eng. Des. 295 (2015) 468–478.

[17] D. Gilbon, A. Soniak, S. Doriot, J.-P. Mardon, Irradiation creep and growth behavior, and microstructural evolution of advanced Zr-base alloys, in: Zirconium in the Nuclear Industry: Twelfth International Symposium, ASTM-STP1354, West Conshohocken, Pennsylvania, USA, 2000: pp. 51–73.

[18] Y.H. Jeong, S. Park, M. Lee, B. Choi, J. Baek, J. Park, J. Kim, H. Kim, Out-of-pile and In-pile Perfomance of Advanded Zirconium Alloys (HANA) for High Burn-up Fuel, J. Nucl. Sci. Technol. 43 (2006) 977–983.

[19] T.R. Allen, R.J.M. Konings, A.T. Motta, Corrosion of Zirconium Alloys, in: R. J. M. Konings (eds.), Comprehensive Nuclear Materials, Elsevier, Amsterdam, Netherland, 2012: vol. 5, pp. 49–68.

[20] C. E. Ells, Hydride precipitates in zirconium alloys (A review), J. Nucl. Mater. 28 (1968) 129–151.

[21] M. Steinbrück, J. Birchley, A. V. Boldyrev, A. V. Goryachev, M. Grosse, T.J. Haste, Z. Hózer, A.E. Kisselev, V.I. Nalivaev, V.P. Semishkin, L. Sepold, J. Stuckert, N. Vér, M.S. Veshchunov, High-temperature oxidation and quench behaviour of Zircaloy-4 and E110 cladding alloys, Prog. Nucl. Energy. 52 (2010) 19–36.

[22] M. Steinbrück, M. Große, L. Sepold, J. Stuckert, Synopsis and outcome of the QUENCH experimental program, Nucl. Eng. Des. 240 (2010) 1714–1727.

[23] J.M. Broughton, P. Kuan, D.A. Petti, E.L. Tolman, A Scenario of the Three Mile Island Unit 2 Accident, Nucl. Technol. 87 (1989) 34–53.

[24] M. Steinbrück, M. Grosse, Deviations From Parabolic Kinetics During Oxidation of Zirconium Alloys, in: Zirconium in the Nuclear Industry: Seventeenth International Symposium, ASTM-STP1543, West Conshohocken, Pennsylvania, USA, 2015: pp. 979–1001.

[25] B. Cheng, Y.J. Kim, P. Chou, Improving Accident Tolerance of Nuclear Fuel with Coated Mo-alloy Cladding, Nucl. Eng. Technol. 48 (2016) 16–25.

[26] M.N. Gussev, K.G. Field, Y. Yamamoto, Design, Properties, and Weldability of Advanced Oxidation-Resistant FeCrAl Alloys, Mater. Des. 129 (2017) 227–238.

[27] X. Hu, K.A. Terrani, B.D. Wirth, L.L. Snead, Hydrogen permeation in FeCrAl alloys for LWR cladding application, J. Nucl. Mater. 461 (2015) 282–291.

[28] K.A. Terrani, B.A. Pint, C.M. Parish, C.M. Silva, L.L. Snead, Y. Katoh, Silicon Carbide Oxidation in Steam up to 2 MPa, J. Am. Ceram. Soc. 97 (2014) 2331–2352.

[29] L.L. Snead, T. Nozawa, Y. Katoh, T.-S. Byun, S. Kondo, D.A. Petti, Handbook of SiC properties for fuel performance modeling, J. Nucl. Mater. 371 (2007) 329–377.

[30] J.-Y. Park, I.-H. Kim, Y.-I. Jung, H.-G. Kim, D.-J. Park, W.-J. Kim, Long-term corrosion behavior of CVD SiC in 360°C water and 400°C steam, J. Nucl. Mater. 443 (2013) 603–607.

[31] N.M. George, K. Terrani, J. Powers, A. Worrall, I. Maldonado, Neutronic analysis of candidate accident-tolerant cladding concepts in pressurized water reactors, Ann. Nucl. Energy. 75 (2015) 703–712.

[32] N.P. Padture, M. Gell, E.H. Jordan, Thermal barrier coatings for gas-turbine engine applications, Science. 296 (2002) 280–284.

[33] M.E. Westwood, J.D. Webster, R.J. Day, F.H. Hayes, R. Taylor, Oxidation protection for carbon fibre composites, J. Mater. Sci. 31 (1996) 1389–1397.

[34] J. Carr, G. Vasudevamurthy, L. Snead, B. Hinderliter, C. Massey, Investigations of Aluminum-Doped Self-Healing Zircaloy Surfaces in Context of Accident-Tolerant Fuel Cladding Research, J. Mater. Eng. Perform. 25 (2016) 2347–2355.

[35] J.C. Brachet, M. Le Saux, V. Lezaud-Chaillioux, M. Dumerval, Q. Houmaire, F. Lomello, F. Schuster, E. Monsifrot, J. Bischoff, E. Pouillier, Behavior under LOCA conditions of Enhanced Accident Tolerant Chromium Coated Zircaloy-4 Claddings, in: Proc. of Top Fuel, Boise, Idaho, USA, 2016: pp. 1173–1178.

[36] J.-H. Park, H.-G. Kim, J. Park, Y.-I. Jung, D.-J. Park, Y.-H. Koo, High temperature steam-oxidation behavior of arc ion plated Cr coatings for accident tolerant fuel claddings, Surf. Coat. Technol. 280 (2015) 256–259.

[37] J.-M. Kim, T.-H. Ha, I.-H. Kim, H.-G. Kim, Microstructure and Oxidation Behavior of CrAl Laser-Coated Zircaloy-4 Alloy, Metals. 7 (2017) 59.

[38] W.G. Luscher, E.R. Gilbert, S.G. Pitman, E.F. Love, Surface modification of Zircaloy-4 substrates with nickel zirconium intermetallics, J. Nucl. Mater. 433 (2013) 514–522.

[39] K.A. Terrani, C.M. Parish, D. Shin, B.A. Pint, Protection of zirconium by alumina- and chromia-forming iron alloys under high-temperature steam exposure, J. Nucl. Mater. 438 (2013) 64–71.

[40] W. Zhong, P.A. Mouche, X. Han, B.J. Heuser, K.K. Mandapaka, G.S. Was, Performance of iron-

chromium-aluminum alloy surface coatings on Zircaloy 2 under high-temperature steam and normal BWR operating conditions, J. Nucl. Mater. 470 (2016) 327–338.

[41] D.J. Park, H.G. Kim, Y. Il Jung, J.H. Park, J.H. Yang, Y.H. Koo, Behavior of an improved Zr fuel cladding with oxidation resistant coating under loss-of-coolant accident conditions, J. Nucl. Mater. 482 (2016) 75–82.

[42] H. Yeom, B. Maier, R. Mariani, D. Bai, S. Fronek, P. Xu, K. Sridharan, Magnetron sputter deposition of zirconium-silicide coating for mitigating high temperature oxidation of zirconium-alloy, Surf. Coat. Technol. 316 (2017) 30–38.

[43] J.H. Sung, T.H. Kim, S.S. Kim, Fretting damage of TiN coated zircaloy-4 tube, Wear. 250 (2001) 658–664.

[44] Y. Al-Olayyan, G.E. Fuchs, R. Baney, J. Tulenko, The effect of Zircaloy-4 substrate surface condition on the adhesion strength and corrosion of SiC coatings, J. Nucl. Mater. 346 (2005) 109–119.

[45] D.J. Tallman, B. Anasori, M.W. Barsoum, A Critical Review of the Oxidation of Ti_2AlC, Ti_3AlC_2 and Cr_2AlC in Air, Mater. Res. Lett. 1 (2013) 115–125.

[46] E.N. Hoffman, D.W. Vinson, R.L. Sindelar, D.J. Tallman, G. Kohse, M.W. Barsoum, MAX phase carbides and nitrides: Properties for future nuclear power plant in-core applications and neutron transmutation analysis, Nucl. Eng. Des. 244 (2012) 17–24.

[47] M. Pantano, V. Avincola, P.A. De Seze, T. McKrell, M.S. Kazimi, High temperature steam oxidation performance of MAX phase (Ti_2AlC) coated ZIRLO, in: International Congress on Advances in Nuclear Power Plants, Charlotte, North Carolina, USA, 2014: pp. 2126–2135.

[48] B.R. Maier, B.L. Garcia-Diaz, B. Hauch, L.C. Olson, R.L. Sindelar, K. Sridharan, Cold spray deposition of Ti_2AlC coatings for improved nuclear fuel cladding, J. Nucl. Mater. 466 (2015) 712–717.

[49] H. Yeom, B. Hauch, G. Cao, B. Garcia-Diaz, M. Martinez-Rodriguez, H. Colon-Mercado, L. Olson, K. Sridharan, Laser surface annealing and characterization of Ti_2AlC plasma vapor deposition coating on zirconium-alloy substrate, Thin Solid Films. 615 (2016) 202–209.

[50] S. PalDey, S.C. Deevi, Single layer and multilayer wear resistant coatings of (Ti,Al)N: A review, Mater. Sci. Eng. A. 342 (2003) 58–79.

[51] F. Khatkhatay, L. Jiao, J. Jian, W. Zhang, Z. Jiao, J. Gan, H. Zhang, X. Zhang, H. Wang, Superior corrosion resistance properties of TiN-based coatings on Zircaloy tubes in supercritical water, J. Nucl. Mater. 451 (2014) 346–351.

[52] E. Alat, A.T. Motta, R.J. Comstock, J.M. Partezana, D.E. Wolfe, Ceramic coating for corrosion (c3) resistance of nuclear fuel cladding, Surf. Coatings Technol. 281 (2015) 133–143.

[53] K. Daub, R. Van Nieuwenhove, H. Nordin, H. Nordin, Investigation of the impact of coatings on corrosion and hydrogen uptake of Zircaloy-4, J. Nucl. Mater. 467 (2015) 260–270.

[54] W.G. Cook, R.P. Olive, Pourbaix diagrams for chromium, aluminum and titanium extended to high-subcritical and low-supercritical conditions, Corros. Sci. 58 (2012) 291–298.

[55] M. Stueber, H. Holleck, H. Leiste, K. Seemann, S. Ulrich, C. Ziebert, Concepts for the design of advanced nanoscale PVD multilayer protective thin films, J. Alloys Compd. 483 (2009) 321–333.

[56] S.T. Park, Amorphous alumina oxidation protective coating for zircaloy based on a compositional gradient layer systerm, PhD thesis, University of Florida, USA, 2004.

[57] A.S. Kuprin, V.A. Belous, V.N. Voyevodin, V.V. Bryk, R.L. Vasilenko, V.D. Ovcharenko, E.N. Reshetnyak, G.N. Tolmachova, P.N. V'yugov, Vacuum-arc chromium-based coatings for protection of zirconium alloys from the high-temperature oxidation in air, J. Nucl. Mater. 465 (2015) 400–406.

[58] S. V. Ivanova, E.M. Glagovsky, K.Y. Nikonorov, I.I. Belugin, I.A. Khazov, Methods to increase corrosion stability and wear resistance of LWR active core zirconium components during

operation and in conditions of loss-of-coolant accident, in: Proc. of Top Fuel, Charlotte, North Carolina, USA, 2013: pp. 334–350.

[59] U. Wiklund, P. Hedenqvist, S. Hogmark, B. Stridh, M. Arbell, Multilayer coatings as corrosion protection of Zircaloy, Surf. Coat. Technol. 86–87 (1996) 530–534.

[60] E. Alat, A.T. Motta, R.J. Comstock, J.M. Partezana, D.E. Wolfe, Multilayer (TiN, TiAlN) ceramic coatings for nuclear fuel cladding, J. Nucl. Mater. 478 (2016) 236–244.

[61] M.W. Barsoum, The $M_{N+1}AX_N$ phases: a new class of solids; thermodynamically stable nanolaminates, Prog. Solid State Chem. 28 (2000) 201–281.

[62] Z.M. Sun, Progress in research and development on MAX phases: a family of layered ternary compounds, Int. Mater. Rev. 56 (2011) 143–166.

[63] P. Eklund, M. Beckers, U. Jansson, H. Högberg, L. Hultman, The $M_{N+1}AX_N$ phases: Materials science and thin-film processing, Thin Solid Films. 518 (2010) 1851–1878.

[64] W. Jeitschko, H. Nowotny, F. Benesovsky, Kohlenstoffhaltige ternaire Verbindungen (H-Phase), Monatsh. Chem. 94 (1963) 672–676.

[65] W. Jeitschko, H. Nowotny, F. Benesovsky, Carbides of formula T_2MC, J. Less Common Met. 7 (1964) 133–138.

[66] M.W. Barsoum, T. El-Raghy, Synthesis and characterization of a remarkable ceramic: Ti_3SiC_2, J. Am. Ceram. Soc. 79 (1996) 1953–1956.

[67] X.H. Wang, Y.C. Zhou, Layered Machinable and Electrically Conductive Ti_2AlC and Ti_3AlC_2 Ceramics: A Review, J. Mater. Sci. Technol. 26 (2010) 385–416.

[68] H.B. Zhang, Y.W. Bao, Y.C. Zhou, Current status in layered ternary carbide Ti_3SiC_2, a review, J. Mater. Sci. Technol. 25 (2009) 1–38.

[69] M.W. Barsoum, M. Radovic, Elastic and Mechanical Properties of the MAX Phases, Annu. Rev. Mater. Res. 41 (2011) 195–227.

[70] C. Hu, H. Zhang, F. Li, Q. Huang, Y. Bao, New phases' discovery in MAX family, Int. J. Refract. Met. Hard Mater. 36 (2013) 300–312.

[71] M. Radovic, M.W. Barsoum, MAX phases: Bridging the gap between metals and ceramics, Am. Ceram. Soc. Bull. 92 (2013) 20–27.

[72] M. Magnuson, M. Mattesini, Chemical bonding and electronic-structure in MAX phases as viewed by X-ray spectroscopy and density functional theory, Thin Solid Films. 621 (2017) 108–130.

[73] M.W. Barsoum, MAX phases: properties of machinable ternary carbides and nitrides, Wiley, 2013.

[74] M. Naguib, G.W. Bentzel, J. Shah, J. Halim, E.N. Caspi, J. Lu, L. Hultman, M.W. Barsoum, New Solid Solution MAX Phases: $(Ti_{0.5},V_{0.5})_3AlC_2$, $(Nb_{0.5},V_{0.5})_2AlC$, $(Nb_{0.5},V_{0.5})_4AlC_3$ and $(Nb_{0.8},Zr_{0.2})_2AlC$, Mater. Res. Lett. 2 (2014) 233–240.

[75] T. Lapauw, D. Tytko, K. Vanmeensel, S. Huang, P.-P. Choi, D. Raabe, E.N. Caspi, O. Ozeri, M. to Baben, J.M. Schneider, K. Lambrinou, J. Vleugels, $(Nb_x, Zr_{1-x})_4AlC_3$ MAX Phase Solid Solutions: Processing, Mechanical Properties, and Density Functional Theory Calculations, Inorg. Chem. 55 (2016) 5445–5452.

[76] H. Fashandi, M. Dahlqvist, J. Lu, J. Palisaitis, S.I. Simak, I.A. Abrikosov, J. Rosen, L. Hultman, M. Andersson, A. Lloyd Spetz, P. Eklund, Synthesis of Ti_3AuC_2, $Ti_3Au_2C_2$ and Ti_3IrC_2 by noble metal substitution reaction in Ti_3SiC_2 for high-temperature-stable Ohmic contacts to SiC, Nat. Mater. 16 (2017) 814-818.

[77] R. Arróyave, A. Talapatra, T. Duong, W. Son, M. Radovic, Out-of-plane ordering in quaternary MAX alloys: an alloy theoretic perspective, Mater. Res. Lett. 6 (2018) 1–12.

[78] D.P. Riley, E.H. Kisi, A new solid state synthesis methodology for ternary and higher order compounds, J. Aust. Ceram. Soc. 43 (2007) 102–109.

[79] O. Wilhelmsson, J.-P. Palmquist, T. Nyberg, U. Jansson, Deposition of Ti_2AlC and Ti_3AlC_2

epitaxial films by magnetron sputtering, Appl. Phys. Lett. 85 (2004) 1066–1068.

[80] R. Grieseler, B. Hähnlein, M. Stubenrauch, T. Kups, M. Wilke, M. Hopfeld, J. Pezoldt, P. Schaaf, Nanostructured plasma etched, magnetron sputtered nanolaminar Cr_2AlC MAX phase thin films, Appl. Surf. Sci. 292 (2014) 997–1001.

[81] M. Beckers, N. Schell, R.M.S. Martins, A. Mücklich, W. Möller, Phase stability of epitaxially grown Ti_2AlN thin films, Appl. Phys. Lett. 89 (2006) 074101.

[82] J. Emmerlich, D. Music, P. Eklund, O. Wilhelmsson, U. Jansson, J.M. Schneider, H. Högberg, L. Hultman, Thermal stability of Ti_3SiC_2 thin films, Acta Mater. 55 (2007) 1479–1488.

[83] Z. Wang, X. Li, J. Zhou, P. Liu, Q. Huang, P. Ke, A. Wang, Microstructure evolution of V–Al–C coatings synthesized from a V_2AlC compound target after vacuum annealing treatment, J. Alloys Compd. 661 (2016) 476–482.

[84] J. Frodelius, P. Eklund, M. Beckers, P.O.Å. Persson, H. Högberg, L. Hultman, Sputter deposition from a Ti_2AlC target: Process characterization and conditions for growth of Ti_2AlC, Thin Solid Films. 518 (2010) 1621–1626.

[85] A. Abdulkadhim, T. Takahashi, D. Music, F. Munnik, J.M. Schneider, MAX phase formation by intercalation upon annealing of TiC_x/Al ($0.4 \leqslant x \leqslant 1$) bilayer thin films, Acta Mater. 59 (2011) 6168–6175.

[86] H. Högberg, J. Emmerlich, P. Eklund, O. Wilhelmsson, J.P. Palmquist, U. Jansson, L. Hultman, Growth and Property Characterization of Epitaxial MAX-Phase Thin Films from the Ti_{n+1}(Si, Ge, Sn)C_n Systems, Adv. Sci. Technol. 45 (2006) 2648–2655.

[87] O. Berger, C. Leyens, S. Heinze, R. Boucher, M. Ruhnow, Characterization of Cr–Al–C and Cr–Al–C–Y films synthesized by High Power Impulse Magnetron Sputtering at a low deposition temperature, Thin Solid Films. 580 (2015) 6–11.

[88] C. Tang, M. Klimenkov, U. Jaentsch, H. Leiste, M. Rinke, S. Ulrich, M. Steinbrück, H.J. Seifert, M. Stueber, Synthesis and characterization of Ti_2AlC coatings by magnetron sputtering from three elemental targets and ex-situ annealing, Surf. Coat. Technol. 309 (2017) 445–455.

[89] C. Lange, M.W. Barsoum, P. Schaaf, Towards the synthesis of MAX-phase functional coatings by pulsed laser deposition, Appl. Surf. Sci. 254 (2007) 1232–1235.

[90] M.C. Guenette, M.D. Tucker, M. Ionescu, M.M.M. Bilek, D.R. McKenzie, Cathodic arc co-deposition of highly oriented hexagonal Ti and Ti_2AlC MAX phase thin films, Thin Solid Films. 519 (2010) 766–769.

[91] E. Pickering, W.J. Lackey, S. Crain, CVD of Ti_3SiC_2, Chem. Vap. Depos. 6 (2000) 289–295.

[92] M. Sonestedt, J. Frodelius, J.P. Palmquist, H. Högberg, L. Hultman, K. Stiller, Microstructure of high velocity oxy-fuel sprayed Ti_2AlC coatings, J. Mater. Sci. 45 (2010) 2760–2769.

[93] S. Rech, A. Surpi, S. Vezzù, A. Patelli, A. Trentin, J. Glor, J. Frodelius, L. Hultman, P. Eklund, Cold-spray deposition of Ti_2AlC coatings, Vacuum. 94 (2013) 69–73.

[94] A.-S. Farle, C. Kwakernaak, S. van der Zwaag, W.G. Sloof, A conceptual study into the potential of $M_{n+1}AX_n$-phase ceramics for self-healing of crack damage, J. Eur. Ceram. Soc. 35 (2015) 37–45.

[95] X.H. Wang, Y.C. Zhou, High-temperature oxidation behavior of Ti_2AlC in air, Oxid. Met. 59 (2003) 303–320.

[96] X.H. Wang, Y.C. Zhou, Oxidation behavior of Ti_3AlC_2 at 1000–1400 °C in air, Corros. Sci. 45 (2003) 891–907.

[97] M. Sundberg, G. Malmqvist, A. Magnusson, T. El-Raghy, Alumina forming high temperature silicides and carbides, Ceram. Int. 30 (2004) 1899–1904.

[98] Z.J. Lin, M.S. Li, J.Y. Wang, Y.C. Zhou, High-temperature oxidation and hot corrosion of Cr_2AlC, Acta Mater. 55 (2007) 6182–6191.

[99] D.B. Lee, T.D. Nguyen, Cyclic oxidation of Cr_2AlC between 1000 and 1300°C in air, J. Alloys

Compd. 464 (2008) 434–439.

[100] J. Xiao, T. Yang, C. Wang, J. Xue, Y. Wang, Investigations on Radiation Tolerance of $M_{n+1}AX_n$ phases: Study of Ti_3SiC_2, Ti_3AlC_2,Cr_2AlC, Cr_2GeC, Ti_2AlC, and Ti_2AlN, J. Am. Ceram. Soc. 98 (2015) 1323–1331.

[101] D.J. Tallman, L. He, B.L. Garcia-Diaz, E.N. Hoffman, G. Kohse, R.L. Sindelar, M.W. Barsoum, Effect of neutron irradiation on defect evolution in Ti_3SiC_2 and Ti_2AlC, J. Nucl. Mater. 468 (2016) 194–206.

[102] D.W. Clark, S.J. Zinkle, M.K. Patel, C.M. Parish, High temperature ion irradiation effects in MAX phase ceramics, Acta Mater. 105 (2016) 130–146.

[103] S.R.J. Saunders, M. Monteiro, F. Rizzo, The oxidation behaviour of metals and alloys at high temperatures in atmospheres containing water vapour: A review, Prog. Mater. Sci. 53 (2008) 775–837.

[104] H. Frey, H.R. Khan, Handbook of thin film technology, Springer, Berlin, Germany, 2015.

[105] S. Rossnagel, Sputtering and Sputter Deposition, in: K. Seshan (eds), Handbook of thin-film deposition processes and techniques: principles, methods, equipment and applications, 2nd Edition, Noyes Publications, New York, USA, 2002, pp. 319-348.

[106] R.S. Ningthoujam, N.S. Gajbhiye, Synthesis, electron transport properties of transition metal nitrides and applications, Prog. Mater. Sci. 70 (2015) 50–154.

[107] P.H. Mayrhofer, C. Mitterer, L. Hultman, H. Clemens, Microstructural design of hard coatings, Prog. Mater. Sci. 51 (2006) 1032–1114.

[108] D.M. Mattox, Handbook of physical vapor deposition (PVD) processing, 2nd Edition, William Andrew Publishing, New York, USA, 2010.

[109] P.J. Kelly, R.D. Arnell, Magnetron sputtering: a review of recent developments and applications, Vacuum. 56 (2000) 159–172.

[110] K. Sarakinos, J. Alami, S. Konstantinidis, High power pulsed magnetron sputtering: A review on scientific and engineering state of the art, Surf. Coat. Technol. 204 (2010) 1661–1684.

[111] M. Samuelsson, D. Lundin, J. Jensen, M.A. Raadu, J.T. Gudmundsson, U. Helmersson, On the film density using high power impulse magnetron sputtering, Surf. Coat. Technol. 205 (2010) 591–596.

[112] I. Petrov, P.B. Barna, L. Hultman, J.E. Greene, Microstructural evolution during film growth, J. Vac. Sci. Technol. A Vacuum, Surfaces, Film. 21 (2003) S117.

[113] Y.X. Wang, S. Zhang, Toward hard yet tough ceramic coatings, Surf. Coat. Technol. 258 (2014) 1–16.

[114] J.A. Venables, G.D.T. Spiller, M. Hanbucken, Nucleation and growth of thin films, Reports Prog. Phys. 47 (1984) 399–459.

[115] J.A. Venables, Introduction to Surface and Thin Film Processes, Cambridge University Press, Cambridge, UK, 2003.

[116] J.A. Thornton, High rate thick film growth, Ann Rev Mat Sci. 7 (1977) 239–260.

[117] M. Ohring, Plasma and Ion Beam Processing of Thin Films, in: Materials Science of Thin Films: Deposition and Structure, 2nd Edition, Academic press, Orlando, Florida, USA, 2002, pp. 203-275.

[118] A.S. Khanna, Introduction to High Temperature Oxidation and Corrosion, ASM International, Materials Park, Ohio, USA, 2002.

[119] V. Kochubey, Effect of Ti, Hf and Zr additions and impurity elements on the oxidation limited lifetime of thick- and thin-walled FeCrAlY-components, PhD thesis, Ruhr-Universität Bochum, Germany, 2005.

[120] D.J. Young, High Temperature Oxidation and Corrosion of Metals, 2nd Edition, Elsevier,

Amsterdam, Netherland, 2016.

[121] P. Tomaszewicz, G.R. Wallwork, The oxidation of high-purity iron-chromium-aluminum alloys at 800°C, Oxid. Met. 20 (1983) 75–109.

[122] R. Mévrel, State of the art on high-temperature corrosion-resistant coatings, Mater. Sci. Eng. A. 120–121 (1989) 13–24.

[123] G. Hübschen, I. Altpeter, R. Tschuncky, H.-G. Herrmann, Materials Characterization using Nondestructive Evaluation (NDE) Methods, 1st Edition, Woodhead Publishing, Sawston, Cambridge, UK, 2016.

[124] B. Fultz, J.M. Howe, Transmission Electron Microscopy and Diffractometry of Materials, Springer, Berlin, Germany, 2012.

[125] M. Sardela, X-ray analysis methods, Advanced Materials Worskshop, Moline, Illinois, USA, 2014.

[126] Y.N. Wang, J.C. Huang, Texture analysis in hexagonal materials, Mater. Chem. Phys. 81 (2003) 11–26.

[127] E. Smith, G. Dent, The Theory of Raman Spectroscopy, in: Modern Raman Spectroscopy - A Practical Approach, Wiley, Hoboken, New Jersey, USA, 2004, pp. 71-92.

[128] J.F. Watts, J. Wolstenholme, An introduction to surface analysis by XPS and AES, Wiley, Hoboken, New Jersey, USA, 2003.

[129] D. Zhao, Y. Zhang, E.J. Essene, Electron probe microanalysis and microscopy: Principles and applications in characterization of mineral inclusions in chromite from diamond deposit, Ore Geol. Rev. 65 (2015) 733–748.

[130] P. K. Chu, Mass and Optical Spectroscopies, in: C.R. Brundle, C.A. Evans, S. Wilson (eds.), Encyclopedia of Materials Characterization: Surfaces, Interfaces, Thin Films, Butterworth-Heinemann (Publisher), Oxford, UK, 1992.

[131] C.A. Schuh, Nanoindentation studies of materials, Mater. Today. 9 (2006) 32–40 .

[132] M.F. Doerner, W.D. Nix, Stresses and deformation processes in thin films on substrates, Crit. Rev. Solid State Mater. Sci. 14 (1988) 225–268.

[133] ASTM International, Standard Test Method for Adhesion Strength and Mechanical Failure Modes of Ceramic Coatings by Quantitative Single Point Scratch Testing (C1624 – 05), 2010.

[134] S. Zhang, X. Zhang, Toughness evaluation of hard coatings and thin films, Thin Solid Films. 520 (2012) 2375–2389.

[135] X. Wang, Y. Zhou, Intermediate-temperature oxidation behavior of Ti_2AlC in air, J. Mater. Res. 17 (2002) 2974–2981.

[136] Z.J. Lin, M.S. Li, J.Y. Wang, Y.C. Zhou, Influence of water vapor on the oxidation behavior of Ti_3AlC_2 and Ti_2AlC, Scr. Mater. 58 (2008) 29–32.

[137] B. Cui, D.D. Jayaseelan, W.E. Lee, Microstructural evolution during high-temperature oxidation of Ti_2AlC ceramics, Acta Mater. 59 (2011) 4116–4125.

[138] S. Basu, N. Obando, A. Gowdy, I. Karaman, M. Radovic, Long-term oxidation of Ti_2AlC in air and water vapor at 1000–1300°C temperature range, J. Electrochem. Soc. 159 (2012) C90.

[139] H. Zhu, X. Qian, H. Wu, J. Lei, Y. Song, X. He, Y. Zhou, Cyclic oxidation of ternary layered Ti_2AlC at 600-1000°C in air, Int. J. Appl. Ceram. Technol. 12 (2015) 403–410.

[140] J.L. Smialek, Kinetic aspects of Ti_2AlC MAX phase oxidation, Oxid. Met. 83 (2015) 351–366.

[141] J.W. Byeon, J. Liu, M. Hopkins, W. Fischer, N. Garimella, K.B. Park, M.P. Brady, M. Radovic, T. El-Raghy, Y.H. Sohn, Microstructure and residual stress of alumina scale formed on Ti_2AlC at high temperature in air, Oxid. Met. 68 (2007) 97–111.

[142] J.L. Smialek, Environmental resistance of a Ti_2AlC-type MAX phase in a high pressure burner rig, J. Eur. Ceram. Soc. 37 (2017) 23–34.

[143] C. Tang, M. Steinbrück, M. Große, T. Bergfeldt, H.J. Seifert, Oxidation behavior of Ti_2AlC in the temperature range of 1400 °C–1600 °C in steam, J. Nucl. Mater. 490 (2017) 130–142.

[144] H.J. Seifert, A. Kussmaul, F. Aldinger, Phase equilibria and diffusion paths in the Ti-Al-O-N system, J. Alloys Compd. 317–318 (2001) 19–25.

[145] J. Wang, Y. Zhou, Z. Lin, F. Meng, F. Li, Raman active phonon modes and heat capacities of Ti_2AlC and Cr_2AlC ceramics: first-principles and experimental investigations, Appl. Phys. Lett. 86 (2005) 101902.

[146] V.T. Witusiewicz, B. Hallstedt, A.A. Bondar, U. Hecht, S.V. Sleptsov, T.Y. Velikanova, Thermodynamic description of the Al–C–Ti system, J. Alloys Compd. 623 (2015) 480–496.

[147] B. Cui, D.D. Jayaseelan, W.E. Lee, TEM study of the early stages of Ti_2AlC oxidation at 900°C, Scr. Mater. 67 (2012) 830–833.

[148] Q.N. Nguyen, High temperature volatility and oxidation measurements of Titanium and Silicon containing ceramic materials, PhD thesis, Cleveland State University, USA, 2008.

[149] M.C. Maris-Sida, G.H. Meier, F.S. Pettit, Some Water Vapor Effects during the Oxidation of Alloys that are α -Al_2O_3 Formers, Metall. Mater. Trans. A. 34A (2003) 2609–2619.

[150] A. Rahmel, W.J. Quadakkers, M. Schütze, Fundamentals of TiAl oxidation - A critical review, Mater. Corros. 46 (1995) 271–285.

[151] A.S. Ingason, A. Petruhins, J. Rosen, Toward Structural Optimization of MAX Phases as Epitaxial Thin Films, Mater. Res. Lett. 4 (2016) 152–160.

[152] O. Wilhelmsson, J.-P. Palmquist, E. Lewin, J. Emmerlich, P. Eklund, P.O.Å. Persson, H. Högberg, S. Li, R. Ahuja, O. Eriksson, L. Hultman, U. Jansson, Deposition and characterization of ternary thin films within the Ti–Al–C system by DC magnetron sputtering, J. Cryst. Growth. 291 (2006) 290–300.

[153] M.D. Tucker, P.O.Å. Persson, M.C. Guenette, J. Rosen, M.M.M. Bilek, D.R. McKenzie, Substrate orientation effects on the nucleation and growth of the $M_{n+1}AX_n$ phase Ti_2AlC, J. Appl. Phys. 109 (2011) 014903.

[154] J.P. Palmquist, S. Li, P.O.Å. Persson, J. Emmerlich, O. Wilhelmsson, H. Högberg, M.I. Katsnelson, B. Johansson, R. Ahuja, O. Eriksson, L. Hultman, U. Jansson, $M_{n+1}AX_n$ phases in the Ti-Si-C system studied by thin-film synthesis and ab initio calculations, Phys. Rev. B. 70 (2004) 165401.

[155] D.P. Sigumonrong, J. Zhang, Y. Zhou, D. Music, J.M. Schneider, Synthesis and elastic properties of V_2AlC thin films by magnetron sputtering from elemental targets, J. Phys. D. Appl. Phys. 42 (2009) 185408.

[156] M. Beckers, N. Schell, R.M.S. Martins, A. Mücklich, W. Möller, L. Hultman, Microstructure and nonbasal-plane growth of epitaxial Ti_2AlN thin films, J. Appl. Phys. 99 (2006) 034902.

[157] P.O.Å. Persson, S. Kodambaka, I. Petrov, L. Hultman, Epitaxial $Ti_2AlN(0001)$ thin film deposition by dual-target reactive magnetron sputtering, Acta Mater. 55 (2007) 4401–4407.

[158] Z. Feng, P. Ke, A. Wang, Preparation of Ti_2AlC MAX Phase Coating by DC Magnetron Sputtering Deposition and Vacuum Heat Treatment, J. Mater. Sci. Technol. 31 (2015) 1193–1197.

[159] D.E. Hajas, M. to Baben, B. Hallstedt, R. Iskandar, J. Mayer, J.M. Schneider, Oxidation of Cr_2AlC coatings in the temperature range of 1230 to 1410°C, Surf. Coat. Technol. 206 (2011) 591–598.

[160] J.P. Palmquist, U. Jansson, T. Seppänen, P.O.Å. Persson, J. Birch, L. Hultman, P. Isberg, Magnetron sputtered epitaxial single-phase Ti_3SiC_2 thin films, Appl. Phys. Lett. 81 (2002) 835–837.

[161] C. Walter, C. Martinez, T. El-Raghy, J.M. Schneider, Towards large area MAX phase coatings on steel, Steel Res. Int. 76 (2005) 225–228.

[162] A. Abdulkadhim, M. to Baben, V. Schnabel, M. Hans, N. Thieme, C. Polzer, P. Polcik, J.M. Schneider, Crystallization kinetics of V_2AlC, Thin Solid Films. 520 (2012) 1930–1933.

[163] I.C. Schramm, C. Pauly, M.P. Johansson Jõesaar, P. Eklund, J. Schmauch, F. Mücklich, M. Odén,

Solid state formation of Ti_4AlN_3 in cathodic arc deposited $(Ti_{1-x}Al_x)_y$ alloys, Acta Mater. 129 (2017) 268–277.

[164] T. Cabioch, M. Alkazaz, M.F. Beaufort, J. Nicolai, D. Eyidi, P. Eklund, Ti_2AlN thin films synthesized by annealing of (Ti+Al)/AlN multilayers, Mater. Res. Bull. 80 (2016) 58–63.

[165] M. Hopfeld, R. Grieseler, T. Kups, M. Wilke, P. Schaaf, Thin film synthesis of Ti_3SiC_2 by rapid thermal processing of magnetron-sputtered Ti-C-Si multilayer systems, Adv. Eng. Mater. 15 (2013) 269–275.

[166] H. Högberg, P. Eklund, J. Emmerlich, J. Birch, L. Hultman, Epitaxial Ti_2GeC, Ti_3GeC_2, and Ti_4GeC_3 MAX-phase thin films grown by magnetron sputtering, J. Mater. Res. 20 (2005) 779–782.

[167] M.D. Tucker, M.M.M. Bilek, D.R. McKenzie, A combinatorial investigation of sputtered Ta-Al-C thin films, Thin Solid Films. 558 (2014) 99–103.

[168] L. Shang, M. to Baben, K. G. Pradeep, S. Sandlöbes, M. Amalraj, M. Hans, K. Chang, D. Music, D. Primetzhofer, J.M. Schneider, Phase formation of Nb_2AlC investigated by combinatorial thin film synthesis and ab initio calculations, J. Eur. Ceram. Soc. 37 (2017) 35–41.

[169] C. Fang, R. Ahuja, O. Eriksson, S. Li, U. Jansson, O. Wilhelmsson, L. Hultman, General trend of the mechanical properties of the ternary carbides M_3SiC_2 (M=transition metal), Phys. Rev. B. 74 (2006) 054106.

[170] A. Abdulkadhim, M. to Baben, T. Takahashi, V. Schnabel, M. Hans, C. Polzer, P. Polcik, J.M. Schneider, Crystallization kinetics of amorphous Cr_2AlC thin films, Surf. Coat. Technol. 206 (2011) 599–603.

[171] O. Wilhelmsson, P. Eklund, H. Högberg, L. Hultman, U. Jansson, Structural, electrical and mechanical characterization of magnetron-sputtered V-Ge-C thin films, Acta Mater. 56 (2008) 2563–2569.

[172] J. Rosen, P.O.Å. Persson, M. Ionescu, A. Kondyurin, D.R. McKenzie, M.M.M. Bilek, Oxygen incorporation in Ti_2AlC thin films, Appl. Phys. Lett. 92 (2008) 064102.

[173] T. Joelsson, A. Flink, J. Birch, L. Hultman, Deposition of single-crystal Ti_2AlN thin films by reactive magnetron sputtering from a 2Ti:Al compound target, J. Appl. Phys. 102 (2007) 074918.

[174] H. Högberg, L. Hultman, J. Emmerlich, T. Joelsson, P. Eklund, J.M. Molina-Aldareguia, J.-P. Palmquist, O. Wilhelmsson, U. Jansson, Growth and characterization of MAX-phase thin films, Surf. Coat. Technol. 193 (2005) 6–10.

[175] Q.M. Wang, W. Garkas, A.F. Renteria, C. Leyens, H.W. Lee, K.H. Kim, Oxidation behaviour of Ti–Al–C films composed mainly of a Ti_2AlC phase, Corros. Sci. 53 (2011) 2948–2955.

[176] W. Garkas, C. Leyens, A. Flores-Renteria, Synthesis and Characterization of Ti_2AlC and Ti_2AlN MAX Phase Coatings Manufactured in an Industrial-Size Coater, Adv. Mater. Res. 89–91 (2010) 208–213.

[177] Z. Feng, P. Ke, Q. Huang, A. Wang, The scaling behavior and mechanism of Ti_2AlC MAX phase coatings in air and pure water vapor, Surf. Coat. Technol. 272 (2015) 380–386.

[178] J. Frodelius, M. Sonestedt, S. Björklund, J.P. Palmquist, K. Stiller, H. Högberg, L. Hultman, Ti_2AlC coatings deposited by High Velocity Oxy-Fuel spraying, Surf. Coat. Technol. 202 (2008) 5976–5981.

[179] M. Sonestedt, J. Frodelius, M. Sundberg, L. Hultman, K. Stiller, Oxidation of Ti_2AlC bulk and spray deposited coatings, Corros. Sci. 52 (2010) 3955–3961.

[180] D.P. Adams, Reactive multilayers fabricated by vapor deposition: A critical review, Thin Solid Films. 576 (2015) 98–128.

[181] J. Robertson, Diamond-like amorphous carbon, Mater. Sci. Eng. R. 37 (2002) 129–281.

[182] H.O. Pierson, Handbook of refractory carbides and nitrides : Properties, characteristics, processing, and applications, William Andrew Publishing, New York, USA, 1996.

[183] A. C. Ferrari, J. Robertson, Interpretation of Raman spectra of disordered and amorphous carbon, Phys. Rev. B. 61 (2000) 14095–14107.

[184] J. E. Spanier, S. Gupta, M. S. Amer, M. W. Barsoum, Vibrational behavior of the $M_{n+1}AX_n$ phases from first-order Raman scattering (M=Ti,V,Cr, A=Si, X=C,N), Phys. Rev. B. 71 (2005) 012103.

[185] V. Vishnyakov, O. Crisan, P. Dobrosz, J.S. Colligon, Ion sputter-deposition and in-air crystallisation of Cr_2AlC films, Vacuum. 100 (2014) 61–65.

[186] H.L. Ma, J.Y. Yang, Y. Dai, Y.B. Zhang, B. Lu, G.H. Ma, Raman study of phase transformation of TiO_2 rutile single crystal irradiated by infrared femtosecond laser, Appl. Surf. Sci. 253 (2007) 7497–7500.

[187] V. Presser, M. Naguib, L. Chaput, A. Togo, G. Hug, M.W. Barsoum, First-order Raman scattering of the MAX phases: Ti_2AlN, $Ti_2AlC_{0.5}N_{0.5}$, Ti_2AlC, $(Ti_{0.5}V_{0.5})_2AlC$, V_2AlC, Ti_3AlC_2, and Ti_3GeC_2, J. Raman Spectrosc. 43 (2012) 168–172.

[188] H. Watanabe, N. Yamada, M. Okaji, Linear thermal expansion coefficient of silicon from 293 to 1000 K, Int. J. Thermophys. 25 (2004) 221–236.

[189] M. W. Barsoum, I. Salama, T. El-Raghy, J. Golczewski, W. D. Porter, H. Wang, H. J. Seifert, F. Aldinger, Thermal and electrical properties of Nb_2AlC, $(Ti, Nb)_2AlC$ and Ti_2AlC, Metall. Mater. Trans. A. 33 (2002) 2775–2779.

[190] C. Tang, M. Klimenkov, U. Jaentsch, H. Leiste, M. Rinke, S. Ulrich, M. Steinbrück, H.J. Seifert, M. Stueber, Synthesis and characterization of Ti_2AlC coatings by magnetron sputtering from three elemental targets and ex-situ annealing, Surf. Coat. Technol. 309 (2017) 445–455.

[191] M.A. Nicolet, Diffusion barriers in thin films, Thin Solid Films. 52 (1978) 415–443.

[192] M. V. Klein, J.A. Holy, W.S. Williams, Raman scattering induced by carbon vacancies in TiC_x, Phys. Rev. B. 17 (1978) 1546–1556.

[193] K. Djebaili, Z. Mekhalif, A. Boumaza, A. Djelloul, XPS, FTIR, EDX, and XRD analysis of Al_2O_3 scales grown on PM2000 alloy, J. Spectrosc. 2015 (2015) 1–16.

[194] Y. Bai, X. He, Y. Li, C. Zhu, S. Zhang, Rapid synthesis of bulk Ti_2AlC by self-propagating high temperature combustion synthesis with a pseudo–hot isostatic pressing process, J. Mater. Res. 24 (2009) 2528–2535.

[195] X. Wang, Y. Zhou, Solid-liquid reaction synthesis and simultaneous densification of polycrystalline Ti_2AlC, Zeitschrift für Metallkunde. 93 (2002) 66–71.

[196] J. Zhu, J. Gao, J. Yang, F. Wang, K. Niihara, Synthesis and microstructure of layered-ternary Ti_2AlC ceramic by high energy milling and hot pressing, Mater. Sci. Eng. A. 490 (2008) 62–65.

[197] T. Joelsson, A. Flink, J. Birch, L. Hultman, Deposition of single-crystal Ti_2AlN thin films by reactive magnetron sputtering from a 2Ti:Al compound target, J. Appl. Phys. 102 (2007) 074918.

[198] Y. Zhou, Z. Sun, Microstructure and mechanism of damage tolerance for Ti_3SiC_2 bulk ceramics, Mater. Res. Innov. 2 (1999) 360–363.

[199] J. Wang, J. Wang, Y. Zhou, Stable $M_2AlC(0001)$ surfaces (M = Ti, V and Cr) by first-principles investigation, J. Phys. Condens. Matter. 20 (2008) 225006.

[200] J. Frodelius, J. Lu, J. Jensen, D. Paul, L. Hultman, P. Eklund, Phase stability and initial low-temperature oxidation mechanism of Ti_2AlC thin films, J. Eur. Ceram. Soc. 33 (2013) 375–382.

[201] I. Gurrappa, S. Weinbruch, D. Naumenko, W.J. Quadakkers, Factors governing breakaway oxidation of FeCrAl-based alloys, Mater. Corros. 51 (2000) 224–235.

[202] X. Li, L. Zheng, Y. Qian, J. Xu, M. Li, Breakaway oxidation of Ti_3AlC_2 during long-term exposure in air at 1100°C, Corros. Sci. 104 (2016) 112–122.

[203] M. Gherrab, V. Garnier, S. Gavarini, N. Millard-Pinard, S. Cardinal, Oxidation behavior of nano-scaled and micron-scaled TiC powders under air, Int. J. Refract. Met. Hard Mater. 41 (2013) 590–596.

[204] A. Onuma, H. Kiyono, S. Shimada, M. Desmaison, High temperature oxidation of sintered TiC in an H_2O-containing atmosphere, Solid State Ionics. 172 (2004) 417–419.

[205] M.W. Barsoum, N. Tzenov, A. Procopio, T. El-Raghy, M. Ali, Oxidation of $Ti_{n+1}AlX_n$ (n=1-3 and X=C, N): II. Experimental Results, J. Electrochem. Soc. 148 (2001) C551-C562.

[206] B. Cui, R. Sa, D.D. Jayaseelan, F. Inam, M.J. Reece, W.E. Lee, Microstructural evolution during high-temperature oxidation of spark plasma sintered Ti_2AlN ceramics, Acta Mater. 60 (2012) 1079–1092.

[207] Y.-C. Zhou, L.-F. He, Z.-J. Lin, J.-Y. Wang, Synthesis and structure–property relationships of a new family of layered carbides in Zr-Al(Si)-C and Hf-Al(Si)-C systems, J. Eur. Ceram. Soc. 33 (2013) 2831–2865.

[208] L.F. He, Y.C. Zhou, Y.W. Bao, J.Y. Wang, M.S. Li, Synthesis and oxidation of $Zr_3Al_3C_5$ powders, Int. J. Mater. Res. 98 (2007) 3–9.

[209] L.F. He, Z.J. Lin, Y.W. Bao, M.S. Li, J.Y. Wang, Y.C. Zhou, Isothermal oxidation of bulk $Zr_2Al_3C_4$ at 500 to 1000 °C in air, J. Mater. Res. 23 (2008) 359–366.

[210] T. Lapauw, K. Lambrinou, T. Cabioc'h, J. Halim, J. Lu, A. Pesach, O. Rivin, O. Ozeri, E.N. Caspi, L. Hultman, P. Eklund, J. Rosén, M.W. Barsoum, J. Vleugels, Synthesis of the new MAX phase Zr_2AlC, J. Eur. Ceram. Soc. 36 (2016) 1847–1853.

[211] T. Lapauw, J. Halim, J. Lu, T. Cabioc'h, L. Hultman, M.W. Barsoum, K. Lambrinou, J. Vleugels, Synthesis of the novel Zr_3AlC_2 MAX phase, J. Eur. Ceram. Soc. 36 (2016) 943–947.

[212] J.C. Schuster, H. Nowotny, Investigations of the ternary systems (Zr, Hf, Nb, Ta)-Al-C and studies on complex carbides, Zeitschrift für Metallkunder. 71 (1980) 341–346.

[213] L. Shang, D. Music, M. to Baben, J.M. Schneider, Phase stability predictions of $(Cr_{1-x}, M_x)_2$ $(Al_{1-y}, A_y)(C_{1-z}, X_z)$ (M = Ti, Hf, Zr; A = Si, X = B), J. Phys. D. Appl. Phys. 47 (2014) 065308.

[214] M. Dahlqvist, Benefits of oxygen incorporation in atomic laminates, J. Phys. Condens. Matter. 28 (2016) 135501.

[215] D. Horlait, S. Grasso, A. Chroneos, W.E. Lee, Attempts to synthesise quaternary MAX phases $(Zr,M)_2AlC$ and $Zr_2(Al,A)C$ as a way to approach Zr_2AlC, Mater. Res. Lett. 4 (2016) 137-144.

[216] M. Opeka, J. Zaykoski, I. Talmy, S. Causey, Synthesis and characterization of Zr_2SC ceramics, Mater. Sci. Eng. A. 528 (2011) 1994–2001.

[217] S. Gupta, E.N. Hoffman, M.W. Barsoum, Synthesis and oxidation of Ti_2InC, Zr_2InC, $(Ti_{0.5},Zr_{0.5})_2InC$ and $(Ti_{0.5},Hf_{0.5})_2InC$ in air, J. Alloys Compd. 426 (2006) 168–175.

[218] C. Tang, M. Stueber, M. Steinbrueck, M. Grosse, S. Ulrich, H.J. Seifert, Evaluation of magnetron sputtered protective Zr-Al-C coatings for accident tolerant Zircaloy claddings, in: Water Reactor Fuel Performance Meeting, Jeju Island, Korea, 2017: pp. 1–9.

[219] E. Zapata-Solvas, S.R.G. Christopoulos, N. Ni, D.C. Parfitt, D. Horlait, M.E. Fitzpatrick, A. Chroneos, W.E. Lee, Experimental synthesis and density functional theory investigation of radiation tolerance of $Zr_3(Al_{1-x}Si_x)C_2$ MAX phases, J. Am. Ceram. Soc. 100 (2017) 1377–1387.

[220] C.-C. Lai, M.D. Tucker, J. Lu, J. Jensen, G. Greczynski, P. Eklund, J. Rosen, Synthesis and characterization of $Zr_2Al_3C_4$ thin films, Thin Solid Films. 595 (2015) 142–147.

[221] D. Holec, R. Rachbauer, L. Chen, L. Wang, D. Luef, P.H. Mayrhofer, Phase stability and alloy-related trends in Ti-Al-N, Zr-Al-N and Hf-Al-N systems from first principles, Surf. Coat. Technol. 206 (2011) 1698–1704.

[222] H.C. Barshilia, M.S. Prakash, A. Jain, K.S. Rajam, Structure, hardness and thermal stability of TiAlN and nanolayered TiAlN/CrN multilayer films, Vacuum. 77 (2005) 169–179.

[223] C. Tang, M. Steinbrueck, M. Grosse, A. Jianu, A. Weisenburger, H.J. Seifert, High-Temperature oxidation behavior of kanthal APM and D alloys in steam, in: International Congress on Advanced Nuclear Power Plants, San Francisco, California, USA, 2016: pp. 2113–2119.

[224] D. McIntyre, J.E. Greene, G. Håkansson, J.E. Sundgren, W.D. Münz, Oxidation of metastable

single-phase polycrystalline $Ti_{0.5}Al_{0.5}N$ films: Kinetics and mechanisms, J. Appl. Phys. 67 (1990) 1542–1553.

[225] Z. Lin, Y. Zhou, M. Li, Synthesis, microstructure, and property of Cr_2AlC, J. Mater. Sci. Technol. 23 (2007) 721–746.

[226] J.M. Schneider, Z. Sun, R. Mertens, F. Uestel, R. Ahuja, Ab initio calculations and experimental determination of the structure of Cr_2AlC, Solid State Commun. 130 (2004) 445–449.

[227] T.H. Scabarozi, S. Amini, O. Leaffer, A. Ganguly, S. Gupta, W. Tambussi, S. Clipper, J.E. Spanier, M.W. Barsoum, J.D. Hettinger, S.E. Lofland, Thermal expansion of select $M_{n+1}AX_n$(M=early transition metal, A=A group element, X=C or N) phases measured by high temperature x-ray diffraction and dilatometry, J. Appl. Phys. 105 (2009) 013543.

[228] W. Tian, P. Wang, G. Zhang, Y. Kan, Y. Li, D. Yan, Synthesis and thermal and electrical properties of bulk Cr_2AlC, Scr. Mater. 54 (2006) 841–846.

[229] S. Gupta, D. Filimonov, T. Palanisamy, M.W. Barsoum, Tribological behavior of select MAX phases against Al_2O_3 at elevated temperatures, Wear. 265 (2008) 560–565.

[230] R. Pei, S.A. McDonald, L. Shen, S. van der Zwaag, W.G. Sloof, P.J. Withers, P.M. Mummery, Crack healing behaviour of Cr_2AlC MAX phase studied by X-ray tomography, J. Eur. Ceram. Soc. 37 (2017) 441–450.

[231] L.M. Aw, R. Amendola, J.W. Ryter, M.W. McCleary, P.E. Gannon, M.E. Leonard, J.L. Smialek, Investigation of Na_2SO_4 Deposit Induced Corrosion of Cr, Al, C Binary and Ternary Thin Film Coatings on Ni-201, J. Electrochem. Soc. 164 (2017) C218–C223.

[232] Z. Sun, S. Li, R. Ahuja, J.M. Schneider, Calculated elastic properties of M_2AlC (M = Ti, V, Cr, Nb and Ta), Solid State Commun. 129 (2004) 589–592.

[233] J.D. Hettinger, S.E. Lofland, P. Finkel, T. Meehan, J. Palma, K. Harrell, S. Gupta, A. Ganguly, T. El-Raghy, M.W. Barsoum, Electrical transport, thermal transport, and elastic properties of M_2AlC (M=Ti, Cr, Nb, and V), Phys. Rev. B. 72 (2005) 115120.

[234] D.B. Lee, T.D. Nguyen, J.H. Han, S.W. Park, Oxidation of Cr_2AlC at 1300°C in air, Corros. Sci. 49 (2007) 3926–3934.

[235] S. Li, X. Chen, Y. Zhou, G. Song, Influence of grain size on high temperature oxidation behavior of Cr_2AlC ceramics, Ceram. Int. 39 (2013) 2715–2721.

[236] S.B. Li, W.B. Yu, H.X. Zhai, G.M. Song, W.G. Sloof, S. van der Zwaag, Mechanical properties of low temperature synthesized dense and fine-grained Cr_2AlC ceramics, J. Eur. Ceram. Soc. 31 (2011) 217–224.

[237] S. Li, L. Xiao, G. Song, X. Wu, W.G. Sloof, S. Van Der Zwaag, Oxidation and crack healing behavior of a fine-grained Cr_2AlC ceramic, J. Am. Ceram. Soc. 96 (2013) 892–899.

[238] J.J. Li, M.S. Li, H.M. Xiang, X.P. Lu, Y.C. Zhou, Short-term oxidation resistance and degradation of Cr_2AlC coating on M38G superalloy at 900-1100 °C, Corros. Sci. 53 (2011) 3813–3820.

[239] J.J. Li, Y.H. Qian, D. Niu, M.M. Zhang, Z.M. Liu, M.S. Li, Phase formation and microstructure evolution of arc ion deposited Cr_2AlC coating after heat treatment, Appl. Surf. Sci. 263 (2012) 457–464.

[240] O. Berger, C. Leyens, S. Heinze, M. Baben, J.M. Schneider, Self-Healing of Yttrium-doped Cr_2AlC MAX Phase Coatings deposited by HIPIMS, Proc. of the 4th International Conference on Self-Healing Materials, Ghent, Belgium, 2013: pp. 319–323.

[241] E.I. Zamulaeva, E.A. Levashov, T.A. Sviridova, N. V. Shvyndina, M.I. Petrzhik, Pulsed electrospark deposition of MAX phase Cr_2AlC based coatings on titanium alloy, Surf. Coat. Technol. 235 (2013) 454–460.

[242] O. Berger, R. Boucher, M. Ruhnow, Part II. Oxidation of yttrium doped Cr_2AlC films in temperature range between 700 and 1200° C, Surf. Eng. 31 (2015) 386-396.

[243] L. Shang, P. Konda Gokuldoss, S. Sandlöbes, M. to Baben, J.M. Schneider, Effect of Si additions

on the Al_2O_3 grain refinement upon oxidation of Cr_2AlC MAX phase, J. Eur. Ceram. Soc. 37 (2017) 1339–1347.

[244] R. Mertens, Z. Sun, D. Music, J.M. Schneider, Effect of the composition on the structure of Cr-Al-C investigated by combinatorial thin film synthesis and ab initio calculations, Adv. Eng. Mater. 6 (2004) 903–907.

[245] C. Walter, D.P. Sigumonrong, T. El-Raghy, J.M. Schneider, Towards large area deposition of Cr_2AlC on steel, Thin Solid Films. 515 (2006) 389–393.

[246] Q.M. Wang, R. Mykhaylonka, A. Flores Renteria, J.L. Zhang, C. Leyens, K.H. Kim, Improving the high-temperature oxidation resistance of a β–γ TiAl alloy by a Cr_2AlC coating, Corros. Sci. 52 (2010) 3793–3802.

[247] Q.M. Wang, A. Flores Renteria, O. Schroeter, R. Mykhaylonka, C. Leyens, W. Garkas, M. to Baben, Fabrication and oxidation behavior of Cr_2AlC coating on Ti6242 alloy, Surf. Coat. Technol. 204 (2010) 2343–2352.

[248] J.J. Li, L.F. Hu, F.Z. Li, M.S. Li, Y.C. Zhou, Variation of microstructure and composition of the Cr_2AlC coating prepared by sputtering at 370 and 500 °C, Surf. Coat. Technol. 204 (2010) 3838–3845.

[249] B. Hallstedt, D. Music, Z. Sun, Thermodynamic evaluation of the Al–Cr–C system, Zeitschrift für Metallkunde. 97 (2006) 539–542.

[250] Y.F. Gu, H. Harada, Y. Ro, Chromium and chromium-based alloys: Problems and possibilities for high-temperature service, Jom. 56 (2004) 28–33.

[251] M. Naveed, A. Obrosov, A. Zak, W. Dudzinski, A. A. Volinsky, S. Weiss, Sputtering Power Effects on Growth and Mechanical Properties of Cr_2AlC MAX Phase, Metals. 6 (2016) 265.

[252] R.G. Coltters, Thermodynamics of binary metallic carbides: A review, Mater. Sci. Eng. 76 (1985) 1–50.

[253] S.S. Kim, T.H. Sanders, Thermodynamic Modeling of the Isomorphous Phase Diagrams in the Al_2O_3–Cr_2O_3 and V_2O_3–Cr_2O_3 Systems, J. Am. Chem. Soc. 84 (2001) 1881–1884.

[254] Y.-S. Chen, D. Haley, S.S.A. Gerstl, A.J. London, F. Sweeney, R.A. Wepf, W.M. Rainforth, P.A.J. Bagot, M.P. Moody, Direct observation of individual hydrogen atoms at trapping sites in a ferritic steel, Science 355 (2017) 1196–1199.

[255] J.B. Bai, C. Prioul, D. François, Hydride embrittlement in ZIRCALOY-4 plate: Part I. Influence of microstructure on the hydride embrittlement in ZIRCALOY-4 at 20 °C and 350 °C, Metall. Mater. Trans. A. 25 (1994) 1185–1197.

[256] J. Takahashi, K. Kawakami, T. Tarui, Direct observation of hydrogen-trapping sites in vanadium carbide precipitation steel by atom probe tomography, Scr. Mater. 67 (2012) 213–216.

[257] G.W. Hollenberg, E.P. Simonen, G. Kalinin, A. Terlain, Tritium/hydrogen barrier development, Fusion Eng. Des. 28 (1995) 190–208.

[258] D. Levchuk, S. Levchuk, H. Maier, H. Bolt, A. Suzuki, Erbium oxide as a new promising tritium permeation barrier, J. Nucl. Mater. 367–370 B (2007) 1033–1037.

[259] C. Tang, M.K. Grosse, P. Trtik, M. Steinbrück, M. Stüber, H.J. Seifert, H_2 permeation behavior of Cr_2AlC and Ti_2AlC MAX phase coated Zircaloy-4 by neutron radiography, Acta Polytech. 58 (2018) 69–76.

[260] G.A. Bickel, L.W. Green, M.W.D. James, T.G. Lamarche, P.K. Leeson, H. Michel, The determination of hydrogen and deuterium in Zr-2.5Nb material by hot vacuum extraction mass spectrometry, J. Nucl. Mater. 306 (2002) 21–29.

[261] M. Grosse, E. Lehmann, P. Vontobel, M. Steinbrueck, Quantitative determination of absorbed hydrogen in oxidised zircaloy by means of neutron radiography, Nucl. Instrum. Methods Phys. Res. A. 566 (2006) 739–745.

[262] Z. Wang, U. Garbe, H. Li, R.P. Harrison, A. Kaestner, E. Lehmann, Observations on the

Zirconium Hydride Precipitation and Distribution in Zircaloy-4, Metall. Mater. Trans. B. 45 (2014) 532–539.

[263] J.C. Brachet, D. Hamon, M. Le Saux, V. Vandenberghe, C. Toffolon-Masclet, E. Rouesne, S. Urvoy, J.L. Béchade, C. Raepsaet, J.L. Lacour, G. Bayon, F. Ott, Study of secondary hydriding at high temperature in zirconium based nuclear fuel cladding tubes by coupling information from neutron radiography/tomography, electron probe micro analysis, micro elastic recoil detection analysis and laser induced breakdown spectroscopy microprobe, J. Nucl. Mater. 488 (2017) 267–286.

[264] T. Smith, H. Bilheux, H. Ray, J.C. Bilheux, Y. Yan, High Resolution Neutron Radiography and Tomography of Hydrided Zircaloy-4 Cladding Materials, Phys. Procedia. 69 (2015) 478–482.

[265] M. Grosse, M. Van Den Berg, C. Goulet, A. Kaestner, In-situ investigation of hydrogen diffusion in Zircaloy-4 by means of neutron radiography, J. Phys. Conf. Ser. 340 (2012) 012106.

[266] A.P. Kaestner, S. Hartmann, G. Kühne, G. Frei, C. Grünzweig, L. Josic, F. Schmid, E.H. Lehmann, The ICON beamline A facility for cold neutron imaging at SINQ, Nucl. Instrum. Methods Phys. Res. A. 659 (2011) 387–393.

[267] R.A. Causey, R.A. Karnesky, C. San Marchi, Tritium Barriers and Tritium Diffusion in Fusion Reactors, in: R. J. M. Konings (eds.), Comprehensive Nuclear Materials, Elsevier, Amsterdam, Netherland, 2012: vol. 5, pp. 511–549.

[268] H. Ding, N. Glandut, X. Fan, Q. Liu, Y. Shi, J. Jie, First-principles study of hydrogen incorporation into the MAX phase Ti_3AlC_2, Int. J. Hydrogen Energy. 41 (2016) 6387–6393.

[269] C. Xu, H. Zhang, S. Hu, X. Zhou, S. Peng, H. Xiao, G. Zhang, First-principles calculations of Ti_3SiC_2 and Ti_3AlC_2 with hydrogen interstitial, J. Nucl. Mater. 488 (2017) 261–266.

[270] Q. Li, J. Wang, Q.Y. Xiang, T. Tang, Y.C. Rao, J.L. Cao, Thickness impacts on permeation reduction factor of Er_2O_3 hydrogen isotopes permeation barriers prepared by magnetron sputtering, Int. J. Hydrogen Energy. 41 (2016) 3299–3306.

[271] Q. Liu, H.M. Ding, B.Q. Du, K.Y. Chu, Y. Shi, Hydrogen insertion in Ti_2AlC and its influence on the crystal structure and bonds, J. Ceram. Sci. Technol. 208 (2017) 201–208.

[272] F. Colonna, C. Elsässer, First principles DFT study of interstitial hydrogen and oxygen atoms in the MAX phase Ti_2AlN, RSC Adv. 7 (2017) 37852–37857.

[273] D. Levchuk, H. Bolt, M. Döbeli, S. Eggenberger, B. Widrig, J. Ramm, Al-Cr-O thin films as an efficient hydrogen barrier, Surf. Coat. Technol. 202 (2008) 5043–5047.

Publications

Journal papers (peer-reviewed)

[1] **C. Tang**, M. Klimenkov, U. Jaentsch, H. Leiste, M. Rinke, S. Ulrich, M. Steinbrück, H.J. Seifert, M. Stueber, Synthesis and characterization of Ti_2AlC coatings by magnetron sputtering from three elemental targets and ex-situ annealing, Surf. Coat. Technol. 309 (2017) 445–455.

[2] **C. Tang**, M. Steinbrück, M. Große, T. Bergfeldt, H.J. Seifert, Oxidation behavior of Ti_2AlC in the temperature range of 1400 °C–1600 °C in steam, J. Nucl. Mater. 490 (2017) 130–142.

[3] **C. Tang**, M. Stueber, H.J. Seifert, M. Steinbrueck, Protective coatings on zirconium-based alloys as accident-tolerant fuel (ATF) claddings, Corros. Rev. 35 (2017) 141–166.

[4] **C. Tang**, M. Steinbrueck, M. Stueber, M. Grosse, X. Yu, S. Ulrich, H.J. Seifert, Deposition, characterization and high-temperature steam oxidation behavior of single-phase Ti_2AlC-coated Zircaloy-4, Corros. Sci. 135 (2018) 87–98.

[5] **C. Tang**, M.K. Grosse, P. Trtik, M. Steinbrück, M. Stüber, H.J. Seifert, H_2 permeation behavior of Cr_2AlC and Ti_2AlC MAX phase coated Zircaloy-4 by neutron radiography, Acta Polytech. 58 (2018) 69–76.

Conference papers (peer-reviewed)

[1] **C. Tang**, M. Steinbrueck, M. Grosse, A. Jianu, A. Weisenburger, H.J. Seifert, High-Temperature oxidation behavior of Kanthal APM and D alloys in steam, in: International Congress on Advances in Nuclear Power Plants, San Francisco, California, USA, 2016: pp. 2113–2119.

[2] **C. Tang**, M. Stueber, M. Steinbrueck, M. Grosse, S. Ulrich, H.J. Seifert, Evaluation of magnetron sputtered protective Zr-Al-C coatings for accident tolerant Zircaloy claddings, in: Water Reactor Fuel Performance Meeting, Jeju Island, Korea, 2017: pp. 1–9.

[3] **C. Tang**, M. Steinbrueck, M. Grosse, S. Ulrich, M. Stueber, H.J. Seifert, Improvement of the High-Temperature Oxidation Resistance of Zr Alloy Cladding by Surface Modification with Aluminum-Containing Ternary Carbide Coatings, in: International Congress on Advances in Nuclear Power Plants, Charlotte, North Carolina, USA, 2018: pp. 694–700.

[4] M.K. Grosse, T. van Duijnhoven, M. Steinbrueck, **C. Tang**, S. Ahmed, U. Gerhards, I.J. Markel, H.J. Seifert, High temperature interaction of SiC and Zry-4, in: International Congress on Advances in Nuclear Power Plants, Charlotte, North Carolina, USA, 2018: pp. 590-597.

Oral presentations

[1] **C. Tang**, M. Steinbrueck, M. Grosse, S. Ulrich, M. Stueber, H.J. Seifert. High-temperature oxidation resistance and self-healing behavior of Cr_2AlC MAX phase coating on Zircaloy-4, 23rd International QUENCH Workshop, Karlsruhe, Germany, Oct. 17 – 19, 2017.

[2] **C. Tang**, M. Steinbrueck, M. Grosse, S. Ulrich, M. Stueber, H.J. Seifert. Evaluation of Magnetron Sputtered Protective Zr-C-Al Coatings for Accident Tolerant Zircaloy Claddings, 2017 Water Reactor Fuel Performance Meeting, Jeju Island, Korea, Sept. 10 – 14, 2017.

[3] **C. Tang**, M. Stueber, M. Steinbrueck, M. Grosse, S. Ulrich, H.J. Seifert. Assessment of high-temperature steam oxidation behavior of Zircaloy-4 with Ti_2AlC coating deposited by magnetron sputtering, The Nuclear Materials Conference 2016, Montpellier, France, Nov.07 – 11, 2016.

[4] **C. Tang**, M. Stueber, M. Steinbrueck, M. Grosse, S. Ulrich, H.J. Seifert. Deposition and high-temperature oxidation behavior of Ti_2AlC coated Zircaloy-4, 22nd QUENCH Workshop, Karlsruhe Institute of Technology, Campus North, Karlsruhe, Germany, Oct.18 – 20, 2016.

[5] **C. Tang**, M. Steinbrueck, M. Grosse, A. Jianu, A. Weisenburger, H.J. Seifert. High temperature oxidation behavior of FeCrAl(RE) alloy in steam, International Congress on Advances in Nuclear Power Plants, ICAPP2016, San Francisco, USA, Apr.17 – 20, 2016.

[6] **C. Tang**, M. Steinbrueck, M. Grosse, A. Jianu, A. Weisenburger, H.J. Seifert. High temperature steam oxidation of potential cladding materials-FeCrAl alloy and Ti_2AlC MAX phase, 21st QUENCH Workshop, Karlsruhe, Germany, Oct. 27 – 29, 2015.

[7] **C. Tang,** M. Steinbrueck, M. Grosse, H.J. Seifert. High temperature steam oxidation of FeCrAl alloy and Ti_2AlC MAX phase, Fourth Meeting of the OECD-NEA Expert Group on Accident Tolerant Fuels for LWRs, PSI, Switzerland, Sept. 17 – 18, 2015.

Poster presentations

[1] A. Jianu, A. Weisenburger, R, Fetzera, **C. Tang**, et al. Corrosion behavior of Fe-Cr-Al-based alloys exposed to oxygen-containing molten lead, supercritical water and steam, NEA International Workshop Structural Materials for Innovative Nuclear Systems (SMINS-4), Manchester, UK, Jul. 11 – 22, 2016.

Acknowledgements

Firstly, I would like to express my sincere appreciation towards my supervisor, Prof. Dr. Hans Jürgen Seifert, for giving me his tremendous guidance, instructive and expert advice through my research and thesis. Without his supervision and kind support, this research work would not have been possible.

I would like to extend my sincere appreciation to Prof. Dr. Jochen M. Schneider for his willingness and precious time to be the co-referee of my thesis.

My very special thanks are indebted to my tutors Dr. Martin Steinbrück and Dr. Michael Stüber for their excellent supervision, unlimited guidance and thoughtful discussions at various stages of my research. I really appreciate their great patience and tolerance on my mistakes and continuous encouragement toward my progress. They are the best leaders I ever met, and my research could not go well without their organization and support.

My thesis work has been built up on an excellent cooperation and support of the colleagues from high-temperature chemistry group and thin film group. I would like to give my deepest gratitude to them for their advices and help. I give my special gratitude to Mirco Große for his advices and discussions and to Ulrike Stegmaier and Petra Severloh for training me and helping me in the lab. I gratefully acknowledge Prof. Dr. Sven Ulrich and Dr. Harald Leiste for their fruitful guidance and discussions during my research. My deepest thanks also go to Stefan Zils for his patience and support in training of the sputtering facility. I acknowledge the help provided by Dr. Jian Ye and Dr. Monika Rinke during the nanoindentation and Raman spectroscopy analyses. My thanks also go to Ingo Markel, Jürgen Glaser, Dr. Sarfraz Ahmad, Dr. Valentina Avincola, Marc Strafela, Yin Gao and Steffen Mumbauer for their invaluable suggestions and kind helps during my research and daily life. I thank Ms. Jutta Howell and Ms. Cathrin Schuler for their help during these years.

I also would like to thank Tobias Weingaertner for AES measurements, Philip Kolja Erbes for EPMA measurements, Dr. Thomas Bergfeldt for chemical analysis, Dr. Holger Geßwein for HTXRD measurements, Dr. Michael Klimenkov and Ute Jäntsch for preparing the samples for TEM imaging.

I acknowledge all members of the institute at IAM for them creating a professional, friendly and pleasant working atmosphere: Dr. Dajian Li, Dr. Weibin Zhang, Wenjiao Zhao, Dr. Juri Stuckert, Dr. Peter Franke, Dr. Yuantao Cui, Marco Klotz, Jutta Laier, Philipp van Appeldorn, and other members.

I thank PSI for providing beam time for H_2 permeation investigations and Dr. Pavel Trtik for kind help during the measurements. Furthermore, I would like to give my thanks to the colleagues from IHM institute, especially to Dr. Adrian Jianu, Dr. Alfons Weisenburger and Hao Shi, for the good cooperation and fruitful discussions.

I also take this opportunity to thank many friends for their help when I arrived and settled in Germany and they make my life here easier. Thanks a lot for the friends from IFG institute. I am very thankful to

the friends and colleagues, especially to Prof. Kuiren Liu, Prof. Jianshe Chen and Prof. Shuchen Shun and Yapeng Kong in Northeastern University, China, for their support and encourage.

My sincerely and deeply gratitude gives to my wife, parents, my younger sister, parents-in-law for their endless love and unwavering support throughout the years. Thanks my beloved wife, Dr. Xiaojuan Yu, for accompanying by my side, endurance and caring support and understanding in difficult times. To live is not just to be alive, one must have dream and poem. Thanks my parents without whose love and support my study in Germany would never be realized. Thanks all my relatives for their support, love and encouragement in my whole life.

Finally, I thank the Helmholtz programs NUSAFE and STN and the China Scholarship Council (CSC) for providing the financial support during my PhD study.